

Novel Low Complexity Biomedical Signal Processing Techniques for Online Applications

THÈSE N° 8522 (2018)

PRÉSENTÉE LE 24 AOÛT 2018

À LA FACULTÉ DES SCIENCES ET TECHNIQUES DE L'INGÉNIEUR
GROUPE SCI STI JMV
PROGRAMME DOCTORAL EN GÉNIE ÉLECTRIQUE

ÉCOLE POLYTECHNIQUE FÉDÉRALE DE LAUSANNE

POUR L'OBTENTION DU GRADE DE DOCTEUR ÈS SCIENCES

PAR

Sasan YAZDANI

acceptée sur proposition du jury:

Prof. P. Frossard, président du jury
Dr J.-M. Vesin, directeur de thèse
Prof. D. Finlay, rapporteur
Dr M. Lemay, rapporteur
Prof. D. Atienza Alonso, rapporteur



ÉCOLE POLYTECHNIQUE
FÉDÉRALE DE LAUSANNE

Suisse
2018

آن کس که بداند و بداند که بداند اسب خرد از گنبد کردون بجماند
 آن کس که بداند و نداند که بداند آگاه ناسید که بس خفته ماند
 آن کس که نداند و بداند که نداند لنگان خرک خویش به منزل برساند
 آن کس که نداند و نداند که نداند در جهل مرکب ابدالدهر ماند
 آن کس که بداند و نخواهد که بداند خود را به بلندای سعادت برساند
 آن کس که بداند و نداند که بداند با کوزه آب است ولی تشنه ماند
 آن کس که نداند و نخواهد که بداند جان و تن خود را ز جهالت برماند
 آن کس که نداند و نخواهد که بداند حیف است چنین جانوری زنده ماند

- ابن یسین

He who knows and knows he knows
 Rides his flying horse on top of the skies
 He who knows but doesn't know he knows
 Rush to wake him up, help him open his eyes
 He who doesn't know and knows he doesn't know
 Drags his limping mule through the lows and highs
 He who doesn't know and doesn't know he doesn't know
 Remains unwise, till the day he dies
 He who knows and wants to know
 Will live in bliss, full of happiness
 He who knows but doesn't know he knows
 Walks around thirsty carrying a jug full of water
 He who doesn't know but wants to know
 Through lifetime of efforts frees himself of ignorance
 He who doesn't know and doesn't want to know
 It a shame for this creature to be alive

- Ebn-e Yamin (Knowledge and oblivion,
circa 1285 – 1368)

Abstract

Biomedical signal processing has become a very active domain of research nowadays. With the advent of portable monitoring devices, from accelerometer-enabled bracelets and smart-phones to more advanced vital sign tracking body area networks, this field has been receiving unprecedented attention. Indeed, portable health monitoring can help uncover the underlying dynamics of human health in a way that has not been possible before. Several challenges have emerged however, as these devices present key differences in terms of signal acquisition and processing in comparison with conventional methods. Hardware constraints such as processing power and limited battery capacity make most established techniques unsuitable and therefore, the need for low-complexity yet robust signal processing methods has appeared. Another issue that needs to be addressed is the quality of the signals captured by these devices. Unlike in clinical scenarios, in portable health monitoring subjects are constantly performing their daily activities. Moreover, signals may be captured from unconventional locations and subsequently, be prone to perturbations. In order to obtain reliable measures from these monitoring devices, one needs to acquire dependable signal quality measures, to avoid false alarms.

Indeed, hardware limitations and low-quality signals can greatly influence the performance of portable monitoring devices. Nevertheless, most devices offer simultaneous acquisition of multiple physiological parameters, such as electrocardiogram (ECG) and photoplethysmogram (PPG). Through multi-modal signal processing the overall performance can be improved, for instance by deriving parameters such as heart rate estimation from the most reliable and uncontaminated source.

This thesis is therefore, dedicated to propose novel low-complexity biomedical processing techniques for real-time/online applications. Throughout this dissertation, several bio-signals such as the ECG, PPG, and electroencephalogram (EEG) are investigated. The main contribution of this dissertation consists in two signal processing techniques : 1) a novel ECG QRS-complex detection and delineation technique, and 2) a short-term event extraction technique for biomedical signals. The former is based on a processing technique called mathematical morphology (MM), and adaptively uses subject QRS-complex amplitude- and morphological attributes for a robust detection and delineation. This method is generalized to intra-cardiac electrograms for atrial activation detection during atrial fibrillation. The second method, called the Relative-Energy algorithm, uses short- and long-term signal energies to highlight events of interest and discard unwanted activities. Collectively, the results obtained by these methods suggest that while presenting low-computational costs, they can efficiently and robustly extract biomedical events of interest.

Using the relative energy algorithm, a continuous non-binary ECG signal quality index is presented. The ECG quality is determined by creating a cleaned-up version of the input ECG and calculating the correlation coefficient between the cleaned-up and the original ECG. The proposed quality index is fast and can be implemented online, making it suitable for portable monitoring scenarios.

The proposed techniques are employed in two miscellaneous applications namely, 1) false alarm reduction in intensive care units (ICU), and 2) the investigation of U-shaped patterns during

sleep in polysomnography recordings. The former is carried out to provide robust arrhythmia detection in ICUs by means of multi-modal signal processing techniques. The latter explores U-shaped phenomenon during sleep, studies their statistical properties, and provides an explanation to how these patterns may correspond to movement events during sleep.

Keywords : Biomedical signal processing, Multi-modal signal processing, Electrocardiogram, Intra-cardiac electrograms, Electroencephalogram, Electromyogram, Imaging photoplethysmography, Polysomnography , Signal quality assessment, Arrhythmia analysis, ECG QRS-complex detection, Atrial activity detection, EEG K-complex detection.

Résumé

Le traitement des signaux biomédicaux est devenu de nos jours un domaine de recherche très actif. Avec l'avènement des dispositifs de surveillance portatifs, des bracelets à accéléromètre et des téléphones intelligents aux réseaux de capteurs de signes vitaux plus avancés, ce domaine a reçu une attention sans précédent. En effet, le suivi d'état physique par dispositif portable peut aider à découvrir la dynamique sous-jacente de la santé humaine d'une manière innovante. Plusieurs défis sont apparus cependant, car ces dispositifs présentent des différences importantes en termes d'acquisition et de traitement du signal par rapport aux méthodes conventionnelles. Les contraintes matérielles telles que puissance de traitement et capacité limitée de la batterie rendent la plupart des techniques établies inadaptées et, par conséquent, le besoin de méthodes de traitement du signal à la fois simples et robustes est apparu.

Un autre problème à résoudre est celui de la qualité des signaux captés par ces appareils. Contrairement à ce qui se passe dans les scénarios cliniques, les sujets sous surveillance poursuivent constamment leurs activités quotidiennes. De plus, les signaux peuvent être capturés sur des emplacements non conventionnels et, de ce fait, être sujets à des perturbations. Afin d'obtenir des mesures fiables à partir de ces dispositifs de surveillance, il est nécessaire de développer des mesures robustes de qualité de signal afin de minimiser les fausses alarmes.

Les limitations matérielles et les signaux de faible qualité peuvent donc grandement influencer les performances des dispositifs de surveillance portables. Cependant, la plupart des dispositifs permettent l'acquisition simultanée de plusieurs paramètres physiologiques, tels que l'électrocardiogramme (ECG) et le photopléthysmogramme (PPG). Grâce à un traitement multimodal, la performance globale peut être améliorée, par exemple en dérivant des paramètres tels que celui de la fréquence cardiaque à partir de la source la plus fiable et la moins contaminée.

Cette thèse est donc dédiée à proposer des techniques nouvelles de traitement biomédical de faible complexité pour des applications en temps réel / en ligne. Tout au long de cette thèse, plusieurs bio-signaux tels que l'ECG, le PPG, et l'électroencéphalogramme (EEG) sont étudiés.

La contribution principale de cette dissertation consiste en deux techniques de traitement du signal : 1) une nouvelle technique de détection et de délimitation du complexe QRS dans l'ECG, et 2) une technique d'extraction d'événements à court terme pour les signaux biomédicaux. Le premier est basé sur une technique de traitement appelée morphologie mathématique (MM), et utilise de manière adaptative les attributs morphologiques du complexe QRS pour une détection et une délimitation robustes. Cette méthode est généralisée aux électrogrammes intra-cardiaques pour la détection de l'activation auriculaire pendant la fibrillation auriculaire. La deuxième méthode, appelée l'algorithme de l'énergie relative, utilise des énergies de signal à court et à long terme pour mettre en évidence les événements d'intérêt et rejeter les activités indésirables. Collectivement, les résultats obtenus par ces méthodes suggèrent que tout en présentant de faibles coûts de calcul, ils peuvent extraire de manière efficace et robuste des événements biomédicaux d'intérêt.

En utilisant l'algorithme d'énergie relative, un indice de qualité du signal ECG, non binaire et continu, est présenté. La qualité de l'ECG est déterminée en créant une version nettoyée de l'ECG

d'entrée et en calculant le coefficient de corrélation entre l'ECG nettoyé et l'ECG d'origine. L'indice de qualité proposé est rapide et peut être mis en œuvre en ligne, ce qui le rend approprié pour des scénarios de surveillance portables.

Les techniques proposées sont employées dans deux applications diverses à savoir, 1) la réduction des fausses alarmes dans les unités de soins intensifs (USI), et 2) l'étude des motifs U pendant le sommeil dans les enregistrements de polysomnographie. Le premier est réalisé pour fournir une détection d'arythmie robuste dans les unités de soins intensifs au moyen de techniques de traitement de signaux multimodaux. Le deuxième explore le phénomène des motifs en U pendant le sommeil, étudie leurs propriétés statistiques et leur relation aux épisodes de mouvement pendant le sommeil.

Mots-clés : Traitement du signal biomédical, Traitement du signal multimodal, Electrocardiogramme, Electrogrammes intra-cardiaques, Électroencéphalogramme, Électromyogramme, Photopléthysmographie par imagerie, Polysomnographie, Évaluation de la qualité du signal, Analyse d'arythmie, Détection ECG complexe QRS, Détection de l'activité auriculaire, Détection EEG K-complexe .

Acknowledgments

Achievements in life maybe obtained solely through focus, desire, and hard work, but for it to be an enjoyable experience, one needs to be surrounded by loved ones and caring friends. In my personal experience, achievements in life can only be satisfying only if accompanied by joy.

- I would like to start by thanking the president of jury Prof. Pascal Frossard, and the experts Prof. Dewar Finlay, Dr. Mathieu Lemay, and Prof. David Atienza for accepting to be a part of my Ph.D. experience. Thank you for reading my manuscript and providing me with constructive comments.
- To Dr. Nicolas Bourdillon and Prof. Gregoire Millet and their hardworking team, thank you for all the invaluable data you have provided me throughout these years. An especial thank you to Nicolas for always being a text message away and providing me with physiological explanations that would take me out of the oblivion time and again. I would also like to thank Prof. Etienne Pruvot and Dr. Patrizio Pascale for their guidance regarding cardiac electrophysiology and the wonderful things they thought me during my PhD. It was fascinating to come to CHUV and see your procedures.
- Thank you to my students Silas Schlatter, Alexandre Cherqui, and Priscille Laub. A especial thank you to Alex for all the time he spent on U-pattern analysis. Thank you Silas and Priscille for helping me with the challenges. It was nice collaborating with you, and I appreciate your efforts.
- A thank you to my sisters and brothers in arms, the "ASPG girls and boys". The Applied Signal Processing Group experience is one I will remember the rest of my life. First, I would like to thank the ASPG members of my generation: Sibylle Fallet, Leila Mir mohamadsadeghi, Andrea Buttu, Adrian Luca, and Ashkan Yazdani. You took me in with open arms. I consider it a privilege to have spent my PhD years with you. To Sibylle and Adrian, thank you for proofreading my manuscript. An especial thanks to Rosie for always being ready to help me with the administrative forms and attestations.
- I would also like to thank the past- and honorary ASPG members: Jerome, Laurent, Yann, Cedric, Mathieu, Vincent, Elda, Martin. Let me just say "Que tout aille bien pour nous ...".
- I would like to thank the coffee group: Sibylle, Leila, Elda, David, Damien, Adrian, Ashkan, and Jean-Marc. Thank you for the coffee, small daily anecdotes and the crazy stories. A man needs energy in the morning. I got it more from you than the coffee. Cheers!!!
- To my multi-national gang of Christina, Marion, Kirell, and Florian, I would like to say "Merci beaucoup". The well-spent time with you was full of jokes, happiness, and joy. Thanks to Christina and Marion for all the delicious desserts. Thanks to Kirell and Florian for the badminton, skying, gaming, and running sessions.
- An especial thanks to all my EPFL friends, the aforementioned and Marina, Anne-Flore,

Irene, Mario-Joao, Didrik, Murat, Gabriel, Dimitris, Christophe, and Vijay. It was quite an adventure: skying, swimming, tennis, geo-chasing, the picnics, and more importantly partying and enjoying each other's company. Thank you.

- To my life-long friends Soroush Pourreza, Amirhossein Zali, Moein Ghodrati, Reza Arababi. The insane time spent with you still hunts me day and night. I cannot even begin to describe the psychological toll you had on me. Thank you for everything. I look forward to the fun times ahead.
- To my close Lausanne friends Christina Boydev and Kirell Benzi, I would like to send an especial "Thank you". It was always easy with you, we would just click!!! Thank you.
- To my family, nothing would be possible without you, so thank you for your life-long support. To my father, I would like to say thank you for teaching me how to think. To my mother, thank you for all your love and sacrifices. To my siblings: Atousa, Anousha, Golchin and Ashkan, thank you all. Atousa, You were always there for me. Anousha, I could always rely on you. Golchin, you have no idea how much you mean to me. Ashkan, you opened my eyes to reality and helped me through hardships, thank you! I would like to especially thank my niece, nephew, and brother-in-law Anita and Arian, and Ali Nikkhah for their ever present support.
- In life you can be nice, kind, giving, nurturing, humble, a mountain of experience, and knowledgeable. But to be all at the same time is a great feat, and that is who you are Jean-Marc. You are so much more than just a supervisor to me. The life lessons I learned from you grew me into a better man and I will always cherish them. Thank you for everything.

Contents

Abstract	v
Résumé	vii
Acknowledgments	ix
1 Introduction	1
1.1 Motivation and Problem Statement	1
1.2 Objectives	2
1.3 Organization	3
1.4 Original Contributions	4
2 The Human Heart, Cardiac Regulation and the Electrocardiography	5
2.1 The Human Heart and the Cardiac Cycle	5
2.2 Heart Rate Control	6
2.3 Electrocardiography	8
2.3.1 Electrocardiogram (ECG)	10
2.4 Normal and Abnormal ECG	12
2.4.1 Cardiac Ectopy	12
2.4.2 Differential Arrhythmia	12
2.5 Ventricular and Atrial Fibrillation-Flutter	15
2.5.1 Ventricular Fibrillation (VF)	15
2.5.2 Ventricular Flutter	15
2.5.3 Atrial Fibrillation (AF)	16
2.5.4 Atrial Flutter	17
3 Real-Time QRS-complex Detection and Delineation in the ECG	19
3.1 Introduction	19
3.2 Mathematical Morphology (MM)	20
3.3 Adaptive Mathematical Morphology (AMM)	21
3.3.1 MM Filtering	22
3.3.2 Feature Signal Analysis and Peak Detection	23
3.3.3 Structuring Element Update	25
3.3.4 Parameter Update	27
3.4 Evaluation Databases	28
3.4.1 The MIT/BIH Arrhythmia Database	28
3.4.2 The Physionet QT Database	28
3.4.3 The Green Goblin Wearable ECG Database	28
3.5 Results and Discussion	29
3.5.1 Finding Optimized Parameters	29

3.5.2	AMM Performance Evaluation	32
3.6	Miscellaneous Applications	38
3.6.1	Adaptive Mathematical Morphology to Extract Atrial Activations from Intracardiac Electrograms	38
3.6.2	Methods	38
3.6.3	Results	40
3.6.4	Remarks on AA detection from the ICEG	41
3.7	Conclusion	42
4	Multimodal Signal Processing to Reduce False Alarms in the Intensive Care Unit	43
4.1	Introduction	43
4.2	Method	45
4.2.1	Data	45
4.2.2	Processing of ECG	51
4.2.3	Processing of PPG and ABP Waveforms	53
4.2.4	Arrhythmia Alarm Processing	55
4.2.5	Evaluation Metrics	58
4.3	Results	59
4.4	Discussion	59
4.5	Conclusion	63
5	Short-Term Event Extraction in Biomedical Signals	65
5.1	Introduction	65
5.2	Method	67
5.2.1	Relative-Energy (Rel-En) Algorithm	67
5.3	Examples of Applications of Rel-En	67
5.3.1	Rel-En for QRS-complex detection in ECG	68
5.3.2	Rel-En for K-complex Detection in EEG	74
5.3.3	Rel-En for Pulse Extraction from IPPG	77
5.4	General Discussion	80
5.5	Miscellaneous Applications	83
5.5.1	Extraction and Analysis of Short-Time Excursions in RR-interval Time Series	83
5.5.2	Principle	84
5.5.3	Adaptation to RR-Interval Time Series	85
5.5.4	Materials	86
5.5.5	Results and Remarks	86
5.6	Conclusion	88
6	Towards Instantaneous Assessment of ECG Signal Quality	91
6.1	Introduction	91
6.2	Method	92
6.2.1	QRS-complex Cancellation	92
6.2.2	Measuring the ECG Quality	94
6.3	Evaluation Data	94
6.3.1	The MIT/BIH Noise-Stress Test Database	94
6.3.2	The MIT/BIH Arrhythmia Database	95
6.3.3	The Physionet/CinC 2011 Challenge Database	96
6.4	Results	97
6.4.1	The MIT/BIH Noise-Stress Test Database	97
6.4.2	The MIT/BIH Arrhythmia Database	97

6.4.3	The Physionet/CinC 2011 Challenge Database	99
6.5	Discussion	101
6.6	Conclusion	103
7	Analysis of U-shaped Patterns in RR-intervals from PSG Recordings	105
7.1	Introduction	105
7.2	Research Material	106
7.2.1	Data	107
7.2.2	Phase A: Over-training	108
7.2.3	Phase B: Sleep Deprivation	109
7.3	U-shape Patterns	110
7.4	U-Pattern Extraction	111
7.4.1	Preprocessing	111
7.4.2	Extraction Method	111
7.5	U-pattern Extraction Performance Evaluation	115
7.5.1	Supervised U-pattern Extraction	115
7.5.2	Synthetic U-pattern Detection	116
7.6	The Incidence of U-Patterns in Sleep Deprivation and Over-training	118
7.6.1	Over-training	118
7.6.2	Sleep Deprivation	119
7.7	Correlation between U-patterns and Movement Events	120
7.7.1	Detection of Movement Events	121
7.7.2	U-Pattern/Movement Agreement Rate	122
7.7.3	Uncorrelated U-patterns	123
7.7.4	Causality	123
7.8	Discussion	125
7.9	Conclusion	126
8	Conclusion	129
8.1	Summary of achievements	130
8.2	Perspectives	133
	Appendix	135
A	Adaptive Frequency Tracking	137
A.1	The Concept of Instantaneous Frequency	137
A.2	Adaptive Frequency Tracking	138
A.2.1	OSC-MSE Algorithm	139
A.2.2	OSC-MSEc Algorithm	141
B	Classifier Evaluation and Ensemble of Classifiers	145
B.1	Evaluation of Classifiers	145
B.2	Classifier Combination: Selection and Fusion	147
B.3	The Wisdom of Crowds	149
C	Further Results on Instantaneous Signal Quality Index	151

D Further Results on U-patterns	155
D.1 Statistical Characteristics of U-patterns	155
D.1.1 The Over-training Study	155
D.1.2 The Sleep Deprivation Study	156
D.2 Agreement Rate	157
D.3 Uncorrelated Events	158
D.3.1 Uncorrelated U-patterns	158
D.3.2 Uncorrelated Movement Events	158
D.4 Causality	159
D.4.1 U-Pattern/Movement Onset Delays	159
D.4.2 U-Pattern/Movement Offset Delays	160
Bibliography	163
Curriculum Vitæ	183
Publications	185

List of Acronyms

AA	Atrial Activation
ABP	Arterial Blood Pressure
AF	Atrial Fibrillation or Flutter
AFCL	Atrial Fibrillation Cycle Length
AIMM	Adaptive Intra-cardiac Mathematical Morphology
AMM	Adaptive Mathematical Morphology
ANS	Autonomic Nervous System
ASPG	Applied Signal Processing Group
AV Node	Atrioventricular Node
BAN	Body Area Networks
bpm	Beat Per Minute
brpm	Breaths Per Minute
BW	Baseline Wander
CCM	Complex Correlation Measure
CNS	Central Nervous System
DER	Detection Error Rate
DF	Dominant Frequency
ECG	Electrocardiogram
EEG	Electroencephalography
EM	Electrode Motion Artifact
EMG	Electromyography
EOG	Electrooculography
F-wave	Flutter Wave
f-wave	Fibrillatory Wave
FN	False Negative Sample
FP	False Positive Sample
HF	High Frequency Band

HR	Heart Rate
HT	Hilbert Transform
IBI	Inter-beat Intervals
ICEG	Intra-cardiac Electrogram
ICU	Intensive Care Unit
IF	Instantaneous Frequency
iPPG	Imaging Photoplethysmography
ISQI	Instantaneous Signal Quality Index
LDA	Linear Discriminant Analysis
LF	Low Frequency Band
MA	Muscle Artifact
MM	Mathematical Morphology
nLF	Normalized Low Frequency Band Power
NREM	Non-Rapid Eye Movement
PA	Peak Activity
PI	Plosion Index
PPG	Photoplethysmography
PPV	Positive Prediction Value
PSD	Power Spectral Density
PSG	Polysomnography
PVI	Pulmonary Vein Isolation
PVT	Psychomotor Vigilance Test
Rel-En	Relative Energy
REM	Rapid Eye Movement
RMS	Root Mean Square
RMSE	Root Mean Square Error
ROI	Region of Interest
RRI	RR Interval Time Series
RSA	Respiratory Sinus Arrhythmia
SA Node	Sinoatrial Node
SE	Structuring Element
Se	Sensitivity
SNR	Signal-to-Noise Ratio
SPI	Spectral Purity Index
SQI	Signal Quality Index

SSA	Singular Spectrum Analysis
TN	True Negative Sample
TNR	True Negative Rate
TP	True Positive Sample
TPR	True Positive Rate
ULF	Ultra-Low Frequency Band
VF	Ventricular Fibrillation or Flutter
VT	Ventricular Tachycardia

List of Tables

2.1	Lead locations used in the 12-lead ECG setting.	9
3.1	Anthropometric parameters of the subjects in the wearable technology database.	29
3.2	Performance of AMM on QRS-complex detection on MIT/BIH arrhythmia database.	34
3.3	Comparison of performance with previously proposed methods on MIT/BIH arrhythmia database.	35
3.4	AMM performance on the manually annotated beats for QRS fiducial points, Physionet QT database.	35
3.5	AMM delineation performance and comparison, QT database.	36
3.6	Comparison of AMM performance with other methods on the wearable ECG database.	37
3.7	Performance comparison of the proposed method on atrial activity extraction on the annotated database.	41
4.1	Definition of the five alarm types.	45
4.2	Algorithms and selected parameters for HR estimation using PPG and/or ABP waveforms.	55
4.3	Results obtained on the hidden-test dataset.	59
4.4	Results for the training set.	59
4.5	Comparison between the proposed scheme and the voting algorithm.	60
4.6	Percentage of processed waveforms for each type of alarm in the training set.	60
4.7	Linear discriminant analysis for ventricular tachycardia alarms.	63
5.1	Rel-En QRS-complex extraction performance comparison with the state-of-the-art.	70
5.2	Detail performance of Rel-En on QRS-complex detection on MIT/BIH arrhythmia database.	71
5.3	Performance of Rel-En on automatic K-complex extraction and its comparison with the state-of-the-art.	75
5.4	Annotation agreement between the two annotators on excerpts annotated by both annotators.	76
5.5	Performance of Rel-En on iPPG peak detection and comparison with classic a threshold method.	79
5.6	Number of subjects out of 15 with a change from baseline to condition coherent with caffeine-induced sympathetic activation.	87
5.7	Asymptotic p -values for the two-sample Kolmogorov-Smirnov test between baseline and caffeine condition.	87
6.1	Recordings, leads and segments from the MIT/BIH arrhythmia database, used to evaluate the proposed method.	96

6.2	Average quality indexes obtained using the proposed method, on the MIT/BIH noise-stress database.	97
6.3	Average quality indexes obtained using the proposed method, on the MIT/BIH arrhythmia database.	99
6.4	Correlation coefficient between ISQI and ISNR for different noise classes, and different SNR levels.	99
6.5	Performance comparison with the stat-of-the-art on the Physionet/CinC 2011 challenge database.	101
7.1	Anthropometric parameters of the over-training study.	108
7.2	Anthropometric parameters of the sleep deprivation study.	109
7.3	Performance of the detection algorithm on the annotated U-patterns.	115
7.4	Performance evaluation on synthetic U-pattern detection.	118
7.5	Subject-by-subject number of extracted U-patterns for each phase of the over-training study.	118
7.6	Inter-subject U-pattern statistical characteristics, reported for each phase of the over-training study.	119
7.7	Two sample <i>t</i> -test <i>p</i> -values for each over-training phase.	119
7.8	Subject-by-subject number of detected U-patterns for different sleep deprivation phases.	119
7.9	Inter-subject U-pattern statistical characteristics, reported for each phase of the sleep deprivation study.	120
7.10	Two sample <i>t</i> -test <i>p</i> -values for each phase of the sleep deprivation study.	120
7.11	Inter-subject U-pattern/movement event agreement rate (%) with respect to 3-EMG, thorax, C3 and C4 channels.	122
7.12	Uncorrelated U-patterns in the sleep deprivation study, with respect to movement events extracted from 3-EMG, thorax, C3 and C4 channels.	124
7.13	Inter-subject averages of U-pattern/Movement onset delays (seconds), with respect to 3-EMG, thorax, C3 and C4 channels.	124
7.14	Inter-subject averages of U-pattern/Movement offset delays (seconds), with respect to 3-EMG, thorax, C3 and C4 channels.	124
B.1	Confusion matrix of hypothetical model trained for a binary classification problem.	145
D.1	Frequency (in mHz) of the detected U-patterns for each subject and for different over-training phases.	155
D.2	Mean duration (in s) of the detected U-patterns for each subject and for different over-training phases.	155
D.3	Mean depth (in ms) of the detected U-patterns for each subject and for different over-training phases.	155
D.4	Mean integral (in ms.s) of the detected U-patterns for each subject and for different over-training phases.	155
D.5	Frequency (in mHz) of the detected U-patterns for each subject and for different sleep deprivation phases.	156
D.6	Mean duration (in s) of the detected U-patterns for each subject and for different sleep deprivation phases.	156
D.7	Mean depth (in ms) of the detected U-patterns for each subject and for different sleep deprivation phases.	156
D.8	Mean integral (in ms.s) of the detected U-patterns for each subject and for the different sleep deprivation phases.	156

D.9 Agreement rates (in %) between U-patterns and the extracted movement events during the baseline phase.	157
D.10 Agreement rates (in %) between U-patterns and the extracted movement events during sleep-deprivation.	157
D.11 Agreement rates (in %) between U-patterns and the extracted movement events during recovery.	157
D.12 Uncorrelated U-patterns in the sleep deprivation study, w.r.t all available PSG channels.	158
D.13 Subject-by-subject percentage of uncorrelated peaks, with respect to the total number of peaks, baseline phase.	158
D.14 Subject-by-subject percentage of uncorrelated peaks, with respect to the total number of peaks, sleep deprivation phase.	158
D.15 Subject-by-subject percentage of uncorrelated peaks, with respect to the total number of peaks, sleep recovery phase.	159
D.16 Subject-by-subject averages of U-pattern/Movement onset delays (seconds), baseline phase.	159
D.17 Subject-by-subject averages of U-pattern/Movement onset delays (seconds), sleep deprivation phase.	159
D.18 Subject-by-subject averages of U-pattern/movement onset delays (seconds), recovery phase.	160
D.19 Subject-by-subject averages of U-pattern/movement offset delays (seconds), baseline phase.	160
D.20 Subject-by-subject averages of U-pattern/movement offset delays (seconds), sleep deprivation phase.	160
D.21 Subject-by-subject averages of U-pattern/movement offset delays (seconds), recovery phase.	161

List of Figures

2.1	The human heart and its four main chambers, the left and right atria and ventricles.	5
2.2	The electrical conduction system of the heart.	6
2.3	Diagram of the human nervous system.	7
2.4	Heart innervation of sympathetic and parasympathetic divisions of the ANS.	7
2.5	Illustration of normal and augmented limb leads.	8
2.6	Illustration of the positioning of precordial leads.	9
2.7	12-lead standard ECG of a normal heart.	9
2.8	ECG of a normal cardiac cycle and the manifestation of repolarization and depolarization on heart muscles.	10
2.9	The cardiac cycle and its correspondence to ECG.	11
2.10	Illustration of RR-interval time series.	11
2.11	Illustration of cardiac ectopic beats.	13
2.12	Illustration bigeminy and trigeminy arrhythmias.	14
2.13	Illustration of bundle branch block arrhythmia.	14
2.14	The initiation and propagation of electrical stimulus during ventricular fibrillation.	15
2.15	Behavior of ventricular fibrillation on the ECG.	15
2.16	Behavior of ventricular flutter on the ECG.	16
2.17	Behavior of atrial fibrillation on the ECG.	17
2.18	Electrical stimulus propagation in the atria during atrial flutter and atrial fibrillation	17
2.19	Behavior of atrial flutter on the ECG.	18
3.1	Block diagram of the adaptive mathematical morphology (AMM) technique.	21
3.2	The synthesized structuring element used to initialize AMM.	22
3.3	Effect of different MM operators on the ECG.	23
3.4	Illustration of the AMM feature signal, i.e. the output of the MM filtering phase.	24
3.5	AMM approach on detecting the polarity of the QRS-complex.	24
3.6	The structuring element update phase of AMM.	25
3.7	Beat-to-beat structuring element update of AMM.	26
3.8	Illustration of AMM performance on tape 108 from the MIT/BIH arrhythmia.	28
3.9	Illustration of MM filtering on tape 106 from the MIT/BIH arrhythmia database using a fixed and adaptive structuring element.	30
3.10	Evolution of the detection accuracy (1-DER), sensitivity and PPV with respect to the ratio between the length of the SE and that of the actual QRS-complex.	31
3.11	Evolution of the detection accuracy (1-DER), sensitivity and PPV with respect to the ratio between the magnitude of the SE and that of the actual QRS-complex.	31
3.12	Evolution of the detection accuracy (1-DER), sensitivity and PPV with respect to the learning coefficient (α).	32
3.13	Evolution of the detection accuracy (1-DER), sensitivity and PPV with respect to different <i>stepsizes</i> (δ).	32

3.14	Illustration of AMM performance on tape 117 from the MIT/BIH arrhythmia database.	33
3.15	Illustration of AMM performance on tape 200 from the MIT/BIH arrhythmia database.	33
3.16	Illustration of AMM performance on the QT database for each fiducial point. . .	36
3.17	Illustration of AMM performance on an ECG recored by a smart shirt, while subject is performing a vigorous running activity.	37
3.18	Block diagram of the proposed method to extract atrial activations from intra-cardiac electrograms	39
3.19	Synthesized structuring element and the selection of its magnitude based on the intra-cardiac electrogram at hand.	39
3.20	Performance of the proposed method on a low quality intra-cardiac electrogram. .	41
3.21	Performance box plot of the proposed method.	41
4.1	The general framework to determine the validity of an alarm.	44
4.2	Example of a true asystole alarm (tape a142s).	46
4.3	Example of a false asystole alarm (tape a134s).	46
4.4	Example of a true bradycardia alarm (tape b455l).	47
4.5	Example of a false bradycardia alarm (tape b332s).	47
4.6	Example of a true tachycardia alarm (tape t174s).	48
4.7	Example of a false tachycardia alarm (tape t409l).	48
4.8	Example of a true ventricular tachycardia alarm (tape v648s).	49
4.9	Example of a false ventricular tachycardia alarm (tape v169l).	49
4.10	Example of a true ventricular flutter/fibrillation alarm (tape f544s).	50
4.11	Example of a false ventricular flutter/fibrillation alarm (tape f121l).	50
4.12	AMM performance on an ECG channels (record a527l) from the training set. . .	51
4.13	AMM performance on ECG channels (record t320s) from the training set. . . .	51
4.14	Example of signal purity index (SPI) for a true ventricular tachycardia alarm. . .	53
4.15	Example to illustrate the interest of using multiple inputs for adaptive frequency tracking.	55
4.16	Example of HR estimation using the proposed adaptive band-pass filter.	56
4.17	Asystole alarm processing.	57
4.18	Extreme bradycardia alarm processing.	57
4.19	Extreme tachycardia alarm processing.	57
4.20	Ventricular flutter/fibrillation alarm processing.	58
4.21	Ventricular tachycardia alarm processing.	58
4.22	Example of a recording in the training set with a good quality ECG lead as well as a bad quality lead.	61
4.23	Examples of PPG signal behavior during true ventricular tachycardia episodes. .	62
5.1	Illustration of different steps of the Rel-En algorithm on a synthetic signal composed of an impulse series added to a sinusoid.	68
5.2	Illustration of different steps of the Rel-En algorithm on tape 105 of the Physionet MIT/BIH arrhythmia database.	69
5.3	Performance of Pan-Tompkins and Rel-En algorithms against an ECG with added synthesized EMG noise.	72
5.4	Illustration of ECG enhancement using Rel-En.	73
5.5	Power spectral density of the Original ECG, noisy ECG and the enhanced ECG by means of Rel-En filtering.	73
5.6	Illustration of performance of Rel-En on excerpt 6 from the K-complex database. .	76
5.7	Region of interest used to extract iPPG waveforms.	77

5.8	Extracted iPPG channels alongside the captured ECG from a recording.	78
5.9	Illustration of Rel-En iPPG peak detection performance.	79
5.10	Effect of short- and long-term window lengths on Rel-En performance.	81
5.11	Effect of the exponent parameter p , on Rel-En performance for K-complex detection.	82
5.12	Illustration of short-duration increase and decrease, present in healthy RR-interval time series.	83
5.13	RR-interval time series of 256 consecutive heartbeats in a normal subject at supine rest.	84
5.14	Synthetic impulse extraction using Rel-En.	85
5.15	RR-intervals acceleration extraction using Rel-En.	86
5.16	The effect of RR-intervals impulse cancellation on the estimation of instantaneous respiration frequency.	88
6.1	Illustration of the different steps of QRS-complex cancellation using Rel-En.	93
6.2	Calculation of the instantaneous signal quality index.	95
6.3	Calculated ISQI on tape 118 (lead MLII) of the MIT/BIH Noise-Stress database.	98
6.4	Correlation between instantaneous signal quality index (ISQI) and instantaneous signal-to-noise ratio (ISNR).	100
6.5	Illustration of the evolution of ISQI against various noise types.	102
7.1	An idealized hypnogram summarizing the distribution of the sleep stages through a typical night.	106
7.2	Image of a subject equipped with the PSG.	108
7.3	Detailed information on data acquisition during the over-training study.	109
7.4	Detailed information on data acquisition during the sleep deprivation study.	110
7.5	Illustration of a U-shaped pattern taking place during sleep.	110
7.6	The preprocessed RR-intervals, used for U-pattern extraction, taken from an ECG excerpt of a baseline sleep deprivation PSG recording.	111
7.7	Illustration of the different steps of the Rel-En algorithm on an inversed RR-intervals.	112
7.8	Output of the Rel-En algorithm on the inversed RR-interval time series.	112
7.9	The difference between a normal thresholding technique and a hysteresis comparator.	113
7.10	Selection of a U-pattern candidate from the output of Rel-En algorithm, using a hysteresis comparator.	114
7.11	Extraction of U-patterns from the output of the Rel-En algorithm.	114
7.12	Automatic U-pattern detection for a night-long recording.	115
7.13	Baseline RR-interval time series generated for synthetic U-pattern detection.	116
7.14	Comparison between a real and a generated U-pattern.	117
7.15	Detection of U-patterns in an 8-hour synthetic recording.	117
7.16	Illustration of a single peak activity detection using Rel-En on the thorax channel.	121
7.17	Illustration of night-long peak activity detection using Rel-En on the thorax channel.	121
7.18	Illustration of night-long movement event extraction from the thorax channel.	122
7.19	U-pattern/thorax movement event agreement for a night-long PSG recording from the sleep deprivation study, baseline phase.	123
7.20	Causality between U-patterns/movement events.	125
A.1	General configuration of the adaptive band-pass filter.	139

A.2	Amplitude and phase responses of the bandpass filter used in the OSC-MSE algorithm	140
A.3	Configuration of the multi-signal adaptive frequency tracker (OSC-MSE-W). . .	141
A.4	Amplitude and phase response of the bandpass filter of the OSC-MSEc algorithm	142
B.1	An example classifier selection technique illustrated in a two attribute subspace. .	147
B.2	Typical framework of classifier fusion.	148
C.1	The correlation coefficient between instantaneous signal quality index and instantaneous signal-to-noise ratio. Tested against baseline wander.	151
C.2	The correlation coefficient between instantaneous signal quality index and instantaneous signal-to-noise ratio. Tested against EMG noise.	152
C.3	The correlation coefficient between instantaneous signal quality index and instantaneous signal-to-noise ratio. Tested against electrode motion artifact.	152
C.4	The correlation coefficient between instantaneous signal quality index and instantaneous signal-to-noise ratio. Tested against baseline wander + electrode motion artifact.	153
C.5	The correlation coefficient between instantaneous signal quality index and instantaneous signal-to-noise ratio. Tested against baseline wander + EMG noise. .	153
C.6	The correlation coefficient between instantaneous signal quality index and instantaneous signal-to-noise ratio. Tested against EMG noise + electrode motion artifact.	154
C.7	The correlation coefficient between instantaneous signal quality index and instantaneous signal-to-noise ratio. Tested against baseline wander + EMG noise + electrode motion artifact.	154

1

Introduction

1.1 Motivation and Problem Statement

We live in exciting times. The willingness to preserve precious lives is getting realized through medical advances made possible by technological breakthroughs. The advent of portable monitoring devices and body area networks (BAN) enables us to record physiological data and assess different aspects of human health. BANs open new horizons to a better understanding of health through the continuous recording of bio-signals over long spans of time (from several hours up to several days), a feat that could not be achieved until recently. Thanks to these portable devices and now ever present smart-phones, we are able to monitor the healthy population alongside the unhealthy. This allows for the identification and subsequently preemptive treatment of subjects who are either prone to certain conditions, or are in the early stages of serious health problems.

Nowadays, vast amounts of physiological data can be recorded through BANs. Indeed, the raw data captured through electrocardiography (ECG), photoplethysmography (PPG), etc., must be further processed in order to obtain sensible measures of health. This however, calls for efficient low-cost algorithms that can provide precise and reliable measures of patient health. Due to this need, even fundamental problems such as ECG-based heartbeat detection, which has already been extensively addressed in conventional settings, have become hot research topics again.

This thesis therefore aims to present efficient and low-cost biomedical signal processing techniques with an emphasis on cardiac bio-signals, suitable for real-time/online scenarios. Indeed, cardiac data embodies the majority of the information recorded by BANs. Cardiac problems are also the main mortality factor worldwide. The first step to assess cardiac health is studying the time variability of successive heartbeats. However, reliable heartbeat detection is of utmost importance to achieve precise measurement. The ECG reflects electrical activity of the heart through time, captured at body surface. Yet, ECGs are often polluted by different perturbation sources such as power-line interference, muscle activity and base-line wander [1]. This is especially true for portable devices, with subjects physically active, unlike in clinical settings. Continuous heartbeat detection in scenarios in which perturbations contaminate ECGs, can be an especially difficult task as signal characteristics vary overtime and become non-stationary.

Another issue that needs to be addressed with the rise of portable monitoring devices is the reliable measurement of signal quality. To put things in perspective, one can speak of ECG waveform delineation. Heartbeat classification and subsequently arrhythmia analysis can be realized through a good QRS-complex fiducial point extraction. Analyses based on heartbeat

morphology [2–4] and its time-frequency properties [5], have shown to provide reliable results. However, morphological properties can be altered with high levels of noise. Moreover, the waveform delineation performance will not be as accurate for noisy ECGs [6]. Therefore, a drop in heartbeat classification performance is inevitable, which can then lead to unreliable arrhythmia analysis [7]. In clinical studies, low quality signals can be manually discarded from analysis to avoid this problem. However, in a portable setting one needs to assess the quality of signals recorded by the device. This is especially true for ECGs, continuous blood pressure recordings, and PPG signals since they constitute a set of fundamental signals from which, several measures such as heart rate, systolic-, diastolic-, and mean-blood pressures are derived. To some extent, PPG and blood pressure quality assessment has been addressed in the literature. Li and Clifford have shown that beat-to-beat variation of fiducial point amplitudes and signal slopes can be used to measure the quality of pulsatile signals (blood pressure and PPG) [8, 9]. ECG quality assessment techniques have also been proposed in the literature. Methods based on missing lead and flat-line information [10–13], high-frequency activity [12, 14, 15], and impulsive noise detection [11, 13] have been proposed to detect noisy signals in a binary fashion. However, there is a sensible lack of continuous non-binary ECG signal quality assessment, which this thesis aims to address.

Additionally, portable e-health devices usually measure several bio-signal in a continuous and instantaneous fashion. Therefore, multi-modal signal processing schemes can be employed to provide reliable measurements. To clarify, consider the intensive care unit, where bedside cardiac monitoring devices have been associated with high false alarm rates [16]. The limited performance of these bedside monitors can have severe repercussions such as desensitization of medical staff and longer response times. However, one can use multi-modal signal processing schemes to alleviate this issue. In a portable setting, for instance, one can estimate the heart rate from either the ECG and/or pulsatile waveforms, by performing quality assessment and using the more reliable bio-signal.

The aforementioned issues are of high concern. Most portable devices today, such as sport-, activity monitors, and GPS watches can only be used as a nice gadget for technology fans. Only by addressing these issues can we depend on the measures provided by portable e-health monitoring systems; Devices that have gone through regulatory procedures and can provide clinically acceptable results.

1.2 Objectives

Although fundamental analyses of biomedical signals, such as ECG heartbeat detection, have been thoroughly carried out in the recent years, the state-of-the-art focuses on conventional settings such as standard 12-lead ECGs and hospital recording conditions. Top performing algorithms are mostly specialized for specific settings or biomedical applications and therefore, when exposed to real-life situations, most techniques are unable to perform at the same level as that of the clinical settings. With the rise of portable recordings, these fundamental analyses have become hot topics of research again. There is an emphasis on reliability and robustness-to-noise, while at the same time computational complexity must be kept low. The assessment of noise in the signal also needs to be addressed as even in the conventional settings, this issue has not been alleviated thoroughly.

This dissertation aims at proposing novel biomedical signal processing techniques that work in near real-time/online scenarios with low computational cost. Throughout this thesis, there is a especial focus on algorithms suitable for portable health monitoring and BANs. As the most common bio-signals recorded today, ECGs, EEGs, and PPGs are the main focus here, however, ECGs are primarily investigated as their importance in uncovering the underlying dynamics of the heart cannot be underestimated.

In summary and as an abstract outlook, the objectives of this dissertation are as follows:

- To develop a robust ECG QRS-complex detection and delineation technique.
 - QRS-complex fiducial point extraction.
 - Investigation of possible extension of the technique to intra-cardiac electrograms for atrial activation detection.
- To investigate the potential of multi-modal bio-signal processing and the application of false alarm detection in the intensive care unit.
- To develop a short-term event extraction technique designed for biomedical signals.
 - ECG QRS-complex detection.
 - EEG K-complex extraction.
 - Imaging PPG peak detection.
- To provide a technique for instantaneous measure of ECG signal quality.

1.3 Organization

Throughout this dissertation, two novel techniques are described, which are then supplemented by their extension to biomedical applications. This dissertation comprises eight chapters and four appendices, the details of which are as follows.

Introduction to bio-signals used in the context of this thesis

Chapter 2 provides some introductory information on the aspects of human physiology studied in this thesis. This chapter describes the human heart and its electrical conduction system. The electrocardiogram, normal and abnormal cardiac cycles are explained, and the description of the most common cardiac arrhythmia is provided.

ECG QRS-complex detection and delineation

A novel heartbeat detection and delineation algorithm is introduced and evaluated in Chapter 3. Through a technique called mathematical morphology, this algorithm adaptively detects and delineates QRS-complexes in the ECG. During its adaptation phase, the morphological attributes of the detected heartbeats are used for robust heartbeat extraction and waveform delineation. The algorithm is thoroughly evaluated on standard and wearable ECG databases. Furthermore, in Chapter 4 the algorithm is used in a multi-modal signal processing scheme to detect false alarms in intensive care units. As a part of an international competition, the proposed scheme outperformed all other algorithms, achieving the highest percentage of false alarm suppression in the Physionet/CinC 2015 challenge.

Short-term event extraction in biomedical signals

Chapter 5 proposes a novel event detection technique for biomedical signal processing applications. The proposed method is easy to implement and is computationally uncostly. Furthermore, it offers a small number of parameters for event extraction. These parameters are easy to determine and near optimal values do not drastically change the performance obtained by the algorithm. Three biomedical signal processing applications were used to assess the proposed method namely, ECG QRS-detection, EEG K-complex detection, and heartbeat detection in imaging PPG.

Continuous ECG signal quality assessment

Based on the same event-extractor algorithm, an ECG signal quality index is developed in Chapter 6. While easily computed, this quality index can be implemented in near real-time, providing continuous measure of ECG quality. The algorithm is thoroughly tested against different types of noise and standard databases.

Miscellaneous

As an exploratory application to the event-extraction algorithm proposed in Chapter 5, a phenomenon referred to as U-patterns in polysomnography recordings is studied. Chapter 7 is focused on these patterns taking place during sleep, providing a definition, detection scheme, and studying the possible correlation between these events and movements during sleep.

Finally, Chapter 8 provides a conclusion to this dissertation with a summary of achievement and possible perspectives. The appendices provide introductory information on adaptive frequency tracking, and two-class machine learning evaluation metrics that are used throughout this dissertation. Moreover, they provide detailed results on some applications discussed in the thesis.

1.4 Original Contributions

The main contributions¹ of this thesis are:

- Development of robust event extraction techniques for biomedical signal processing.
 - Low complexity ECG QRS-complex detection schemes.
 - QRS-complex fiducial point detection and delineation.
 - EEG K-complex extraction.
 - Imaging PPG heartbeat detection.
- Multi-modal bio-signal analysis.
 - Analyzing ECG, blood pressure and PPG signals to identify false alarms in intensive care units.
 - Detection of life threatening arrhythmias such as tachycardia, bradycardia, ventricular tachycardia, ventricular flutter/ fibrillation, and asystole.
- Development of a continuous on-line ECG signal quality assessment technique.
- Definition of U-pattern phenomenon taking place during sleep in polysomnography (PSG) recordings.
 - A robust scheme for U-pattern extraction from PSG recordings.
 - Study of U-pattern statistical attributes during sleep deprivation and over-training.
 - Study of the correlation between U-patterns and movement events during sleep.

1. See also the list of publications at the end of this manuscript (pages 185-187).

The Human Heart, Cardiac Regulation and the Electrocardiography

2

This chapter provides an introduction to the human heart, the cardiac conduction system, the study of electrical characteristic of the heart, and the influence of the autonomic nervous system on heart. Furthermore, electrocardiography is described with introduction to normal and abnormal electrocardiograms. Finally, a short description of the most common arrhythmia is provided with an especial focus on the ones used within the context of this dissertation.

2.1 The Human Heart and the Cardiac Cycle

The human heart is a muscular organ that performs the task of re-oxygenation and distribution of the re-oxygenated blood through the body. Located in the middle and slightly to the left of the chest, between the two lungs, it comprises four main chambers as illustrated in 2.1. The two upper chambers, called the atria, are relatively smaller than the two bottom chambers, the ventricles. The right atrium receives the de-oxygenated blood from the body through the superior and inferior venae cavae and through the tricuspid valve, pumps it into the right ventricle. While contracting, the right ventricle ejects the blood into the lungs for re-oxygenation. The left atrium gets the oxygenated blood from the lungs via pulmonary veins and pumps it through the mitral valve, to the left ventricle, which then pumps the oxygenated blood to the body [17].

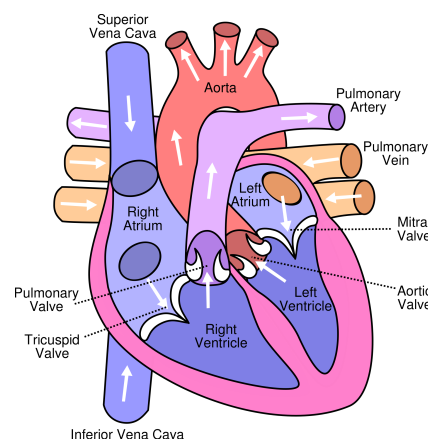


Figure 2.1 – The human heart and its four main chambers, the left and right atria and ventricles.

The contraction of atria and ventricles are due to the stimulating electrical signals transmitted by the electrical conduction system of the heart, as illustrated in Fig. 2.2. The normal heartbeat contraction starts by an electrical signal generated in the sinoatrial (SA) node in the right atrium, depolarizing cardiac cells and propagating through both atria, causing simultaneous atrial contraction [18, 19]. Once the electrical signal reaches the bottom of the right atrium to the atrioventricular (AV) node, it traverses the node and the bundle of His, splits through the left and right bundle branches, and causes ventricular contraction once it reaches the Purkinje fibers [20].

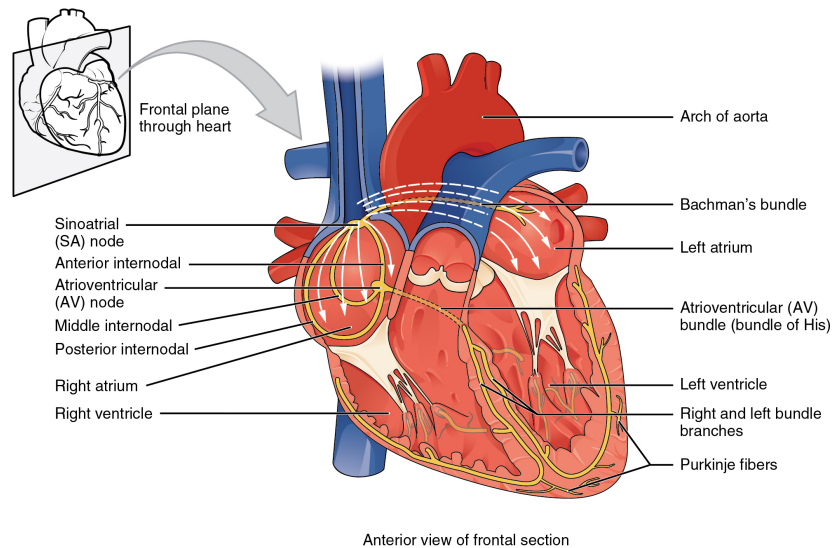


Figure 2.2 – The cardiac electrical conduction system showing nodes, bundles and Purkinje fibers. © OpenStax, Anatomy & Physiology.

After contraction (depolarization), cardiac cells undergo a relaxation (repolarization) phase, during which they cannot be depolarized until they reach their resting potential. The myocardium contracts again as a new electrical stimulus is generated in the SA node and propagated throughout the heart. This cycle of depolarization and repolarization of the myocardium is called the cardiac cycle.

2.2 Heart Rate Control

Heartbeats are initiated by the electrical stimulus generated from the SA node. However, the rate of these initiations is controlled by the human nervous system and more specifically the autonomic nervous system (ANS) [21]. Fig. 2.3 illustrates a block diagram of the human nervous system. Based on the feedback from the sensory division, via the peripheral nervous system, the central nervous system (CNS) provides the necessary control for the motor division. In the motor division, the somatic nervous system is in charge of conveying directives to skeletal muscles, while the ANS is in control of heartbeat regulation. ANS has two subdivisions namely, the sympathetic and parasympathetic nervous systems. The sympathetic division, also known as the "fight or flight" system, is the accelerator and is typically active when quick responses are required, while the parasympathetic division, known as the "rest and digest" system, is involved with functions that do not need quick reaction, such as food digestion [22].

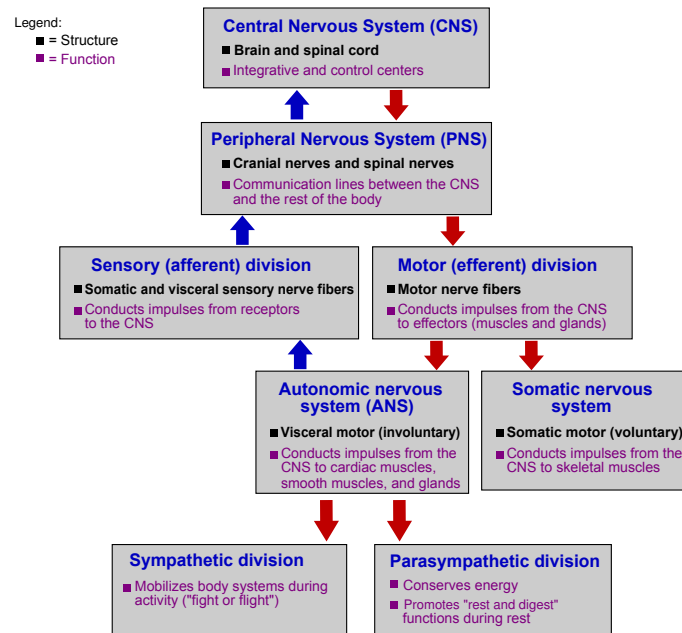


Figure 2.3 – Diagram of the human nervous system.

Both subdivisions of the ANS innervate the heart with the parasympathetic division stimulating the SA and AV nodes, while the sympathetic efferent nerves are present throughout the atria (especially the SA node) and ventricles. The influence of the sympathetic and parasympathetic divisions of the ANS is illustrated in Fig. 2.4. Although these divisions have contradictory functions, they have a more complementary than an antagonistic behavior. The parasympathetic division, also known as the vagal division, lowers the heart rate by releasing acetylcholine. Conversely, the sympathetic division increases the heart rate based on both internal and external stimuli by releasing noradrenaline, which not only increases the SA node firing rate, but also increases the velocity in the heart conduction system as well as the ventricular contraction force [23].

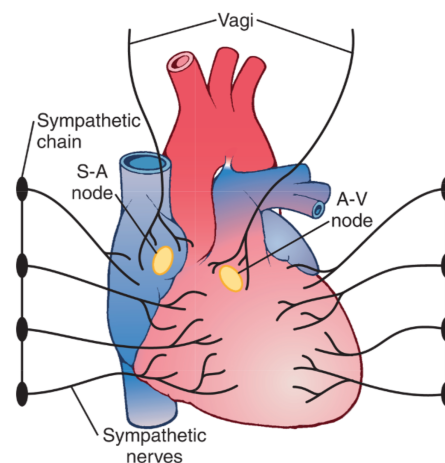


Figure 2.4 – Heart innervation of sympathetic and parasympathetic divisions of the ANS. Taken from [23] with permission.

2.3 Electrocardiography

The electrical activity propagated through the heart can be captured at body surface using the electrocardiograph. As the cardiac cycle takes place, the electrocardiograph records the electrical changes through its leads, which are placed at different positions on the body. The electrocardiograph leads can be placed either on the limbs (limb leads) or on the chest (precordial leads).

Limb leads are located one on each arm and one on the left leg. Lead I, II, and III are respectively defined as the voltage between the left (LA) and right (RA) arms, left leg (LL) and the right arm, and left leg and left arm, as reported in Eq. 2.1-2.3.

$$I = V_{LA} - V_{RA} \quad (2.1)$$

$$II = V_{LL} - V_{RA} \quad (2.2)$$

$$III = V_{LL} - V_{LA} \quad (2.3)$$

Moreover, three augmented leads can be derived from leads I, II, and III. Fig. 2.5 demonstrates how the limb leads and augmented limb leads are calculated.

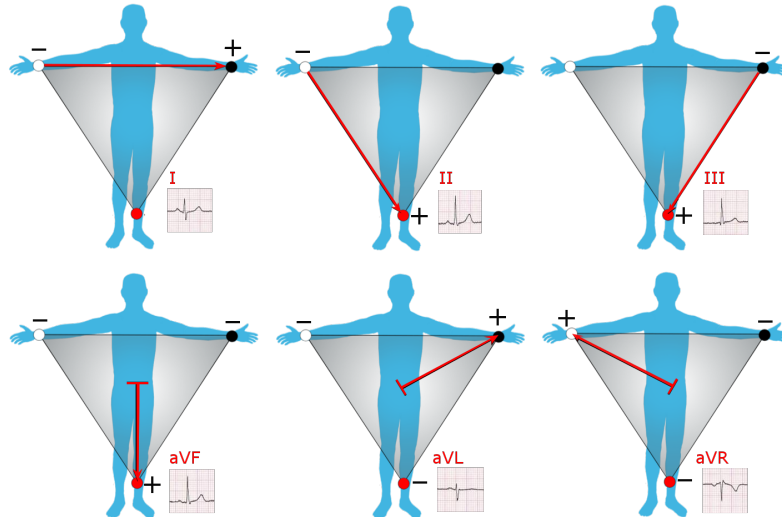


Figure 2.5 – Illustration of normal (I, II, and III) and augmented limb leads (aVF, aVL, aVR).
© Nicholas Patchett, Rice University.

In Fig. 2.5, aVR, aVL and aVF respectively stands for augmented vector right, augmented vector left and augmented vector foot. These three augmented leads can be calculated through the Eq. 2.4-2.6

$$aVR = V_{RA} - \frac{1}{2}(V_{LA} + V_{LL}) \quad (2.4)$$

$$aVL = V_{LA} - \frac{1}{2}(V_{RA} + V_{LL}) \quad (2.5)$$

$$aVF = V_{LL} - \frac{1}{2}(V_{RA} + V_{LA}) \quad (2.6)$$

On the other hand, precordial leads comprise six leads, V1-V6, placed on subject chest, as illustrated in Fig. 2.6. The heart surface is very close to the chest and therefore, each precordial

lead mainly records the electrical potential of the cardiac muscle structure directly underneath them. In this way, even minuscule ventricular abnormalities can be detected by studying precordial lead electrocardiograms.

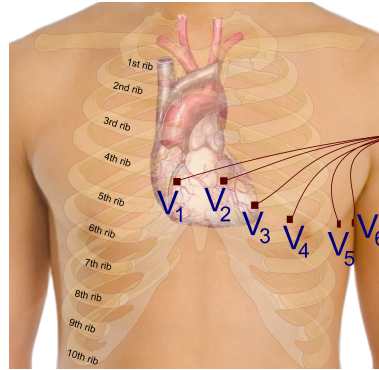


Figure 2.6 – Illustration of the positioning of precordial leads.

The 12-lead ECG is the standard setting used for electrocardiography, which is measured by the six precordial leads and the four limb leads. Table 2.1, summarizes the location used for each lead with regard to the body surface. Furthermore, Fig. 2.7 illustrates a normal ECG captured in a 12 lead setting.

Table 2.1 – Lead locations used in the 12-lead ECG setting.

Lead Name	Lead Location on with Regard to the Body
RA	On the right arm, avoiding muscles to reduce muscle activity interferences.
LA	At the same location where RA was placed, but on the left arm.
RL	On the right leg, lower end of calf muscle. Works as the ECG ground.
LL	At the same location where RL was placed, but on the left leg.
V1	Between ribs 4 and 5 just to the right of the sternum.
V2	Between ribs 4 and 5 just to the left of the sternum.
V4	Between ribs 5 and 6 in the mid-clavicular line.
V3	Between leads V2 and V4.
V5	Horizontally even with V4, in the left anterior axillary line.
V6	Horizontally even with V4 and V5 in the midaxillary line.

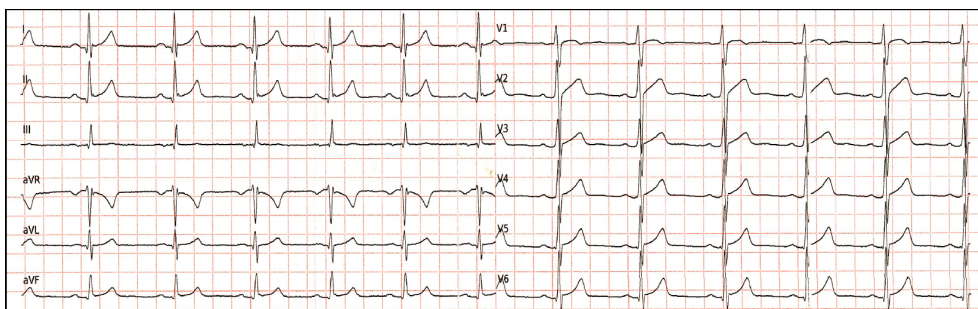


Figure 2.7 – 12-lead standard ECG of a normal heart (author's ECG). Vertical grid lines represent the amplitude with lines spaced at 1mV. Horizontal lines represent time with lines corresponding to 250ms.

2.3.1 Electrocardiogram (ECG)

The electrocardiogram (ECG) shows the electrical activity changes of heart through time. Repolarization and depolarization of atria and ventricles manifest themselves differently in the ECG. Fig. 2.8 shows a normal cardiac cycle for a human heart as seen on the ECG.

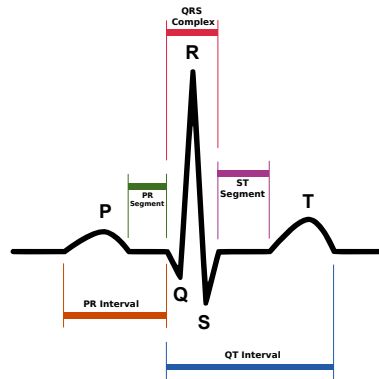


Figure 2.8 – ECG of a normal cardiac cycle and the manifestation of repolarization and depolarization on heart muscles.

In this figure, three major waves can be observed, namely the P-wave, the QRS-complex, and the T-wave. P-wave represents the depolarization of right and left atria, starting from the SA node towards the AV node. The QRS-complex is the depolarization of the ventricles. As the ventricles are much larger than the atria, the QRS-complex has a more prominent amplitude than that of the P-wave. The T-wave represents the repolarization of the ventricles. When studying the ECG, intervals between these waveforms reveal various information on subject health. The PR-interval, measured from the beginning of the P-wave to the start of the QRS-complex, denotes the propagation time of the electrical stimulus from the SA node through the AV node. The QT-interval represents the cycle of depolarization and repolarization of the ventricles. PR- and ST-segment respectively represent the AV traversal time and the interval in which the ventricles remain depolarized [24]. Fig. 2.9 illustrates different steps in the cardiac cycle and its correlation with the ECG.

Alongside inter-cycle intervals, inter-beat intervals (IBI) also reveal important information of subject health. More specifically, in the ECG, the successive difference between R-waves, i.e. the peak in the QRS-complex, constitute a time-series known as the RR-intervals. Fig. 2.10 illustrates an RR-interval time series extracted from an ECG in normal sinus rhythm. As demonstrated in Fig. 2.10-b, the interval between successive heartbeats fluctuates through time. This fluctuation is known as heart rate variability (HRV) [25]. Over the past decades, the relevant literature has provided several HRV indexes that facilitated the understanding of the underlying mechanism of the ANS [25]. By performing spectral analysis of RR-intervals in different frequency bands one can obtain useful information on the symapatho-vagal balance. Especially, the power in the low frequency (LF) band [0.04 - 0.15] Hz is known to reflect both sympathetic and parasympathetic activities, while the high frequency (HF) band [0.15 - 0.4] Hz is known to represent solely parasympathetic activity. Furthermore, the peak frequencies and powers in the LF and HF bands change through time, which is believed to reflect ANS modulation of the heart [26–28]. HRV analysis has been used to study cardiac and mental health. Several works have reported the usefulness of HRV indexes in the detection of myocardial dysfunction [29, 30], cardiac arrhythmia [31, 32], sepsis [33, 34], and schizophrenia [35, 36]. Furthermore, HRV has been used as a marker of stress [37, 38], or even emotion [39, 40], which shows the importance of HRV analysis.

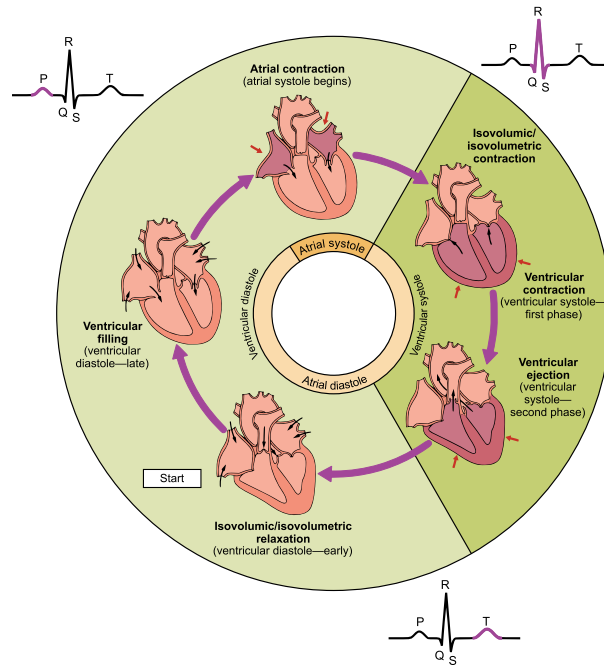


Figure 2.9 – The cardiac cycle and its correspondence to ECG. © OpenStax, Anatomy & Physiology.

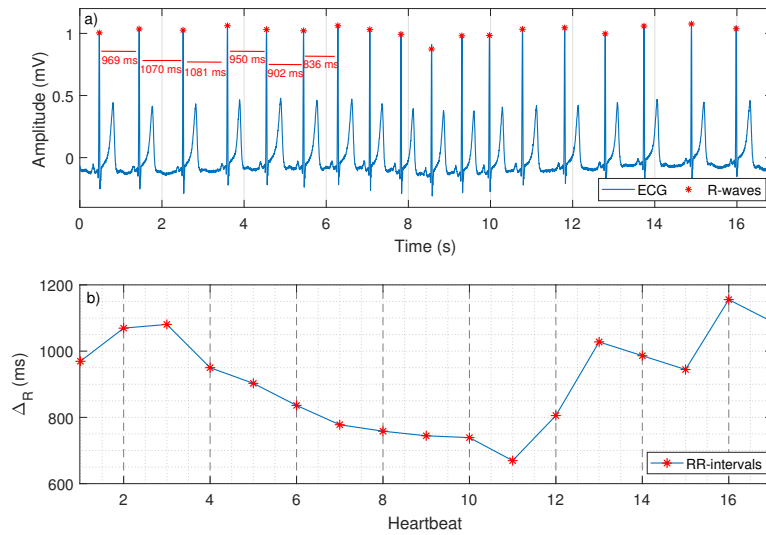


Figure 2.10 – Illustration of RR-intervals. a) ECG together with the detected QRS-complexes b) The extracted RR-interval time series, defined as the successive time difference between the detected R-waves.

2.4 Normal and Abnormal ECG

The ECG helps reveal the electrical conduction mechanism of the heart. A normal conduction originates from the pacemaker cells in the SA node and reaches the ventricles via the AV node. Therefore, a normal sinus rhythm ECG comprises the P-wave, the QRS-complex, and the T-wave. Deviation from this pattern is generally considered abnormal, with different abnormalities having different effects on the ECG. These abnormalities are known as cardiac arrhythmia and can be categorized in multiple fashions. For instance to identify the origin of the cardiac arrhythmia, it can be classified as supra-ventricular (i.e. originating in the atria), junctional (junction between atria and ventricles), or ventricular (i.e. originated in the ventricles). Another way to categorize them is to study arrhythmia separately or in a sequence, which are introduced next.

2.4.1 Cardiac Ectopy

This type of arrhythmia is caused by electrical discharges, self generated from a group of cardiac cells that are not a part of cardiac electrical conduction system. Ectopic beats can be sub-categorized as follows:

- **Premature Atrial Contraction (PAC).** This arrhythmia occurs when a region within the atria depolarizes before the electrical stimulus generated from the SA node [41]. The cause of PACs is unclear but it is common in healthy young and elderly subjects [42, 43]. Fig. 2.11-a illustrates an example of this arrhythmia. On the ECG, PACs are characterized by a different P-wave morphology. As the source of PAC is initiated in the atria, the electrical stimulus traverses the AV node normally and therefore the QRS-complex generally has a normal shape.
- **Premature Junctional Contraction (PJC).** Similarly to the PACs, this arrhythmia is due to impulses being generated by cells in the AV node. This rhythm generally manifest itself with an inverted P-wave or without a P-wave, a narrower QRS-complex, and can be diagnosed by studying the ECG [44, 45]. Fig. 2.11-b shows a premature junctional beat.
- **Premature Ventricular Contraction (PVC).** This arrhythmia takes place when ventricular contraction is initiated by Purkinje fibers ahead of the electrical stimulus from the SA node [45], as illustrated in Fig. 2.11-c. These ectopic beats have a different QRS-complex morphology that that of a normal heartbeat, creating wider complexes with generally more prominent T-waves [46]. PVCs have been associated with inefficient heart muscle oxygenation, but are often benign and can be seen even in healthy hearts [47].

2.4.2 Differential Arrhythmia

This type of arrhythmia comprise of groups of events in which cardiac cycles are irregular. These arrhythmias can be supra-ventricular or ventricular, and are generally associated with heart rate. The main differential arrhythmias studied in the context of this dissertation are listed below. Further information on rhythmic arrhythmia can be found in [43–45].

- **Cardiac Bradycardia.** This arrhythmia is defined as a slow cardiac rhythm with less than 60 beats per minute. Bradycardia are due to slowed SA activation or caused by blocks in either the SA node or the AV node, where the electrical activity stimulus is unable to travel its normal path.

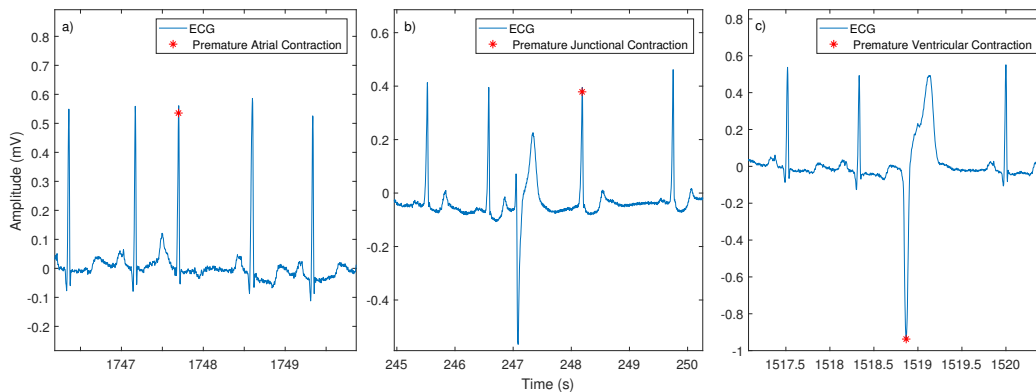


Figure 2.11 – Illustration of cardiac ectopic beats. a) Isolated premature atrial contraction, tape 100 from the MIT/BIH arrhythmia database [48]. b) Isolated premature junctional contraction, taking place right after a premature ventricular contraction, tape 114 from the MIT/BIH arrhythmia database. c) Isolated premature ventricular contraction, tape 100 from the MIT/BIH arrhythmia database. All depicted ECGs are recorded in modified lead II configuration [48].

- Cardiac Tachycardia.** Inversely to bradycardia, tachycardia is defined as fast heart rates above 100 beats per minute. Of course an increase in heart rate due to physical activity and stress is normal but if not generated from the SA node, for instance due to electrical activity re-entry in the atria, it might need to be treated.
- Bigeminy and Trigeminy.** These arrhythmia are due to the continuous alternation of sinus rhythm and ectopic beats. They can be both atrial or ventricular and are defined as a premature beat after one (bigeminy) or two (trigeminy) normal sinus beats. [45, 49]. Fig. 2.12 illustrates two ECG excerpts with bigeminy in sub-figure 2.12-a and trigeminy in 2.12-b.
- Atrio-Ventricular Blocks.** AV blocks are due to slowed to intermittent conduction (first and second degree AV blocks), or even a complete block on electrical stimulus in AV node (third degree block), see 2.13-b. These blocks can be seen in the ECG as PR-interval prolongation or as a P-wave without a following QRS-complex, usually detected by analyzing the RR-intervals.
- Bundle Branch Blocks (BBB).** These blocks are due to the heart electrical pathway defects, which alter conduction pathways and subsequently, alter the depolarization of the ventricles. This arrhythmia can alter the left (left bundle branch block) or the right (right bundle branch block) ventricle pathways. Fig. 2.13 illustrates two ECG excerpts with left BBB in sub-figure 2.13-a and right BBB in 2.13-b.

The electrical conduction system of the heart is designed to propagate the electrical stimulus from one end to the other, i.e. top to bottom from atria to ventricles. However, sometime the electrical stimulus travels in a circular path due to slow conduction in a region of atria or ventricles. Since cardiac cells are able to propagate the electrical stimulus once they reach their resting potential, this slow conductance can create vertices of electrical impulses propagating haphazardly through the heart. This re-entry of electrical stimulus that is not due to impulses generated from the SA node can result in supra-ventricular or ventricular fibrillation/flutter. As in the context of

this dissertation, both atrial and ventricular fibrillation/flutter are studied, a detailed description of these arrhythmias is provided next.

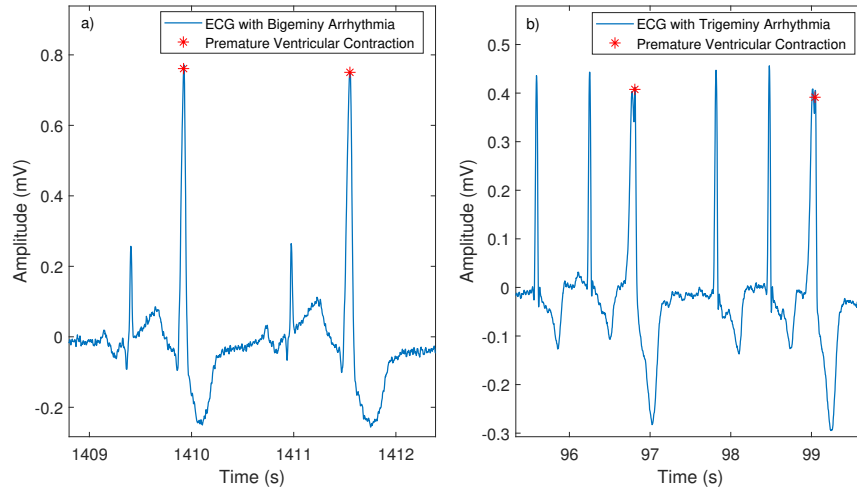


Figure 2.12 – Illustration bigeminy and trigeminy arrhythmias. a) bigeminy with highlighted premature ventricular contractions, tape 228 from the MIT/BIH arrhythmia database. a) trigeminy with highlighted premature ventricular contractions, tape 219 from the MIT/BIH arrhythmia database. All depicted ECGs are recorded in modified lead II configuration [48].

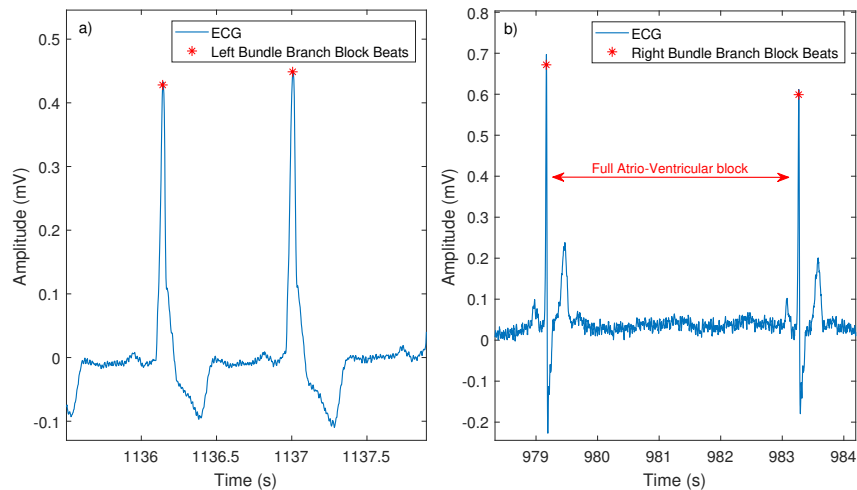


Figure 2.13 – Illustration of bundle branch block arrhythmia. a) Left bundle branch block, tape 214 from the MIT/BIH arrhythmia database. b) Right bundle branch block together with a full AV block in between, tape 232 from the MIT/BIH arrhythmia database. All depicted ECGs are recorded in modified lead II configuration [48].

2.5 Ventricular and Atrial Fibrillation-Flutter

2.5.1 Ventricular Fibrillation (VF)

Identified as the most dangerous cardiac arrhythmia, ventricular fibrillation (VF) is almost certain to be fatal, if the patient is not resuscitated within one to three minutes with cardiac defibrillators [23, 50, 51]. This arrhythmia is due to the unpredictable electrical stimulus behavior within the ventricular muscle. The source of this stimulus is known to start from one region of the ventricular muscle multiple times to a point that it eventually feeds itself and completely overrides the stimulus generated from the SA node [23]. During this arrhythmia, certain regions of ventricles contract while other regions relax, and therefore the ventricle cells are never working in harmony. This leads to little to no blood ejection and subsequently, the patient loses consciousness [23]. Fig. 2.14 depicts the initiation of ventricular fibrillation as well as the stimulus propagation during this arrhythmia.

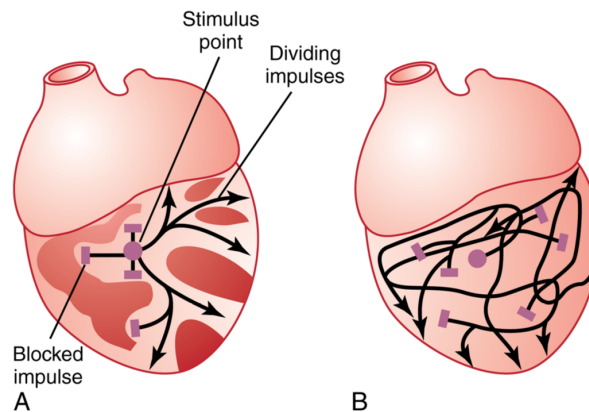


Figure 2.14 – a) The initiation of ventricular fibrillation and b) propagation of electrical stimulus during ventricular fibrillation. Taken from [23] with permission.

Ventricular fibrillation manifest in the ECG with a sinusoidal behavior, which is completely irregular in terms of amplitude, duration and the frequency, as illustrated in Fig. 2.15.

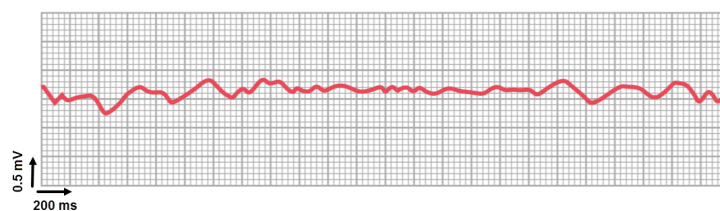


Figure 2.15 – Behavior of ventricular fibrillation on the ECG. Modified from [23] with permission.

2.5.2 Ventricular Flutter

Ventricular flutter, is a ventricular tachycardia (VT) with extremely rapid heart rates which vary between 250 to 350 beats per minute. Ventricular flutter is an unstable arrhythmia that is hardly seen, and is known to be the transition to ventricular fibrillation. On the ECG, ventricular

flutter manifests itself as high amplitude oscillations with no clear QRS-T waveform definition. Fig. 2.16 illustrates an ECG during ventricular flutter.

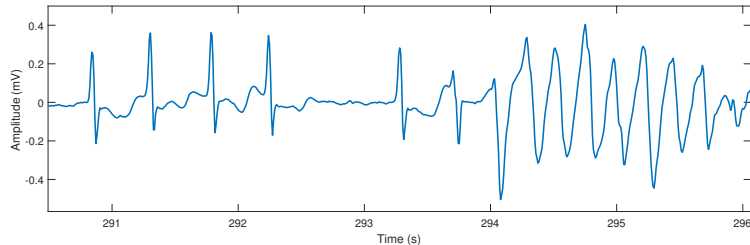


Figure 2.16 – Behavior of ventricular flutter on the ECG. Ventricular flutter begins after second 294. This is a Lead II ECG taken from the 2015 Physionet/CinC Challenge database [9].

2.5.3 Atrial Fibrillation (AF)

As previously pointed out, the electrical stimulus generated from the SA node can only reach the ventricles through AV node. This is because the ventricle muscles are separated from that of the atria by some fibrous tissue [23]. Therefore, the fibrillatory wave generated in the ventricles does not affect the atria. However, the fibrillatory wave can also initiate somewhere within the atria and cause what is known as atrial fibrillation (AF). The mechanism for AF is identical to that of the VF. One of the common causes of AF is the enlargement of atria, which is believed to be caused by valve lesions. These lesions do not allow for the atria to empty properly and over time the atrial wall dilates, which enhances the chances of fibrillatory wave propagation within the atria [23]. Similarly to VF, during AF, the atria do not pump the blood to the ventricles, causing a decrease (up to 30%) in cardiac blood pumping efficiency. Unlike VF, this arrhythmia is not imminently fatal but can cause severe health problems over time.

As the ventricular muscles are separated from the atrial muscles, and the AV node has a refractory period (period to reach the resting state after excitation), the ventricles do not get excited periodically but their contraction become irregular, influencing the characteristics of cardiac cycles on the ECG. As illustrated in Fig. 2.17-a, during AF, P-waves are replaced by rapid oscillations called the f-waves (fibrillatory waves), which vary in small amplitudes, as well as shape, and timing. The QRS-T segment of the ECG remains normal, unless the patient is suffering from some ventricular pathology. At the same time the RR-intervals become completely irregular, as illustrated in Fig. 2.17-b.

AF may occur as a unique episode or be recurrent. Depending on the duration of the episode, recurrent AF is further classified as: paroxysmal if it terminates spontaneously within 7 days, persistent if sustained beyond 7 days (<7 days if cardioversion, medical treatment to convert tachycardia to normal rhythm, is performed) or longstanding persistent in case of a continuous episode lasting more than one year. Finally, AF is defined as permanent if cardioversion has failed or was not attempted [53, 54].

AF is the most common arrhythmia in clinical practice, and is the leading cause for hospitalizations due to arrhythmias, heart failure and strokes. AF affects 2% of the general population [55] and its prevalence increases with age, from 0.5% between 50-59 years to 9% between 80-89 years [56, 57]. AF is complicated by hemodynamic impairment (loss of atrial contraction, irregular and rapid ventricular rate). This condition may lead to a tachycardia-induced atrial and ventricular cardiomyopathy with severe ventricular dysfunction and heart failure [58]. The most common and severe complications of AF are related to thromboembolic events [59]. AF compromises the mechanical function of both atria, leading to blood stasis and thrombus formation.

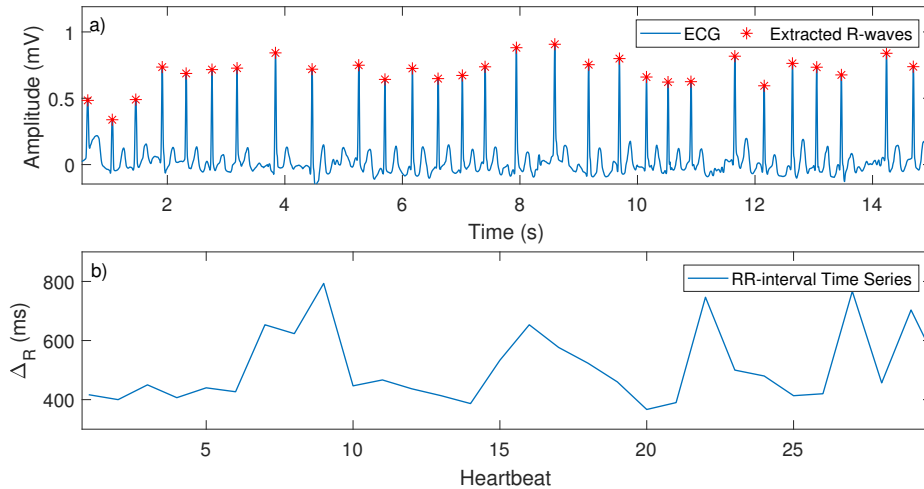


Figure 2.17 – Behavior of atrial fibrillation on the ECG. a) ECG during AF together with the detected R-waves. b) The RR-interval time series during AF. ECG from tape A00739 from the 2017 Physionet/CinC Challenge database [52], a custom lead representing the difference between left and right arms.

Dislodgement of thrombus secondary to AF is estimated to account for 20% of all ischemic strokes [57]. Importantly, AF is also associated with a 1.5- to 1.9-fold mortality risk [60]. With increasing life expectancy, the prevalence of AF is expected to double over the next fifty years. There is thus a growing need to develop curative strategies of AF, which, by restoring sinus rhythm, may prevent morbid and fatal complications.

2.5.4 Atrial Flutter

Atrial Flutter is a supra-ventricular tachycardia, similar to AF except that the electrical stimulus does not propagate randomly but rather in a circular path, as illustrated in Fig. 2.18. During this arrhythmia the atrial contraction rate varies between 200-350 beats per minute. The atrial pumping efficiency is higher compared to atrial fibrillation, but still inefficient. On the ECG, the RR-intervals remain irregular while the characteristics of the P-wave change (see Fig. 2.19-b). Similar to ventricular flutter, the saw-toothed flutter wave (F-wave) oscillations are easily discernible, as illustrated in Fig. 2.19-a.

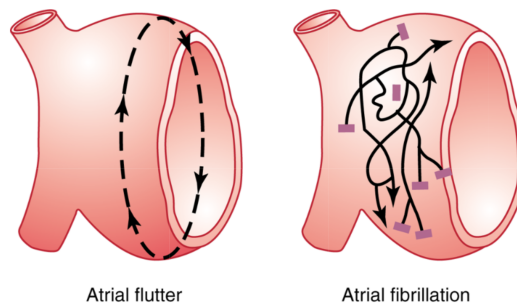


Figure 2.18 – Electrical stimulus propagation in the atria during atrial flutter (on the left) and atrial fibrillation (on the right). Taken from [23] with permission.

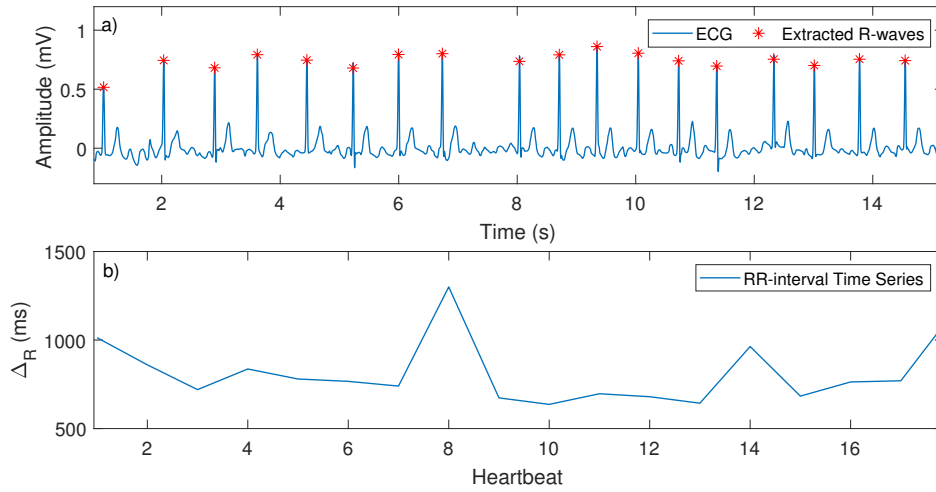


Figure 2.19 – Behavior of atrial flutter on the ECG. a) ECG during atrial flutter together with the detected R-waves. b) The RR-interval time series during atrial flutter. ECG from tape A00542 from the 2017 Physionet/CinC Challenge database [52], a custom lead representing the difference between left and right arms.

Real-Time QRS-complex Detection and Delineation in the ECG

3

3.1 Introduction

As mentioned in Chapter 2, the electrocardiogram (ECG) comprises different electrical waveforms, each representing either depolarization or repolarization of different muscles in the heart. Among these waveforms, the QRS-complex, corresponding to the ventricular contraction is the most prominent. The shape of this complex as well as the time of its appearance provides significant information for arrhythmia [7, 61–63], and heart rate variability analysis [37, 64, 65]. Due to its peaky shape and the fact that other waveforms can be small, or in some cases not even present in the ECG, the QRS-complex plays a fundamental role in the automatic detection of heartbeats [1].

However, the detection of QRS-complexes in the ECG is not always an easy task due to the physiological variability of the QRS and more importantly, the presence of perturbations caused by different sources such as power-line interference, muscle activity and baseline drift.

Generally, approaches consider two stages in QRS-complex detection, namely the filtering stage and the decision stage. In most methods, the ECG is first preprocessed by a low-pass filter to remove power-line interference at 50 Hz. Some approaches employ a band-pass filter with cutoff frequencies at about 10 and 25 Hz not only to suppress the acquisition noise and the baseline drift, but also other waveforms such as P-waves, T-waves.

Subsequently, in the decision stage, a feature signal is extracted from the filter output and compared with some heuristically chosen thresholds to determine whether a QRS-complex is taking place at a certain point in the ECG.

Over the years, several QRS detection approaches have been proposed in the literature. Derivative-based techniques, which can normally be found in the older studies, take advantage of the steep slope characteristic of the QRS-complex in the detection phase [66–72]. Approaches have used difference equations based on the first- [66, 69, 70], second derivatives [67, 71] or a combination of the former and latter [71].

More sophisticated algorithms were introduced in the literature based on digital filters [72–83]. Among these approaches, Pan and Tompkins [73] is maybe the most popular. This algorithm takes advantage of the amplitude, width and the steep slope characteristic of the QRS-complex for heartbeat detection. It is carried out by applying a bandpass filter on the original ECG followed by differentiation. Then, a feature signal is obtained by calculating the average of the squared differentiated signal. Subsequently, QRS-complexes are extracted by comparing the feature signal against an amplitude threshold.

Wavelet and filter bank methods have also been used for QRS-complex detection [74, 84–

89]. Li et al. [84] applied a wavelet transform (WT) to the ECG and found that R-peaks can be picked out from perturbations such as baseline drift and other waveforms if there are concurrent local modulus maxima at different WT scales, a detection logic concept also used in [85, 86, 88]. This work has had a major influence on other wavelet-based QRS-complex detectors. The work of Bahoura et al. [87] proposes a simplified version of [84].

Trahanias [53] used mathematical morphology (MM) operators on the ECG, both in the noise removal and detection phases, in which a different fixed structuring element (SE) was used. More recently, Zhang and Lian [90] proposed a three-stage MM approach. They studied how SEs with different lengths and slopes affect the output of the MM operators. Yet, at each filtering stage, a fixed SE was employed by the MM operators. Finally, the extracted feature signal was compared with a fixed or adaptive threshold to detect R-peaks.

Various other automatic QRS-detection techniques based on matched filtering [91–93], Hidden Markov Models [94], genetic algorithm [95], Shannon entropy [96], zero-crossing [97, 98], KNN classifiers [99], and other heuristics known as the length- and energy transforms have also been proposed in the literature [100–102]. Thorough reviews and comparisons of these methods can be found in [1, 103, 104].

The automatic detection of QRS-complexes is generally carried out by applying thresholds on the output of a filtering phase. These thresholds comprise physiological constraints, e.g. the time interval between two beats cannot be smaller than 250 milliseconds, and arbitrary thresholds, e.g. comparing the feature signal to a specific value to decrease the false detection rate. The former are always valid and can be useful for detection but the latter are based on the data at hand, can be hard to adapt when dealing with several subjects, or may need adjustment in different acquisition scenarios.

Even though automatic detection of QRS-complexes has been extensively investigated over the past few decades, some issues remain pending due to the diversity of QRS-complex shapes and perturbations, notably baseline drift. This is especially true for ECG signals acquired using wearable devices. The method proposed in this chapter aims at extracting QRS-complexes and their fiducial points using mathematical morphology (MM) with an adaptive structuring element, on a beat-to-beat basis. The structuring element is updated based on the characteristics of the previously detected QRS-complexes for a more robust and precise detection. Moreover, this method takes advantage of physiological constraints alongside a few, empirically selected, arbitrary thresholds. The MIT-BIH arrhythmia and Physionet QT databases were used to assess the detection performance of R-waves and other fiducial points. Furthermore, the proposed method was evaluated on a wearable-device dataset of ECGs during vigorous exercises.

The rest of this chapter is organized as follows. Section 3.2 focuses on a brief introduction on MM. The proposed approach and its implementation are explained in Section 3.3. Section 3.4 provides the description of the evaluation databases used in this study. In Section 3.5, the experimental results are presented and the quality of the QRS-complex detection is validated. Finally in Section 3.6, the main conclusions of this work are drawn. Elements of the methods and results in this chapter were originally presented as a conference paper [105], then published as a journal paper [6].

3.2 Mathematical Morphology (MM)

MM is a methodology proposed to extract topological information based on the analysis of geometrical structures. MM was first introduced for binary images with strong set-theoretic concepts, designed to extract useful information in images regarding shape and size [106]. Operators in MM non-linearly transform the signal of interest using another signal called the structuring element (SE). The outcome of an MM operator depends on the shape and length of the SE.

Essentially, MM is based on two elementary operators named dilation and erosion. Com-

binning dilation and erosion leads to additional operators such as opening, closing, top-hat and bottom-hat, the definitions of which are:

$$\text{Dilation } \oplus : (f \oplus g)(n) = \max_i \{f(n-i) + g(i)\} \quad (3.1)$$

$$\text{Erosion } \ominus : (f \ominus g)(n) = \min_i \{f(n+i) - g(i)\} \quad (3.2)$$

$$\text{Opening } \circ : f \circ g = (f \ominus g) \oplus g \quad (3.3)$$

$$\text{Closing } \bullet : f \bullet g = (f \oplus g) \ominus g \quad (3.4)$$

$$\text{Top_Hat } : \text{THat}(f) = f - f \circ g \quad (3.5)$$

$$\text{Bottom_Hat } : \text{BHat}(f) = f - f \bullet g \quad (3.6)$$

Where g represents the SE of length L . f is the signal with a length of N to which the MM operator is applied. These operators are easy to compute and simply defined. Therefore, they constitute a suitable option in cases where computation load plays an important role such as body-area networks. Figures 3.3-b through 3.3-g illustrate examples of these MM operators applied to an ECG. In these figures a peaky SE is used to enhance QRS-complexes.

In biomedical signal processing and more specifically QRS-complex detection, MM can be very useful due to their distinctive shape. By employing a peaky structure in MM operations, a filter can be designed which makes QRS-complexes more prominent and suppresses other waveforms, the desired effect sought in QRS-complex detection.

3.3 Adaptive Mathematical Morphology (AMM)

AMM is an MM filtering technique with an adaptive SE. This novel technique, proposed in the context of this thesis, adaptively changes this element used in MM filters for QRS-complex detection and delineation. The adaptation takes advantage of the topological features of the subject's heartbeats and uses them for a more robust and precise detection. AMM can be considered as a 4-step algorithm, a block diagram of which is shown in Figure 3.1.

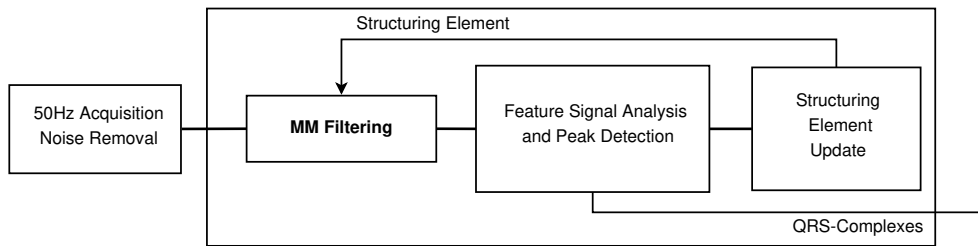


Figure 3.1 – Block diagram of AMM.

Before the detection of QRS-complexes in the ECG is carried out, the signal must be conditioned by removing various potential perturbations. Power-line interference, high frequency muscle activity and low-frequency baseline drift are among the most dominant perturbations. The proposed method, however, only uses a low-pass filter with a cutoff frequency at 50 Hz, mainly to remove the power-line interference.

3.3.1 MM Filtering

As mentioned in Section 3.2, MM operators use an SE to manipulate the signal. However, there is usually no information about the specific shape and magnitude of the QRS-complexes of a specific subject, before detecting heartbeats in the ECG. Therefore, a synthesized QRS-like SE is necessary for the initialization of the AMM. This SE is synthesized using a priori knowledge on a general QRS-complex. Like a typical heartbeat complex, this SE comprises five fiducial points namely, R-peak, Q-point, S-point together with onset and offset, equally spaced in time in the synthesized element, as shown in Figure 3.2. The duration of the element is 90 milliseconds, which represents an average normal QRS duration [107].

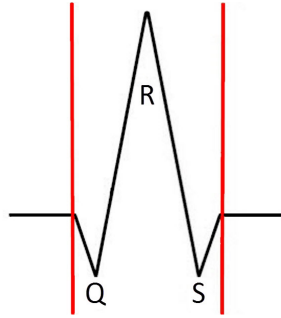


Figure 3.2 – The synthesized structuring element used to initialize AMM. This structuring element has a duration of 90 ms, with fiducial points equally spaced in time. The vertical lines before the Q-point and after the S-point respectively represent the onset and offset of the structuring element. The iso-electric lines are added to this figure for demonstration purposes.

However, the magnitude of the SE is both lead- and subject-dependent and cannot be determined using a priori knowledge. Therefore, this value should be determined from the ECG at hand. To initialize AMM, the magnitude of the SE is considered as the difference between the maximum and minimum of the first two seconds of the ECG.

Using the synthesized SE, the average of top-hat and bottom-hat is calculated on a one-second window of the ECG. This average can be computed using Equation 3.7, which results in a feature signal (FS) with only non-zero values at peaks and valleys, mostly corresponding to QRS-complexes.

$$FS = f - \frac{f \circ g + f \bullet g}{2} \quad (3.7)$$

Figure 3.3 shows the effect of each MM operator using the structuring element described above. It is worth mentioning that dilation and erosion operators not only expand and shrink the QRS-complexes, but also have a direct impact on their amplitude. Opening and closing, demonstrated in Figures 3.3-c and 3.3-e, are obtained by eroding the ECG with the SE, followed by dilating the output with the same SE, and vice versa. The top- (Figure 3.3-d) and bottom-hat (Figure 3.3-f) operators respectively give rise to peaks and valleys in their output. The average of these operators, i.e. the feature signal (Figure 3.3-h), extracts the peaks and valleys from the original signal, i.e. f in Equation 3.7, and discards other activities.

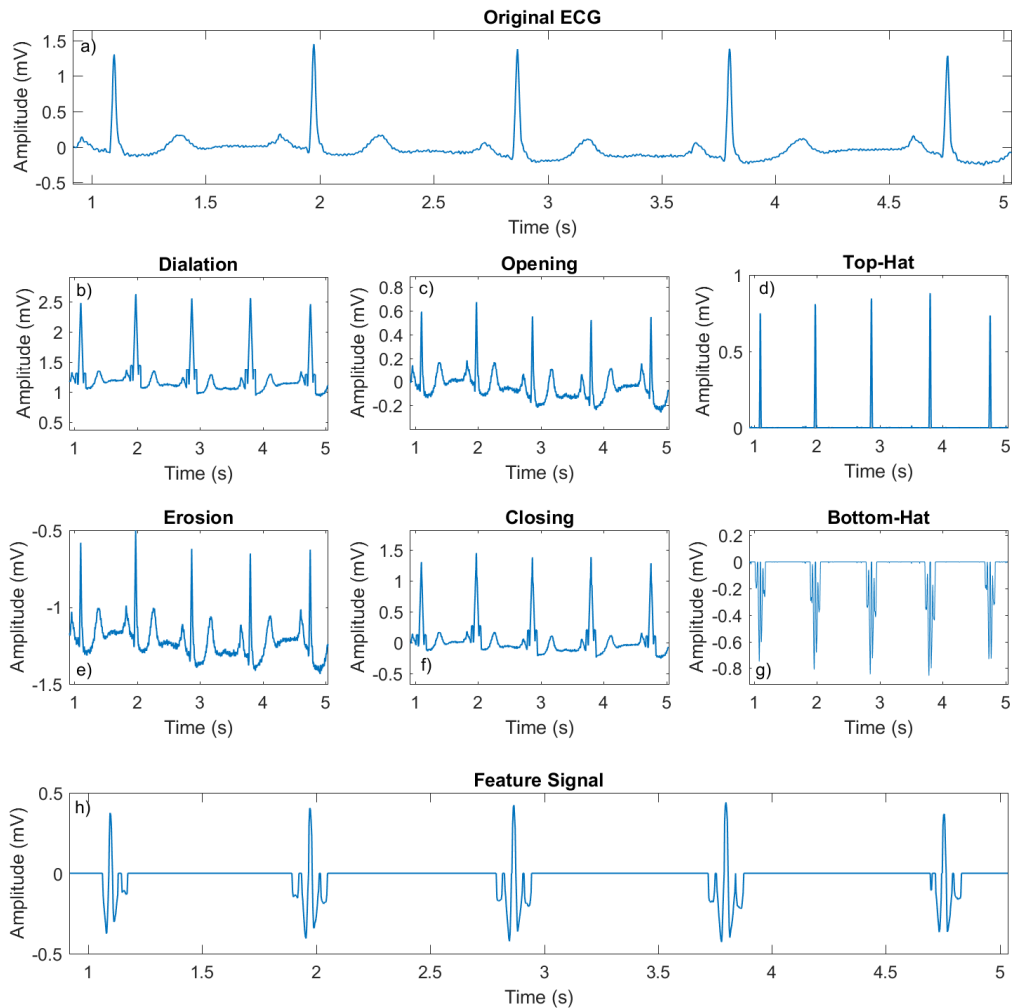


Figure 3.3 – Effect of each MM operator on the ECG. a) The original ECG, tape 101 from the MIT/BIH arrhythmia database, together with the output of b) dilation, c) opening, d) top-hat, e) erosion, f) closing, and g) bottom-hat operators. h) The average of the top- and bottom-hats, i.e. the feature signal.

3.3.2 Feature Signal Analysis and Peak Detection

After the MM filtering phase of AMM, the extracted feature signal is scrutinized for QRS-complex detection. In this phase, first, non-zero segments of the feature signal, defined as segments in the feature signal without three consecutive zero values, are extracted. Then, non-zero segments (referred to as active periods) with durations longer than 70ms are considered as QRS candidates. This 70ms threshold on the minimum duration of a QRS candidate is set based on the physiological constraint of minimum possible QRS-complex duration observed in patients with extreme heart conditions [108][109].

Figure 3.4 illustrates the feature analysis phase of AMM on an 8-second window of tape 101 from the MIT/BIH arrhythmia database. In this figure, a low-amplitude active period with a duration of 8ms takes place around second 133 of the feature signal extracted from the tape, and therefore it is discarded as a non-candidate section. The highlighted sections of this figure represent the extracted QRS candidates.

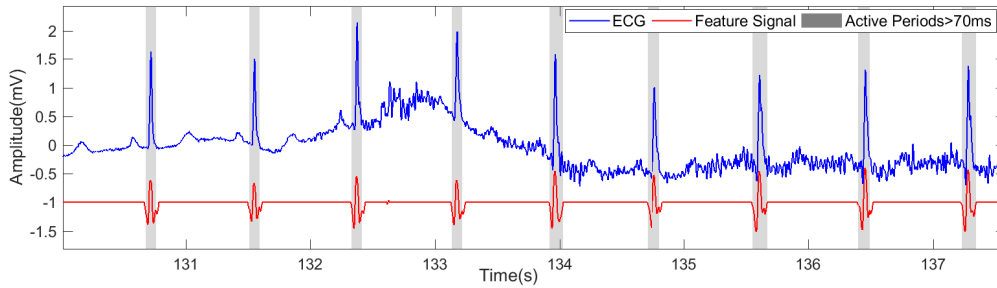


Figure 3.4 – Illustration of the extracted feature signal, i.e. the output of the MM filtering phase. For the purpose of demonstration, the signal length of 8 seconds is chosen. Also, a -1mV DC value is added to the extracted feature signal.

Subsequently, active periods with duration longer than 70ms are further processed as follows:

1. QRS-onset and QRS-offset are temporarily considered respectively as the start and end of the active period.
2. R-peak is defined as the most significant peak, and the polarity of R-peak are extracted from the active period. Schematics of this sub algorithm is illustrated in Figure 3.5.
3. The minimum (maximum) between the onset and R-peak is considered as the Q-point of the QRS-complex, in case R-peak has a positive (negative) polarity.
4. The minimum (maximum) between R-peak and the offset point is considered as the S-point of the complex, in case R-peak has a positive (negative) polarity.
5. QRS-onset (QRS-offset) is shifted to a maximum or minimum of the features signal, if it exists between the provisional onset (offset) and the Q-point (S-point).

In Figure 3.4, highlighted sections show the extracted onset-offset periods for every viable QRS-candidate, based on step 5.

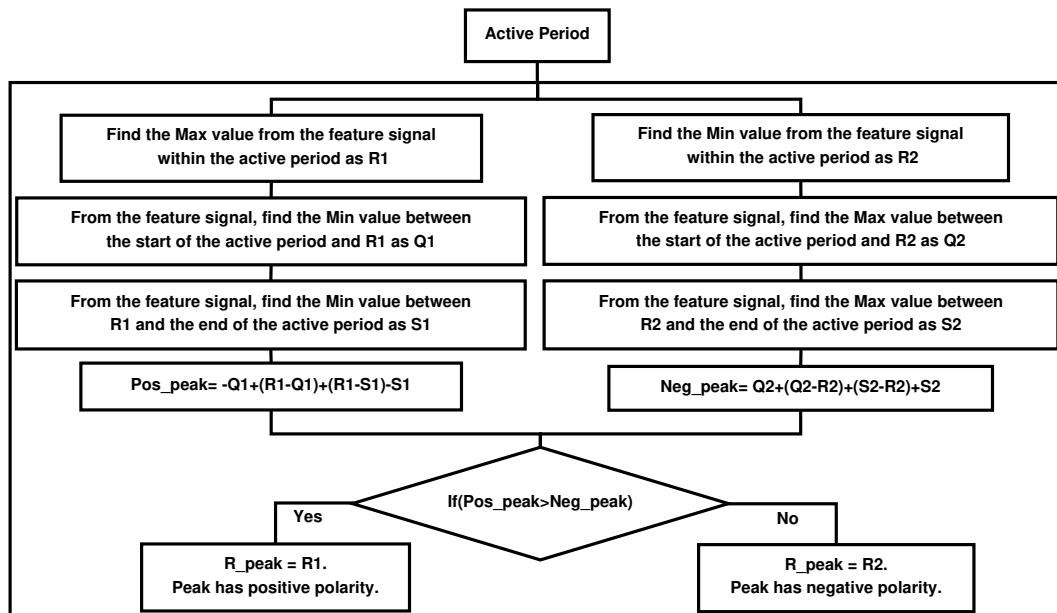


Figure 3.5 – AMM approach on detecting the polarity of the QRS-complex.

3.3.3 Structuring Element Update

After the detection of a QRS-complex, the update phase of AMM is invoked in order to adapt the SE so that it best represents the current QRS morphology of the subject. In other words, this phase extracts features such as shape, length and magnitude of the newly detected complex and uses them to update the SE to enhance QRS detection. More specifically, for each fiducial point, first its amplitude and relative distance with respect to the QRS-onset are extracted from the feature signal. Then, using a learning coefficient, location indices and amplitude values are updated based on the extracted topological features from the newly detected QRS and the ones from the synthesized QRS-complexes, as shown in the following equations:

$$NewLoc = (1 - \alpha) \times Curr_Loc + \alpha \times ExtractedLoc \quad (3.8)$$

$$NewAmp = (1 - \alpha) \times Curr_Amp + \alpha \times ExtractedAmp \quad (3.9)$$

In these equations, α represents the learning coefficient. For each fiducial point, $Curr_Loc$ is extracted from the current SE, calculated as its time distance with regard to the QRS-onset. $ExtractedLoc$, is extracted in the same manner for each fiducial point, using the feature signal. Additionally, $Curr_amp$ and $ExtractedAmp$ represent the amplitude of each fiducial point respectively in the current SE and the feature signal.

Once $NewLoc$ and $NewAmp$ values have been calculated using the extracted onset, offset, Q-point, S-point and R-peak, the SE is reconstructed by means of linear interpolation. The updated SE is later used in the MM filtering phase of AMM in the next ECG windows. Figure 3.6 shows how the SE is updated after a QRS-complex is detected.

In this figure, $(1 - \alpha)$ -scaled Current SE and α -scaled Extracted SE illustrate simultaneous changes on fiducial points' amplitudes and locations, respectively on the current structuring element and the extracted SE. The structuring element update of the AMM ensures that SE always has a positive polarity. When inverted QRS polarities are detected, the update on SE is performed on the negated amplitude values of the fiducial points in order to avoid zeroing of the update SE.

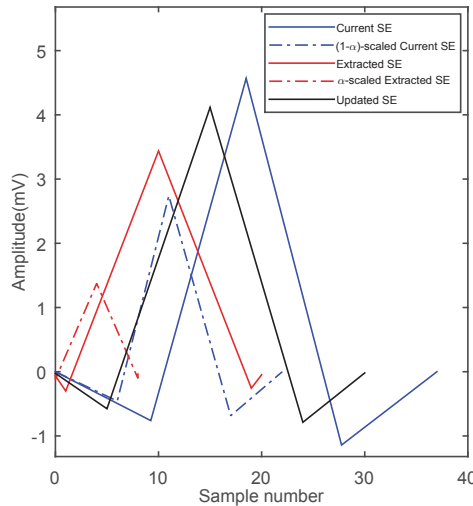


Figure 3.6 – The structuring element update phase of AMM. This update takes place after detection of a QRS-complex for a better and more precise detection of R-waves and other fiducial points in the complex. α was considered as 0.4 for demonstration.

Generally, AMM processes the ECG on a non-overlapping second-by-second basis. Nevertheless, sometimes only a part of a QRS-complex is accessible through the one-second sliding

window. In these cases where the feature signal ends while a non-zero period is not completely extracted, the window is slid to the start of the final non-zero period instead of the start of a new one-second window.

Ideally, after the detection of a complex, the updated MM filter should be applied to the signal from the last extracted offset point. However, observations showed that the QRS-complex morphology variations are usually small when multiple active periods are detected in the one-second feature signal, for instance in case of tachycardia. Therefore, in order to avoid computational overhead, the MM filter is applied only once to each window of the ECG signal. Still, the update on the SE takes place after the detection of each heartbeat so that it represents the current QRS morphology of the subject for the future ECG windows.

On the other hand, if the subject has an instantaneous heart rate lower than 60 beats per minute, i.e. when dealing with bradycardia, Mobitz (atrioventricular block) or asystole (flat line or no heartbeat for at least two seconds), it is possible that no active periods are found in the feature signal. In these cases the MM filtering is applied to the next window of the ECG.

Figure 3.7 illustrates a beat-to-beat evolution of the SE on an ECG from the MIT/BIH arrhythmia database. As seen in this figure, QRS-complexes with high amplitude do not drastically alter the synthetic SE as the learning coefficient is set to gradually change the morphology of the synthetic SE. Once QRS-complexes following these high amplitude heartbeats are detected, the synthetic SE gradually morphs back to the shape it had before these beats in the span of two to five heartbeats.

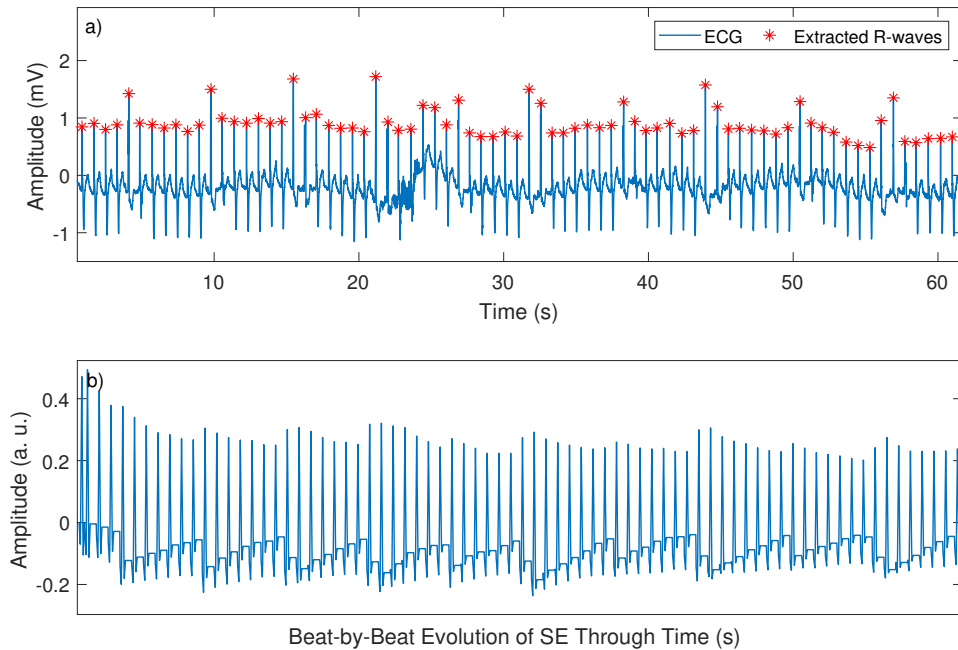


Figure 3.7 – Beat-to-beat structuring element update of AMM. a) The original ECG together with the detected R-waves (Tape 104 from the MIT/BIH arrhythmia database). b) Beat-to-beat evolution of the SE.

3.3.4 Parameter Update

Due to perturbations, small activity periods of the non-zero feature signal, yet longer than 70ms, may be spotted at positions where QRS-complexes do not occur. Observations have shown these non-zero activities mostly occur right before or after an actual heartbeat due to P-waves or T-waves that take place closer than usual to the QRS-complexes. To address this issue, an additional feature is extracted for each active period in the feature signal called *PeakActivity* (*PA*). This feature is defined as follows.

$$PA_{QRS-candidate} = \sum_{i \in \text{Nonzero-Activity}} |FS(i)| \quad (3.10)$$

where *FS* is the extracted feature signal. Since the feature signal artifacts are usually located right after or before an actual QRS-complex, they can be effortlessly removed since it is physiologically unlikely to have two consecutive heartbeats within 250ms [110]. Therefore, if two QRS consecutive candidates take place in an interval smaller than 250ms, the candidate with the bigger *PA* value is selected.

Another issue is that a fixed learning coefficient in Equations 3.8-3.9 might lead to active periods in the feature signal that cannot precisely estimate the onset and offset points of the corresponding QRS-complex. To alleviate this issue, after the detection of a complex, the newly extracted *PA* feature is compared with that of the previous heartbeat and as a result, the learning coefficient α is updated using Equation 3.11.

$$\alpha = \begin{cases} \alpha - \delta & PA_{Extracted} > PA_{Previous} \times th_{high} \\ \alpha + \delta & PA_{Extracted} < PA_{Previous} \times th_{low} \\ 0.3 & otherwise \end{cases} \quad (3.11)$$

where δ is the step size with which the learning coefficient is adjusted. th_{high} and th_{low} respectively define the lower and higher *PA* thresholds. $PA_{Extracted}$ and $PA_{Previous}$ respectively represent the extracted and previous peak activities.

Results showed that a default α value of 0.3 and a δ of 0.05 are optimal for the learning coefficient. Also, th_{low} and th_{high} were chosen as 0.9 and 1.1 respectively (see Section 3.5). Since the initializing SE does not fully represent the QRS-complex morphology of the subject, α is set to 0.9 at the beginning of the algorithm. After detection of the second QRS-complex, the *PeakActivity* feature of the newly detected QRS-complex is compared to that of the previous heartbeat and α is updated using Equation 3.11.

This *PA* feedback plays an important role when large changes take place in the ECG, for instance when respiration highly modulates the amplitude of the R-waves. When there is a decrease larger than 10 percent in *PA*, the SE should be updated to look more like the newly found QRS since a sudden change takes place in the ECG. This phenomenon is usually observed when baseline drift contaminates the ECG. On the other hand, a sudden increase in *PA* indicates that the SE should be less affected to avoid miss detection of future beats. Thus, the decrease in α is needed when an irregular beat with higher *PA* occurs in the ECG, such as premature ventricular contraction. Results show not only this adaptation improves heartbeat detection but also provides accurate positions of the Q, S, onset and offset points.

The last phase of the algorithm, i.e. the SE and parameter update, makes AMM flexible and robust again perturbations. Figure 3.8 illustrates the performance of AMM on a part of tape number 108 of the MIT/BIH arrhythmia database. This tape is among the most difficult ones since it is polluted with high-amplitude perturbations.

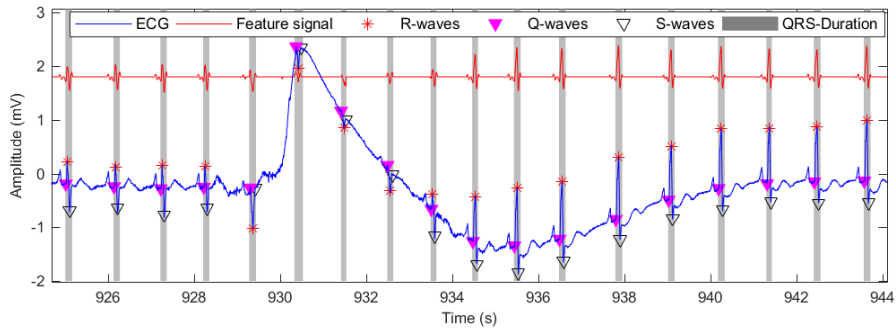


Figure 3.8 – Illustration of AMM performance on tape 108 from the MIT/BIH arrhythmia. A DC value of 1.8mv is added to the feature signal for demonstration.

3.4 Evaluation Databases

In order to find the optimal parameters for AMM as well as to evaluate the performance of the proposed method, the MIT/BIH arrhythmia [48] and Physionet QT [111] databases were used for the detection of QRS and other fiducial points.

3.4.1 The MIT/BIH Arrhythmia Database

The MIT/BIH arrhythmia database consists of 48 half-hour two-lead ECG recordings with a sampling rate of 360 Hz and an 11-bit resolution within the range of 10 mV. Heartbeats in the ECGs were annotated by two or more cardiologists, who independently studied the two leads and annotated the ECG recordings. Disagreements in their annotations were resolved to have a reference annotation for the QRS-complexes for each records. The evaluation on this database was performed on the first lead, which is either a modified lead II (46 records) or lead V5 (two records). Results were checked with the reference annotation file provided for this database.

3.4.2 The Physionet QT Database

The QT database, designed for waveform boundary evaluation, consists of 105 15-minute two-channel ECGs with a variety of QRS morphologies sampled at 250 Hz. The QT database was used in order to evaluate the delineation performance of AMM. In this database, for each record at least 30 beats (from 30 to more than 100 beats) were manually annotated. The records for the QT database were annotated by two cardiologists, who provided annotations by examining both ECG channels. One expert annotated all tapes in the database while the other only provided annotations for 11 records. In this study, for a precise evaluation on boundary and fiducial point detection, only the manually annotated waveforms, totaling 3622 beats, were considered in the experiments. In other words, only the annotations provided by the cardiologist who examined all records of the QT database was used. In order to have a fair comparison with the cardiologist's annotations, both channels were processed separately by AMM and for each fiducial point the channel with less error was selected.

3.4.3 The Green Goblin Wearable ECG Database

In order to evaluate AMM performance on wearable acquisition platforms, the algorithm was tested on an energy expenditure database recorded from smart shirts, developed at the Swiss Center for Electronics and Microtechnology (CSEM). In this database, ECGs were acquired at 250 Hz from chest-located dry electrodes, over 13 healthy male subjects in laboratory settings. The

distribution of anthropometric parameters of the subjects is shown in Table 3.1. The standardized protocol consisted in three 3-minute phases of resting (lying down, standing up and sitting) and 3-minute walking/running phases (from 0.5 m/s to exhaustion; with steps of 0.5 m/s). ECG segments were annotated by experts for performance evaluation.

Table 3.1 – Anthropometric parameters of the subjects in the wearable technology database.

Characteristic	<i>mean</i> \pm <i>std</i> ($N = 13$)	Range
Age (years)	35.95 \pm 6.74	27 – 46
Height (m)	1.82 \pm 0.07	1.72 – 1.95
Weight (kg)	75.88 \pm 6.35	65 – 87

3.5 Results and Discussion

As the core of all MM operations, the shape and length of the SE should be carefully chosen as they play important roles in the outcome of these operators [53][90][106]. For instance, the average of an opening and closing of a signal with a small length flat SE, e.g. a 6 ms zero vector, can be used for noise suppression [53] while the same average with a peaky SE tends to enhance peaks and valleys in the signal and discard other activities.

In ECG waveform detection, specifically QRS-complex detection, MM approaches use fixed-shape and -magnitude QRS-like SE to manipulate the signal and detect the R-waves. However, the magnitude and length of the SE are important factors. The steeper the slope, the less sensitive the operator becomes to low amplitude activities in the signal. Therefore, when perturbations are present in a part of a signal, SEs with steeper slopes tend to detect more dominant changes, resulting in a better feature signal. However, if the magnitude is too large, sometimes the QRS-complexes may not be detected. This phenomenon can be observed when arrhythmia is present. The length of the SE is decisive as well. A longer SE has more averaging effect, and therefore removes more unwanted activities. However, this noise reduction significantly decreases the amplitude of the R-waves. Also, it changes the relative positions of other fiducial points, especially the onsets and offsets. For this reason, a compromise should be made in order to have a more efficient detection.

Observations led to the conclusion that a fixed SE may not always detect QRS-complexes, especially when sudden changes, amplitude modulation, or baseline drift are present in the ECG. Figure 3.9-a illustrates the fixed-SE problem. In this example, the SE is simply too large in magnitude to detect all heartbeats. As a result, low amplitude heartbeats are considered as undesired ECG activities. Once the heartbeats get larger again at the end of the signal, they are correctly detected. Figure 3.9-b illustrates the outcome of an adaptive SE on the same ECG segment, where these beats are correctly detected. In order to detect the low amplitude heartbeats, one can use an SE with a smaller magnitude. However, the output of the MM filtering phase will become more sensitive to smaller changes in the ECG and the feature signal will have active periods where there is no heartbeat.

As the heart of AMM, the SE is adapted on a beat-to-beat basis. This adaptation changes the locations of the fiducial points as well as their amplitudes in the SE. The updated SE enables AMM to extract the other fiducial points more accurately. As a result, the outcome of the MM filter is less affected by sudden changes compared to a fixed SE.

3.5.1 Finding Optimized Parameters

In order to optimize performance, the effect of magnitude and length of the SE on AMM performance was studied. To this end, true positives (TP), false negative (FN), and false positives (FP) values were studied. TP indicates the number of correctly detected QRS-complexes while

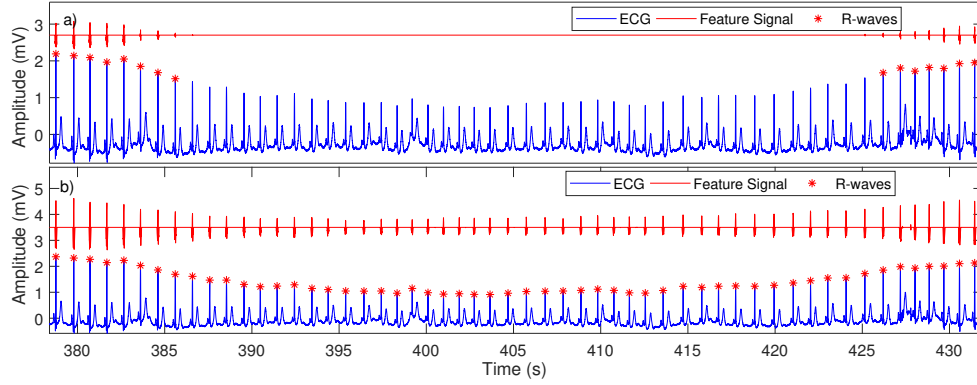


Figure 3.9 – a) Illustration of MM filtering on tape 106 from the MIT/BIH arrhythmia database using a fixed SE throughout the ECG. The used SE has a magnitude equal to that of the first peak in this figure. A DC value of 2.7mV is added to the feature signal. b) MM filtering output using an adaptive SE. A DC value of 3.5mV is added to the feature signal.

FN represents the number of miss-detected complexes. FP specifies the number of complexes declared by AMM where no actual heartbeat takes place in the ECG. Using these statistics, the detection error rate (DER) as well as sensitivity (Se), and positive prediction value (PPV) were computed¹ through Equation 3.12-3.14. In order to find the optimal parameters for AMM, these measures were calculated over all 48 tapes of the MIT/BIH arrhythmia database.

$$Sensitivity (Se) = \frac{TP}{TP + FN} \quad (3.12)$$

$$PositivePredictionValue(PPV) = \frac{TP}{TP + FP} \quad (3.13)$$

$$Detection\ Error\ Rate\ (DER) = \frac{FP + FN}{Total\ No.\ of\ Beats} \quad (3.14)$$

In figures 3.10 through 3.13, *DetectionAccuracy* is defined as $1 - DetectionError$ for demonstration purposes.

Figure 3.10 shows the effect of SE length on the overall QRS-complex detection performance of AMM. The update phase of AMM was modified to reconstruct the SEs with a fraction of the length of the extracted complexes. Different lengths in a range of 0.6 to 1.3 times the extracted length of QRS-complexes, by steps of 0.1, were studied. Results show consistently high performance in the range of 0.7 to 1.1, with the actual QRS-complex length as the optimal parameter. However the performance drops for coefficients larger than 1.1.

Figure 3.11 illustrates how the SE magnitude affects R-wave detection performance. In order to find the best magnitude, the SE was scaled from 0.05 up to 1.15 times the actual magnitude of the QRS-complex with a step size of 0.05. The performance strictly improves from the beginning to 0.6. After this point, the performance gradually decreases until 0.95, and then a drastic drop in performance is observed as the magnitude of the SE gets larger than the actual complex. This sudden drop in performance is caused by the increasing number of undetected heartbeats, which have lower amplitudes than their predecessors. This phenomenon can be the consequence of respiratory modulation of the ECG or a simple baseline drift.

1. Detailed description of classifier evaluation metrics can be found in Appendix B

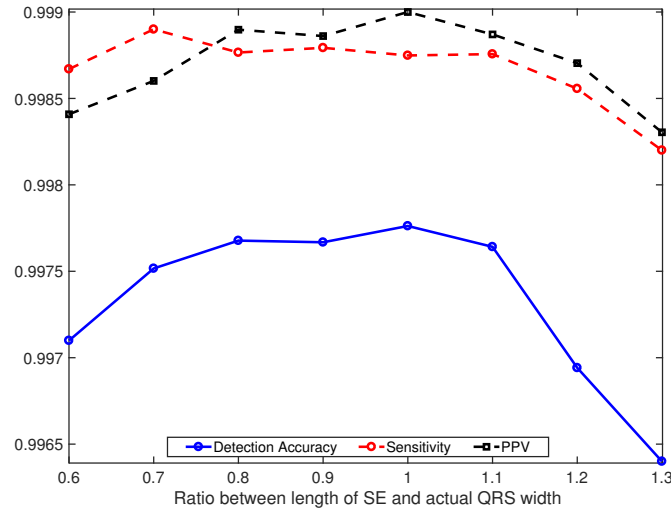


Figure 3.10 – Evolution of the detection accuracy (1-DER), sensitivity and PPV with respect to the ratio between the length of the SE and that of the actual QRS-complex.

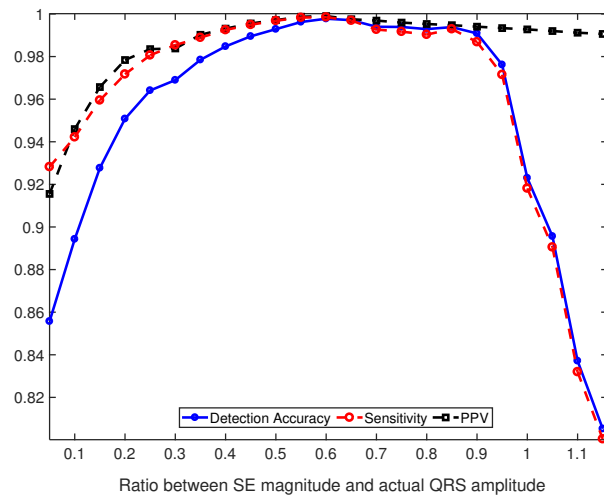


Figure 3.11 – Evolution of the detection accuracy (1-DER), sensitivity and PPV with respect to the ratio between the magnitude of the SE and that of the actual QRS-complex.

Heartbeats in the MIT/BIH database are annotated with different labels representing normal and abnormal beats, e.g. N represents normal beats and V is the label of premature ventricular beats. In order to find the optimal thresholds for Equation 3.11, the *PeakActivity* feature (Equation 3.10) was calculated for normal and ventricular beats (premature ventricular contractions and supra-ventricular premature beats). By comparing the *PeakActivity* feature of these two groups, it was observed that there is a difference of at least 10% in *PeakActivity* value between these two sets of beats. Therefore, th_{low} and th_{high} were selected respectively as 0.9 and 1.1. Using the optimal length, magnitude, and *PeakActivity* thresholds, the effect of the learning coefficient on AMM performance was studied. As shown in Figure 3.12, the optimal learning coefficient, i.e. α in Equation 3.11, was 0.3. Figure 3.13 illustrates how fine tuning the learning coefficient enhances the overall performance of AMM. Updating the learning coefficient based on the extracted *PeakActivity* feature is especially important when abnormal beats with extra large amplitude take

place in the ECG. If the learning coefficient is not updated, extra large (or small) outlier beats can alter the SE excessively, which results in a feature signal that is less (more) sensitive to changes in the ECG.

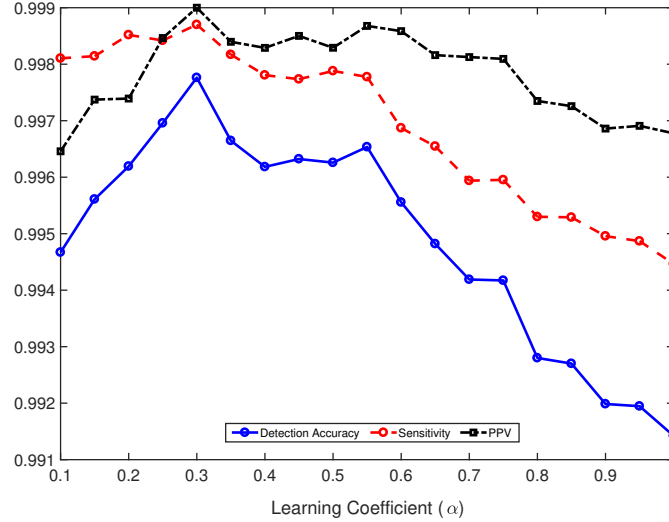


Figure 3.12 – Evolution of the detection accuracy (1-DER), sensitivity and PPV with respect to the learning coefficient (α) in Equations 3.8 and 3.9.

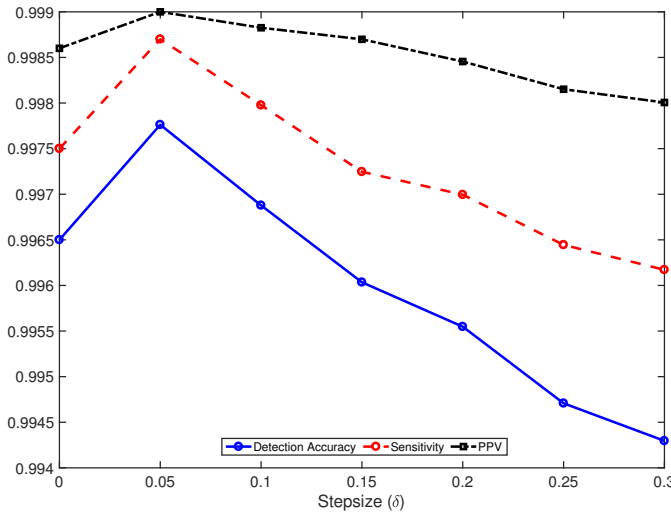


Figure 3.13 – Evolution of the detection accuracy (1-DER), sensitivity and PPV with respect to different *stepsizes*(δ). δ fine tunes the learning coefficient, as described in Equation 3.11.

3.5.2 AMM Performance Evaluation

Over the past two decades, many QRS detection approaches have been proposed. Therefore, in order to compare AMM performance with the state-of-the-art, the MIT/BIH arrhythmia database was used. Figure 3.14 illustrates AMM performance when strong baseline drift and muscle activity pollute the ECG. In this example, one can see a low-amplitude active period in the feature signal due to the elevated T-wave right after the first QRS-complex.

Figure 3.15 displays how AMM performs when switches of QRS polarity take place. This part of the tape 200 is especially selected, not only to show how AMM performs when premature ventricular contractions are present, but also to show the benefit of adapting the learning coefficient. As one can see, the QRS-complex in the 110-111 second period has a significantly larger *PeakActivity* in the feature signal compared to that of the previous beat. Subsequently, the learning coefficient is decreased through Equation 3.11, and the SE is less affected in the update phase of the algorithm. This leads to an active period with a duration longer than 70ms and therefore the detection of the final QRS-complex in this figure.

When it comes to Q- and S-points, the presence of baseline and muscle activities, e.g. Figure 3.14, lowers the estimation accuracy, due to the fact that these waves do not necessarily form a valley in the ECG. However, observations have shown that, even in the presence of these perturbations, fiducial point extraction is acceptable.

More detailed evaluation on tapes from the MIT/BIH database can be found in Table 3.2. Note that what is performed is QRS detection not R-peak extraction. Consequently, a detection is considered valid whenever the annotated R-peak is inside the detected QRS-complex.

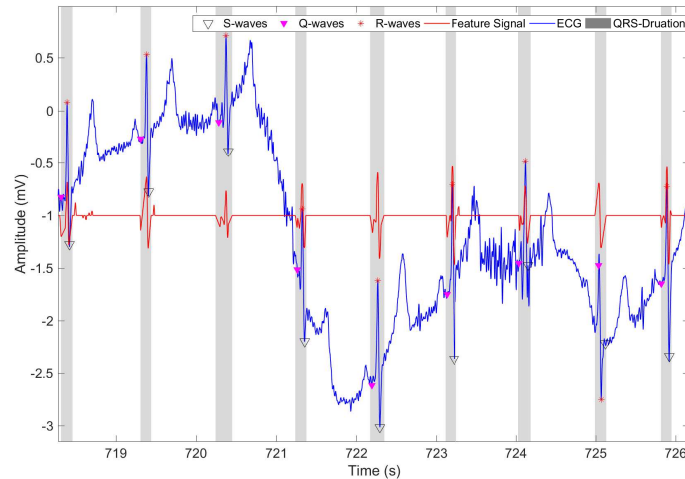


Figure 3.14 – Illustration of AMM performance on tape 117 from the MIT/BIH arrhythmia database. For demonstration, a DC value of -1mV is added to the feature signal.

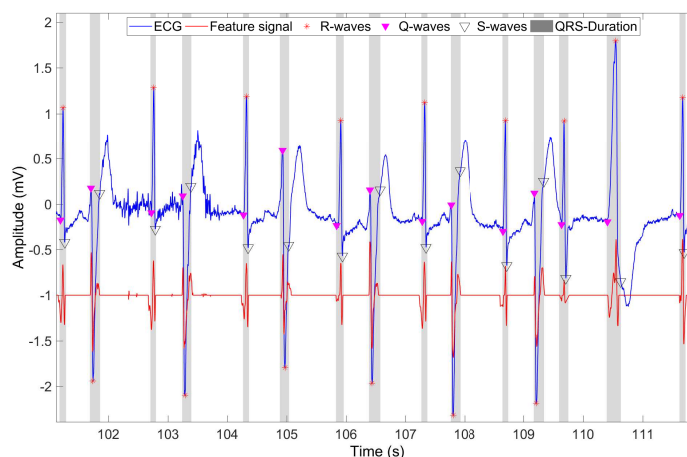


Figure 3.15 – Illustration of AMM performance on tape 200 from the MIT/BIH arrhythmia database. For demonstration, a DC value of -1mV is added to the feature signal.

Table 3.2 – Performance of AMM on QRS-complex detection on MIT/BIH arrhythmia database.

Tape	Beats	FP	FN	QRS DER (%)	Sensitivity	PPV
100	2273	0	0	0	1	1
101	1865	1	0	0.0536	1	0.9995
102	2187	0	0	0	1	1
103	2084	0	0	0	1	1
104	2229	7	1	0.3589	0.9996	0.9969
105	2572	22	15	1.4386	0.9942	0.9915
106	2027	0	4	0.1973	0.998	1
107	2137	0	1	0.0468	0.9995	1
108	1763	3	17	1.1344	0.9904	0.9983
109	2532	0	1	0.0395	0.9996	1
111	2124	2	1	0.1412	0.9995	0.9991
112	2539	0	0	0	1	1
113	1795	0	0	0	1	1
114	1879	4	2	0.3193	0.9989	0.9979
115	1953	0	0	0	1	1
116	2412	0	20	0.8292	0.9917	1
117	1535	0	0	0	1	1
118	2278	2	0	0.0878	1	0.9991
119	1987	0	0	0	1	1
121	1863	0	2	0.1074	0.9989	1
122	2476	0	0	0	1	1
123	1518	0	0	0	1	1
124	1619	0	0	0	1	1
200	2601	4	1	0.1922	0.9996	0.9985
201	1963	0	12	0.6113	0.9939	1
202	2136	0	2	0.0936	0.9991	1
203	2980	18	12	1.0067	0.996	0.994
205	2656	1	2	0.113	0.9992	0.9996
207	1860	3	3	0.3226	0.9984	0.9984
208	2955	2	9	0.3723	0.997	0.9993
209	3005	4	0	0.1331	1	0.9987
210	2650	3	4	0.2642	0.9985	0.9989
212	2748	0	0	0	1	1
213	3251	0	3	0.0923	0.9991	1
214	2262	0	0	0	1	1
215	3363	0	0	0	1	1
217	2208	6	4	0.4529	0.9982	0.9973
219	2154	0	0	0	1	1
220	2048	0	0	0	1	1
221	2427	0	6	0.2472	0.9975	1
222	2483	4	4	0.3222	0.9984	0.9984
223	2605	2	0	0.0768	1	0.9992
228	2053	11	8	0.9255	0.9961	0.9946
230	2256	0	0	0	1	1
231	1571	0	2	0.1273	0.9987	1
232	1780	4	0	0.2247	1	0.9978
233	3079	5	1	0.1949	0.9997	0.9984
234	2753	0	0	0	1	1
Total	109494	108	137	0.2238	0.9987	0.999

For each tape, numbers of false positives and false negatives and total number of beats as well as sensitivity, positive prediction value and detection error rate are reported.

Furthermore, Table 3.3 compares the performance of AMM to those of well-known QRS detection methods. As shown in this table, AMM provides better or comparable results.

Table 3.3 – Comparison of performance with previously proposed methods on MIT/BIH arrhythmia database.

Method	No. of Beats	FP	FN	DER (%)
AMM (this work)	109494	108	137	0.224
Pan and Tompkins [73]	109809	507	277	0.710
Li et al. [84]	104184	65	112	0.170
Zhang and Lian [90]	109510	204	213	0.38
Ravanshad et al. [97]	109428	651	1216	1.71
Martinez et al. [112]	109428	153	220	0.34
Bahoura et al. [87]	109809	135	184	0.29
Moody and Mark [113]	109428	94	1861	1.79
Lee et al. [114]	109481	137	135	0.43
Hamilton and Tompkins [76]	109267	248	340	0.54
Poli et al. [95]	109963	545	441	0.90
Chen et al. [115]	102654	529	459	0.96
Afonso et al. [89]	90909	406	374	0.86

Regarding the state-of-the-art, most methods isolate the location of QRS-complexes by means of thresholding, and then extract the R-peaks using local search [73][84][90][115]. However, AMM not only provides the necessary means to extract the R-peaks, but also the onset, offset, Q- and S-points can be estimated directly from the feature signal. Location and amplitude of these fiducial points can be used in beat classification and arrhythmia analysis [2][116][117]. In [2], features based on RR-intervals, QRS duration and segmented morphology (down sampled extracted QRS-complex) were used to develop an automated heartbeat classifier. Arrhythmia analysis is possible through the processing of RR-intervals [118] using adaptive filters [119] or time-frequency analysis [120]. Nevertheless, once accurate locations of QRS fiducial points are available, heartbeat classification and arrhythmia detection can be improved [2]. In this context the performance of AMM was evaluated on the manually annotated QRS-complexes in the QT database, with results presented in Table 3.4. The QRS-complex annotation provided in this database consists of the locations of R-peaks as well as the onset and offset points. In order to further assess AMM performance on Q- and S-point extraction, the ground truth for these fiducial points were respectively considered as the maximum (minimum) between the onset-peak and the peak-offset interval for a positive (negative) beat.

Table 3.4 – AMM performance on the manually annotated beats for QRS fiducial points, Physionet QT database.

Fiducial point	Sensitivity	Detection Rate	Tolerance (ms)	DER(%) (mean \pm std)
R-peak	0.9987	0.9990	4	0.001 \pm 0.0011
QRS-Onset	0.9684	0.9791	12	0.0209 \pm 0.0266
Q-point	0.9903	0.9902	4	0.0098 \pm 0.0201
S-point	0.9966	0.9966	4	0.0036 \pm 0.04
QRS-Offset	0.9820	0.9818	12	0.0182 \pm 0.0055

Table 3.4 reports the sensitivity and detection rate for each QRS-complex fiducial point. For each point an error tolerance was considered in order to measure the overall AMM performance on each fiducial point. Considering the sampling frequency of the records available in the QT database, i.e. 250 Hz, respectively one and three samples were considered as tolerable error for the Q-/R-/S- and QRS-onset/QRS-offset points. Figure 3.16 shows a box plot of the detection error rate for each fiducial point. Furthermore, AMM delineation errors were computed with respect to manual annotations provided by a cardiologist for the QT database. Table 3.5 reports these values for AMM and compares them with the work of Martinez et al. [112]. In Tables 3.4 and 3.5, reported results are in comparison with the label provided by the cardiologist who has annotated all records in the QTDB.

Table 3.5 – AMM delineation performance and comparison, QT database.

Method	<i>QRS Onset</i> mean \pm std(ms)	<i>R – waves</i> mean \pm std(ms)	<i>QRS Offset</i> mean \pm std(ms)
AMM	6.1 \pm 8.3	2.1 \pm 1.2	1.5 \pm 4.2
Martinez et al. [112]	4.6 \pm 7.7	Not Reported	0.8 \pm 8.7

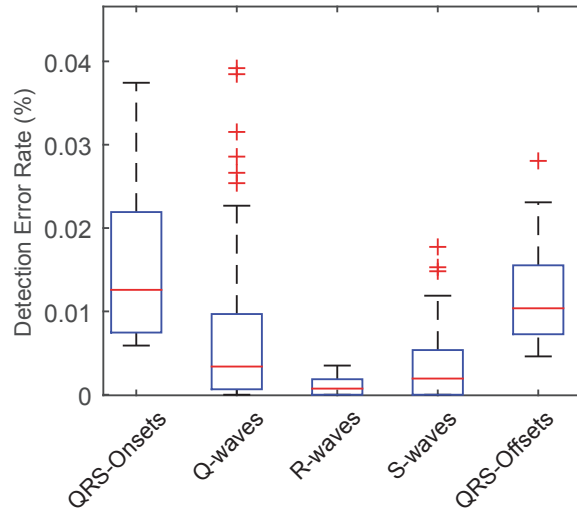


Figure 3.16 – Illustration of AMM performance on the QT database for each fiducial point.

Another contribution of the proposed algorithm is its ability to be used in body-area network platforms. While having limited resources, these platforms are expected to offer long term monitoring of subjects and provide robust extraction of heartbeats as a first step to more elaborated algorithms such as arrhythmia detection and heart rate variability analysis. The computation load of AMM consists of two elements, namely MM operation and peak detection, and SE update. The total computation load can be expressed as $O(l \times n) + O(l \times r)$ where n represents the number of samples in the ECG, l the length of the structuring element and r the number of detected heartbeats. Since $l \ll n$ and $r \ll n$ the second term can be omitted and the order of complexity of AMM can be written as $O(n)$.

AMM performs well on the MIT/BIH database. However, ECGs in this database are recorded using standard acquisition devices, and may be devoid of perturbations characteristic of portable and continuous recording devices such as electrode movement and contact problems, continuous

muscle activity contamination and large baseline drift. Therefore, AMM performance was evaluated on a dataset of ECGs that were recorded using smart shirts. In this database, subjects were asked to perform a series of walking/running exercises. The levels of exercises were categorized into low, moderate, and vigorous classes. For each subject, a six minute vigorous ECG segment was chosen and annotated by experts in order to evaluate the performance of AMM in extreme conditions. Figure 3.17 illustrates AMM outcome on one of these challenging segments. In this figure, the ECG suffers from a large baseline drift that is contaminating the signal, making QRS-complex detection a hard task.

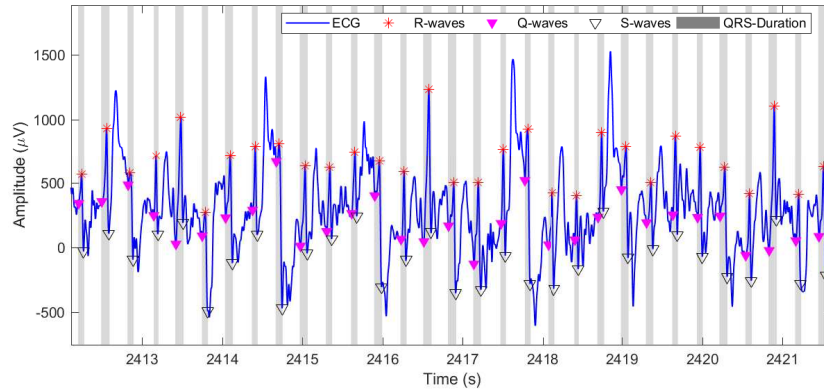


Figure 3.17 – Illustration of AMM performance on an ECG recored by a smart shirt, while subject is performing a vigorous running activity.

The overall performance of AMM is reported in Table 3.6, against two other methods namely, Pan-Tompkins and fixed mathematical morphology. Results show how AMM outperforms these methods and highlights the importance of the adaptation of the structuring element. Globally, in comparison to Pan-Tompkins and fixed mathematical morphology, a sensible improvement in performance with respectively over ten and five percents was achieved. This performance together with the low computation cost of AMM, makes it a suitable approach for body area network platforms, in which power consumption plays a vital role.

Table 3.6 – Comparison of AMM performance with other methods on the wearable ECG database.

Method	No. of Beats	FP	FN	Detection Rate (%)	Sensitivity	PPV
AMM	11806	59	142	98.39	0.9883	0.995
Fixed-MM	11806	161	780	92.57	0.9362	0.9836
Pan-Tompkins [73]	11806	534	1085	88.33	0.912	0.9511

The adaptation performed on the structuring element changes the behavior of the MM filtering phase. During the initialization of the algorithm, the structuring element is adapted so that it represents the general QRS-complex morphology of the subject. As AMM processes more QRS-complexes, the adaptation on the structuring element makes AMM more robust against possible noise in the ECG. However, observations on the miss detected complexes show that AMM under-senses when beats that become too wide (longer duration compared to previous beats) and at the same time lose their peaky shape. Moreover, false positives by AMM are mostly due to impulsive baseline changes, isolated QRS-like artifacts and clipping of the signal.

3.6 Miscellaneous Applications

3.6.1 Adaptive Mathematical Morphology to Extract Atrial Activations from Intracardiac Electrograms

Introduction to Intracardiac Electrograms (ICEG)

ICEG is the recording of electrical potentials via electrodes directly placed within the heart. The electrodes in contact with the myocardium sense the ionic changes underneath them and convert them into an electrical current, which can be recorded by a bed-side monitoring device. Therefore one can use ICEG to record local activations within the atria and ventricles.

As mentioned in Chapter 2, AF is a supra-ventricular tachycardia that can persist for a long time. Therefore, it is important to prevent AF progression from paroxysmal AF to persistent and permanent AF. Moreover, some patients do not respond well to cardioversion or cannot take antiarrhythmic drugs to restore sinus rhythm. Therefore, in order to prevent AF progression or relieve patients from ongoing AF, an invasive procedure called pulmonary vein isolation (PVI) might be chosen as a necessary treatment. PVI is a procedure during which pulmonary veins are electrically disconnected by creating radio-frequency lesions at left atrium/pulmonary vein ostium. It is believed that a main cause of AF is the presence of ectopic foci at the junction between atrial tissue and the pulmonary veins, disrupting sinus rhythm and causing AF. Therefore, by ablating the pulmonary veins these foci are isolated and, subsequently, sinus rhythm can be restored.

Intracardiac activation-time detection algorithms can be used in AF electrogram analysis as a first step in estimating AF characteristics. Characteristics such as cycle lengths (AFCLs) of atrial activations (AAs) can help predict persistent AF ablation outcomes [121, 122]. Moreover, AFCLs can be used to determine sites with high frequency activities which may help identify critical ablation targets to restore sinus rhythm [123].

However, the varying amplitudes and morphologies of AA during AF makes AA extraction difficult. Through a time consuming task, one can always measure activation intervals manually by using calipers and then average several measurements to determine the mean AFCL. Alternatively, automatic detection methods can be used to extract AAs even though most are limited due to the use of various thresholds [124]. Spectral analysis can also help to determine AFCL by extracting the AF dominant frequency (DF), i.e the frequency of the largest peak in the estimated spectral density [125]. DF methods try to approximate AFCL by a single sinusoid. Therefore, by nature, these methods are not suitable when AF electrograms present irregularities. A time domain iterative method has been proposed [126] to extract AAs from ICEGs. The detection threshold level is iteratively adjusted until the mean and the median of AFCL converge on a signal segment.

The purpose of this study is to evaluate the proposed adaptive mathematical morphology (AMM) approach introduced in this chapter, to extract AAs based on their morphological features. Similarly to QRS-complex extraction, the structuring element used in this method is adapted after each AA extraction to have a more reliable extraction. Elements of the methods and results in this section were originally presented as a conference paper [127].

3.6.2 Methods

Patients and Data Acquisition

Study Population. The study group for this research consists of three consecutive patients (63 ± 1 years) with chronic AF (sustained AF duration 17 ± 8 months) who underwent catheter ablation.

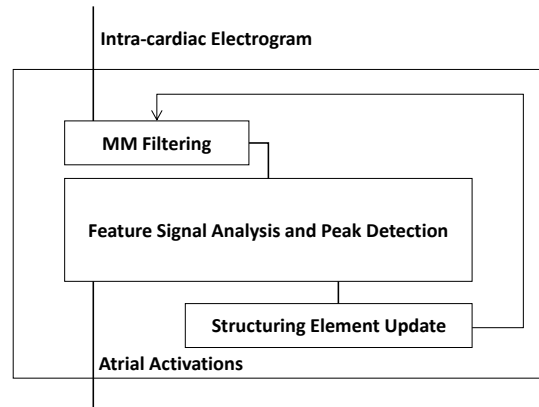


Figure 3.18 – Block diagram of the proposed method to extract atrial activations from intra-cardiac electrograms

Electrophysiological Study. The following catheters were introduced via the femoral veins: 1) a 3.5 mm cooled-tip catheter for mapping and ablation (Navistar[®] Thermocool[®], Biosense Webster[®]); and 2) a circumferential duodecapolar Lasso[®] catheter within the LA (2-6-2 25-15 mm, Biosense Webster[®]). Intracardiac electrograms were continuously monitored and sampled at 2 kHz (Axiom Sensis XP[®], Siemens[®]) for off-line analysis. Intracardiac electrograms were filtered with a pass band of [0.05,400] Hz. Then a notch filter at 50 Hz was applied to the signals in order to remove the acquisition noise. Electro-anatomical mapping and 3D reconstruction of the LA were performed with the CARTO[®] 3 system (Biosense Webster[®]).

Adaptive Intracardiac Mathematical Morphology (AIMM).

AIMM works in the same way as AMM, with the same three-step principle illustrated by the block diagram in Figure 3.18.

In AIMM, a non-overlapping sliding window with a length of 200 ms is rolled over the ICEG at hand. In each window, the MM filter is applied on the ICEG using the current SE. Afterwards, the filtered signal called the feature signal is scrutinized in order to extract AAs. Subsequently, AAs are probed and topological features such as height and length are extracted from them in order to update the SE that is used in the MM filtering phase.

AAs have different morphologies throughout AF. Moreover, these morphologies vary with respect to the location of the catheters inside the atria. Therefore, AIMM is initiated using an synthesized SE. The morphology of this synthesized SE is empirically chosen, as shown in figure 3.19. The magnitude of the synthesized SE is considered as 70% of the difference between the maximum and minimum values of the first 500 ms.

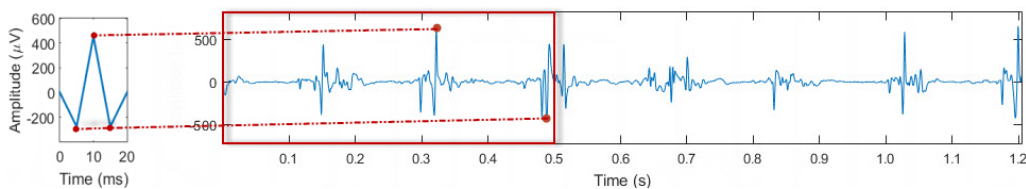


Figure 3.19 – Synthesized structuring element and the selection of its magnitude based on the intra-cardiac electrogram at hand.

Furthermore, the duration of the synthesized SE is empirically chosen as 20 ms, representing

the average AA duration. The synthesized SE in AIMM comprises five points representing onset, offset, peak of AA, the minimum between the onset the peak, and the minimum between the peak and the offset.

AIMM is initiated by applying the MM filter, which uses the synthesized SE, to the first window of the ICEG. As for to AMM, in the MM filtering step the top- and bottom-hat operators are applied to the window and then averaged (Equation 3.7). Once the MM filtering phase is carried out, the extracted feature signal is scrutinized in order to extract AAs. In this phase, first, non-zero segments of the feature signal are extracted. Then, segments are further processed as follows:

1. Onset and offset are considered respectively as the start and end of the non-zero segment.
2. The most significant peak is extracted from the active period as AA.
3. The minimum between the onset and AA together with the minimum between AA and the offset point are extracted for the SE update phase.

Perturbations might cause non-zero feature signal values at locations where AAs do not occur. Therefore, the following physiological thresholds are used to prevent false AA extraction:

$$AA_{valid} = \begin{cases} AA_{duration} \geq 8 \text{ ms} \\ AA_{candidate} - AA_{previous} \geq 60 \text{ ms} \end{cases} \quad (3.15)$$

where $AA_{candidate}$ represents the time index of the peak of the AA candidate in the feature signal, $AA_{previous}$ the time index of the peak of the previous AA and $AA_{duration}$, the duration of the AA candidate. The last condition corresponds to the fact that AA cycle length is unlikely to be smaller than 60 milliseconds.

Once an AA is detected, the extracted topological features, i.e. time indices and amplitude values of the onset, offset, AA peak and the two local minima are used to update the SE for further AA extraction.

Similar to AMM, the SE update is applied using Equations 3.8-3.9. The update on SE takes place after each AA extraction. Therefore, if multiple AAs are extracted from a window, SE is updated multiple times.

In order to avoid excessive changes on SE, for instance in case of large AA amplitude changes, AIMM uses a variable learning coefficient to make SE adaptation flexible. After the detection of an AA, its PA is compared to that of the previous AA and the learning coefficient is updated using Equation 3.16.

$$\alpha = \begin{cases} \alpha + 0.05 & \text{NewPA} < \text{PreviousPA} \times 0.7 \\ \alpha - 0.05 & \text{NewPA} > \text{PreviousPA} \times 1.3 \\ 0.2 & \text{otherwise} \end{cases} \quad (3.16)$$

3.6.3 Results

For performance evaluation, atrial activation times estimated by AIMM were compared with the manual annotation provided by a blinded clinical expert, as a ground truth. The expert was asked to annotate AAs through a graphical user interface created using MATLAB (Mathworks, Natick, MA). Furthermore, AIMM was compared against an MM method with fixed SE, and a recent state-of-the-art approach called cycle length iteration (CLI) [126]. The fixed MM method was implemented based on AIMM but with no structuring element update. The CLI method, is a block based method that extract AAs from an ICEG by iteratively changing a detection threshold and removing the extracted AAs from the ICEG. The algorithm stops its iterations when the mean AFCL is within five ms of median AFCL or if there are no peaks with an amplitude higher than 0.8 times the amplitude of current peak.

The best performance was obtained with AIMM with a 99.1% detection rate, 99.5% specificity and 99.5% PPV. The results are summarized in Table 3.7. In addition, an example of the performance of AIMM is illustrated in figure 3.20 and a more detailed evaluation of AIMM performance is presented in Figure 3.21.

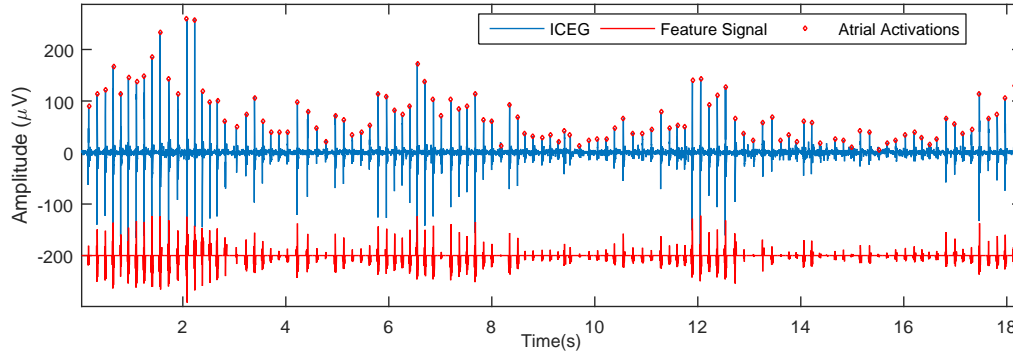


Figure 3.20 – Performance of the proposed method on a low quality intra-cardiac electrogram.

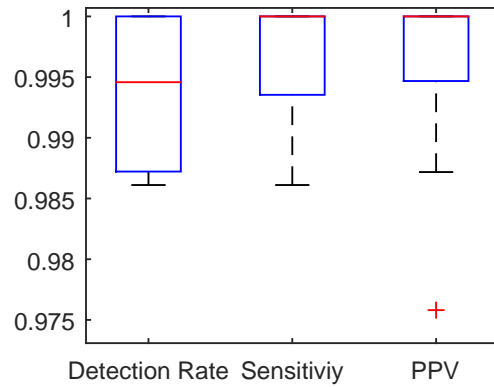


Figure 3.21 – Performance box plot of the proposed method.

Table 3.7 – Performance comparison of the proposed method on atrial activity extraction on the annotated database.

Method	Beats	FP	FN	Detection Rate (%)	Sensitivity	PPV
AIMM	5216	25	22	99.1	99.58	99.52
MM	5216	116	310	91.83	94.39	97.82
CLI [126]	5216	55	280	93.58	94.91	98.96

3.6.4 Remarks on AA detection from the ICEG

As for QRS-complex detection, employing a fixed SE for AA detection may lead to unwanted activity in the feature signal which results in over-sensing or under-sensing of the MM-based method. This is due to the fact that length and magnitude changes on the SE can weaken or strengthen high frequency activities which can lead to drastic effects on the feature signal [90,

105]. Hence, by adapting the SE, MM filters can become more sensitive to AAs and less to perturbations.

Results have shown that the best length of the SE is 20 ms. Also, AIMM achieves its best performance when the ratio of the magnitude of the SE to that of the actual AA is taken as 0.7. Moreover, different learning coefficients in the update phase of the AIMM were examined in order to apply the optimal changes on the SE with respect to the activities in the ICEG. At the beginning, α is set to 0.5 to have a bigger impact on the synthesized SE. As more AAs are detected, the topology of the SE becomes closer to that of AAs which results in a more robust detection of the next AAs.

Results suggest that the adaptive structuring element can efficiently estimate atrial activation times. AIMM works on an activation-to-activation basis, avoids excessive use of arbitrary thresholds, and incorporates physiological constraints. Being fast and computationally not costly, AIMM makes for viable approach for real-time/online scenarios.

3.7 Conclusion

This chapter presents an scheme, called the adaptive mathematical morphology, for QRS-complex and fiducial point detection. The proposed approach updates the structuring element used in MM operators after the detection of each heartbeat for a better and more reliable detection. The adaptation makes the proposed algorithm robust against perturbations such as baseline drifts and muscle activity interference. Achieving a high detection rate of 98.39% and a sensitivity of 0.988 against a smart shirt database, while benefiting from low computation load, makes this approach a suitable choice where limited resources are available such as for body-area networks.

Despite of the term "QRS detectors", most methods focus on detecting the R-waves and not the other fiducial points in the QRS-complex such as QRS-onset, QRS-offset, Q-point and S-point. The proposed method detects the aforementioned fiducial points alongside the R-peaks with a low detection error rate. These fiducial points provide the necessary information for more precise arrhythmia detection and heartbeat classification. Against the Physionet QT database, AMM achieved a detection rate of 99.90% for the R-peaks while estimating the location of the QRS-onsets and QRS-offsets respectively with detection rates of 97.91%, 98.18%.

Finally, the proposed algorithm was adapted for the detection of atrial activations from intracardiac electrograms. With the same principles as the QRS-detection scheme, the proposed algorithm obtained superior results to the state-of-the-art with a sensitivity of 0.99 and a detection rate of 99.1%.

Multimodal Signal Processing to Reduce False Alarms in the Intensive Care Unit

4

4.1 Introduction¹

High false alarm (FA) rates are a persistent concern in the Intensive Care Unit (ICU). Limited performance of ICU monitoring devices results in the desensitization of the medical staff and longer response times, which can have severe repercussions. In addition, the noise disturbances that are induced may lead to patient sleep deprivation [16]. Artifacts and momentary fluctuations in the signals are main causes of these high FA rates. In order to suppress FAs, studies based on heart rate (HR) trend analysis have been proposed. Sitting and Factor [128] used a multi-state Kalman filtering approach to identify trends, abrupt changes and artifacts in multiple physiological data. Makivirta et al. [129] proposed an alternative approach based on a two-stage recursive median filter. The resulting proportion of true alarms increased from 12% to 49% during postoperative haemodynamic monitoring of cardiac patients. Several other methods have been proposed to eliminate FAs by means of multimodal signal processing. Aboukhalil et al. [130] showed that the use of arterial blood pressure (ABP) alongside ECG can lead to an overall FA suppression of 59.7% on various alarm types, while preserving the true alarm rates, except in case of ventricular tachycardia.

In addition to the processing of cardiovascular signals from independent sources, the automated identification of bad-quality signals and the development of signal quality indexes (SQIs) can contribute to the improvement of the decision-making process to determine the validity of an alarm [8, 131–133]. Sun et al. [131] used several features such as HR, heartbeat duration, systolic and diastolic blood pressure values to detect anomalies in the ABP waveforms and compute a signal abnormality index. Another ABP quality assessment method based on a fuzzy logic approach was proposed in [132]. These two approaches were combined in [8] to develop an ABP SQI, which was then employed to reduce the number of FAs in the ICU, resulting in FA reduction rates of 74% and 53% for extreme bradycardia and extreme tachycardia, respectively. Same authors developed a more complete processing scheme by including photoplethysmogram (PPG) signals [134] and developing a PPG SQI [133]. This scheme was evaluated on a database composed of different types of life-threatening arrhythmia alarms, resulting in FA suppression rates of 86.4% for asystole, 100% for extreme bradycardia and 27.8% for extreme tachycardia,

1. The study presented in this chapter is the result of a joint collaboration with Sibylle Fallet (ASPG), which in turn will be also published in another dissertation entitled 'Signal Processing Techniques for Cardiovascular Monitoring Applications Using Conventional and Video-based Photoplethysmography', thesis director Dr. J.M. Vesin.

while preserving true alarms. For ventricular tachycardia alarms an FA suppression of 30% was achieved, with a true alarm suppression below 1%. The quality of ECG waveforms also plays an important role. Indeed, as arrhythmia alarms in the ICU are mainly triggered by the ECGs, poor quality ECG waveforms are associated with increases in FA rate. Behar et al. [135] developed a complete scheme based on machine learning to compute SQIs for ECG waveforms. In this study, the authors pointed out the challenges linked to the evaluation of ECG waveform quality in case of abnormal rhythms and proposed to train classifiers independently for the different types of rhythms.

FA suppression in case of ventricular arrhythmia alarms can be especially arduous. Previous studies have emphasized the difficulties in classifying ventricular tachycardia and ventricular fibrillation episodes [8, 130, 136, 137]. Indeed, in these cases, accurate HR values are not sufficient to identify the presence of an arrhythmia and additional features are required to detect morphological changes in the waveforms. Moreover, there is no clear evidence yet that PPG/ABP waveforms can be used as surrogates to characterize these arrhythmias. Salas-Boni et. al. [136] proposed a method to reduce the number of false ventricular tachycardia alarms based on wavelet transform of ECGs. In their work, the ECG waveform was first decomposed in three sub-signals using multi-level wavelet transform. Then, different features were extracted from the sub-signals and machine learning was used to determine the validity of the alarms. An FA suppression of 21% on the PhysioNet MIMIC II dataset [138] was achieved. Regarding the classification of ventricular fibrillation episodes, a study showed that an accuracy of 96.3% could be achieved using two features derived from ECG waveforms after the removal of noisy segments [137].

The purpose of this chapter was to develop algorithms to lower the incidence of false alarms (FAs) in the ICU using information from independent sources, namely ECG, ABP and PPG. This approach relies on robust adaptive signal processing techniques in order to extract accurate HR values from the different waveforms. Based on the quality of available signals, heart rate was either estimated from pulsatile waveforms using an adaptive frequency tracking algorithm or computed from ECGs using the adaptive mathematical morphology introduced in Chapter 3. Furthermore, a supplementary measure was developed based on the spectral purity index (SPI) of the ECGs to determine whether a ventricular tachycardia or flutter/fibrillation arrhythmia has taken place. Finally, alarm veracity was determined based on a set of decision rules on HR and spectral purity values. The proposed method was evaluated on the PhysioNet/CinC Challenge 2015 database [9], which is composed of 1250 life-threatening alarm recordings, each categorized as a bradycardia, tachycardia, asystole, ventricular tachycardia or ventricular flutter/fibrillation arrhythmia. Figure 4.1 shows the main steps of the proposed framework to identify false alarms in the ICU.

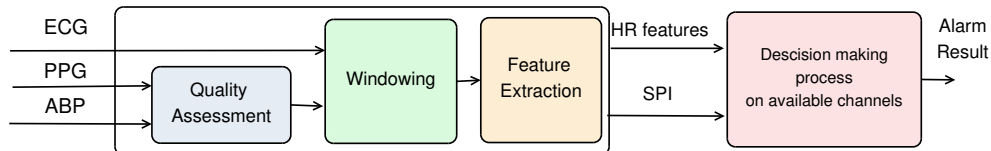


Figure 4.1 – The general framework to determine the validity of an alarm.

Elements of the methods and results in this chapter were originally presented as a conference paper [139], then published as a journal paper [7].

4.2 Method

4.2.1 Data

The PhysioNet/CinC Challenge 2015 multimodal database consists of 1250 life-threatening alarm recordings, each categorized as bradycardia, tachycardia, asystole, ventricular tachycardia or ventricular flutter/fibrillation arrhythmia. Each record contains two ECG leads and at least one pulsatile waveform (PPG and/or ABP). The nature of each alarm was manually labeled by a team of experts according to the definitions of the five arrhythmia alarm types reported in Table 4.1. The database was divided into two subsets: a “real-time” subset, for which the data was available only before the alarm was triggered and a “retrospective” subset, in which each record contains an additional 30 seconds of data following the time of the alarm.

Table 4.1 – Definition of the five alarm types [9].

Alarm type	Definition
Asystole	No QRS for at least four seconds.
Extreme Bradycardia	Heart rate lower than 40 bpm for five consecutive beats.
Extreme Tachycardia	Heart rate higher than 140 bpm for 17 consecutive beats.
Ventricular Tachycardia	Five or more ventricular beats with heart rate higher than 100 bpm.
Ventricular Flutter/Fibrillation	Fibrillatory, flutter, or oscillatory waveform for at least four seconds.

For each type of alarm described in Table 4.1, a true and a false arrhythmia alarm are demonstrated next. In these figures, one can see example available waveforms in a window with a duration of 16 seconds, preceding the alarm. Figures 4.2 and 4.3 respectively show a true and a false asystole alarm. In Figure 4.3 one can see the asystole alarm would be true had the ECG leads were only used for alarm veracity analysis.

Figures 4.4 and 4.5 illustrate a true and a false extreme bradycardia alarm, respectively. The previous argument is true for Figure 4.5 as well, where there are missing ECG leads in the recording.

Examples of true and a false extreme tachycardia are reported in Figures 4.6 and 4.7, respectively. In the latter, the ECG channels present oscillatory behavior. If the oscillatory peaks were to be selected as heartbeats, the arrhythmia would be considered as a true alarm.

Ventricular tachycardia examples are illustrated in Figure 4.8, a true alarm, and Figure 4.9, representing a false alarm. One may blame the low quality of some signals in this example causing the false arrhythmia alarm.

Finally, Figures 4.10 and 4.11 provide examples of a true and a false extreme ventricular flutter/fibrillation alarm, respectively. Figure 4.10 illustrates an interesting fact that during ventricular flutter/fibrillation, the pulsatile waveforms may not be suitable for alarm veracity, as there is virtually no fluctuation in the ABP signal.

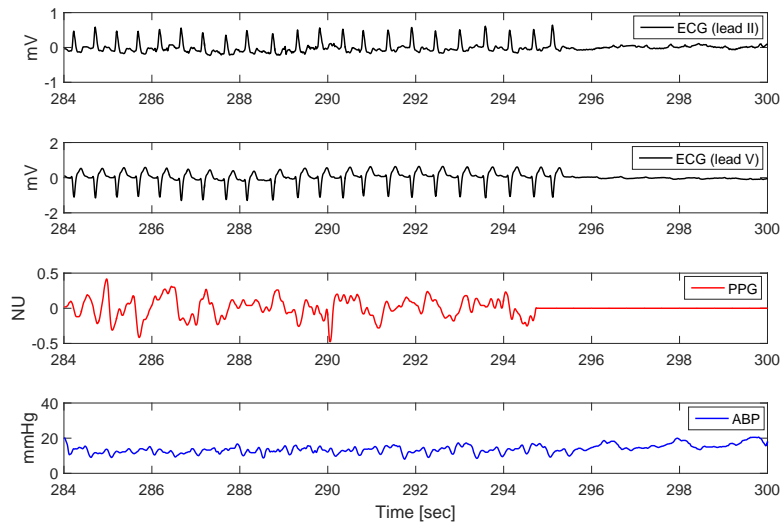


Figure 4.2 – Example of a true asystole alarm (tape a142s).

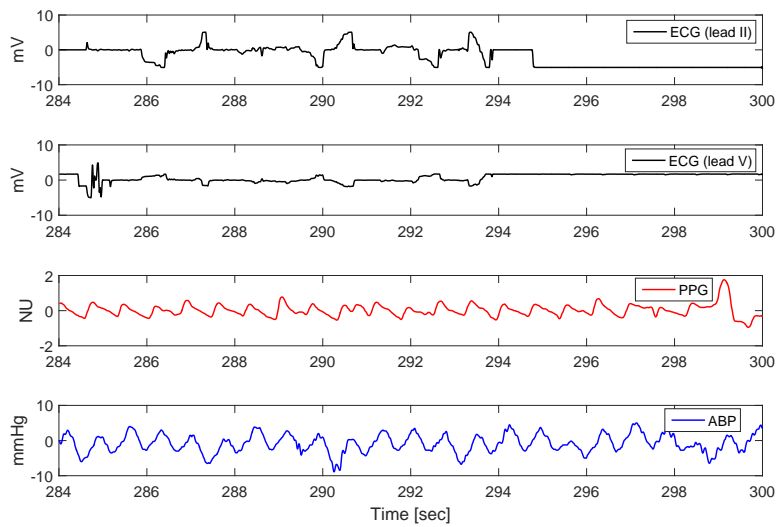


Figure 4.3 – Example of a false asystole alarm (tape a134s).

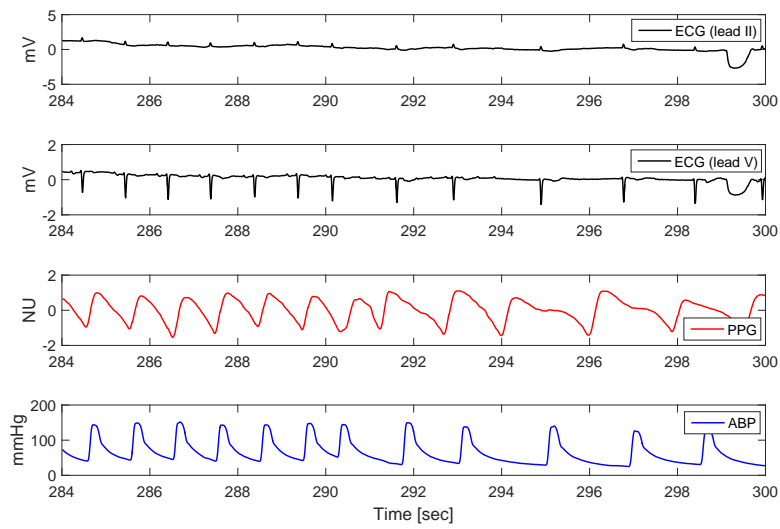


Figure 4.4 – Example of a true bradycardia alarm (tape b4551).

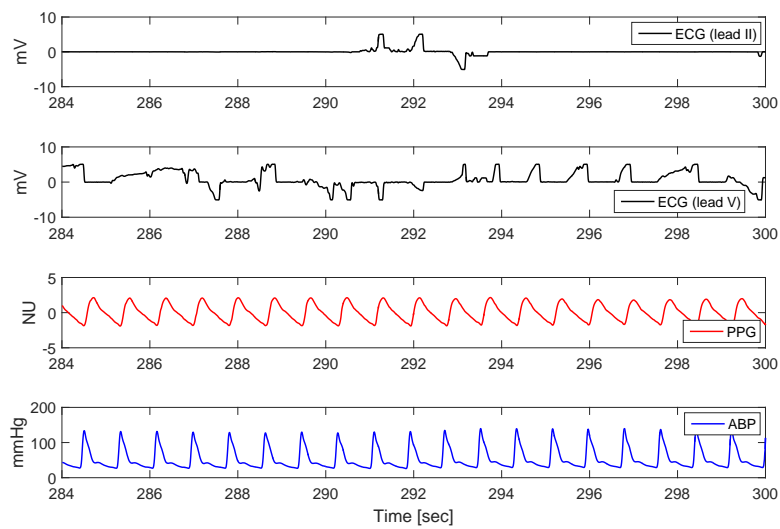


Figure 4.5 – Example of a false bradycardia alarm (tape b332s).

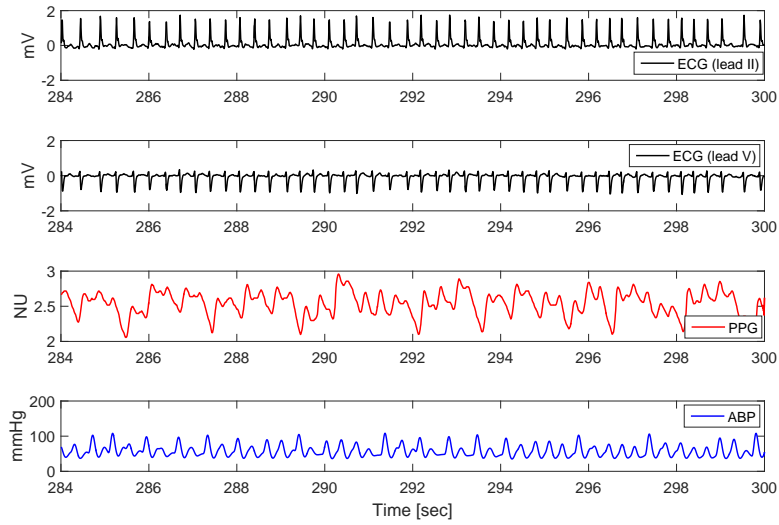


Figure 4.6 – Example of a true tachycardia alarm (tape t174s).

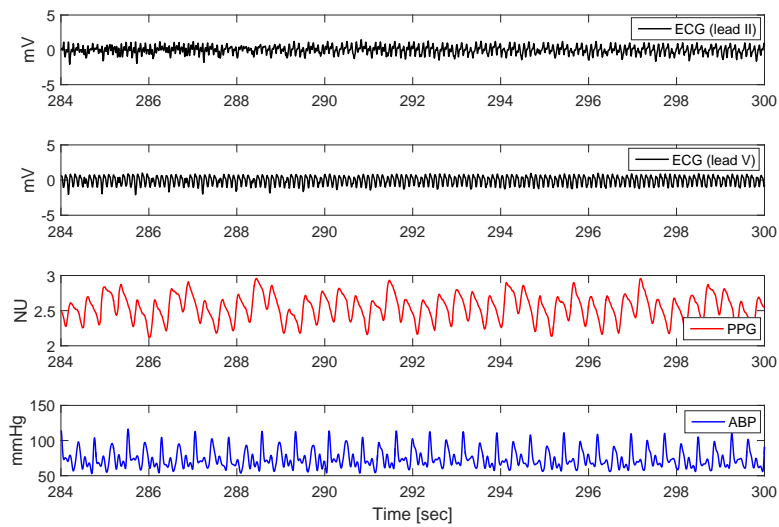


Figure 4.7 – Example of a false tachycardia alarm (tape t409I).

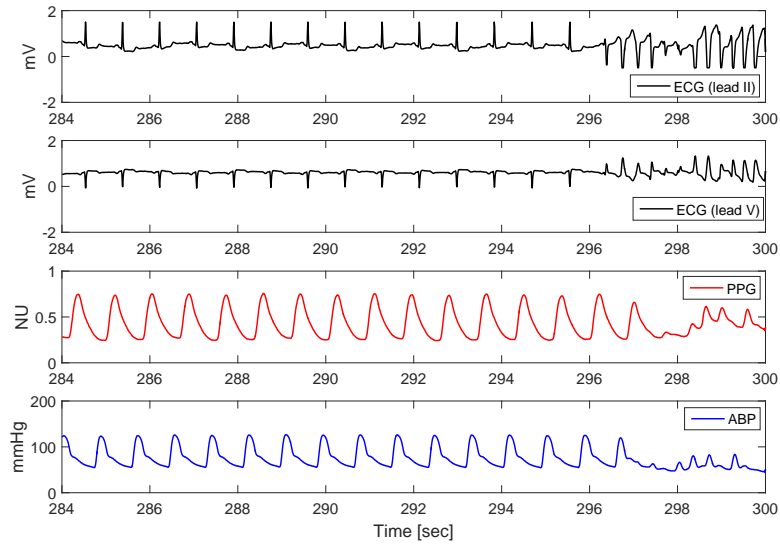


Figure 4.8 – Example of a true ventricular tachycardia alarm (tape v648s).

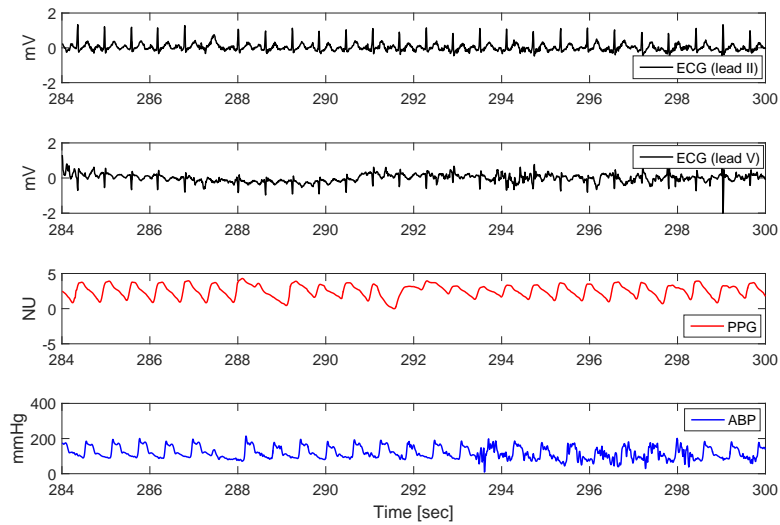


Figure 4.9 – Example of a false ventricular tachycardia alarm (tape v169l).

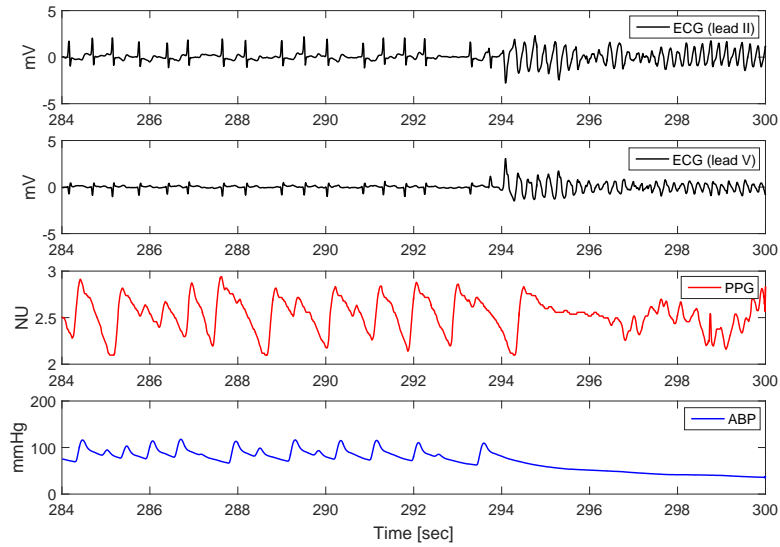


Figure 4.10 – Example of a true ventricular flutter/fibrillation alarm (tape f544s).

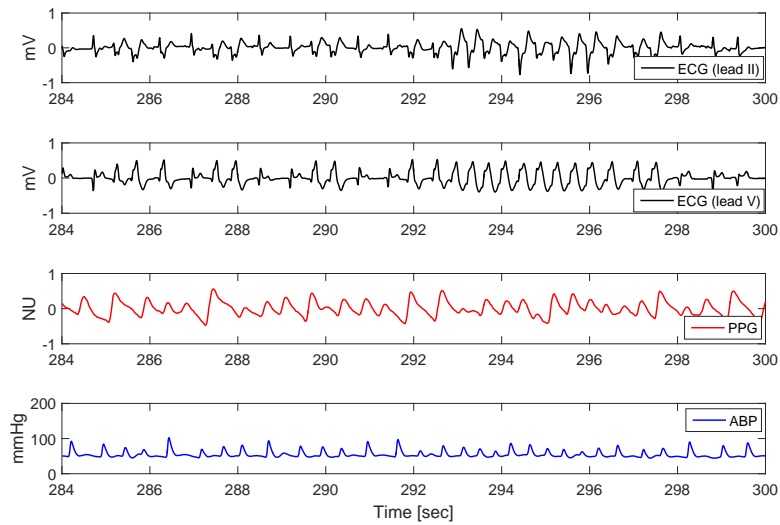


Figure 4.11 – Example of a false ventricular flutter/fibrillation alarm (tape f1211).

4.2.2 Processing of ECG

HR Estimation.

Observations of the available ECG channels in the training set indicated that they present various perturbations such as clipping of the QRS complexes, large baseline drift and high muscle activity noise. Therefore, a robust heartbeat detection algorithm was needed in order to have a reliable FA suppression. To this end the AMM (see Chapter 3) was used to extract the QRS-complexes. As mentioned before, in MM filtering settings, operators nonlinearly transform the signal of interest using an SE, designed to extract useful information regarding shape and size. In AMM however the SE is continuously updated based on the QRS-complex morphological features, which makes AMM flexible and robust against perturbations. Another attractive property of the AMM algorithm that it avoids excessive use of arbitrary thresholds, while relying on more physiological constraints. These two properties of AMM, together with the evaluation performed on the MIT/BIH arrhythmia database and especially the wearable technology ECG database, made it appealing for this challenge. Moreover, AMM entails a low computational cost, linear with respect to the length of the signal. Figures 4.12-4.13 illustrate the performance of AMM on two low quality signals from the training dataset.

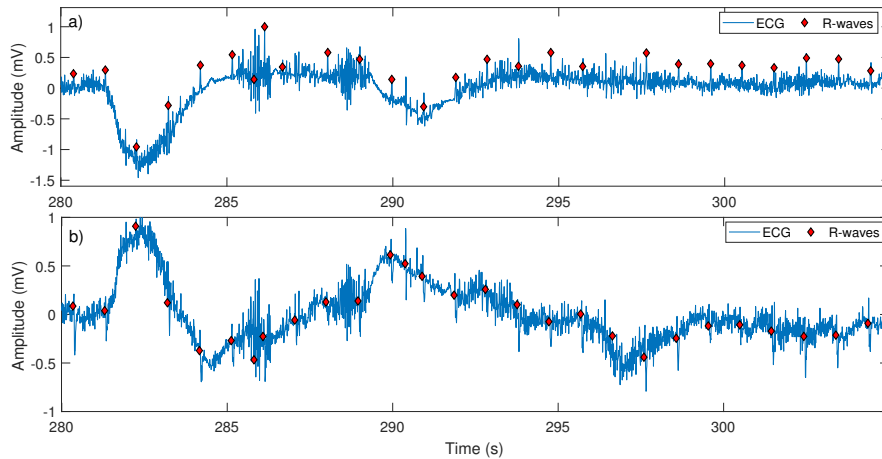


Figure 4.12 – AMM performance on an ECG channels (record a527l) from the training set.

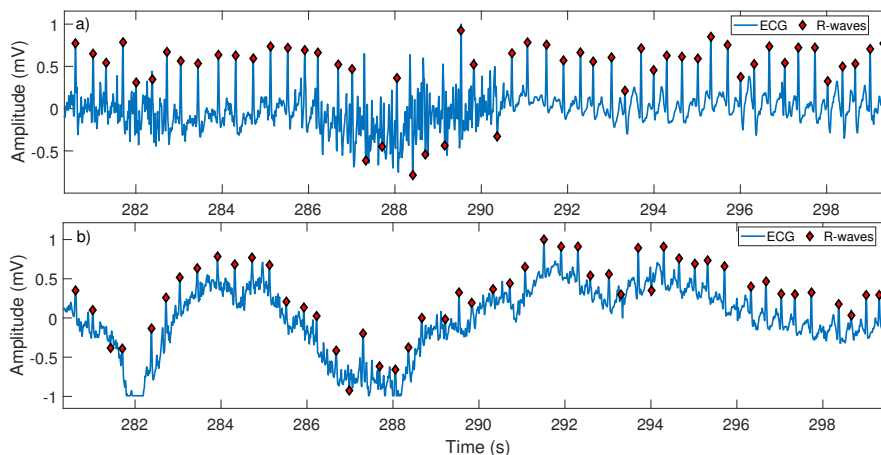


Figure 4.13 – AMM performance on ECG channels (record t320s) from the training set.

Even though the quality of the ECG in Figure 4.12-4.13 is of very low quality, one can see how AMM manages to robustly extract the QRS-complexes. However, the quality of many ECGs in the recordings available in the challenge were of such low quality that made the determination of false arrhythmia alarms virtually impossible, solely by means of ECG HR analysis. Therefore, to improve the overall performance of false alarm detection, one needs to analyze the pulsatile waveforms alongside ECGs as well. Furthermore, in some arrhythmia such as ventricular flutter or ventricular fibrillation HR analysis is simply not enough as one needs to scrutinize more the signal behavior as opposed to the variation in HR (see Section 4.2.4).

Spectral Purity Index (SPI).

Defining the characteristics of ventricular arrhythmia is challenging from a signal processing point of view. More specifically, in case of ventricular tachycardia, the definition includes both a constraint on the rhythm (HR higher than 100 bpm) and morphological changes in QRS complexes (five or more ventricular beats). Although many methods have been proposed to estimate the HR, methods to identify a succession of ventricular beats are scarce. Observations have shown that ECGs become closer to a sinusoid during ventricular tachycardia/flutter/fibrillation episodes, due to a widening of the QRS complexes. Such kind of behavior can be quantified with a measure called the spectral purity index (SPI). This measure, which was originally developed in the context of the analysis of electroencephalogram signals [140, 141], ranges between zero and one and indicates how well the signal of interest can be described by a single frequency. It is defined as the running squared second-order spectral moment divided by the product of the running total power and fourth-order spectral moment:

$$SPI(n) = \frac{\bar{\omega}_2^2(n)}{\bar{\omega}_0(n)\bar{\omega}_4(n)}, \quad (4.1)$$

with $\bar{\omega}_n$, the n th-order spectral moment, defined by:

$$\bar{\omega}_n = \int_{-\pi}^{\pi} \omega^n S_x(e^{jw}) dw, \quad (4.2)$$

where $S_x(e^{jw})$ represents the power spectrum. In this study, the spectral moments $\bar{\omega}_n$ were estimated in time domain, as proposed in [141]. The following difference equations can be used to estimate the first and second derivatives:

$$x^{(1)}(n) = x(n) - x(n-1) \quad (4.3)$$

$$x^{(2)}(n) = x(n+1) - 2x(n) + x(n-1). \quad (4.4)$$

Then, from these derivatives, spectral moments can be estimated using Equation 4.5:

$$\hat{\omega}_i \approx \frac{2\pi}{N} \sum_{n=0}^{N-1} (x^{(i/2)}(n))^2 \quad (4.5)$$

with $i = 0, 2, 4$ and N the length of the signal. In addition, the SPI can be measured recursively using a sliding window. The expression for the $SPI(n)$ is then written as:

$$SPI(n) = \frac{(\sum_{k=n-L+1}^n (x^{(1)}(k))^2)}{\sum_{k=n-L+1}^n (x^{(0)}(k))^2 \sum_{k=n-L+1}^n (x^{(2)}(k))^2} \quad (4.6)$$

with L the length of the sliding window. In this study, the SPI of the available ECG channels was measured for ventricular tachycardia and ventricular flutter/fibrillation alarms. Higher SPIs are expected for true arrhythmias. In order for the SPI to be more representative of the general changes in the signals, ECG waveforms were first smoothed by down-sampling to 35 Hz and by applying a 5-sample moving average filter. A 2-second sliding window ($L=70$) was used for SPI calculation. Figure 4.14 illustrates an example of the SPI during a true ventricular tachycardia alarm.

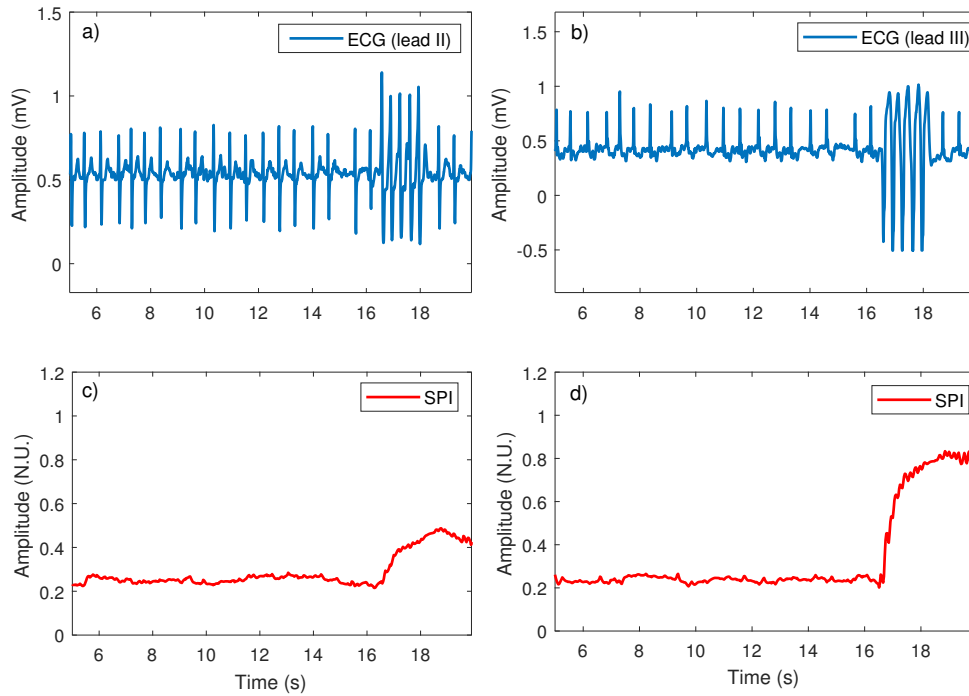


Figure 4.14 – Example of SPI for a true ventricular tachycardia (record v194s). (a) and (b) show the two ECG waveforms. (c) and (d) represent the corresponding SPIs. In both cases, it can be observed that the SPI significantly increases when the arrhythmia takes place.

4.2.3 Processing of PPG and ABP Waveforms

Quality Assessment.

In order to assess the quality of the PPG and ABP signals, respectively the *ppgSQI* and the *jsQI* algorithms were used, which were provided for the PhysioNet/CinC 2015 challenge [9]. Based on the detected heartbeats, these algorithms compute the features needed to estimate the signal quality. Heartbeats were detected using the algorithm described by Arberet et al.

[142]. The resulting signal quality indexes (SQIs), that ranged between zero and one, determined whether PPG/ABP waveforms should be analyzed.

HR Estimation.²

In order to suppress FAs and preserve true alarms, it is necessary to have an accurate HR extraction. However, a precise HR estimation has proven to be difficult when signal quality is low. Moreover, abnormal heart rhythms are expected to be present in the waveforms. In this study, the pulsatile nature of PPG and ABP waveforms was exploited by using an adaptive frequency tracking algorithm, which consists of an adaptive band-pass filter, to estimate HR. The basic algorithm, described by Liao [143], is an oscillator-based mean-square-error band-pass filter (OSC-MSE). In this algorithm, the central frequency of the filter is constantly updated to track the instantaneous frequency of the signal. The underlying adaptive mechanism involves a cost function that is derived from the oscillator equation. This OSC-MSE algorithm was extended to multi-signal (OSC-MSE-W) [144], in order to track the common frequency component present in multiple input signals. More specifically, input signals are filtered by an adaptive band-pass filter in order to calculate individual frequency estimates. Then, a global frequency estimate is computed by weighting the individual estimates. Importantly, it should be mentioned that the phase difference between the input signals does not affect the frequency tracking. In addition, the OSC-MSE-W was further expanded to work in the complex domain (OSC-MSEc-W) [145], as it was empirically observed that using the complex-domain approach improved the frequency tracking on some signals. This algorithm has been used to compute accurate HR values from PPG signals acquired on running subjects [146].

Here, an 8th-order Butterworth low-pass filter with a cutoff frequency of 5 Hz was first applied to the PPG signals. Then, the baseline of PPG and ABP signals was removed by subtracting the mean of the upper and lower signal envelopes estimated using maximum/minimum detection on a sliding window. Finally, when the SQIs of the PPG/ABP signal reached a certain threshold, the OSC-MSE-W/OSC-MSEc-W algorithms were used to compute the instantaneous HR of the available signals. In order to increase the robustness of HR estimation, smoothed versions of the input signals, obtained with a moving average of length l , were also fed to the algorithm. It is especially important to attenuate the dicrotic notch and to ensure the tracking of the main oscillation and not of the first harmonic. The example illustrated in Figure 4.15 shows why it is necessary to use also the smoothed signal as an input to the adaptive frequency tracking algorithms for a precise HR estimation. In this example, the ABP signal has a lower frequency component, which is the frequency corresponding to instantaneous HR, and a higher frequency component, due to the presence of the dicrotic notch. It can be seen that, when the smoothed ABP signal is also provided to the OSC-MSE-W algorithm, the common frequency between the inputs is the frequency of interest and the HR can be accurately estimated, which is not the case when only the ABP signal is used. In order to further optimize HR estimation, the parameters required for adaptive frequency tracking, were empirically selected for each type of arrhythmia. These parameters are summarized in Table 4.2, where f_{re} indicates the re-sampling frequency of the waveforms, β is related to the bandwidth of the adaptive band-pass filter and δ is a forgetting factor. Figure 4.16 shows an example of HR estimation using the OSC-MSE-W algorithm, during a true extreme tachycardia episode. As illustrated, despite the moderate quality of the waveforms, the oscillation of interest is correctly isolated by the adaptive band-pass filter and instantaneous HR can be estimated. It should be noted that, for asystole alarms, a smaller δ was used in order to detect decreases in HR faster. It was noticed that the complex version of the algorithm (OCS-MSEc-W) was more suitable for arrhythmia associated with low HR, i.e. asystole and bradycardia.

². For an introduction to instantaneous frequency and the adaptive frequency tracking algorithms presented here, see Appendix A

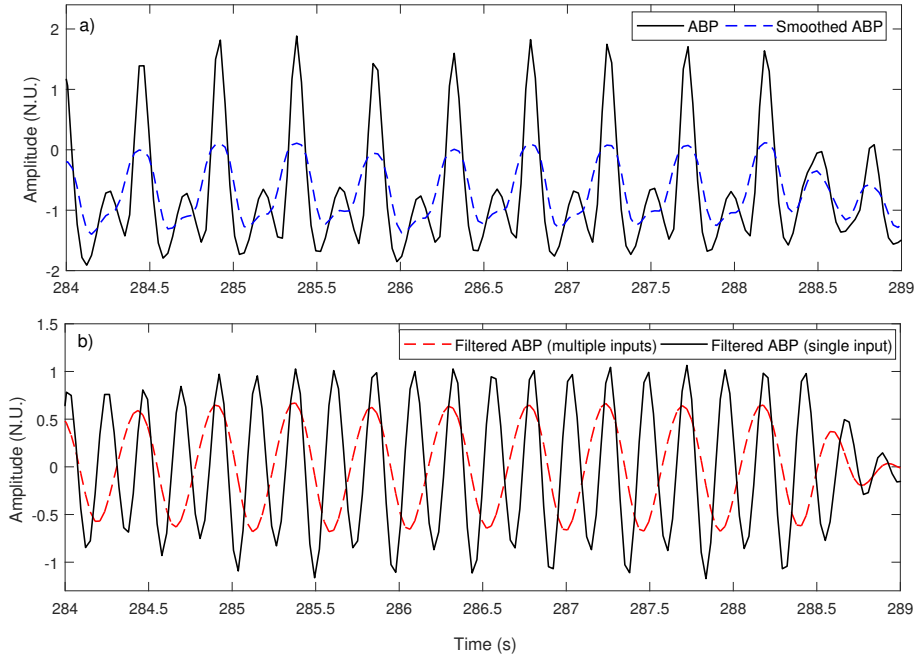


Figure 4.15 – Example to illustrate the interest of using multiple inputs for adaptive frequency tracking. (a) Original ABP signal (solid line) and smoothed ABP signal (dashed line). (b) ABP signal filtered with the adaptive band-pass filter using only the original ABP signal as input (solid line) or both original and smoothed ABP signals (dashed line).

Table 4.2 – Algorithms and selected parameters for HR estimation using PPG and/or ABP waveforms.

Arrhythmia	Algorithm	f_{re} (Hz)	l_{PPG} (samples)	l_{ABP} (samples)	β	δ
Asystole	OSC-MSEc-W	15	3	3	0.8	0.8
Extreme Bradycardia	OSC-MSEc-W	15	3,5,11	7	0.87	0.87
Extreme Tachycardia	OSC-MSE-W	35	5	7	0.89	0.9
Ventricular Tachycardia	OSC-MSE-W	35	5	7	0.89	0.9

4.2.4 Arrhythmia Alarm Processing

Definition of the five alarm types (see Table 4.1) allowed for the development of processing schemes specific to each arrhythmia, which are described throughout the upcoming subsections. In each scheme, thresholds were empirically selected in order to maximize the corresponding TNR while keeping TPR as close as possible to 100% in the training dataset.

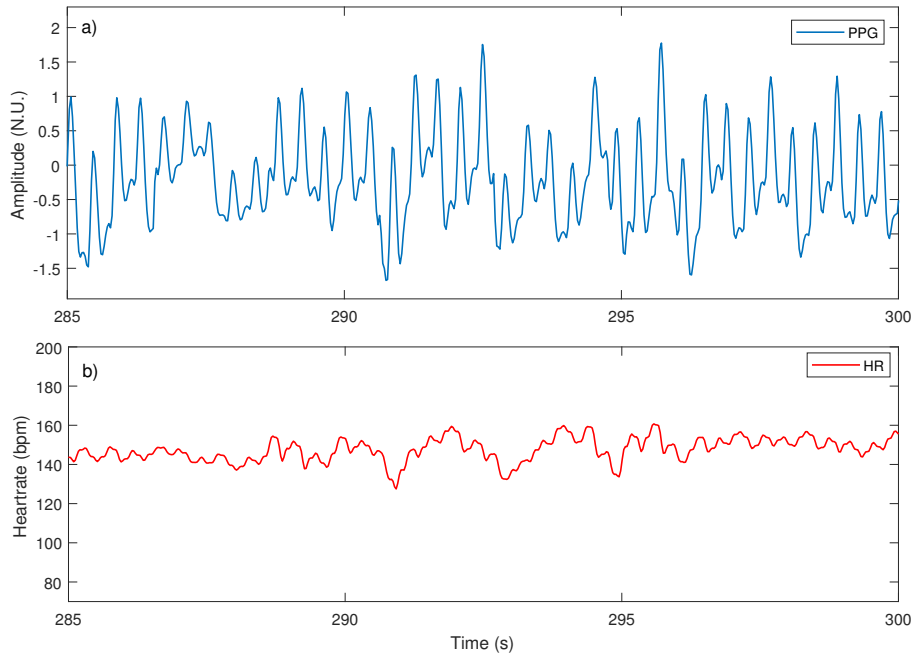


Figure 4.16 – Example of HR estimation using the adaptive band-pass filter. (a) PPG waveform. (b) Instantaneous HR.

Asystole Processing.

Figure 4.17 illustrates the processing scheme for asystole. For this arrhythmia, available ECGs and high quality pulsatile waveforms were processed separately and alarm veracity was determined by means of voting. More specifically, the alarm was suppressed if at least one processed waveforms suppressed the alarm. For the retrospective setting, a few seconds of data after the alarm were also taken into account for the calculation of the HR features, i.e. the mean HR and the decrease of HR for the pulsatile waveforms and the maximum RR-interval for ECG waveforms. Linear discriminant analysis (LDA) was used to compute the alarm result derived from the pulsatile waveforms. In order to have consistency with the performance metric that was used in this study (see Section 4.2.5), the false negative cost was set as five time larger than that of false positive in the LDA. The classifier was trained on the training dataset. Regarding the processing of the ECG signals, a threshold of 3.5 seconds was put on the maximum RR-interval value during the last 20 seconds before alarm was triggered (+ 5 seconds after in case retrospective data were available) to compute the ECG alarm results.

Extreme Bradycardia Processing.

Two different processing schemes are possible in case of extreme bradycardia alarm, depending on the quality of the waveforms (Figure 4.18). When at least one of the pulsatile waveforms had an acceptable quality (SQI higher than 0.5), alarm validity was determined based on a threshold of 54 bpm on the mean and median HR values extracted from the pulsatile waveforms during the last five seconds before the alarm was triggered. On the other hand, when the SQIs of PPG and ABP waveforms were both below 0.5, the ECG waveforms were analyzed. A threshold of 40 bpm was used on the minimum HR derived from five consecutive beats to discriminate

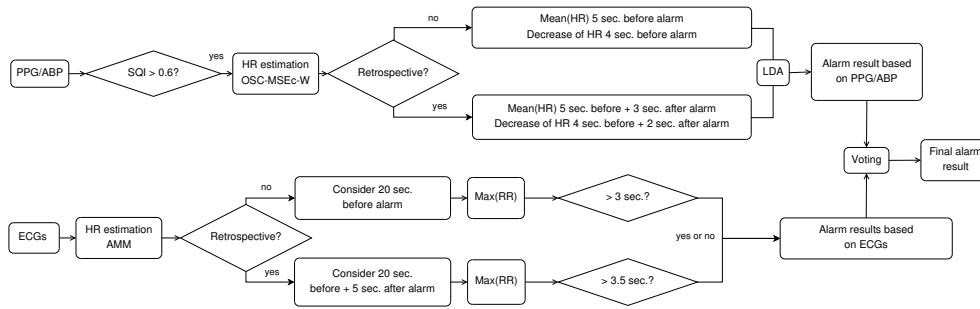


Figure 4.17 – Asystole alarm processing.

between true and false alarms. A period of 16 seconds before the alarm was considered and, if available, 5 seconds after the alarm were also taken into account.

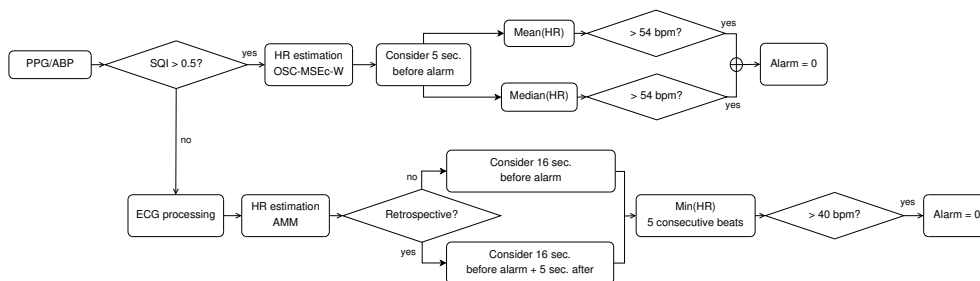


Figure 4.18 – Extreme bradycardia alarm processing.

Extreme Tachycardia Processing.

In case of extreme tachycardia alarm, only the pulsatile waveforms were processed, as shown in Figure 4.19. The decision about alarm veracity was made from the mean and maximum HR values during the last four seconds preceding the alarm. More precisely, the alarm was suppressed if the maximum HR was below 115 bpm while the mean HR was below 100 bpm. For this arrhythmia, ECG waveforms were not analyzed.

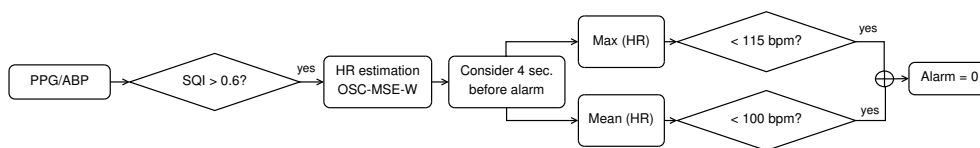


Figure 4.19 – Extreme tachycardia alarm processing.

Ventricular Flutter/Fibrillation Processing.

As can be seen in Figure 4.20, a single feature, the maximum average SPI on a 3-second sliding window (2-second overlap), was used to suppress false ventricular flutter/fibrillation alarms. More precisely, the alarm was suppressed if this SPI feature was smaller than 0.63 during the 15 seconds preceding the alarm. Pulsatile waveforms were not processed for this arrhythmia.

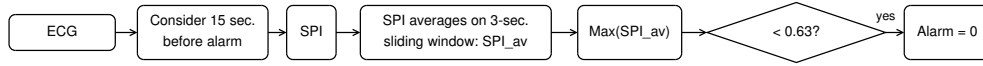


Figure 4.20 – Ventricular flutter/fibrillation alarm processing.

Ventricular Tachycardia Processing.

The processing of ventricular tachycardia alarms was the most challenging one (Figure 4.21). On one hand, pulsatile waveforms were used to compute HR and suppress the alarm if the HR ranged between 60 and 90 bpm. On the other hand, the ECG SPI was employed to detect morphological changes during ventricular contractions. It should be noted that pulsatile waveforms and ECGs were processed independently, and that both could lead to the suppression of the alarm. The first feature was the maximum of the average SPI on a 3-second sliding window (2-second overlap) during the 20 seconds preceding the alarm. The maximum difference between every other value of these SPI averages were used to compute a second feature reflecting SPI increase. Three different conditions led to alarm suppression based on the SPI features described above. Either the maximum SPI increase had to be below 0.012, or the maximum SPI average was below 0.25, or both the maximum SPI average and the maximum SPI increase were below 0.36 and 0.2, respectively.

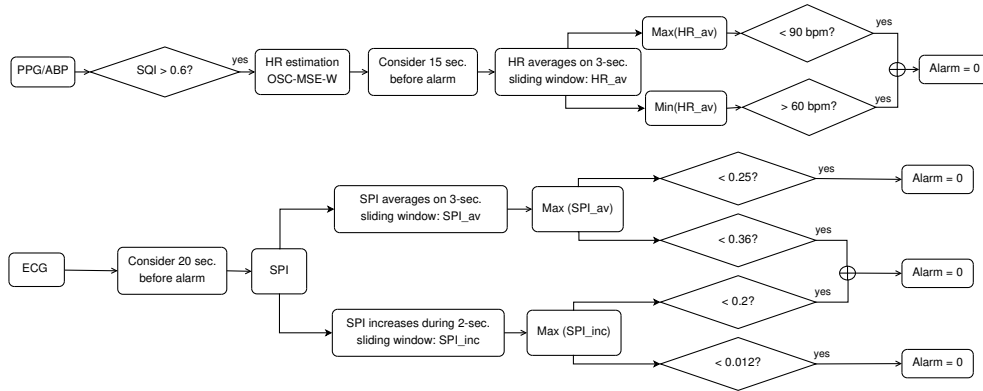


Figure 4.21 – Ventricular tachycardia alarm processing.

4.2.5 Evaluation Metrics

A training set of 750 records was provided for this challenge. Then, the performance of the developed scheme was evaluated on a hidden test set of 500 records (extended to 750 records for the second phase). It is important to eliminate false alarms while preserving true alarms, since the life of the patient is threatened if true alarms are suppressed. To enforce this, a specific score function was selected for this challenge [9]. This score is a function of the number of true positives (TP), false positives (FP), false negatives (FN) and true negatives (TN), computed by the following equation:

$$Score = \frac{100 \cdot (TP + TN)}{(TP + TN + FP + 5 \cdot FN)} \quad (4.7)$$

As shown in Equation 4.7, FN alarms are penalized five times more than FP alarms. In addition to this score, true positive rates (TPRs) and true negative rates (TNRs) were reported for the different alarm types.

4.3 Results

After feature extraction and training on the available training set, the presented scheme was first evaluated on a test set of 500 records, and was ranked as the second best method with an overall score of 73. For the second phase of this challenge, the main focus was on the optimization of the parameters that were used by the different algorithms in the presented scheme. At the same time, different voting strategies were studied in order to find the best way to aggregate the results provided by each processing component. It is worth mentioning that, for this phase, an additional dataset of 250 records was added to the evaluation dataset. For the real-time test dataset, the proposed framework achieved a TPR of 94%, a TNR of 77%, and an overall score of 76.11. Regarding the retrospective subset, a TPR of 99% and a TNR of 80% were achieved, with an overall score of 85.04 [139]. This scheme was ranked fifth in the real-time event and first in the retrospective event of the second phase of this challenge [9]. A follow-up phase was also considered for this challenge. After applying minor changes to the decision-making process of the asystole and extreme tachycardia alarms, an improvement of one percent in TPR was achieved for the real time event, resulting in a real-time score of 77.07. More details on the performance of the proposed scheme on the training and the test datasets can be found in Tables 4.3 and 4.4, respectively.

Table 4.3 – Results obtained on the hidden-test dataset.

	Phase I			Phase II			Follow-up		
	TPR (%)	TNR (%)	Score	TPR (%)	TNR (%)	Score	TPR (%)	TNR (%)	Score
Arrhythmia									
Asystole	92	78	76.42	83	88	81.44	94	85	84.28
Extreme brady.	96	66	73.53	100	71	82.47	100	71	82.47
Extreme tachy.	96	60	80.00	97	60	86.18	97	80	86.99
Ventricular flutter/fib.	83	88	79.55	89	94	87.10	89	94	87.10
Ventricular tachy.	93	65	67.38	94	72	72.75	94	72	72.75
Real-time	93	65	68.15	94	77	76.11	95	76	77.07
Retrospective	95	77	77.82	99	80	85.04	99	80	85.04

Table 4.4 – Results for the training set.

Arrhythmia	TP (%)	FP (%)	FN (%)	TN (%)	TPR (%)	TNR (%)	Score
Asystole	18	12	0	70	100	85	87.70
Extreme bradycardia	51	18	1	30	98	63	77.49
Extreme tachycardia	94	3	0	4	100	55	97.10
Ventricular flutter/fibrillation	10	16	0	74	100	83	84.48
Ventricular tachycardia	22	19	4	55	85	75	67.45
Average	39	13	1	47	98	78	82.31
Gross	37	14	2	47	95	76	77.88

4.4 Discussion

In this challenge, the highest score in both real-time and retrospective events was achieved by a meta-algorithm, which uses a voting system on the 13 best performing entries. Table 4.5

compares the results achieved by the proposed scheme with the meta-algorithm developed by the challenge organizers. More details about the top scoring entries from the other participants can be found in [9]. Regardless of the final scores, the main goal was to achieve the highest TPR since the applicability of the developed method in the ICU would be most acceptable with a TPR of 100%. This was reflected in the final results, as the proposed approach reached the highest TPR for both real-time and retrospective events [9].

Table 4.5 – Comparison between the proposed scheme and the voting algorithm.

	Real-time subset			Retrospective subset		
	TPR	TNR	Score	TPR	TNR	Score
Voting algorithm [9]	94%	90%	84.26	94%	94%	87.03
The proposed scheme	95%	76%	77.07	99%	80%	85.04

Of course, quality assessment of the signals plays an important role in FA suppression in the ICU. Indeed, in the presented scheme, the use of the PPG/ABP SQI was necessary to obtain satisfying results. Table 4.6 shows the percentage of records that were analyzed based on the SQI threshold set in the proposed scheme. It should be noted that for extreme tachycardia alarms, only 51% of the records had quality acceptable enough to be analyzed. Therefore, excluding 49% of signals undoubtedly affects the final TPR and TNR that can be achieved for this arrhythmia, as shown by the low TNR on the training set reported in Table 4.4. The use of an ECG quality assessment method was also investigated in this study. As mentioned in Section 4.2.2, the ECGs in the database usually present various perturbations. Therefore, during the training phase of this study, an ECG quality assessment classifier was developed, in order to categorize the ECGs into low, moderate, and high quality classes. To this end, all ECGs in the dataset were manually labeled by an operator and various features were extracted from them. Initially, third and fourth moments, i.e. skewness [147, 148] and kurtosis [147, 149], as well as ECG baseline and QRS-complex powers were extracted from recordings, as proposed in [135]. Then ECGs were processed by AMM and several QRS-complex driven features were extracted from the output of the AMM. More specifically, features such as maximum, minimum, average duration of QRS-complexes and RR-intervals were extracted from the signals. Subsequently, a support vector machine based ECG signal quality assessment classifier was trained and validated (10-fold cross-validation). The classification accuracy of the trained classifier was 81.6% against the training set. However, when this ECG quality assessment was incorporated into AMM, a performance decrease was observed in the training set. For this reason, the use of ECG quality assessment was discontinued for this challenge. This was especially interesting as there were quite a few recordings in the training dataset where one ECG lead had acceptable quality while the other was suffering from low quality. Figure 4.22 illustrates a recording in the training set with unequal ECG lead qualities.

Table 4.6 – Percentage of processed waveforms for each type of alarm in the training set.

Arrhythmia	ABP	PPG	PPG or ABP	ECG	% of processed records
Asystole	35%	45%	80%	100%	100%
Extreme bradycardia	40%	64%	80%	20%	100%
Extreme tachycardia	29%	26%	51%	0%	51%
Ventricular flutter/fibrillation	0%	0%	0%	100%	100%
Ventricular tachycardia	45%	52%	78%	100%	100%

Based on the results presented above, it seems that adaptive frequency tracking is an appropriate technique to obtain instantaneous HR from the pulsatile waveforms. This method does not

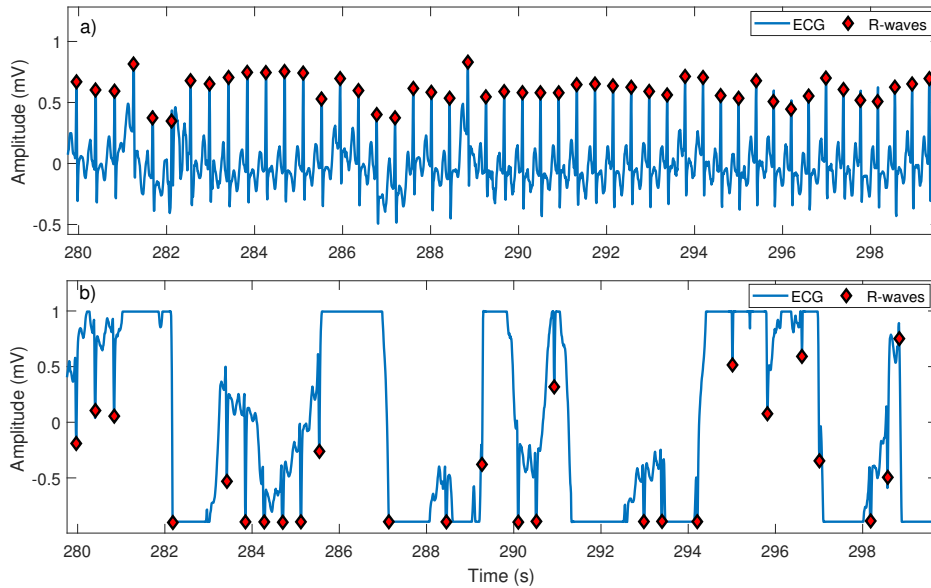


Figure 4.22 – Example of a recording (t114s) in the training set with a good quality ECG lead as well as a bad quality lead.

provide any information about heart rate variability, but results suggest that precise HR averages and trends are most of the time sufficient to determine the validity of the alarm. Moreover, adaptive frequency tracking enabled us to process moderate quality waveforms, and as a result increased the numbers of potential FA candidates for suppression. Furthermore, information from ABP and PPG can be easily combined using this technique.

The elimination of false ventricular tachycardia alarms on the basis of solely processing the PPG/ABP waveforms is very difficult. Observations showed that ventricular tachycardia episodes sometimes induce amplitude decreases in the pulsatile signals. However, as illustrated in Figure 4.23, this effect was not consistent over records. In this figure, the PPG waveforms, as well as the ECG waveforms are displayed for two records corresponding to true ventricular tachycardia episodes. It can be noted that the pulse amplitudes decrease during the ventricular beats for the first record, from second 295 to 298, but the same behavior can not be observed for the second record. For this reason, PPG/ABP amplitude changes were excluded from the scheme. This phenomenon has also been reported in the literature [150]. In this work the pulse amplitude, among other features, was used to detect ventricular premature beats. The authors noted that different pulse patterns are possible in the PPG signal when a premature ventricular beat occurs, depending on blood pumping efficiency. Finally, as a compromise, it was decided to rely on pulsatile waveforms for HR estimation and on ECGs for the detection of the morphological changes. As far as the state-of-the-art, it is the first time SPI is used to characterize the morphological changes related to ventricular arrhythmias. This measure undoubtedly has a potential to be used for ventricular tachycardia and ventricular flutter/fibrillation arrhythmias, as confirmed by the good results achieved with a very limited number of features. Moreover, the computation of this index can be performed on-line in the time domain, at a very low cost.

The decision-making process of the presented scheme is very straightforward, as it mainly uses simple thresholds on a few features to eliminate FAs. In order to find the optimal way to ag-

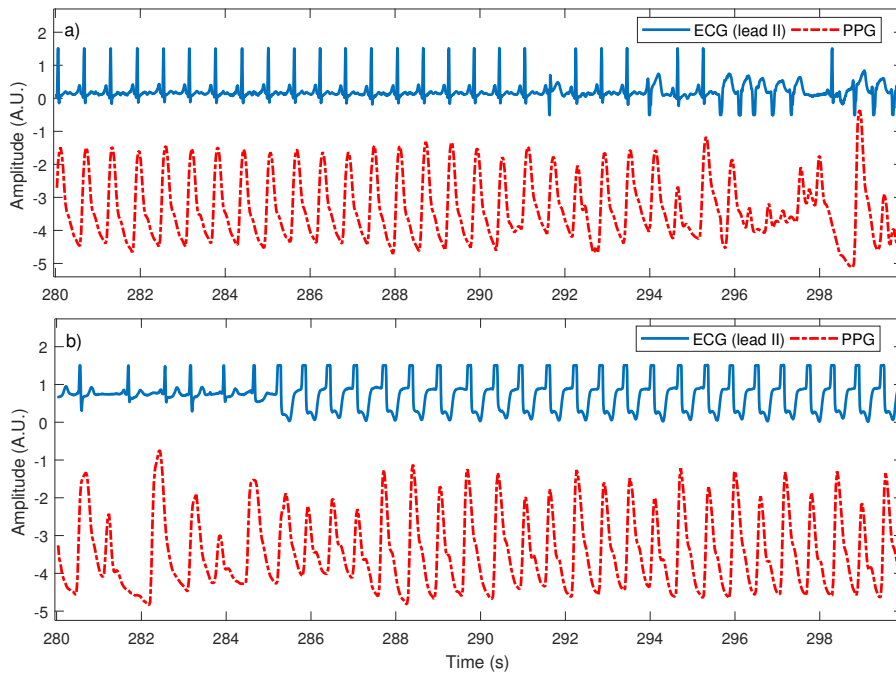


Figure 4.23 – Two examples of PPG signal behavior during true ventricular tachycardia episodes. (a) Record v628s. A decrease in pulse amplitude can be observed in the PPG signal during the arrhythmia; (b) Record v159l. No decrease in PPG pulse amplitude.

gregate the results provided by different components of the proposed scheme, both learner fusion and learner selection methods were studied³. As illustrated by the arrhythmia alarm processing schemes (figures 4.17 - 4.21), for asystole and ventricular tachycardia alarms, a fusion-based method lead to the best results. For extreme bradycardia, the alarm verification procedure is chosen based on the threshold of 0.5 on the PPG/ABP SQI, which represents the learner selection that was incorporated for this arrhythmia. For extreme tachycardia and ventricular flutter/fibrillation, results showed that the use of pulsatile waveforms alone and ECG waveforms alone, respectively, were more effective.

It should also be noted that, compared to the exact alarm definitions (see Table 4.1), most HR thresholds in the proposed method were set to have a certain degree of tolerance, which was necessary to avoid the suppression of true alarm. Using a decision-making process based on sophisticated machine learning algorithms is debatable within the context of this challenge. Indeed, machine learning-based approaches have already proven their efficiency, as shown by the results from the other participants in the challenge [9]. However, limited number of features allowed to keep the presented scheme more simple while rendering a physiological interpretation possible. The similarities between the performance achieved on training and test datasets confirm the relevance of the empirically chosen parameters (see Tables 4.3 and 4.4), and suggest that overfitting was avoided despite the limited number of available records for some types of arrhythmia. It is worth mentioning that, during the development of the presented method for the processing of ventricular tachycardia, it was studied to see weather it was possible to replace the thresholds on SPI derived features (see Figure 4.21) by an LDA classifier. However, despite the better results obtained on the training set, lower performance were achieved in the test dataset, as shown in

3. Detailed description on classifier combination can be found in Appendix B

Table 4.7.

Table 4.7 – Linear discriminant analysis for ventricular tachycardia alarms.

	Training dataset			Test dataset		
	TPR (%)	TNR (%)	Score	TPR (%)	TNR (%)	Score
With LDA	90	77	72.83	81	74	64.83
No LDA	85	75	67.45	94	72	72.75

4.5 Conclusion

This study confirms that the use of cardiovascular signals from independent sources is of great interest to reduce the number of FAs in the ICU. This chapter presents an innovative approach, based on the capture of specific signal behavior that occur during arrhythmia episodes, in addition to the traditional HR measures derived from the ECGs and pulsatile waveforms. The efficiency of the presented approach was demonstrated on the PhysioNet/CinC Challenge 2015 dataset, for which TNRs of 76/80% were achieved, with corresponding TPRs of 95/99% for the real-time and retrospective subsets, respectively.

Short-Term Event Extraction in Biomedical Signals

5

This chapter presents a fast non-linear filtering method called Relative-Energy (Rel-En), for robust short-term event extraction from biomedical signals. Rel-En extracts short- and long-term energies in a signal and provides a coefficient vector with which the signal is multiplied, heightening events of interest. The proposed algorithm is implemented using two filters and its parameters can be selected easily and intuitively. This algorithm is thoroughly assessed on benchmark datasets in three different biomedical applications namely, ECG QRS-complex detection, EEG K-complex detection, and imaging photoplethysmography (iPPG) peak detection. Rel-En successfully identified the events in these settings. Compared to the state-of-the-art, better or comparable results were obtained on QRS-complex and K-complex detection. For iPPG peak detection, the proposed method was used as a preprocessing step to a fixed threshold algorithm that lead to a significant improvement in overall results. Furthermore, the Rel-En algorithm can be used in other biomedical signal processing applications in which short-term event extraction is needed. Elements of the methods and results in this chapter were originally presented as a conference paper [151], then published as a journal paper [102].

5.1 Introduction

Biomedical signal processing is the study of the measurements recorded by physiological instruments. Analysis of these measurements provides physicians with important physiological information that may help them to uncover underlying dynamics of human health. It also allows them to determine patient health state and to choose the right treatment.

Physiological signals comprise different waveforms, the extraction of which often being the first step in their investigation. Over the last decades, several spike/waveform extraction methods have been proposed in the literature. Generally, the signal is preprocessed by means of high-, low-, or band-pass filtering, followed by a comparison against detection logics and thresholds, to determine the veracity of the peaks [152]. A simple approach is to apply a threshold on the raw or the absolute value of a signal to extract impulsive events, as proposed for neural recordings [153–155]. A common way to set this simple threshold is to base it on an estimate of the standard deviation of the noise [153, 154]. The Plosion index (PI) is another method used to detect impulse-like events in signals [101]. This index is defined as,

$$PI(n) = \frac{|x(n)|}{\left(\sum_{j=n-m_1}^{n+m_2} |x(j)|\right)/(m_2 + m_1 + 1)} \quad (5.1)$$

where $x(n)$ denotes the n th sample of the input signal x . Parameters m_1 and m_2 describe the interval on which the average is applied. PI has been used in speech processing to detect closure burst transitions of stops and affricates [101]. This index has also been used to extract R-waves from ECGs [156]. The slope characteristics of the input signal have proven to be a good feature for short-term event extraction. The idea is to scrutinize the first derivative of the input signal in order to detect abrupt changes in the amplitude, which represent the onset of action potentials or impulsive waveforms [73, 76, 157–159]. The nonlinear energy operator [160], also known as Teager energy, has also been used to detect impulses. This operator captures high frequency local activities using an input sample and its immediate neighbors. After applying this operator, the output is compared against a threshold and impulses are extracted [153, 161]. The aforementioned methods are easy to implement and perform well in normal settings in which the input signal is not contaminated by perturbations. More elaborated yet robust methods such as template matching and wavelet transforms have been proposed to deal with noise-contaminated signals. Template matching methods scan the signal in order to find instances that are similar to a pre-defined set of templates. Usually the matching operation is carried out by studying a similarity measure such as the Euclidean distance between an instance and the predefined templates [41, 157, 162, 163], or by calculating their cross-correlation [164, 165]. Template matching algorithms generally perform better compared to the aforementioned ‘thresholding’ methods. Moreover, they can identify different morphologies and extract several types of waveform from the signal. However, these methods require a priori knowledge of the morphology of the waveform(s) of interest. Since these morphologies can be application- or even subject-dependent, they need to be studied and might even require expert input in order to be extracted. The wavelet transform is another interesting approach for waveform extraction [84]. By offering good frequency resolution at low frequencies and high time resolution at high frequencies, wavelet-based methods are vastly popular in automatic waveform detection [84, 154, 166]. Furthermore, these methods can be implemented as filter banks, leading to low computation cost [152, 153]. In this approach, generally, the stationary wavelet transform is calculated across several dyadic scales and the optimum scale is chosen. Then, element-wise product between the optimum scale and its two previous scales is calculated and smoothed. Finally, the product is compared to a threshold for spike extraction. As a drawback to wavelet approaches, it is worth noting that even at small scales, wavelet functions are oscillations but short-term events, such as spikes, do not necessarily have an oscillatory behavior. Apart from the aforementioned methods, over the years, other diverse detection techniques such as filter-banks [89], adaptive filters [167, 168], mathematical morphology filters [6, 90], matched filters [167, 169], genetic algorithms [95], hidden Markov models [94], artificial neural networks [167, 170], and fuzzy-logic detection [171, 172] have been proposed in the literature. However, several problems remains partially unsolved in the automatic extraction of waveforms. Most methods, especially simple ones that can be adapted in many biomedical signal processing settings, focus on the sample at hand and its close vicinity while discarding the important ‘long-term’ information in the signal. Therefore, any source of noise can result in values higher than the chosen threshold and subsequently lead to false detection. On the other hand, more elaborated methods become task-specific, rendering them either ineffective for a wide scope of applications, in need of expert input, or even dependent on long training and optimization times.

In this chapter, a simple, easy to compute algorithm for short-term event detection in biomedical signals is proposed. This algorithm uses the relative information between short- and long-term energies in the signal, which can be robustly specified, to compute a coefficient vector. The coefficient vector is then multiplied with the original signal, heightening impulse-like complexes while suppressing unwanted information from the signal. The proposed algorithm is evaluated on three biomedical signal processing applications in order to have a comprehensive evaluation of its performance.

5.2 Method

Careful analysis of waveforms in different biomedical settings lead to the understanding that even in cases where the biomedical signal is severely contaminated by perturbations, there is a significant difference in terms of signal power in the baseline and in the waveform of interest. Therefore, by analyzing the relative short- and long-term energies in the signal, given the short- and long-term window lengths are properly chosen, one can extract the peaks from the baseline.

5.2.1 Relative-Energy (Rel-En) Algorithm

Using two sliding windows, centered at sample n of the input signal x , a coefficient signal $c(\cdot)$, defined as the ratio between short- and long-term signal energies, is obtained through,

$$c(n) = \frac{\sum_{i=n-s_{win}}^{n+s_{win}} |x(i)|^p}{\sum_{j=n-l_{win}}^{n+l_{win}} |w(j) \times x(j)|^p} \quad (5.2)$$

Where parameters s_{win} and l_{win} represent the half-lengths of the short and long sliding windows, respectively. Parameters p and w denote respectively the exponent and window function of interest. It is worth noting that absolute values of x are considered in Equation 5.2, in order to allow odd p values. Finally, the output signal is calculated using,

$$x_{RE}(n) = x(n)c(n) \quad (5.3)$$

Therefore, element-wise multiplication of the coefficient vector by the original signal results in an output, x_{RE} , in which impulsive waveforms with duration close to that of the short window are amplified, while other signal components are dimmed. This element-wise multiplication not only enhances these impulsive waveforms but also preserves their polarity. As a rule of thumb, the short-term window should be long enough to contain the desired waveform. At the same time, the long-term window duration should be selected to reflect long-term behavior of the signal. However, it should not be so long that the short-term window variations are made insignificant in Equation 5.2.

The successive steps of the proposed algorithm are illustrated in Figure 5.1, where Rel-En is applied to a synthesized signal comprised of a series of impulses added to a sinusoid (Figure 5.1-a). The sinusoid oscillates with a frequency of 25 Hz at a 500 Hz sampling frequency. Impulses are generated randomly as half-periods of the sinusoid multiplied by an integer (Figure 5.1-b). In this example a short- and long-term durations of respectively 10 and 100 samples were selected for the windows. Furthermore, an exponent of $p = 2$, and a Hamming windowing function was used to calculate the long-term energy. For demonstration purposes a normalized evolution of the input signal and short- and long-term energies are illustrated in Figure 5.1-c. using these parameters, the Rel-En algorithm successfully detects the impulses and almost fully discards the baseline sinusoidal activity (Figure 5.1-d).

5.3 Examples of Applications of Rel-En

Having defined the Rel-En algorithm, we examined its performance in different biomedical signal processing applications. Rel-En performance was evaluated in QRS-complex detection from the ECG, K-complex detection from the EEG, and pulse extraction from iPPG. Throughout the remainder of this section, these applications are described in details and evaluated.

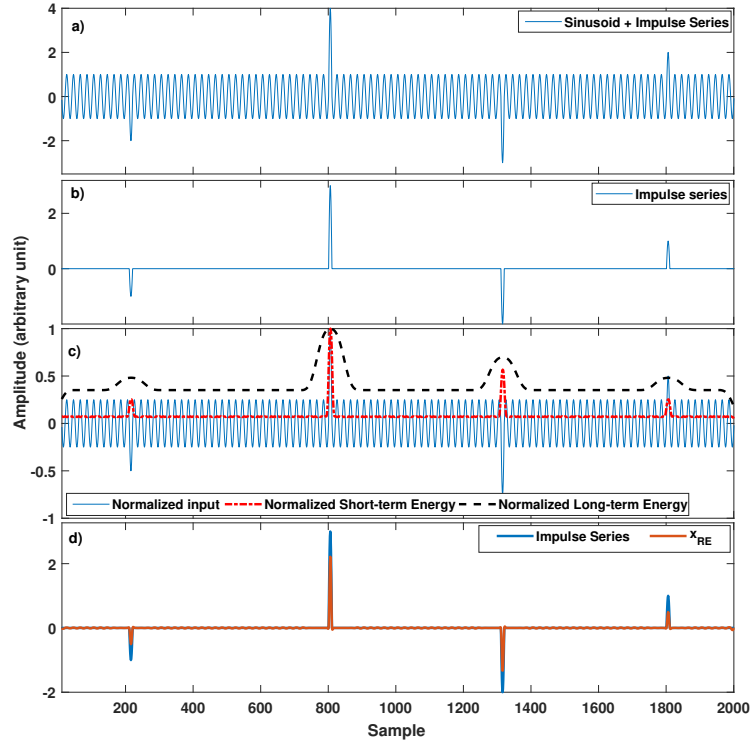


Figure 5.1 – Illustration of different steps of the Rel-En algorithm on a synthetic signal composed of an impulse series added to a sinusoid. a) The input signal, i.e. the sinusoid + the impulse series. b) The impulse series. c) Normalized Short- and long-term energy, respectively the numerator and denominator in Equation 5.2, evolution. d) The output of Rel-En, x_{RE} .

5.3.1 Rel-En for QRS-complex detection in ECG

Due to their peaky morphological characteristics, QRS-complexes are primarily used for automatic heartbeat detection. A review of classical QRS-complex detection approaches can be found in Chapter 3 and [103, 152]. Several studies have been performed on ECG QRS-complex detection, varying in terms of performance and complexity. Of course, in a conventional setting, complexity is not a major issue due to the ever-increasing computation power available. However, with the rise of wearable technologies and body area networks, there has been a new trend, with studies aiming at offering good performance while requiring lower computation complexity. The simplicity of Rel-En made QRS-complex detection an appealing application.

Materials

The Physionet MIT/BIH arrhythmia database was used in order to evaluate the performance of Rel-En [48]. This publicly available database has been used to evaluate several automatic QRS-complex detection methods (for more details see Section 3.4.1). The evaluation on this database was performed on the first lead, which is either a modified lead II (46 records) or lead V5 (two records). Results were checked with the reference annotation file provided for this database.

Parameters and Detection Logic

In order to evaluate the Rel-En algorithm on the MIT/BIH arrhythmia database, first the ECG was band-pass filtered in the range of 4 – 40 Hz. The filtered ECG was then passed through the Rel-En algorithm with short and long sliding window durations of respectively 140ms and 950ms, and a value of $p = 2$ was selected for the exponent. The Hamming windowing was used in this application to avoid spurious peaks and to have a smooth long-term energy variation. In order to apply the detection logic, x_{RE} was normalized using min-max normalization, i.e.,

$$z(n) = \frac{x(n) - \min(x)}{\max(x) - \min(x)} \quad (5.4)$$

Where $x(n)$ denotes the n th sample of x . Finally, the mean of the normalized signal was removed. For QRS-complex detection, a very simple detection logic was considered. First, local extrema with a minimum time distance of 250ms were extracted from the mean-removed normalized x_{RE} , and the QRS-complex locations were considered as those of the maxima with an absolute amplitude of at least 0.02 (arbitrary unit). Figure 5.2 illustrates successive steps of the Rel-En algorithm on a low quality segment of tape 105 of the MIT/BIH arrhythmia database. Among the 48 tapes of this database, tape 105 is one of the most challenging records for automatic QRS-complex detection due to the presence of perturbations such as baseline wandering and muscular activities. Although band-pass filtering improves the behavior of the signal, the detection of QRS-complexes is still challenging. However, after calculating the coefficient signal using Rel-En and multiplying it with the band passed filtered ECG, one can clearly observe the QRS-complexes in the output.

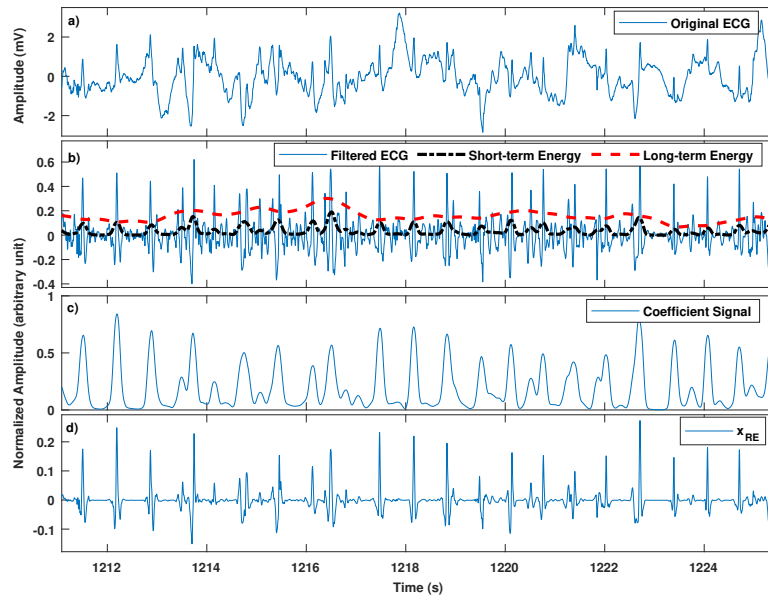


Figure 5.2 – Illustration of different steps of the Rel-En algorithm on tape 105 of the Physionet MIT/BIH arrhythmia database. a) Original ECG. b) Band-pass filtered [4 – 40]Hz ECG, and the evolution of short- and long-term energies in the ECG. c) The extracted coefficient signal, c (Equation 5.2). d) The output of Rel-En, x_{RE} (Equation 5.3).

Results and Remarks on QRS-complex Detection

The extracted QRS-complexes by Rel-En were compared with those in the annotation files. Table 5.1 compares Rel-En performance with that of the state-of-the-art approaches. As shown in this table, Rel-En yielded the lowest number of false negatives, while providing better or comparable results with the state-of-the-art. More specifically, tape-by-tape results are reported in Table 5.2. In this tables, the detection error rate (DER) as well as sensitivity (Se) and positive prediction value (PPV) are calculated in the same fashion as in Section 3.5.1.

As the main parameters of Rel-En, p as well as short- and long-term window durations must be appropriately chosen. Since typical QRS-complexes have a duration around 100 – 150ms [107], different short-term window durations in the range of 80 – 200ms were examined. Simultaneously, the long-term window was studied in the range of 0.5 – 5 seconds. Short- and long-term windows of respectively 140ms and 950ms provided to the best performance. In the general discussion section, we demonstrate that a wide range of parameter values actually lead to very similar performance, suggesting that parameter selection is not critical. Since the long-term window was not relatively much longer than the short-term window, Hamming windowing was used to smooth the long-term energy variations. Of course, having longer durations for the long-term window leads to a smoother variation in the energy signal, but observations have shown that in most cases, low amplitude QRS-complexes, such as some ventricular beats, were miss detected. The exponent parameter was also studied in the integer range of 1 – 5, with $p = 2$ leading to the best results. A larger p has the tendency to improve the extraction of the complexes while higher levels of perturbation are present. However, like the long-term window duration, larger values lead to miss detection of low amplitude QRS-complexes.

Table 5.1 – Rel-En QRS-complex extraction performance comparison with the state-of-the-art.

Method	No. of Beats	FP	FN	DER %
Relative-Energy	110070	134	103	0.21
AMM (Yazdani. and Vesin) [6]	109494	108	137	0.224
Pan and Tompkins [73]	109809	507	277	0.710
Li et al. [84]	104184	65	112	0.170
Zhang and Lian [90]	109510	204	213	0.38
Ravanshad et al. [97]	109428	651	1216	1.71
Martinez et al. [112]	109428	153	220	0.34
Bahoura et al. [87]	109809	135	184	0.29
Moody and Mark [113]	109428	94	1861	1.79
Lee et al. [114]	109481	137	135	0.43
Hamilton and Tompkins [76]	109267	248	340	0.54
Poli et al. [95]	109963	545	441	0.90
Chen et al. [115]	102654	529	459	0.96
Afonso et al. [89]	90909	406	374	0.86

Results reported in Tables 5.1 and 5.2, suggest that the proposed method can efficiently extract R-waves from the ECG. In order to find out how the proposed method performs when perturbations are present the ECG, Rel-En was evaluated against white and synthetic EMG noise, created by fitting an autoregressive model on EMG recordings from the Physionet/CinC2014 challenge database. The purpose of this challenge was the robust extraction of heartbeats by means of multi-modal signal processing. In this challenge, ABP, PPG, EMG and even EEG signals were available alongside ECG channels. More information about this challenge and database can be found in [173].

Using clean segments of ECGs in the MIT/BIH arrhythmia database, different levels of noise, from an input signal-to-noise ratio (SNR) of 100 to -20, were incrementally added to the ECG.

Table 5.2 – Detail performance of Rel-En on QRS-complex detection on MIT/BIH arrhythmia database.

Tape No.	No. of Beats	FP	FN	DER %	Sensitivity	PPV
100	2272	0	0	0	1	1
101	1869	2	2	0.11	0.9989	0.9989
102	2186	0	0	0	1	1
103	2083	0	0	0	1	1
104	2228	28	0	0	1	0.9874
105	2602	15	12	0.1	0.9954	0.9942
106	2027	1	0	0	1	0.9995
107	2137	0	0	0	1	1
108	1771	20	1	0.056	0.9994	0.9887
109	2531	0	0	0	1	1
111	2124	2	1	0.047	0.9995	0.9991
112	2538	0	0	0	1	1
113	1794	0	0	0	1	1
114	1880	1	0	0	1	0.9995
115	1958	0	1	0.051	0.9995	1
116	2411	1	7	0.33	0.9971	0.9996
117	1534	1	0	0	1	0.9993
118	2278	1	0	0	1	0.9996
119	1987	0	0	0	1	1
121	1862	0	0	0	1	1
122	2477	0	2	0.081	0.9992	1
123	1518	0	0	0	1	1
124	1618	1	0	0	1	0.9994
200	2600	4	2	0.023	0.9992	0.9985
201	1963	0	6	0.31	0.9969	1
202	2137	2	3	0.14	0.9986	0.9991
203	3006	7	18	0.83	0.9934	0.9977
205	2656	0	5	0.19	0.9981	1
207	2334	7	1	0.043	0.9996	0.997
208	2962	1	11	0.41	0.9963	0.9997
209	3011	2	0	0	1	0.9993
210	2650	6	10	0.38	0.9962	0.9977
212	2748	1	0	0	1	0.9996
213	3250	0	1	0.031	0.9997	1
214	2266	2	4	0.18	0.9982	0.9991
215	3362	0	1	0.03	0.9997	1
217	2209	0	1	0.045	0.9995	1
219	2154	0	0	0	1	1
220	2047	0	0	0	1	1
221	2427	0	3	0.12	0.9988	1
222	2482	2	0	0	1	0.9992
223	2604	0	0	0	1	1
228	2077	18	6	0.12	0.9971	0.9913
230	2257	0	0	0	1	1
231	1570	0	0	0	1	1
232	1780	9	0	0	1	0.9957
233	3080	0	4	0.13	0.9987	1
234	2753	0	1	0.036	0.9996	1
Total	110070	134	103	0.21	0.9991	0.9988

Then, R-wave extraction performance was tested against Pan-Tompkins algorithm and Rel-En algorithm. Results showed robust extraction of R-waves up to an input SNR of 0 or below, both against white and synthetic EMG noises. Figure 5.3 illustrates the performance of Rel-En and compares it with that of Pan-Tompkins. In this example, an EMG noise was added to the first lead of tape 100 from the MIT/BIH arrhythmia database making an input SNR of -0.12. Since the number of extracted R-waves are different in the top three sub-figures, the calculated RR-intervals were uniformly sampled in time in order to have a more sensible comparison. As seen in this figure, the RR-interval extraction is significantly improved when Rel-EN is applied to the ECG. With similar results obtained when white noise was added to the ECG, this simply defined algorithm is rendered useful in robust R-wave detection.

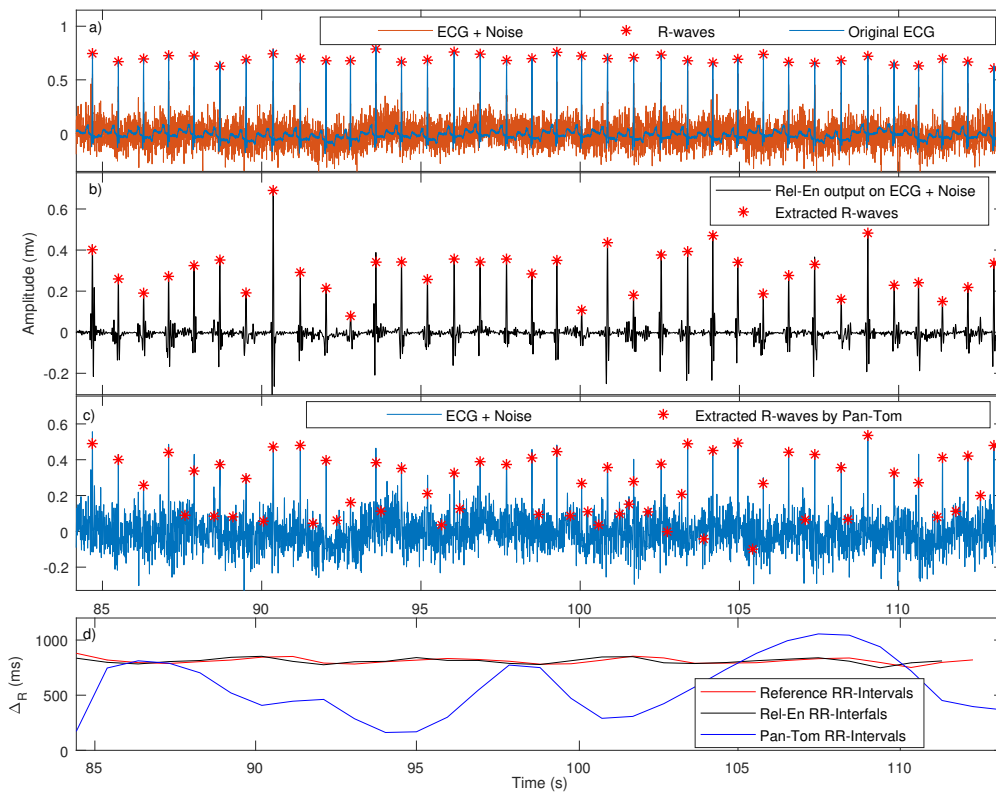


Figure 5.3 – Performance of Pan-Tompkins and Rel-En algorithms against an ECG with added synthesized EMG noise. a) Original ECG together with reference QRS-complexes and the noisy ECG. b) Output of the Rel-En algorithm on the noisy ECG, alongside the extracted R-waves. c) The noisy ECG and the detected QRS-complexes extracted by the Pan-Tompkins algorithm. d) Reference and extracted RR-intervals time series from Rel-En and Pan-Tompkins algorithm. These RR-intervals are uniformly sampled in time, for demonstration. Tape 100 of the MIT/BIH arrhythmia database.

As illustrated in Figure 5.3, one can "enhance" ECGs by multiplying the coefficient signal and the original ECG. As QRS-complexes have relatively higher energy in comparison with P-, T-waves and the noise in the signal, the coefficient signal values are close to one where QRS-complexes take place in the ECG while smaller elsewhere. Figure 5.4 illustrates an example of ECG enhancement on a noisy segment of the first lead of tape 104 from the MIT/BIH arrhythmia database. It would be also interesting to see the frequency domain characteristics of this en-

hancement. Figure 5.5 illustrates the power spectral density estimate (PSD) calculated for the ECG, noisy ECG and the Rel-En output depicted in Figure 5.3. It is clear that the PSD of the noisy ECG, is completely different from that of the original ECG. On the other hand the PSD of the enhanced ECG is quite similar to that of the original ECG, retaining the main frequency components of the original signal.

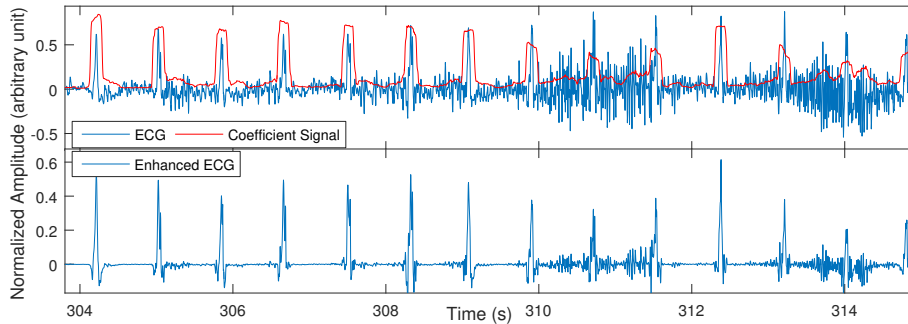


Figure 5.4 – Illustration of ECG enhancement using Rel-En. On top the original noisy ECG is depicted together with the coefficient signal calculated by Rel-En. The bottom figure shows the enhanced ECG calculated by element-wise multiplication of the coefficient vector by the original ECG. The ECG segment is taken from tape 100 of the MIT/BIH arrhythmia database.

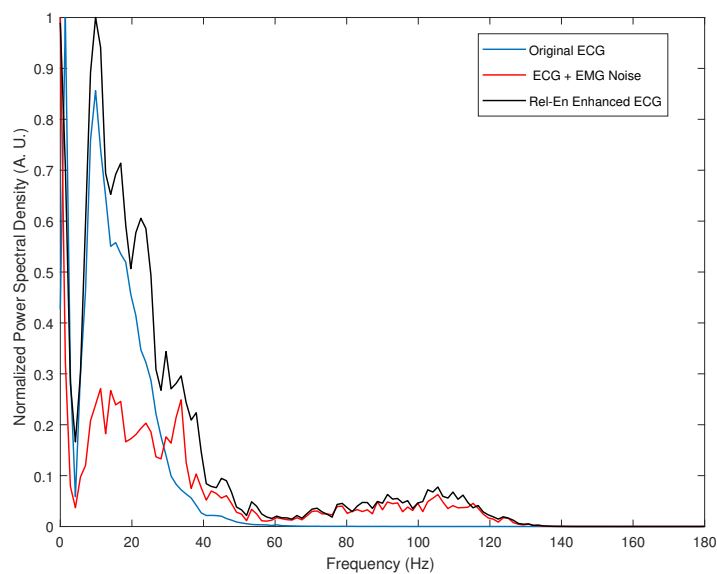


Figure 5.5 – Power spectral density of the Original ECG, noisy ECG and the enhanced ECG by means of Rel-En filtering. Tape 100 of the MIT/BIH arrhythmia database. The PSDs are normalized for demonstration.

5.3.2 Rel-En for K-complex Detection in EEG

A K-complex is characterized as a negative-positive peak in the EEG. Automatic detection of these complexes is of high importance for sleep-stage detection as they are thought to occur mostly in the second stage of Non-REM sleep in which subject is in light sleep. K-complex detection was specifically selected for Rel-En evaluation since in most cases these complexes are mixed with waveforms of similar amplitude in the EEG. Therefore, automatic extraction of K-complexes is an arduous task, which requires a large number of detection thresholds. In fact, to the best of knowledge, the state-of-the-art extract K-complexes by training classifiers in order to best discriminate between these complexes and others in the EEG [89, 170, 174]. Bremer et al. proposed a filter and thresholding system to detect K-complexes across different sleep stages in the EEG [174]. Bankman et al. extracted a set of features such as the maximum and minimum amplitude, duration of a complex, distance between the negative and positive peaks of the complex, and trained an artificial neural network in order to detect K-complexes in the EEG [170]. Devuyst et al. extracted a set of similar features and used fuzzy thresholds in order to compute a K-complex likelihood to find out the veracity of a K-complex [171].

Materials

For evaluation and comparison purposes, we used a public K-complex database, acquired in the sleep laboratory of a Belgian hospital using a digital 32-channel polygraph (BrainnetTM system of MEDATEC, Brussels, Belgium) [171]. This database comprises 10 whole-night polysomnography¹ recordings from healthy subjects. Each recording consists of two Electrooculography (EOG) channels, three Electroencephalogram (EEG) channels (CZ-A1 or C3-A1, FP1-A1 and O1-A1) and one submental Electromyography (EMG) channel, sampled at 200Hz. In this database, a 30-min EEG segment is selected from each whole-night recording for K-complex scoring. These 30-min excerpts were independently submitted to two experts for annotation. Out of the two experts, one provided annotations for only five excerpts. Here, the CZ-A1/C3-A1 EEG channel for K-complex extraction and Rel-En performance evaluation on channels annotated by both experts is used.

Parameters and Detection Logic

For each excerpt, the CZ-A1/C3-A1 channel was first high-pass filtered with a cutoff frequency of 3 Hz. The filtered EEG was then used as input to the Rel-En algorithm with a short- and long-term window durations of respectively 0.75 and 5 seconds. The exponent parameter p was set to 5. The output of the Rel-En algorithm was further processed as follows:

- Small values of the coefficient signal (≤ 0.005) were set to zero.
- Non-zero segments, defined as at least two consecutive non-zero values, were extracted from the coefficient signal, as K-complex candidates.
- Candidates were scrutinized and were selected as a viable K-complex if the following conditions were met,

$$Valid_{K_{complex}} = \begin{cases} k_{max} > 40\mu V \\ k_{min} < -20\mu V \\ k_{max} - k_{min} > 75\mu V \\ 0.5s < (t_{k_{max}} - t_{k_{min}}) < 0.75s \\ k_{max} > 0.5 \times MaxAmp_{left-and-right} \\ k_{max} > 40 \times MaxAmp_{left-or-right} \end{cases} \quad (5.5)$$

where K_{min} , K_{max} , t_{min} , and t_{max} respectively denote the minimum amplitude, maximum amplitude, and time of their occurrence in a K-complex candidate. $MaxAmp_{left}$ and $MaxAmp_{right}$ are

1. For more information on polysomnography recordings see Chapter 7.

maximum amplitudes within a 5-second search window respectively preceding and following the K-complex candidate. For K-complex detection a subset of intuitive and interpretable thresholds was used, which previously proposed by other studies such as minimum duration [175], minimal K-complex amplitude [174, 176], minimum negative-to-positive peak [174], and checking for high amplitude neighbor peaks [177].

Results

For performance comparison the assessment algorithm provided with the public K-complex detection database² was used. This algorithm calculates the TP, FP, FN, and TN values by comparing the time and the duration of K-complexes detected by Rel-En with those of expert annotations. Excerpts that were not annotated by both experts were used to find thresholds in Equation 5.5, while the remaining excerpts were used for testing. Table 5.3 shows detailed results on the performance of Rel-En and compares it with the automatic annotation method proposed by Devuyst et al. [171]. For evaluation and comparison, the performance of Rel-En and the automatic method proposed in [171] were assessed with respect to annotations from the first, second experts, and also a merged annotation (implemented by the assessment algorithm) where a K-complex is considered as a true positive if it is in accordance with any of the expert annotations. As seen in Table 5.3, Rel-En outperforms the state-of-the-art, providing higher sensitivity, positive prediction value, and at the same time lower detection error rate.

Table 5.3 – Performance of Rel-En on automatic K-complex extraction and its comparison with the state-of-the-art.

Results by Rel-En								
	Labeled Expert 1	Not Labeled Expert 1	Labeled Expert 2	Not Labeled Expert 2	Labeled Expert 1 or Expert 2	Not Labeled Expert 1 or Expert 2		
Detected Rel-En	141	43	46	138	149	35		
Not Detected Rel-En	67	8749	17	8799	80	8736		
Sensitivity	PPV	DER %	Sensitivity	PPV	DER %	Sensitivity	PPV	DER %
0.6779	0.7663	1.24	0.7302	0.25	1.75	0.6505	0.8098	1.29
Results by Devuyst et al. [171]								
	Labeled Expert 1	Not Labeled Expert 1	Labeled Expert 2	Not Labeled Expert 2	Labeled Expert 1 or Expert 2	Not Labeled Expert 1 or Expert 2		
Detected	129	46	38	137	135	40		
Not Detected	79	8746	25	8800	94	8731		
Sensitivity	PPV	DER %	Sensitivity	PPV	DER %	Sensitivity	PPV	DER %
0.6202	0.7371	1.41	0.6032	0.2171	1.83	0.5895	0.7714	1.36
Bold fields denote the better performing algorithm.								

Remarks on K-complex detection

In terms of Rel-En parameters, the short-term window duration of 750ms was chosen by studying the duration distribution of annotated complexes in the training excerpts, while the long-term duration and the exponent were empirically chosen. The application of Rel-En to K-complex extraction was especially chosen to show the importance of the exponent parameter p . Since K-complexes can be interspersed with other waveforms of similar amplitude, small values of p can lead to a high number of false positives. Figure 5.6 illustrates this important feature. As can be seen, if $p = 2$ is considered, the Rel-En algorithm becomes more sensitive to EEG activities which do not necessarily represent K-complexes. As the exponent parameter gets larger, Rel-En becomes more selective, discarding lower amplitude peaks. Of course, some

2. <http://www.tcts.fpms.ac.be/~devuyst/Databases/AssessmentAlgorithm/>

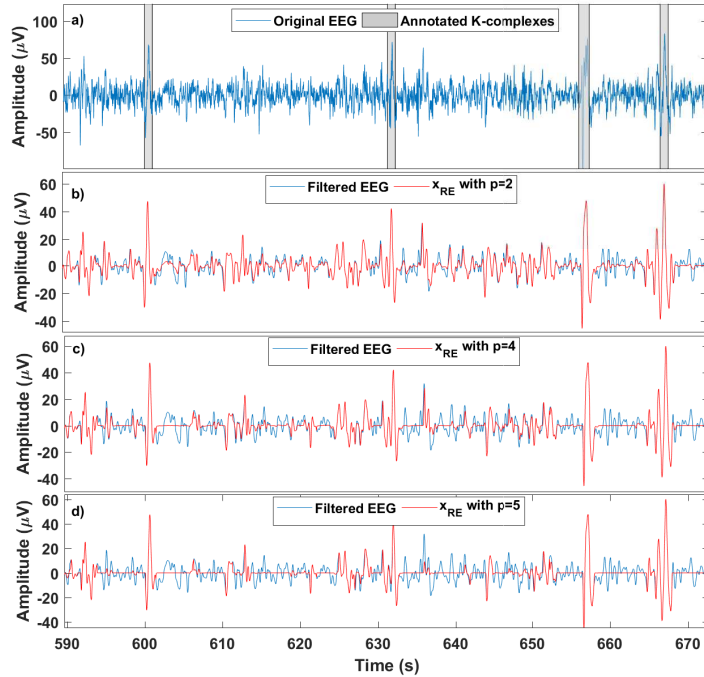


Figure 5.6 – Illustration of performance of Rel-En on excerpt 6 from the K-complex database. a) The original EEG and annotated K-complexes (annotator 1). b) high-passed filtered EEG and x_{RE} with $p = 2$. c) x_{RE} with $p = 4$. d) x_{RE} with $p = 5$.

p values lead to better performance but as shown in the general discussion section, the performance does not change drastically around the optimal p value. The fact that K-complexes can occur in between waveforms with similar amplitudes in the EEG could be the main reason why the detection of K-complexes is a difficult task. More specifically, comparison of the annotations on excerpts that have been provided by both experts, as reported in Table 5.4, demonstrates there is a significant disagreement between the annotations. When it comes to automatic detection, the state-of-the-art focuses on extracting numerous features in order to suppress false positive predictions. For instance, the method proposed by Devuyt et al. [171] was trained on a set of 13 features. The same number of features was used in [166] for the training of an artificial neural network. In both methods a series of interpretable features, descriptive of the shape and amplitude of the K-complexes, such as features used in Equation 5.5, as well as use non intuitive features such as t_{mid1} , and t_{mid2} which represent the time the EEG signal crosses the $0 \mu V$ respectively after the negative peak, and before the positive peak.

Table 5.4 – Annotation agreement between the two annotators on excerpts annotated by both annotators.

Annotators	Labeled Expert 1	Not Labeled Expert 2
Labeled Expert 2	42	21
Not Labeled Expert 2	166	8770

5.3.3 Rel-En for Pulse Extraction from iPPG

Imaging photoplethysmography (iPPG) is a non-contact method to measure the heart rate from skin color changes, using simple color video cameras. By analyzing video channels, i.e. RGB channels, Verkruysse et al. showed that blood flow variability can be observed in all video channels [178]. iPPG is still a new field of research in which the main challenge is to estimate the heart rate [179]. A review of iPPG heart rate estimation techniques can be found in [180]. In this section, a simple fixed threshold approach is presented, which is applied directly on a smoothed iPPG, and the Rel-En filtered iPPG, for performance comparison.

Materials

The database is composed of 23 4-minute recordings, from 12 healthy subjects. For each record, a one-lead ECG and video sequence of the upper body region were recorded simultaneously. In order to induce HR variations, the subjects were asked to perform an isometric hand-grip exercise (one subject did not participate) or to modulate their respiration according to a given protocol. They were also asked to move as least as possible. All subjects gave their informed consent. The sequences were recorded in the presence of artificial light using an RGB camera and sampled at 20 frames per second with a resolution of 1.3 megapixels. The raw RGB traces were obtained by averaging the pixels within a manually determined and fixed rectangular region of interest (ROI) on the forehead, as shown in Figure 5.7. These raw iPPG signals were



Figure 5.7 – Region of interest used to extract iPPG waveforms.

then band-pass filtered between 0.6-4 Hz using an 8th-order Butterworth filter. After visual inspection of the iPPG waveforms derived from the video-sequences, it was noted that the quality of the green iPPG waveform was generally higher compared to the blue and red iPPG waveforms, which was in agreement with [178], as illustrated in Figure 5.8. For this reason, the green iPPG waveform was used for evaluation and iPPG waveforms from red and blue channels were discarded. QRS-complexes were extracted from the ECG, using the method presented here, and then visually verified to be used as the ground truth. Four recordings, two from the hand-grip exercise and two from respiration modulation, were used for training and Rel-En parameter tuning. The remaining recordings were used for evaluation.

Parameters and Detection Logic

The green iPPG channel was first normalized using the min-max normalization method described in Equation 5.4. After removing the mean value, the normalized iPPG was then passed through the Rel-En algorithm with a short sliding window duration of 100ms while the longer sliding window had a 600ms duration. An exponent of 10 was selected for p . A Hamming windowing function was used in order to smooth the long-term energy variation. Optimal values of

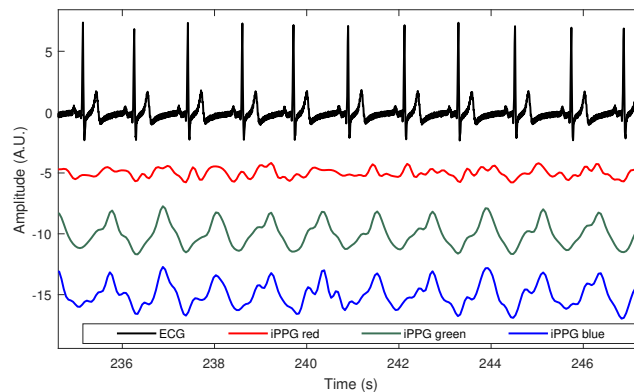


Figure 5.8 – Extracted iPPG channels alongside the captured ECG from a recording. As illustrated, the green iPPG provides the highest quality in comparison with the red and blue iPPG.

the exponent, the short-term and long-term window durations were selected by performing a grid search on the training recordings. Short-term and long-term windows were studied in a range of respectively 100-800ms and 400-4000ms with a step size of 50ms, while the power was studied in the integer range of 2–20. Finally, iPPG peaks were extracted from the output of Rel-En using simple thresholds, defined as local extrema with a minimum distance of 250ms from previous peaks, and a minimum amplitude of zero.

Results

The results obtained by Rel-En were compared to a fixed threshold method. The fixed method uses the same detection logic as Rel-En, however after min-max normalization and the removing of the mean value, the signal was further smoothed using a moving average algorithm with a window length of five samples, in order to avoid spurious peak detection. The extracted peaks from the smoothed normalized green iPPG as well as the output of Rel-En, x_{RE} , were compared to those extracted from the ECG. An extracted iPPG peak was considered as a correct detection if it took place up to 200ms after the reference beat, in order to compensate for the ECG-iPPG peak transit time. Table 5.5 reports the detailed results obtained for each method. Performance is measured for the isometric handgrip exercise, respiration modulation, and both settings at the same time. Rel-En consistently provided better performance compared to the smoothed signal approach. More specifically, Rel-En provides significantly less false positive detections compared to the fixed threshold method.

Remarks on iPPG Peak Detection

Unlike ECG QRS-complex and EEG K-complex extraction, the peaks in an iPPG signal are not as impulsive either in terms of duration or in terms of amplitude. In other words, the iPPG has more oscillatory behavior as opposed to the impulsive behavior of complexes in the ECG and EEG. For this reason, iPPG peak detection was selected to assess the performance of Rel-En in case waveforms represent oscillatory behavior. Our observations on iPPG waveforms showed that the detection of spurious peaks, due to the presence of moderate amplitude oscillations, is a major issue in this biomedical application. Although moving average smoothing can help remove spurious peaks to some extent, one cannot use a large number of neighboring samples as moving average can suppress useful information in the iPPG. The exponent parameter in Rel-En makes it possible to heighten peaks that are more prominent even if other peaks are present in the signal at hand, as illustrated in Figure 5.9. In this figure, the moving average does not provide a robust

Table 5.5 – Performance of Rel-En on iPPG peak detection and comparison with classic a threshold method.

Method	Beats	FP	FN	DER%	Sensitivity (Se)	PPV
Respiration Modulation						
Rel-En	3515	22	24	1.31	99.31	99.37
Fixed Threshold	3515	48	23	2.02	99.34	98.63
Isometric Handgrip Exercise						
Rel-En	3145	61	95	4.96	96.62	98.00
Fixed Threshold	3145	83	137	7.00	95.53	97.24
Respiration Modulation and Isometric Handgrip Exercise						
Rel-En	6660	83	119	3.03	98.19	98.73
Fixed Threshold	6660	131	160	4.37	97.55	97.98

Bold fields denote the better performing algorithm.

performance, which leads to signal over-sensing and miss estimation of the heart rate, such as the detection of spurious peaks between seconds 560-561 and 563-564 Figure 5.9-b). However, Rel-En successfully suppresses these spurious peaks and leads to a correct estimation of heart rate (Figure 5.9-c).

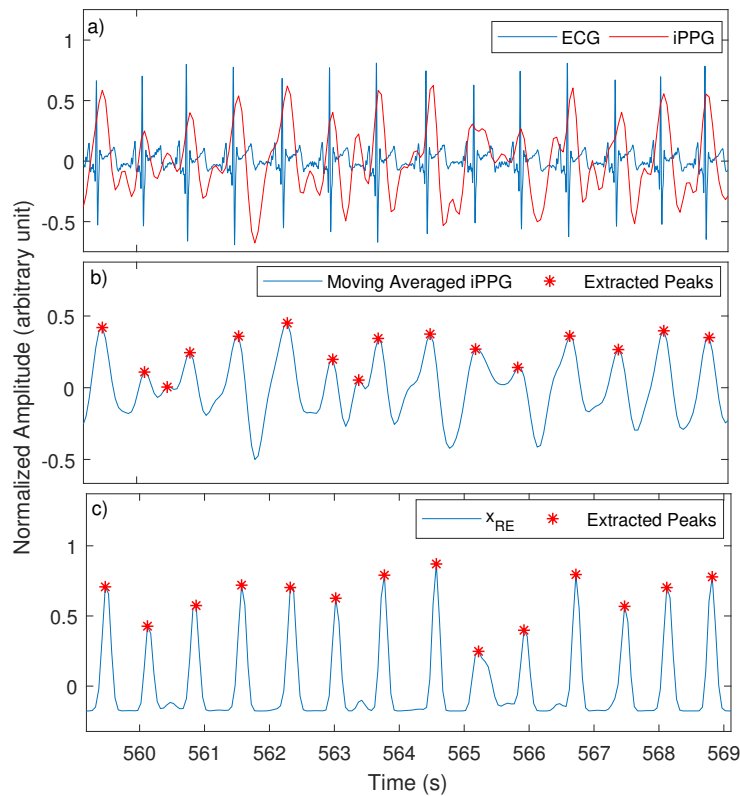


Figure 5.9 – Illustration of performance of Rel-En a recoding from the iPPG database. a) Original ECG and the extracted iPPG waveform. b) Moving averaged iPPG and the extracted peaks. c) x_{RE} and the extracted peaks.

5.4 General Discussion

The proposed method in this chapter uses short- and long-term energies in the signal to detect peaks. Rel-En has some similarities to the plosion index, described in Section 5.1. However, there are major differences between the two methods that makes Rel-En more attractive. First, unlike PI, the short-term window duration in Rel-En allows for the extraction of peaks in general and not only impulse-like events, such in iPPG application. Moreover, different windowing functions such as Hamming or rectangular windows can be used to tailor the algorithm for a more robust output. Finally, the exponent parameter plays an important role in the outcome of Rel-En, determining the sensitivity of the algorithm to peaks. What sets Rel-En apart from other methods is the element-wise multiplication of the coefficient signal with the signal at hand. While preserving the polarity of events, this element-wise multiplication enables Rel-En to suppress spurious peaks and leads to a robust peak extraction. Moreover, the element-wise multiplication in Rel-En makes it a simple tool to highlight peaks and suppress perturbations, used as a pre-processing step for more elaborate methods. The coefficient signal is simply calculated using two filters, which makes Rel-En straightforward and computationally uncstly.

Rel-En parameter selection is also robust. The short- and long-term windows can be selected based on the physiological constraints of the complex or waveform of interest. Our observations have demonstrated that the short-term window should encompass the event of interest. The long-term window duration should reflect the local baseline behavior. However, it should not be so long that the short-term window variations are discarded, or the selected signal segment becomes non-stationary. Of course, short- and long-term window durations influence performance measures such as Se, PPV, and DER. Figure 5.10 illustrates how these parameters affect the overall performance in QRS-complex detection. Figure 5.10-a, shows that sensitivity is almost constant whereas the positive predictive value is more dependent of the short-term window duration (Figure 5.10-b). Still, the flat shape of the three surfaces in Figure 5.10 clearly indicate that the performance is almost constant for a wide range of parameter values.

The windowing function provides the smoothing of long-term variation in the signal, and can be especially important if the difference between the short- and long-term windows is relatively small. The exponent parameter determines the sensitivity of the algorithm. Larger exponent values should be selected in a low signal to noise ratio situation, in order for the algorithm to become more selective. However, the exponent cannot be too large if the desired waveform varies widely in terms of duration and amplitude. Figure 5.11 illustrates the effect of p on the overall Rel-En performance. The exponent p has a larger, although limited, influence on sensitivity than on positive predictive value. The detection error rate does not drastically change around the optimal parameter. Finally, it should be mentioned that although this chapter demonstrates the potential of Rel-En in various settings, there is no theoretical guarantee that Rel-En performs well in all biomedical applications. Obviously, Rel-En is not suited for the detection of short-term events that are not characterized by a local change in amplitude but rather, for instance, by a change in instantaneous frequency. Problems may also arise in situations where short-time events are too close in time.

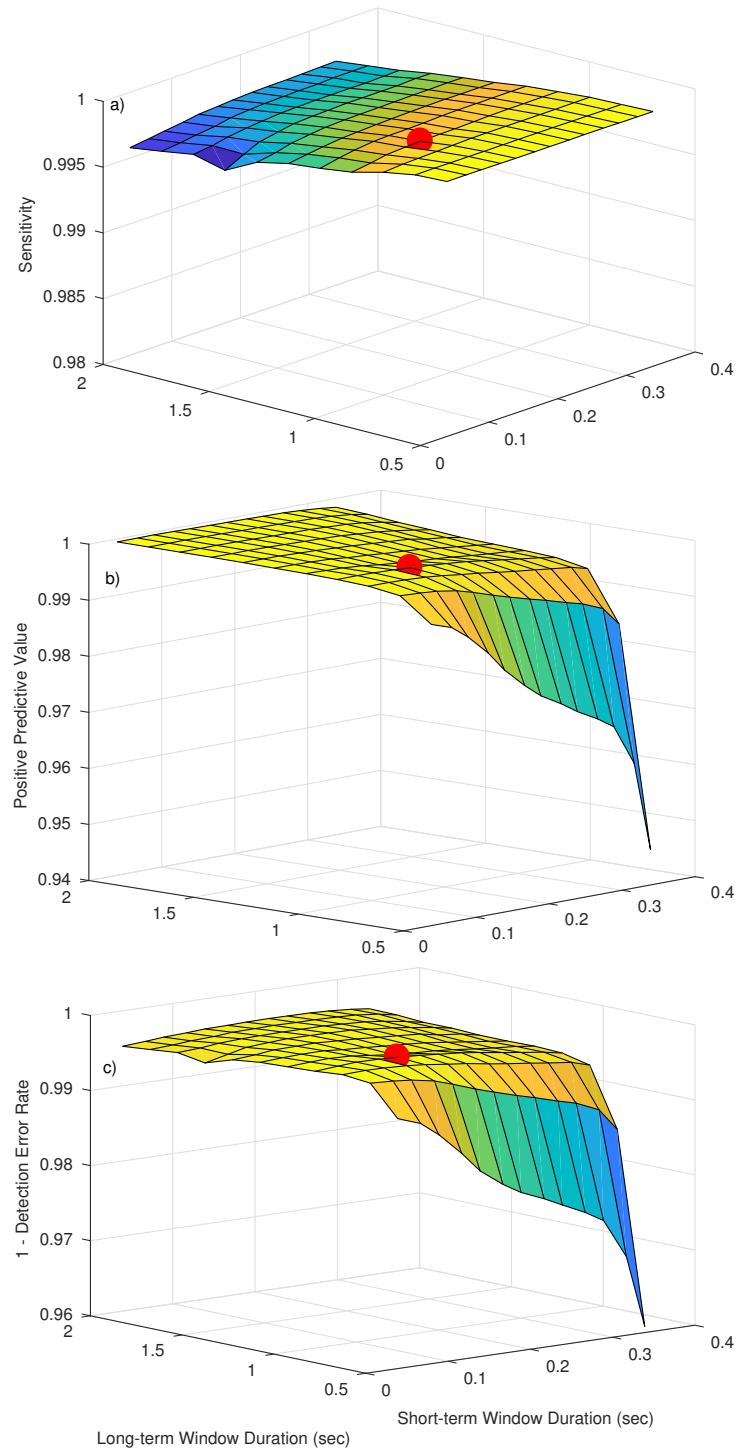


Figure 5.10 – Effect of short- and long-term window lengths on Rel-En performance. a) Evolution of sensitivity. b) Evolution of positive predictive value. c) Evolution of detection error rate (for demonstration purposes, 1- detection error rate has been plotted). In all sub figures, the depicted red point represents the coordinates with lowest detection error rate (short- and long-term window durations of respectively 140 and 950 ms, with a fixed exponent of $p = 2$).

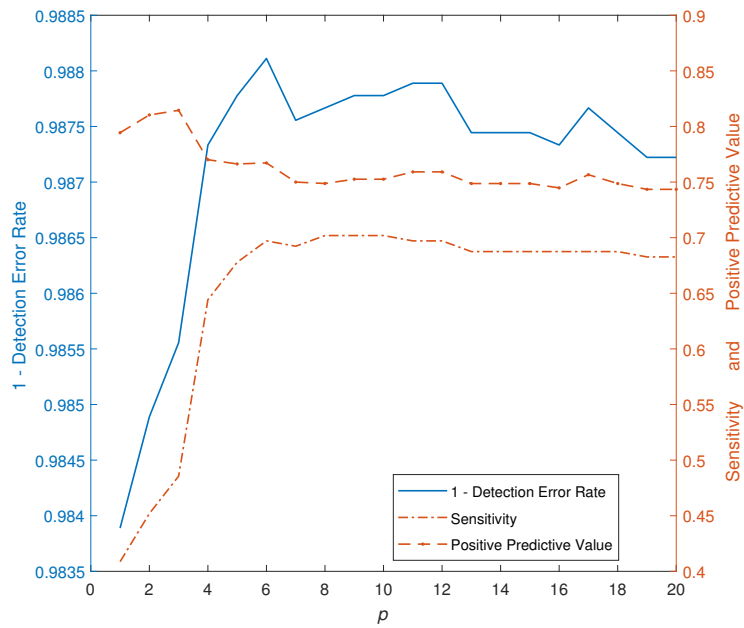


Figure 5.11 – Effect of the exponent parameter p , on Rel-En performance for K-complex detection. Evolution of detection error rate (for demonstration purposes, 1- detection error rate has been plotted; values on the left axis), as well as sensitivity and positive predictive value (values on the right axis). Short- and long-term window durations of respectively 750 ms and 5 seconds were selected. Illustrated results in comparison with annotations of expert 1.

5.5 Miscellaneous Applications

5.5.1 Extraction and Analysis of Short-Time Excursions in RR-interval Time Series

RR-interval time series often present impulses corresponding to short-duration increases or decreases in the heart rate, most probably due to bursts in autonomic activity. The time-domain heart rate variability index pNN50, defined as the ratio of consecutive normal-to-normal intervals that differ by more than 50 ms [181], is obviously linked to these spikes. As linear filtering is not appropriate for the extraction of these spikes, Rel-En was used for this task. This section demonstrates the potential of this approach to assess caffeine-induced changes in the autonomic tone. Elements of the methods and results in this section were originally presented as a conference paper [182].

Introduction

Even after correcting for possible ectopic beats [183], observation of RR-interval time series often reveals the presence of downward and upward impulses corresponding to short-term increases and decreases in the heart rate. Downward and upward impulses are predominantly present when the subject is respectively in a supine or standing position. In Figure 5.12 an RR-interval time series (regularly resampled at 4 Hz) from a healthy subject lying for the first 360 seconds and then standing up is displayed.

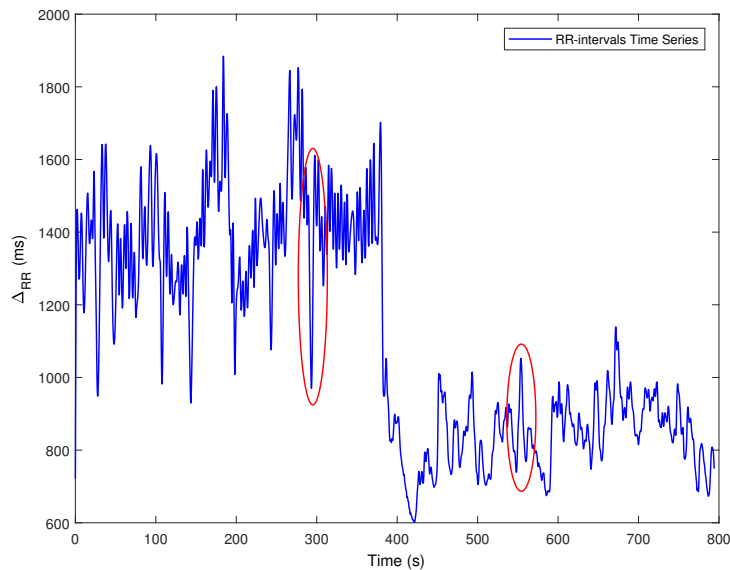


Figure 5.12 – RR-interval time series from a healthy subject. Change from supine to standing at second 360. Two impulses are highlighted by the red ellipses.

In this figure, the impulses as well as their inversion in polarity are clearly visible (two of them highlighted by the red ellipses). This phenomenon can be observed in several studies published in the field of heart rate variability (HRV). For instance, Figure 5.13 illustrates the image used in a classical reference [184], in which this phenomenon is present. Yet, those impulses have rarely been the main focus of previous studies. Actually, several HRV parameters proposed

in the relevant literature are more or less directly connected to these impulses. The most classical one [65] is the pNNx, i.e. the mean number of times per hour that successive normal-to-normal heartbeats differ by more than x ms, the most common value being $x = 50$. Also, the SD1 parameter corresponding to the minor axis of the ellipse fitted to the Poincaré plot of an RR-interval time series measures the short-term variability of the latter [185]. An extension of this approach, the complex correlation measure (CCM) aims at quantifying the point-to-point variation of the RR-intervals rather than the global short-term variability [186].

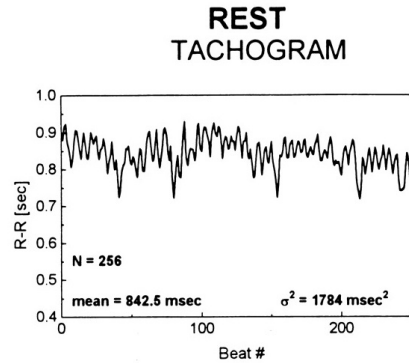


Figure 5.13 – RR-interval time series of 256 consecutive heartbeats in a normal subject at supine rest. Taken from [184], Figure 5-a, with permission.

However, direct extraction of these impulses is a difficult problem due to their limited time extent and asymmetry, and due to respiratory sinus arrhythmia (RSA). In [187], an encoding of RR-intervals using a bank of optimized linear filters was proposed, with short filters corresponding to fast regulation mechanisms. These filters being bandpass ones, only short-term oscillations can be retrieved. The same problem arises with the nonlinear approach described in [188], which proposes a sparse joint decomposition on a pair of wavelet bases with high and low Q-factors. Again, only short- and long-term oscillations can be separated. Extraction of asymmetric impulses is not possible using these methods.

This section, presents an application to Rel-En, in which a small database is analyzed and it is illustrated how the extracted impulse signals can be used to assess drug-induced changes in autonomic activity.

5.5.2 Principle

The principle of using Rel-En is quite simple. Since an impulse is characterized by a local surge in signal energy, the idea is to measure the ratio between a short-term variance estimate and a long-term variance estimate on a sample-by-sample basis. The larger this ratio is, the more impulsive the local signal is. Rel-En does not conserve amplitudes, i.e. the extracted impulses are known only up to a multiplicative coefficient. While not relevant in a detection context, this raises issues if impulse extraction is sought for. An empirical solution consists in scaling the resulting impulse signal so that, when subtracted from the original signal, the resulting signal has minimum skewness, i.e., the asymmetry induced by the impulses is minimized. Also, extraction is improved by applying the Rel-En scheme in additional iterations (by experience two iterations is usually enough) to the successive impulse signals, in order to remove spurious impulses. Of course skewness minimization should still be performed using the original signal.

Figure 5.14 presents an example on a 2000-sample signal generated as follows: a sinusoid with normalized frequency 0.05 was created, and for five half-periods the amplitude was multi-

plied by a factor of two or three. This signal presents some similarity with an RR-interval time series, as the sinusoid corresponds to an RSA at a breathing frequency of 0.2 Hz for a standard sampling frequency of 4 Hz, and the impulses are similar to those in Figure 5.12. The lengths of the short and long windows were respectively 7 and 61 samples. Figure 5.14, from top to bottom, displays the original signal, the true impulse signal (original signal minus sinusoid), the first estimated impulse signal, and the estimated impulse signal after two iterations. The error-to-signal variance ratio between the true impulse signal and the estimated one is 0.027. The relative amplitude errors for the smaller impulses are about 0.001, but they amount to 0.09 for the two largest impulses.

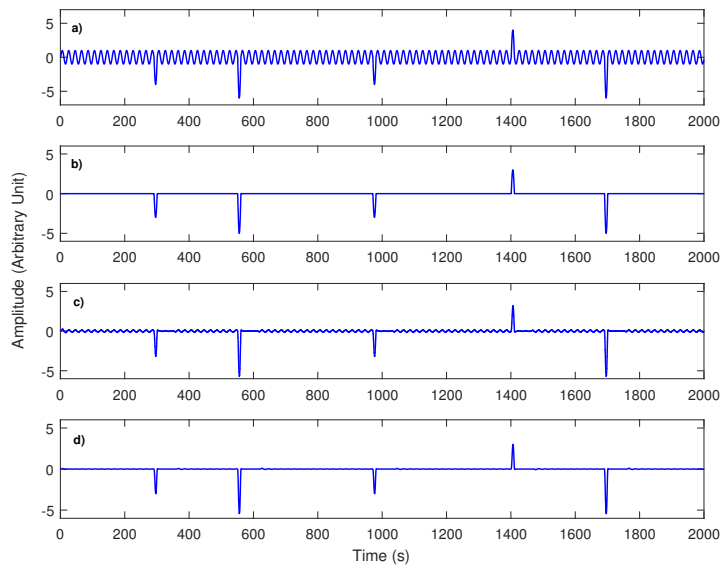


Figure 5.14 – (a) Original signal. (b) True impulse signal. (c) Estimated impulse signal, first iteration. (d) Estimated impulse signal, second iteration.

5.5.3 Adaptation to RR-Interval Time Series

The Rel-En extraction scheme can of course be applied on the raw RR-intervals. In order to make time and frequency interpretations possible, this analysis was performed on cubic-spline regularly-resampled RR-interval signals using the standard 4 Hz sampling frequency. Components present in most RR-interval time series, and that would obviously impair the performance of the Rel-En algorithm, are the positive mean value and ultra-low frequency (ULF, <0.01 Hz) activity. These components were canceled by removing the mean RR-intervals value, and high pass filtering (an 8-order Butterworth) the mean-removed RR-interval time series. Figure 5.15 illustrates the impulse extraction process on a recording from a healthy subject in supine position. The top graph displays the raw regularly-resampled RR-intervals. The middle graph displays the RR-interval time series after mean/ULF subtraction. The bottom graph displays the extracted impulse signal, two Rel-En iterations, short and long window lengths of respectively 7 and 61 samples. The impulses are obviously mainly negative ones, which is, as mentioned in Section 5.5.1, a common feature for RR-intervals in the supine position.

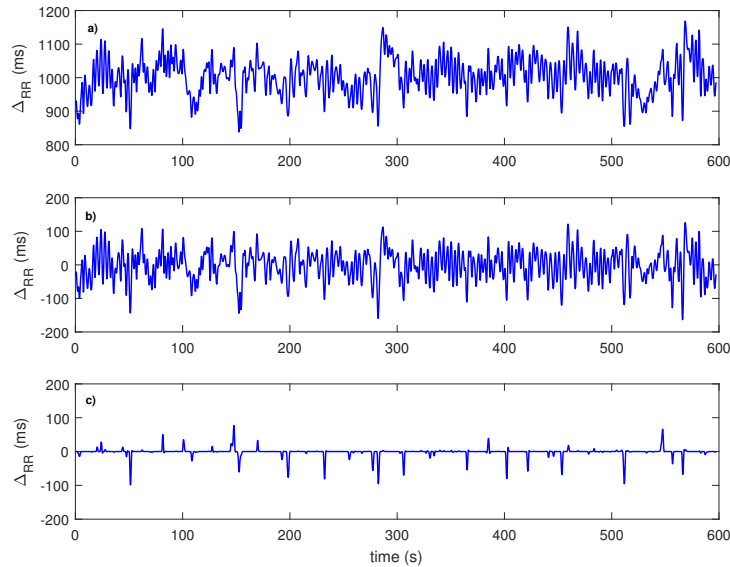


Figure 5.15 – (a) Original RR-intervals. (b) RR-intervals after subtraction of mean/ULF. (c) Estimated impulse signal, two iterations.

5.5.4 Materials

Data were recorded from 15 healthy subjects. The protocol followed the Declaration of Helsinki and was approved by the Ethical Committee of Lausanne University. All participants provided oral and written informed consent prior to participation. Airflow was monitored breath-by-breath (Medgraphics, CPX, St. Paul, MN, USA) at the mouth (Pitot tube). 3-lead ECG was monitored using an analogue amplifier. The ECG and airflow were acquired simultaneously at 1000 Hz, using an analogue-to-digital converter (PowerLab 16/30, ADInstruments, Bella Vista, Australia) and recorded with commercially available software (LabChart v.7.2 ADInstruments, Bella Vista, Australia). The participants were asked to abstain from caffeine, heavy exercise and alcohol for 12h. The subjects underwent recording first in control condition and then under the influence of caffeine (6 mg/kg) administered by pills. Each recording session consisted of 10 minutes spontaneous breathing (SB), 10 minutes breathing at 9 breaths-per-minute (brpm) and 10 minutes breathing at 12 brpm in a randomized order. To ensure correct cadence of breathing, the subjects were instructed to follow continuously a metronome at 9 and 12 brpm. Baseline recordings were performed in all three breathing modes before the subjects ingested the caffeine. Caffeine recordings started 45 minutes after the ingestion. RR-intervals were extracted from the ECG and regularly resampled at 4 Hz after compensation of ectopic beats.

5.5.5 Results and Remarks

The impulse signals were extracted from all RR-interval time series, with two Rel-En iterations and short and long windows of 7 and 61 samples. The asymmetry in the impulse signals were characterized by their mean. For comparison purposes, the power in the LF band (0.04 – 0.15 Hz), its version normalized by the total power nLF, and the ratio LF/HF between the power in the LF band and that in the HF band (0.15 – 0.4 Hz), were computed. As caffeine elicits a sympathetic reaction, one should expect a decrease in the mean of impulse signals (i.e. more

negative impulses), and an increase in LF, nLF, and LF/HF, from baseline to caffeine conditions. In Table 5.6, the numbers of subjects out of 15 for whom the impulse mean decreased, and the LF, nLF, LF/HF increased, are listed for the three respiration modes. One can observe that the impulse mean decreases in most subjects, especially in the spontaneous breathing mode, while increases in the LF-related values are far less predominant. The somewhat paradoxical LF/HF decrease in 14 subjects for the respiration rate of 9 brpm may be explained by the fact that this rate corresponds to a frequency of 0.15 Hz, i.e. the upper and lower bound respectively for the LF and HF bands. The RSA at the same frequency has a major (and in this case negative) impact on the LF/HF ratio.

Table 5.6 – Number of subjects out of 15 with a change from baseline to condition coherent with caffeine-induced sympathetic activation.

Respiration	SB	9 bpm	12 bpm
Imp. mean	14	12	11
LF	9	8	7
nLF	7	8	4
LF/HF	9	1	7

Table 5.7 displays the asymptotic p -values for the two-sample Kolmogorov-Smirnov test [189], that confirm the significant (marginally at 12 brpm) changes in impulse mean induced by caffeine.

Table 5.7 – Asymptotic p -values for the two-sample Kolmogorov-Smirnov test [189] between baseline and caffeine condition.

Respiration	SB	9 bpm	12 bpm
Imp. mean	0.001	0.017	0.31
LF	0.89	0.99	0.89
nLF	0.89	0.59	0.89
LF/HF	0.89	0.052	0.99

The main idea of this section is draw the attention of the HRV community on the impulses that can be often observed in RR-Interval time series. The nonlinear nature Rel-En makes approximate impulse extraction possible. There is interest in elucidating the origin of these impulses, but this requires obviously microneurographic recordings of sympathetic and vagal activities. It is worth noting that in most RR-interval signals in this study, the average time interval between large negative (due to supine position) impulses was between 40 and 50 seconds.

In terms of applications, extraction of the impulse signal presents interesting aspects that have been illustrated in this section. Specifically, although these impulses represent but a small fraction of the total HRV power, they seem to be representative of the sympatho-vagal balance, and have the advantage to be insensitive to RSA fluctuations and independent of the LF and HF bands. Here, only a very simple parameter, namely impulse signal mean value was used, but more elaborate measures can obviously be employed, for instance by processing positive and negative impulses separately. A salient point in these experiments is the poor sensitivity of frequency-based HRV parameters to caffeine-based sympathetic activation, especially at a respiration rate of 9 brpm. These parameters are widely used in bio-psychological works, in stress assessment for instance [190]. However, a factor that is often overlooked is respiration. Of course in most subjects the average respiration (and thus RSA) frequency is above 0.15 Hz, but it may intermittently cross this boundary. Also, especially in supine position, subjects such athletes may have a respiration frequency below 0.15 Hz. Impulse extraction, that is not influenced

by respiration, does not present this problem. Subtracting the extracted impulse signal from the original RR-interval time series may also be useful prior to bandpass filtering of the latter. Indeed, the impulses may contaminate the filter output due to their wideband nature. Figure 5.16 illustrates this point. The upper plot is an RR-intervals regularly resampled at 4 Hz, acquired from a normal subject in supine position with an imposed respiration frequency of 0.225 Hz. A zero-phase bandpass filter centered on this frequency was used to extract the RSA, both on the raw RR-intervals and after impulse signal subtraction. The bottom plot shows the instantaneous frequency (IF) estimates of the two RSAs obtained through the Hilbert transform (HT). The thin and thick lines are the RSA IF estimates respectively without and with impulse subtraction. As is well known, the HT-based instantaneous frequency estimation gives sensible results for narrowband signals only. Visibly, the IF estimate for the original RR-interval time series contains aberrant values, especially around times 25 and 180 seconds for this reason. The IF estimate after impulse subtraction is more coherent.

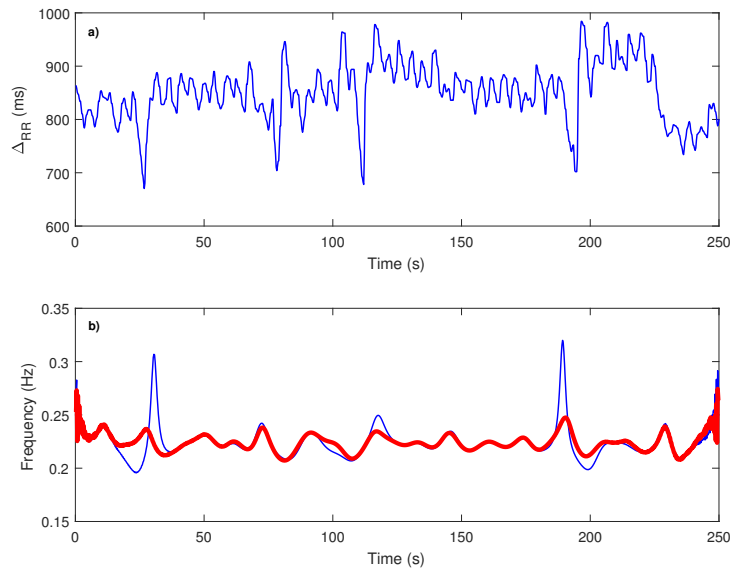


Figure 5.16 – (a) Original RR-intervals. (b) RSA instantaneous frequency estimate using the original RR-intervals (in blue) together with RSA instantaneous frequency estimate after impulse subtraction (in red).

Impulses are often present in RR-interval time series, and correspond to short-term accelerations and decelerations of the heart rate. This section demonstrates that features drawn from the extracted impulse signals are of interest to assess sympathetic activation.

5.6 Conclusion

This chapter presents a simple non-linear filtering method that uses the short- and long-term energies in the signal to heighten peaks and suppress perturbations. The proposed non-linear filtering technique is evaluated in three different biomedical settings namely, ECG QRS-complex detection, EEG K-complex detection, and iPPG peak detection. While providing better or comparable results to the state-of-the-art, the proposed algorithm is easy to compute and implementable by two digital filters, making it a suitable option for biomedical signal processing

applications. As a miscellaneous application to Rel-En, the extraction of impulses in RR-interval time series was demonstrated.

Towards Instantaneous Assessment of ECG Signal Quality

6

Numerous ECG recordings have been performed all over the world for over a century. Representing the electrophysiological activity of the heart at body surface, ECG has become an essential part of health monitors and its use has well exceeded clinical settings. Low quality ECG due to power-line interference, body movement and muscle activity has always been a concern in clinical and non-clinical studies, and has previously been dealt with by manual or semi-supervised exclusion of ECG recordings or segments. There is however a lack of automatic ECG quality assessment. This chapter presents a novel instantaneous ECG quality assessment technique to facilitate this task. This measure is based on relative energy (Rel-En) presented in Chapter 5. Using Rel-En, QRS-complexes are identified and removed from the ECG. QRS-less ECG is then band-pass filtered and added back to the extracted QRS-complexes. Finally, a sliding window correlation coefficient between the new and the original ECG is calculated to measure the instantaneous signal quality index. The method is evaluated against different types of noise, i.e. baseline wander, electrode motion artifact, and EMG noise. Furthermore, performance evaluation is performed on the Physionet/CinC 2011 mobile ECG quality assessment database, the MIT/BIH arrhythmia database, and the MIT-BIH noise stress database. Results show a clear discrimination between noisy and non-noisy ECG segments. Furthermore, this quality index can be implemented in real-time/online scenarios, which makes this index suitable for portable and e-health scenarios.

Methods and results obtained from these analysis are submitted for publication in the journal of biomedical signal processing and control.

6.1 Introduction

As discussed in Chapter 2, the ECG represents the electrical activity propagated through the heart and provides valuable information on the different heart chamber states such as time, duration and the dynamics of chamber depolarization/repolarization. Being cheap and non-invasive, electrocardiographs have seen an ever-growing use from their inception, making ECG the gold standard to assess cardiovascular health [191]. ECG has been thoroughly studied over the past decades from fundamental QRS-complex extraction [152], heart rate estimation [7] and studies on heart rate variability [25] to more elaborated studies such as heart rhythm classification and arrhythmia detection [7, 192] (see Chapter 2 for examples such as bradycardia, tachycardia, atrial and ventricular flutter/fibrillation, etc.), as well as heartbeat classification [2, 3] (such as normal, premature atrial or ventricular beat detection, fusion beats and etc.), cardiac disease and abnormality detection (such as ST elevation and depression, bundle blocks) [193, 194]. In

most cases, these studies require good to high quality ECG recordings in order to provide reliable results. However, the task of ECG quality assessment has proven to be challenging due to the unpredictable nature of ECG-related perturbations. In most clinical research works, low quality ECG recordings or segments are manually selected and removed from the study.

Low quality of ECG and related biomedical signals have also been causing severe problems in intensive care units (ICU) [195, 196] as well as coronary care units (CCU) [197]. As discussed in Chapter 4, high rates of false alarms have been an ongoing concern in these settings due to the limited performance of bedside monitors, causing patient sleep deprivation and more importantly medical staff desensitization [16].

Compared to the ever growing use of the ECG, the subject of ECG quality assessment has not been sufficiently addressed. An effort was made to address this issue in the 2011 Physionet/CinC challenge. The goal was to determine the quality of short-term (10 seconds) 12-lead ECG recordings in a binary fashion (good quality vs poor quality) [198]. With 49 teams participating in this challenge, ECG quality assessment was generally carried out based on missing lead and flat-line information [10–13], high-frequency activity [12, 14, 15], and impulsive noise detection [11, 13] as well as assessment of the heartbeat detection performance [15, 199]. Other perturbation measurement techniques have also been proposed that take into consideration factors such as root mean square (RMS) power in the iso-electric region [200], spectral energy distribution, high order moments such as skewness [147, 148] and kurtosis [147, 149]. Inter-lead and inter-algorithm beat detection agreements have also been effective in noisy ECG detection [196, 199]. More recently, wavelet entropy extracted from different RR-intervals bandwidths was used alongside heart rate to determine ECG signal quality [201].

Automatic ECG management with quality metrics has shown to improve ECG annotation quality, leading to lower expert review time and cost [197]. Still, by studying the state-of-the-art, one can see that quality assessment measures work in a block-based fashion, while an instantaneous measure would be of practical interest. This chapter propose such a quality assessment measure that uses a simple non-linear filtering algorithm, i.e. Rel-En. Using Rel-En, a denoised ECG is created and used to calculate the ECG signal quality. This method can be implemented in real-time/online scenarios, and easily using two filters.

6.2 Method

The principle of signal quality assessment presented in this paper consists in extracting a cleaned-up version of the ECG and comparing it through cross-correlation to the original ECG. The lower the similarity is, the lower the ECG quality should be. In order to extract the cleaned-up ECG, the Rel-En (see Chapter 5) is used. QRS-complexes are first removed from the ECG and a new signal is created by bandpass filtering the Rel-En output and adding it back the extracted QRS-complexes. The correlation coefficient between the original ECG and the new signal is then calculated using a sliding window to measure the ECG signal quality.

6.2.1 QRS-complex Cancellation

Using Rel-En with a short and long window durations of respectively 100 and 450ms, a Hamming window for w , and an exponent of $p = 2$, the coefficient vector c is first binarized into c' to extract impulses using Equation 6.1. Then, the QRS-complexes q , and the residual ECG r are calculated through Equations 6.2 - 6.3.

$$c'(n) = \begin{cases} 1 & c(n) \geq 0.6 \\ 0 & c(n) < 0.6 \end{cases} \quad (6.1)$$

$$q(n) = c'(n)x(n) \quad (6.2)$$

$$r(n) = x(n) - q(n) \quad (6.3)$$

Observations on ECG recordings have shown these s_{win} , l_{win} , w , and p values together with the threshold applied on c , can efficiently remove QRS-complex activity from the ECG. Figure 6.1 illustrates the different steps for the QRS-cancellation. In this figure, a segment of modified lead-II ECG of tape 105 from the MIT/BIH arrhythmia database was chosen, Figure 6.1-a. This segment was especially chosen to show the performance of the QRS canceling technique even in low-quality ECG. Figure 6.1-b, represents the band-passed ECG alongside the short- and long-term energy evolutions, and the extracted coefficient signal. Figure 6.1-c and Figure 6.1-d respectively show the extracted QRS-complexes and the residual, i.e. QRS-less ECG.

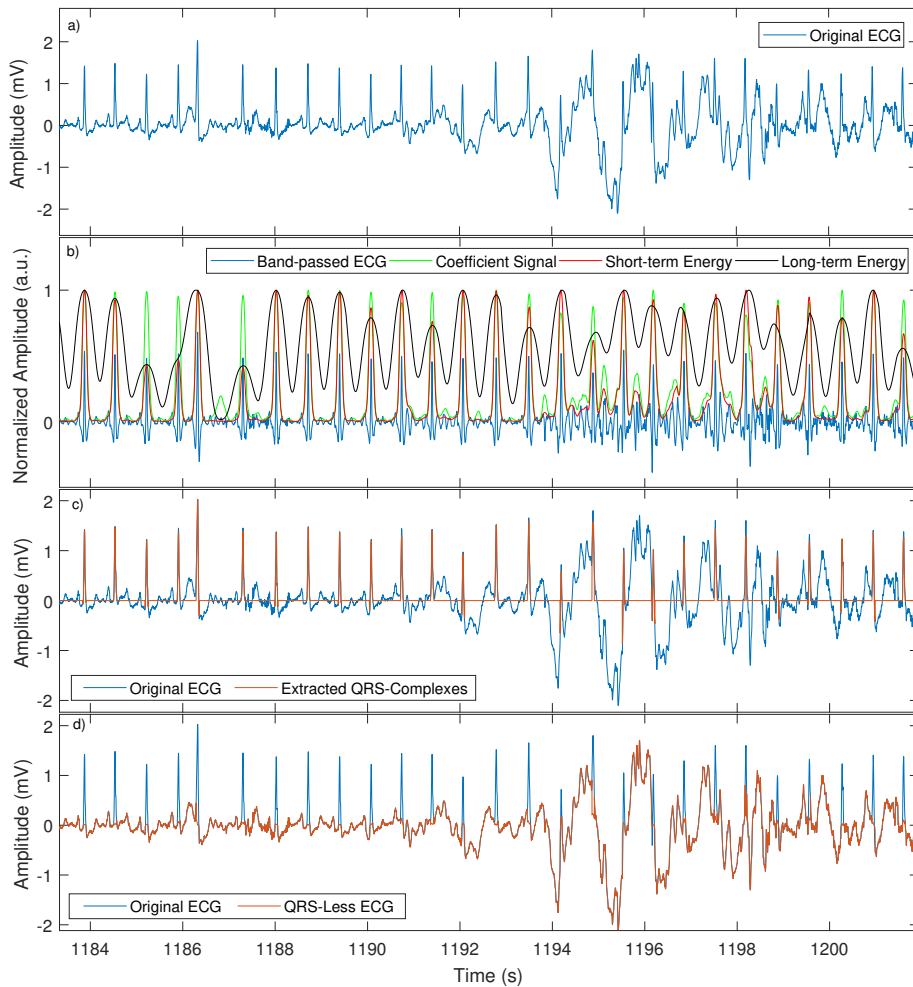


Figure 6.1 – Illustration of the different steps of QRS-complex cancellation using Rel-En. a) Lead II ECG of tape 105 from the MIT/BIH arrhythmia database. b) Band-passed ECG together with the calculated coefficient signal (i.e. c), short- and long-term energy evolution. c) Original ECG and the extracted QRS-complexes (Equation 6.2). d) Original ECG and the QRS-less ECG, i.e. r , (Equation 6.3).

6.2.2 Measuring the ECG Quality

Creation of the Denoised ECG

After the separation of the QRS-complexes from the ECG, the residual signal r is then band passed filtered in a band [5, 15] Hz, to create the residual ventricular activity r' . This pass-band is chosen in order to conserve the typical ventricular frequency components. The denoised ECG is then created by adding the extracted QRS-complexes to the residual ventricular activity.

$$d(n) = q(n) + r'(n) \quad (6.4)$$

Calculating the Instantaneous Signal Quality Index (ISQI)

Once the denoised signal is obtained, the instantaneous signal quality index (ISQI) is measured as the correlation coefficient between the original ECG and d , calculated in a sliding window of length N , i.e.:

$$\rho_{x,d}(n) = \frac{1}{N-1} \sum_{j=i-\frac{N}{2}}^{i+\frac{N}{2}-1} \left(\frac{x_j - \mu_{x_i}}{\sigma_{x_i}} \right) \left(\frac{d_j - \mu_{d_i}}{\sigma_{d_i}} \right), i = (1, \dots, n) \quad (6.5)$$

where μ_{x_i} and σ_{x_i} denote the mean and the standard deviation of the original ECG for the i^{th} window, and μ_{d_i} and σ_{d_i} are the mean and the standard deviation of the denoised ECG for the i^{th} window. In this study an empirical duration of three seconds was chosen to select N . Observations have shown that computing ρ on a three-second sliding window with an overlap of 2.5 seconds, provides an adequate time resolution. As ρ is the correlation coefficient between the original ECG and the d , the ISQI ranges between $[-1, 1]$. Figure 6.2, illustrates the successive steps in the computation of ρ . The same ECG segment as that of Figure 6.1 was chosen for this example. Figure 6.2-a and 6.2-b, respectively show the extracted QRS-complexes and the QRS-less ECG. The band-passed QRS-less ECG is depicted in Figure 6.2-c. Figure 6.2-d shows the two signals on which the sliding correlation coefficient is calculated. Finally, the instantaneous quality index is depicted alongside the original ECG in Figure 6.2-e. As seen in this figure, the instantaneous quality gradually drops as more noise is manifest in the ECG, and the quality index rises again as the noise level decreases.

6.3 Evaluation Data

6.3.1 The MIT/BIH Noise-Stress Test Database

In this database, three noise recordings namely baseline wander (BW), EMG artifact (MA), and electrode motion artifact (EM), which are typical in ambulatory ECGs [202], were assembled. These noise recordings were collected by placing the electrodes at specific limb positions, where the ECG was not visible, using active volunteers and with standard ECG recorders, leads, and electrodes. Each noise recording has an overall duration of half an hour, assembled by selecting segments that predominantly contain the noise of interest, i.e. BW, MA, or EM. This database comprises 12 half-hour, two-lead ECG recordings, that were created by taking two clean recordings (118 and 119) from the MIT-BIH Arrhythmia Database (see subsection 6.3.2), and adding calibrated amounts of noise (from an SNR of -6dB up to 24dB with steps of 6dB). For all the recorded ECGs in this database, the calibrated noise was added from the fifth minute of each recording, two-minute noisy segments alternating with two-minute clean ECG segments.

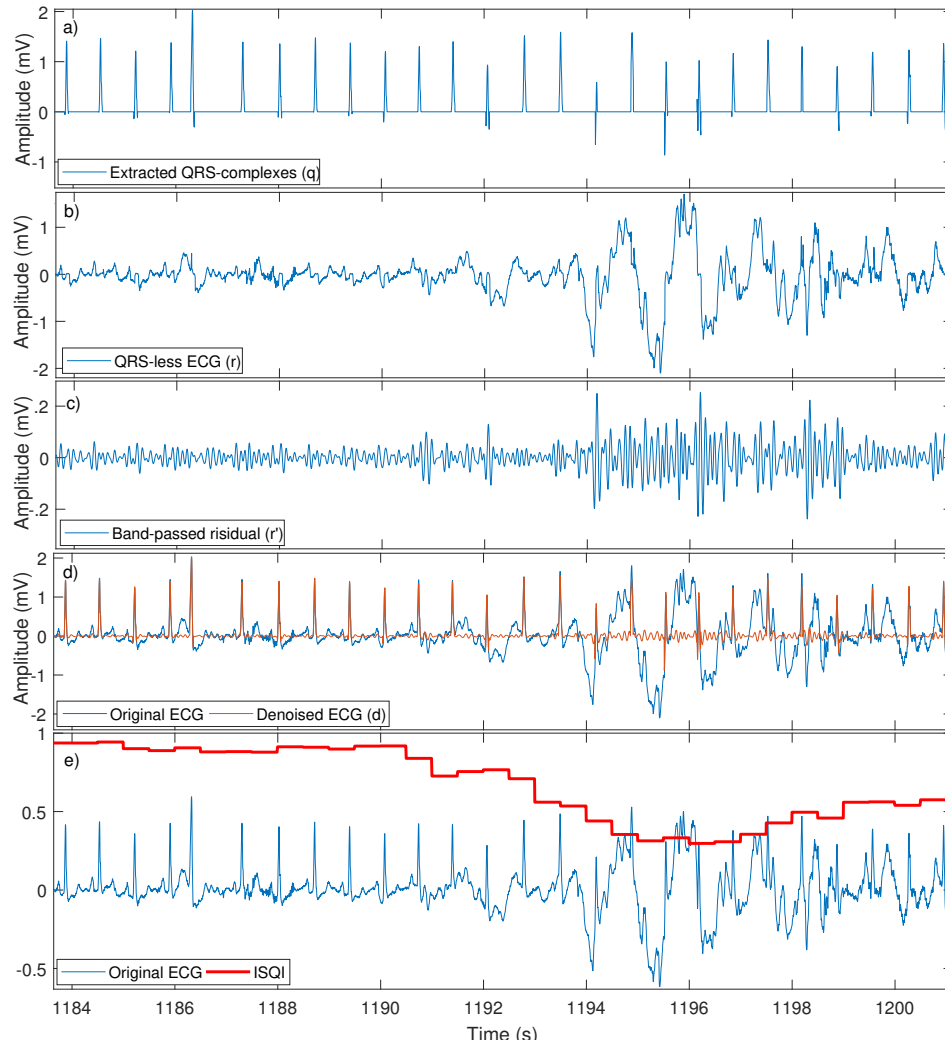


Figure 6.2 – Calculation of the instantaneous signal quality index. a) Extracted QRS-complexes (Equation 6.2). b) QRS-less ECG (Equation 6.3). c) Band-passed QRS-less ECG. d) Original ECG alongside the denoised ECG (Equation 6.4). e) Original ECG and the calculated ISQI (Equation 6.5). The amplitude of the original ECG has been altered for demonstration purpose.

6.3.2 The MIT/BIH Arrhythmia Database

The Physionet MIT/BIH arrhythmia database was also used in this study to further evaluate the performance of the proposed ISQI. The MIT/BIH arrhythmia database consists of 48 half-hour two-lead, modified lead II (MLII), lead V1, lead V2, and lead V5, ECG recordings with a sampling rate of 360 Hz and an 11-bit resolution within the range of 10 mV [48].

Using the noise recordings from the MIT/BIH noise-stress database, we manually selected 32 five-minute clean ECG segments and added calibrated amounts of each noise type (as for the MIT/BIH noise-stress database). Table 6.1 reports the record numbers together with the leads and the extracted intervals that were used in this paper for further performance evaluation.

Table 6.1 – Recordings, leads and segments from the MIT/BIH arrhythmia database, used to evaluate the proposed method.

Tape Name	Lead Name	Start Time (sec)	End Time (sec)
100	MLII	1	300
100	V5	397	697
101	MLII	327	626
101	MLII	858	1157
103	MLII	1	300
103	MLII	1332	1631
103	V2	1	300
112	V1	1174	1474
114	MLII	1450	1749
115	MLII	97	396
115	MLII	621	920
115	MLII	1300	1600
122	MLII	75	375
123	MLII	108	408
123	MLII	1439	1739
123	V5	107	407
123	V5	529	828
201	MLII	50	350
201	V1	1	300
202	V1	1	300
202	V1	1341	1640
207	MLII	1117	1417
220	MLII	1	300
220	MLII	1445	1744
220	V1	1	300
220	V1	450	750
220	V1	1456	1755
222	V1	811	1110
222	V1	1503	1802
230	MLII	273	573
231	V1	1409	1709
234	MLII	434	734

6.3.3 The Physionet/CinC 2011 Challenge Database

The aim of the 2011 Physionet/CinC challenge was to develop efficient algorithms, running in near real-time/online scenarios on a portable device such as a cellphone to provide feedback, regarding the quality of the captured ECG, to a person or expert in the process of acquiring a diagnostically acceptable ECG recording [198]. The challenge data consist of standard 12-lead ECG recordings (leads I, II, III, aVR, aVL, aVF, V1, V2, V3, V4, V5, and V6). The leads were recorded simultaneously for a duration of 10 seconds, sampled at 500 Hz with a 16-bit resolution. Each ECG was analyzed independently and blindly by at least three and up to 18 annotators with different levels of expertise and assigned different grades, namely grade A as excellent, B as good, C as adequate, D as poor, and F as unacceptable signal quality. Finally, the annotated grades

were then averaged and each ECG was deemed acceptable, intermediate or unacceptable. Three datasets were used in this challenge. Dataset-a, with 1000 ECGs and reference annotations (that challengers used for training their algorithms). Dataset-b with 500 ECGs but without annotations (used for evaluation of the submitted methods, and available publicly for visual inspection). And finally Dataset-c with 500 ECGs, hidden from the public and used only for evaluation. For the analysis in this chapter, solely Dataset-a was used to evaluate the proposed method, as it was the only dataset with annotations publicly available.

6.4 Results

6.4.1 The MIT/BIH Noise-Stress Test Database

The effectiveness of the measure was evaluated for different noise levels. To this end the MIT/BIH noise-stress database was used, in which calibrated amounts of noise were added to clean signals. As the positions of the noisy segments are provided in this database (see subsection 6.3.1), the instantaneous quality indexes calculated by the proposed method for the noisy, clean, and overall (clean + noisy) segments were studied. Moreover, for each of the 24 series (12 two-lead recordings), the results for each noise level, i.e. from -6dB to 24dB with steps of 6dB were calculated. Table 6.2 reports the quality index averages for the aforementioned segments, and for each noise level. As reported in this table, there is a clear difference between the average quality index values calculated for noise levels in the range of -6dB to 12dB. However, as the SNR rises to 18 and 24dB this difference becomes smaller. Of course, in the later case, the noise added to the ECG is so small that it barely affects signal quality, and therefore, the signal quality values for the 'Clean+Noisy', 'Clean', and 'Noisy' are close to one another (almost identical in case of 24dB).

Table 6.2 – Average quality indexes obtained using the proposed method, on the MIT/BIH noise-stress database.

Segment \ Noise	Clean + Noisy	Clean	Noisy
-6 dB	0.8 ± 0.14	0.91 ± 0.04	0.66 ± 0.1*
0 dB	0.81 ± 0.13	0.91 ± 0.04	0.68 ± 0.1*
6 dB	0.83 ± 0.11	0.91 ± 0.04	0.73 ± 0.08*
12 dB	0.87 ± 0.08	0.91 ± 0.04	0.81 ± 0.07†
18 dB	0.89 ± 0.05	0.91 ± 0.04	0.87 ± 0.05‡
24 dB	0.91 ± 0.04	0.91 ± 0.04	0.91 ± 0.04

Reported results in mean ± standard deviation.

Clean vs Noisy segments: * $p < 0.0001$. † $p < 0.01$. ‡ $p < 0.05$.

Figure 6.3 illustrates the calculated ISQI, for different levels of noise (from -6dB to 24 dB), on lead MLII of tape 118 from the MIT/BIH noise-stress database. In this figure, the noise is added to the clean ECG from second 540. As one can see, the calculated ISQI improves as the noise level decreases.

6.4.2 The MIT/BIH Arrhythmia Database

Results on the MIT/BIH noise-stress test show the effectiveness of the proposed method. The proposed method was further tested on more ECG recordings from the MIT/BIH arrhythmia database for two main reasons. First, although different levels of noise were applied to the ECGs

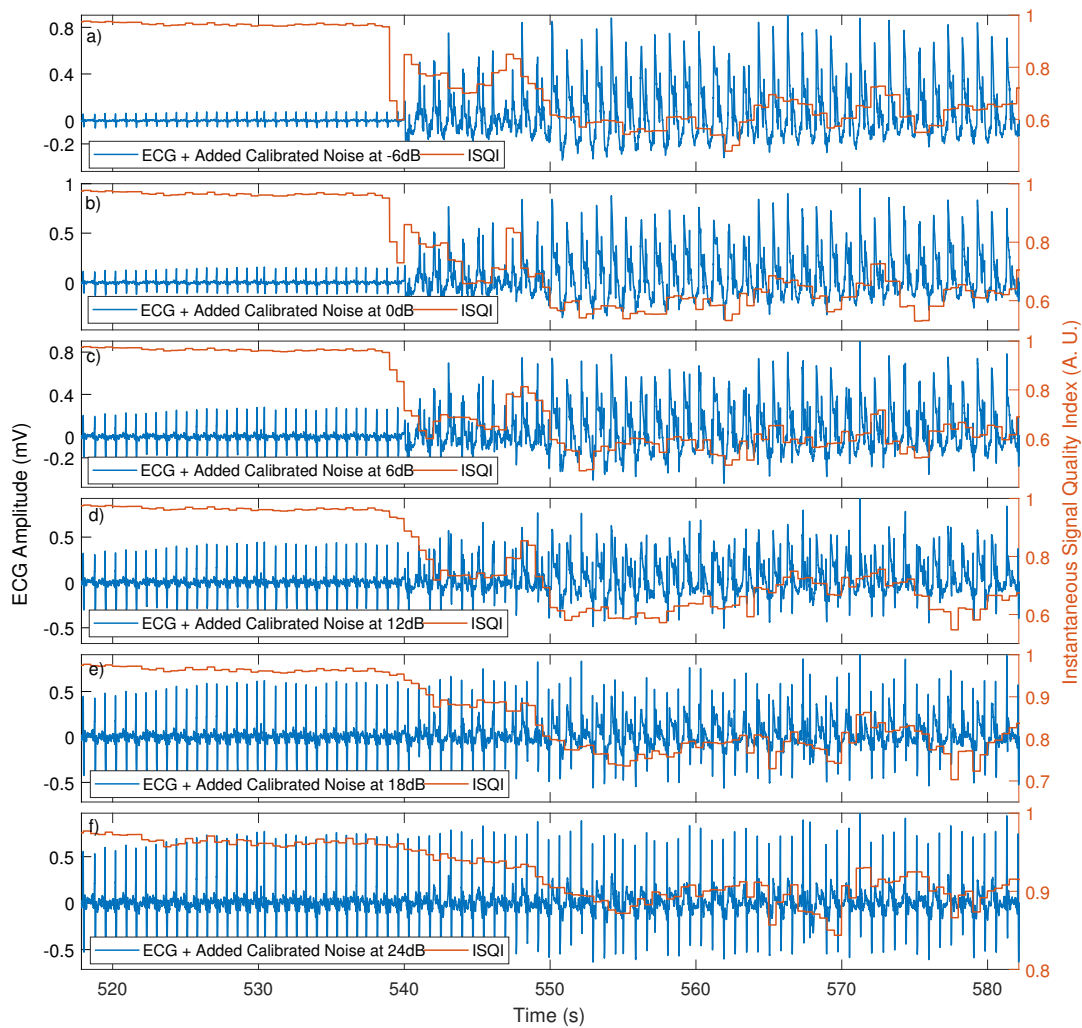


Figure 6.3 – Calculated ISQI on tape 118 (lead MLII) of the MIT/BIH Noise-Stress database. a) ECG with added calibrated noise with an SNR of -6dB. b) ECG with added calibrated noise with an SNR of 0dB. c) ECG with added calibrated noise with an SNR of 6dB. d) ECG with added calibrated noise with an SNR of 12dB. e) ECG with added calibrated noise with an SNR of 18dB. f) ECG with added calibrated noise with an SNR of 24dB. The calibrated noise is added to the ECG from second 540.

in the MIT/BIH noise-stress test, the added noise in this database comprises all noise classes, i.e. BW, EM and MA, and the effectiveness of the algorithm versus each noise class was not studied. Second, even though the noise-stress database contains 12 two-lead ECGs, only two clean ECG recordings were used to assemble the database. Therefore, ECG segments from the MIT/BIH arrhythmia database were manually examined and a set of 32 five-minute ECG excerpts with good or highly acceptable quality was selected. Then, for each noise class, new ECGs with different levels of SNRs, from -12dB to 24dB (steps of 6dB), were created. In order to add noise to these ECGs, the noise recordings from the noise-stress database was used. In this way, not only the proposed method could be evaluated on a larger set of ECGs, but also different noise

classes could be studied separately. The results showed a behavior similar to that of the noise-stress database, with -12dB SNR yielding the lowest quality index and an ever increasing ISQI with respect to the increasing SNRs were observed. Detail results on the MIT/BIH arrhythmia database is reported in Table 6.3.

Table 6.3 – Average quality indexes obtained using the proposed method, on the MIT/BIH arrhythmia database.

Noise SNR	BW	MA	EM	BW+EM	BW+MA	EM+MA	BW+EM+MA
-12 dB	0.73 ± 0.25	0.66 ± 0.3	0.67 ± 0.26	0.68 ± 0.26	0.69 ± 0.27	0.67 ± 0.27	0.67 ± 0.27
-6 dB	0.83 ± 0.17	0.76 ± 0.22	0.74 ± 0.21	0.76 ± 0.19	0.81 ± 0.17	0.74 ± 0.2	0.76 ± 0.2
0 dB	0.9 ± 0.09	0.87 ± 0.12	0.85 ± 0.12	0.86 ± 0.11	0.89 ± 0.1	0.85 ± 0.11	0.86 ± 0.11
6 dB	0.94 ± 0.04	0.93 ± 0.05	0.92 ± 0.05	0.92 ± 0.05	0.93 ± 0.05	0.92 ± 0.05	0.92 ± 0.05
12 dB	0.95 ± 0.02	0.95 ± 0.02	0.95 ± 0.02	0.95 ± 0.02	0.95 ± 0.02	0.95 ± 0.02	0.95 ± 0.02
18 dB	0.96 ± 0.01	0.96 ± 0.01	0.96 ± 0.01	0.96 ± 0.01	0.96 ± 0.01	0.96 ± 0.01	0.96 ± 0.01
24 dB	0.97 ± 0.01	0.97 ± 0.01	0.97 ± 0.01	0.97 ± 0.01	0.97 ± 0.01	0.97 ± 0.01	0.97 ± 0.01
Clean ECGs	0.97 ± 0.01	0.97 ± 0.01	0.97 ± 0.01	0.97 ± 0.01	0.97 ± 0.01	0.97 ± 0.01	0.97 ± 0.01

Additionally, the correlation between the proposed ISQI and the instantaneous signal to noise ratio (ISNR) was studied. The ISNR was calculated using a 3-second sliding window, with an overlap of 2.5 seconds, and then the correlation coefficient between the median filtered ISQI and ISNR series was measured. Median filtering was performed on a 10-second sliding window to provide smooth ISQI and ISNR changes, as illustrated by Figure 6.4. Table 6.4 reports the correlation coefficient between the ISQI and ISNR with respect to different noise types and noise levels¹.

Table 6.4 – Correlation coefficient between ISQI and ISNR for different noise classes, and different SNR levels.

Noise SNR	BW	MA	EM	BW+EM	BW+MA	EM+MA	BW+EM+MA
-12 dB	0.87 ± 0.1	0.65 ± 0.3	0.6 ± 0.31	0.81 ± 0.15	0.85 ± 0.11	0.65 ± 0.26	0.83 ± 0.13
-6 dB	0.93 ± 0.02	0.85 ± 0.07	0.77 ± 0.13	0.91 ± 0.06	0.93 ± 0.02	0.9 ± 0.04	0.92 ± 0.02
0 dB	0.9 ± 0.01	0.86 ± 0.02	0.8 ± 0.06	0.88 ± 0.04	0.91 ± 0.01	0.88 ± 0.02	0.9 ± 0.01
6dB	0.85 ± 0.03	0.79 ± 0.04	0.76 ± 0.04	0.82 ± 0.03	0.86 ± 0.03	0.82 ± 0.04	0.83 ± 0.02
12 dB	0.79 ± 0.03	0.62 ± 0.05	0.67 ± 0.05	0.69 ± 0.11	0.77 ± 0.03	0.75 ± 0.03	0.72 ± 0.02
18 dB	0.61 ± 0.06	0.34 ± 0.08	0.48 ± 0.06	0.46 ± 0.21	0.48 ± 0.07	0.57 ± 0.05	0.45 ± 0.07
24 dB	0.36 ± 0.15	0.15 ± 0.05	0.31 ± 0.07	0.23 ± 0.18	0.1 ± 0.16	0.39 ± 0.08	0.21 ± 0.09

6.4.3 The Physionet/CinC 2011 Challenge Database

This database was used to compare the presented scheme to existing SQI approaches. A short-term ECG quality assessment challenge was recently held in 2011 (Physionet/CinC 2011 challenge). To this end, for each lead of the 12-lead ECG recording in the database, four basic features were extracted. The first three features were the mean, standard deviation, and the difference between the maximum and the minimum of the calculated ISQI. The last feature and the only feature that was not derived from the ISQI, was a binary feature which checked for flat-line or ECG-saturation information. Using a sliding window, this feature was calculated by checking for constant ECG values for a duration of at least 250ms. This feature is true for ECG saturation or flat-line, in which cases all ECG values are constant.

The 48 extracted features were used to train a 10-fold cross-validated linear K-NN classifier, (K=11). For dataset-a, an overall accuracy of 94.12% was obtained with a noise classification

1. More detailed results are reported in Appendix C

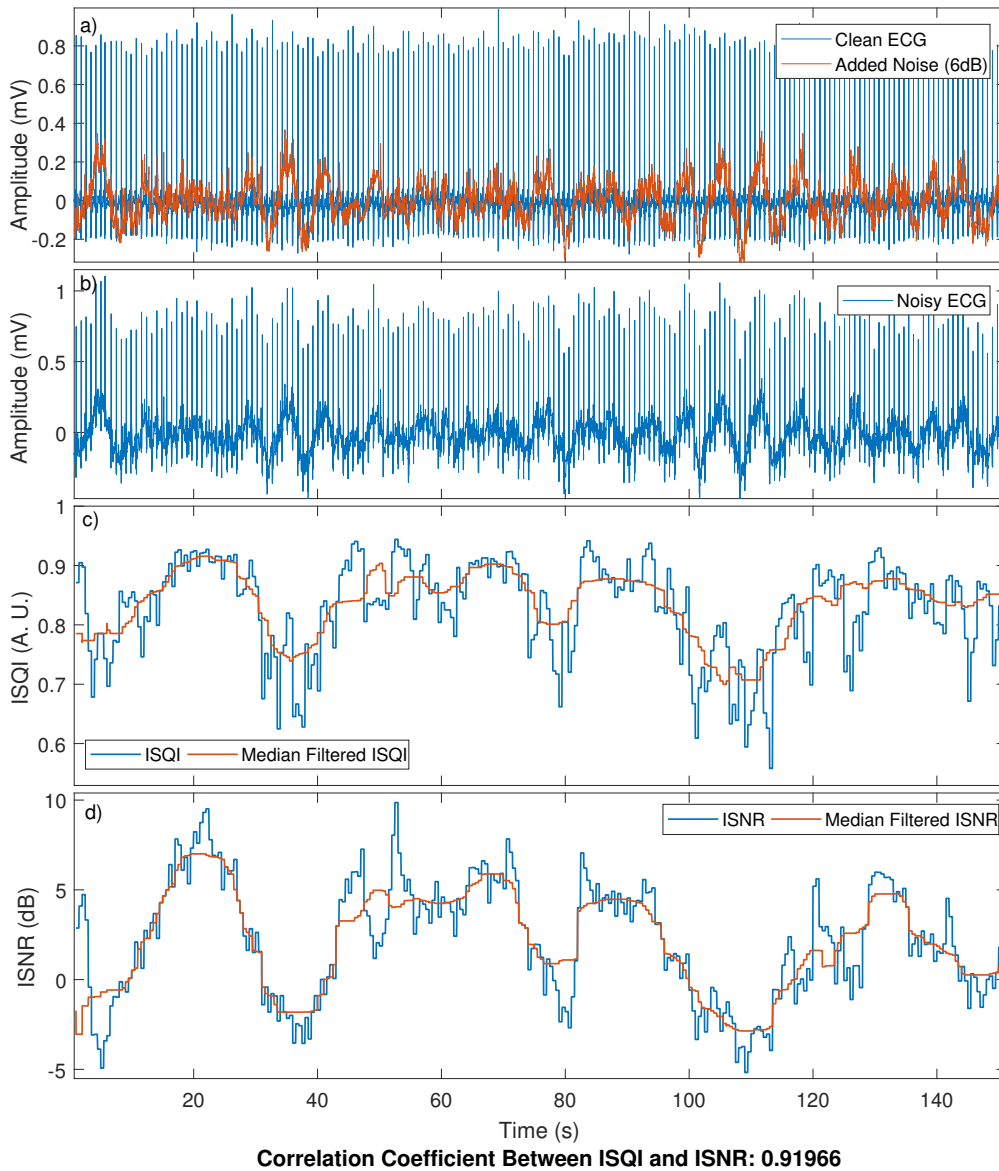


Figure 6.4 – Correlation between ISQI and ISNR. a) Clean ECG (Tape 100 MIT/BIH Arrhythmia database, baseline removed) and the added noise (from the MIT/BIH Noise Stress database). b) Noisy ECG, i.e. clean ECG + added noise. c) Calculated ISQI using together with the median filtered ISQI (sliding window with a duration of 10 seconds). d) Calculated ISNR using together with the median filtered ISNR (sliding window with a duration of 10 seconds).

sensitivity of 0.94 and a specificity of 0.93 and an F-score of 0.87². Table 6.5 compares the proposed method performance with the state-of-the-art on dataset-a. As the labels were not publicly available, it was not possible to assess the performance of the presented algorithm on the test set. This is because performance on the test set could only be performed through the Physionet/CinC 2011 challenge portal that requires the algorithm to be implemented in Java,

2. Detailed description of classifier evaluation metrics can be found in Appendix B

Table 6.5 – Performance comparison with the stat-of-the-art on the Physionet/CinC 2011 challenge database.

Method	Sensitivity	Specificity	Accuracy %
ISQI	0.94	0.93	93.6
Xia et al. [10]	0.88	0.97	95.1
Di Marco et al. [11]	—	—	92.72
Joh. and Gal. [12]	0.76	0.97	92.4
Hayn et al. [13]	—	—	93.3
Tat et al. [14]	—	—	92.0
Jekova et al. [15]	0.98	0.80	94.2
Clifford et al. [199]	0.99 [†]	1 [†]	99.0 [†]

[†] Results based on their annotations, different from the publicly available annotations.

which was different from the programming language used to develop this method (Matlab).

6.5 Discussion

When it comes to the state-of-the-art, most methods extract features from the ECG and perform machine learning for ECG quality assessment [10–15, 199]. This is due to the ever changing characteristics of noises contaminating the ECG, making feature-based quality assessment task difficult. Electrode movement, baseline wander, muscle activity and impulsive noise each manifest themselves differently in the ECG. Therefore, in practice, machine learning approaches extract several features to best describe each noise type and assess ECG quality. However, the drawback with these approaches is that they are block-based, i.e. they are for instance trained on 10-seconds segments of ECG. Moreover, they mostly provide binary classification into either noisy or clean segments and therefore fail to quantify how noisy the ECG segment is. To the best of knowledge, the proposed method is the first approach to assess ECG signal quality directly from the recording. At the same time, the ISQI can be measured for all ECGs regardless of their durations. Results reported in Table 6.2 confirm that the ISQI has lower values with higher SNR and higher values with lower SNR. Furthermore, Table 6.4 shows that the variation of ISQI is in accordance with the variation of ISNR, providing an instantaneous measure of how noisy the recording of interest is at each point in time. Figure 6.5 illustrates how the ISQI changes over time with different noise types. This method is also easy to implement and is computationally uncostly, making it possible to run in near real-time or online fashion. It should be mentioned that, although the presented signal quality assessment method is proposed as an instantaneous measure, there is a small delay in the output. This delay is equal to the half duration of the large window on which the correlation coefficient between the original ECG and the denoised ECG is calculated, i.e. 1.5 seconds.

Results provided in Table 6.2 suggest that the ISQI efficiently separates the clean and noisy ECG segments. Of course, as expected, the significance in the difference decreases as the SNR improves and at high SNRs there is no significant difference between the noisy and non-noisy ECG segments.

The same trend can also be observed in the correlation coefficient between the ISQI and the ISNR, reported in Table 6.4. As it can be seen, with higher levels of SNR and regardless of the noise type, the correlation coefficient between the ISQI and the ISNR decreases (except for -12dB). Given that we start from an ECG that is not totally clean, this behavior is expected: as the noise in the original "clean ECG" affects the calculate ISQI more and more as the SNR

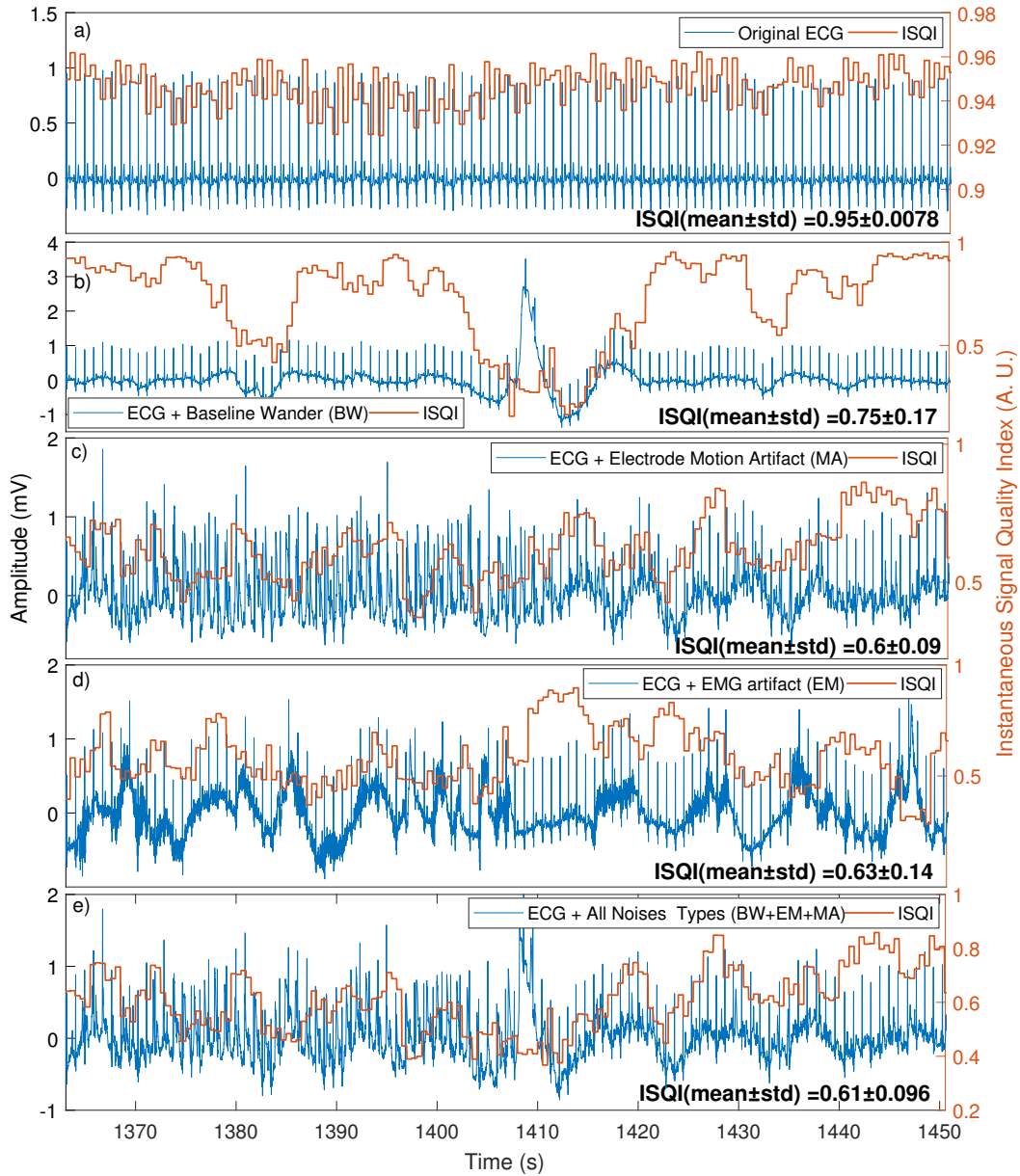


Figure 6.5 – Illustration of the evolution of ISQI against various noise types. a) Clean ECG (Tape 103 MIT/BIH Arrhythmia database, baseline removed) and the measured ISQI. b) ECG + baseline wander (BW) and the measured ISQI. c) ECG + Electrode Motion Artifact (MA) and the measured ISQI. d) ECG + EMG artifact (EM) and the measured ISQI. e) ECG + all noise types, and the measured ISQI.

improves. At both extremities, i.e. -12 and 24 dB added noise, the measured ISQI becomes flat, leading to a lower correlation coefficient between the ISQI and the ISNR. This flat ISQI is due to the very low amplitude of noise at 24 dB and conversely to the dominating noise amplitude at -12 dB. Looking more closely at Table 6.4, one can see that the electrode motion artifact noise has the highest impact in lowering the correlation coefficient between the ISQI and the ISNR. This is also expected as, for this type of noise, artifacts look similar to QRS complexes and therefore, are much harder to deal with.

Although the ISQI values could in theory be in the range of $[-1, 1]$, observations have shown that the values of ISQI rarely become negative. In fact, negative ISQI values were obtained only when the original ECG was contaminated using a synthetic white Gaussian noise. On noise sources used throughout this paper, even with high levels of perturbation in the ECG, the ISQI generally ranged between $[0.4, 1]$. Furthermore, observations have shown the ECG has acceptable quality for ISQI values higher than 0.6 , moderate quality for values greater than 0.7 , high quality for values larger than 0.8 . If there is a need for waveform amplitude and duration analysis, such as P-wave or QRS-complex analysis, ECG segments with ISQI values larger than 0.9 are optimal. It should also be mentioned that the ISQI provides a measure of overall ECG signal quality. Therefore, it is possible that the same ISQI value be provided for two ECGs contaminated with different types of perturbations. For instance, consider the same ISQI is measured for an ECG contaminated with baseline drift and another contaminated by electrode motion artifacts. The baseline-drift contaminated ECG is easier to deal with as high-pass filtering can significantly attenuate this noise, while the ECG contaminated with electrode motion artifact might not be usable. Of course, one can create an ISQI for each noise type, but in practice all perturbation are present to some extent and therefore, a general ISQI provides a more interpretable information.

6.6 Conclusion

This chapter presents a novel technique to measure ECG signal quality index in an instantaneous fashion. Based on a non-linear filtering technique, the QRS-complexes are first removed. Subsequently, the ECG residue is filtered and added to the extracted QRS-complexes. Finally, the instantaneous signal quality index is calculated as the correlation coefficient between the original ECG and that of the previous step on a sliding window. The method was tested on well known databases and against different ECG perturbations. Results showed the proposed quality measure effectively reflects ECG quality. The proposed method is simple to calculate, enabling an implementation in near real-time/online scenarios.

Analysis of U-shaped Patterns in RR-intervals from PSG Recordings

7

7.1 Introduction

In recent years, sleep assessment has gained momentum in clinical practice. Sleep studies record human physiological parameters and through analysis, provide insightful information on possible disorders. A comprehensive sleep analysis is made possible using polysomnography (PSG), which consists in simultaneously recording several bio-physiological signals during sleep. These recordings usually comprise different body function parameters such as the electrical activity of the brain, i.e. electroencephalography (EEG), by placing electrodes along the scalp and measuring ionic current of the neurons [203]. Eye movement can also be recorded through electrooculography (EOG) by placing electrodes above and below each eye. Moreover, muscle activity and heart rhythm are obtained, respectively via EMG and ECG recordings.

Sleep assessment has proven useful in practice, with studies showing that sleep deprivation can lead to negative physiological effects such as myocardial hypertrophy [204], cognitive impairment [205–207] and hypertension [208, 209]. Studies have demonstrated the efficacy of PSG analysis in other disorders such as sleep apnea [210–213], insomnia [214–216], fatigue [217–220], and pulmonary function disorder [221, 222].

Mainly, one can divide sleep into two main stages namely, rapid eye movement (REM) and non-rapid eye movement (NREM). These stages present different characteristics. During NREM sleep, also called dreamless sleep, a decrease in heart rate and body temperature is observed [223]. NREM is sub-categorized into four phases [224]:

- **Stage 1** occurs at the beginning of sleep and is considered as a shallow sleep stage, during which subjects drift in and out of sleep, and experience hypnic jerks (involuntary muscle contraction) [225]. On the EEG, alpha waves disappear and are replaced by theta waves.
- **Stage 2** is the phase during which eye movements stop and K-complexes and sleep spindles appear on the EEG. During this phase the subject is still in shallow sleep.
- **Stage 3** is considered as deep sleep. In stage 3 of NREM sleep delta waves appear in the EEG. This phase is known to associate with parasomnias such as sleep walking, bed-wetting and night terrors [226, 227].
- **Stage 4** is the continuation of stage 3 phase and is associated with dominant EEG delta wave activity.¹

REM sleep, on the other hand, is associated with eye movement and fast and desynchronized brain waves [229]. The oscillation between the NREM and REM phases of sleep are referred to as sleep cycles, which have a frequency of four to six cycles during a good night sleep [230, 231].

1. Sometimes Stage 3 and 4 of NREM sleep is considered as one [228].

Sometimes, during sleep subjects can momentarily (3-14 seconds) wake up. These stages are known as brief awakening or micro-arousal stages. The evolution of sleep stages through time can be studied using a hypnogram, an example of which is illustrated in Figure 7.1.

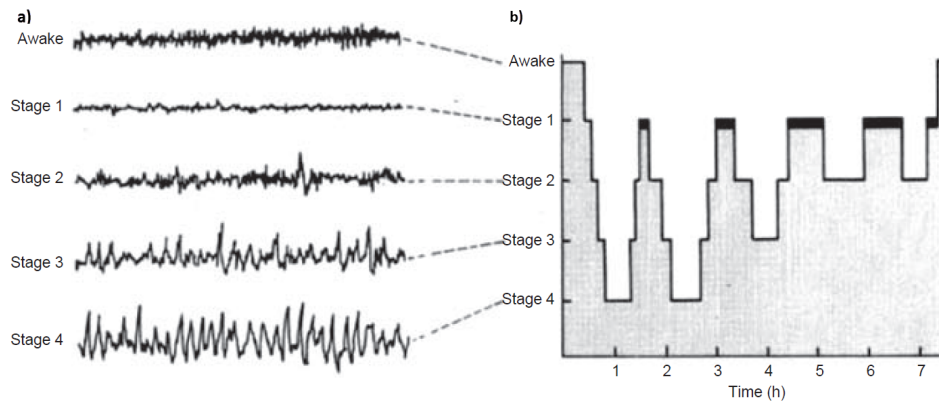


Figure 7.1 – a) EEG waveforms that define awake and non-rapid eye movement (non-REM) sleep stages. b) An idealized hypnogram summarizing the distribution of the sleep stages through a typical night. Black bars refer to REM sleep during which the EEG pattern returns to that seen in wakefulness. Figure taken from [224], with permission.

Although numerous studies have been performed in the context of sleep analysis, research on different aspects of this important field is still much active. This is especially true for ECG-based sleep analysis, which have received less attention in comparison with EEG-based techniques. In this context, this chapter is dedicated to the investigation of a phenomenon that takes place during sleep, namely U-shaped patterns in the RR-interval time series. The state-of-the-art has not addressed this phenomenon to a meaningful degree. Very recently, Solinski et al. [232] have reported the existence of these U-shaped patterns and have shown they have a significant influence on the power in the very low frequency band of HRV (i.e. [0.01-0.04] Hz). Mendez et al. [233] observed a quickening of heart rate during EEG A-phases, recurrent events during sleep that last between 2-60 seconds (average duration of 7 seconds) [234–236], and showed there is a significant difference in HRV indexes between a group of healthy subjects and patients suffering from nocturnal front lobe epilepsy.

This chapter provides a definition to these patterns and studies their statistical characteristics during sleep using data from two protocols. Furthermore, the correlation between U-patterns and movement events is studied by analyzing available channels from PSG recordings. The following sections are organized as follows. Section 7.2 provides the description of the database used for U-pattern analysis. U-patterns are defined in Section 7.3. The technique used to extract these patterns is described in Section 7.4, and evaluated in 7.5. Statistical analysis performed on U-patterns are presented in Section 7.6. Section 7.8 provides a general discussion and finally, conclusions are drawn in 7.9.

7.2 Research Material

U-pattern analysis is performed throughout this chapter on a database created to evaluate the effect of stress and fatigue on healthy subjects. The study was directed by Prof. G. Millet and Dr. N. Bourdillon from the Institute of Sciences and Sport of the Lausanne University²

2. Institut des Sciences du Sport de l'Université de Lausanne

(ISSUL). In more detail, data analysis was carried out for two separate experiments, designed to assess the effect of fatigue induced respectively by physical activity and sleep deprivation. Eligible subjects participating in this study, had to be healthy, young and living in the Lausanne region in Switzerland. Furthermore, subjects had to be in good psychiatric condition and have no sleep disorders. A total of 15 subjects participated in each experiment (no intersection between subjects participating in these studies).

It is worth mentioning that throughout night-long PSG recordings, sometimes ECGs present poor quality due to the recording protocol and movement events during sleep. Therefore, the availability of a robust QRS-complex detector was of high importance to obtain reliable RR-intervals. Furthermore, for a comprehensive statistical analysis of U-patterns, one needs to extract these patterns accurately. To this end, the Rel-En algorithm (see Chapter 5) was used to extract QRS-complexes and subsequently the RR-intervals, as well as the U-patterns taking place within the RR-intervals during sleep.

7.2.1 Data

The data gathered during this study comprise questionnaires, laboratory and non-laboratory bio-recordings, which are described next.

Non-PSG Recordings

Every morning, after waking up, subjects filled either three (q) or five (Q) questionnaires. These questionnaires were designed to measure subjective fatigue and sleep quality. The q comprised "Fatigue 8-item" [237], "Groningen Sleep Quality Scale" [238], and "Karolinska Level of Drowsiness" [239] questionnaires. In addition to the items in q , for Q , subjects filled the "Levels of Fatigue 14-item" [240] and "Profile of Mood States" questionnaires [241].

In addition to the questionnaires, subjects recorded their RR-intervals every morning using a polar belt and recorder watch (V800, Polar, Kempele, Finland). These recordings comprised either 3-minute supine followed by 3-minute standing (hrv), or 6-minute supine followed by 6-minute standing (HRV). Certain nights during the experiments, subjects wore portable monitoring bracelets on their non-dominant wrist (Shimmer GSF+R, Dublin, Ireland) for night-long PPG recordings. Finally, psycho-motor vigilance tests (PVT) were carried out to measure subject response to visual stimuli.

PSG Recordings

PSG recordings were carried out for a comprehensive sleep analysis. These recordings comprised different physiological data, recorded by EMBLA devices (Embletta MPR, Ontario, Canada: EMBLA ST+ Proxy, Ontario, Canada), details of which are provided next. Figure 7.2 illustrates a subject equipped with the PSG recording device.

- **EEG.** For the purpose of brain activity analysis, and more specifically sleep evaluation, a 6-electrode EEG was considered for this study. Electrodes were placed at the conventional locations (F3-F4, frontal lobes; C3-C4, central lobes; O1-O2, occipital lobes) to follow the international standards.
- **EOG.** A 2-electrode EOG (M1, M2) was recorded by placing one above the right and another below the left eye, in order to record eye movements.
- **EMG.** Using three electrodes (ChinL, ChinR, ChinC) mentalis and submentalis movements were captured. These electrodes are classically used for sleep analysis, as during

deep sleep stages, jaw muscles are known to relax.

- **ECG.** A 2-lead ECG was also recorded to study cardiac activity during sleep. One lead was placed five centimeters above the right nipple while the other one was placed at the same distance below the left nipple.
- **Respiration.** Using an impedance belt, thoracic respiration was recorded for the assessment of respiration and possible sleep apnea analysis.

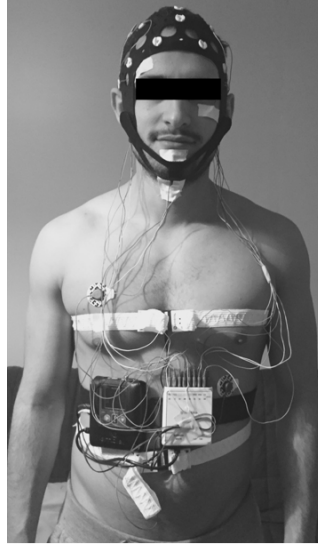


Figure 7.2 – Image of a subject equipped with the PSG.

Post-PSG Recordings

The day following PSG recordings, subjects underwent a 10-minute continuous blood pressure recording (BPV) as well as a saliva withdrawal (SAL) for follow up analysis.

In the context of this dissertation, only the PSG, and night time recorded RR-intervals were used for U-pattern extraction and analysis. The two following sections describe respectively the over-training and the sleep deprivation setting in details.

7.2.2 Phase A: Over-training

Population.

The over-training study comprised 15 subjects (8 males and 7 females), the anthropometric parameters of which are as follows:

Table 7.1 – Anthropometric parameters of the over-training study.

Characteristic	<i>mean ± std(N = 15)</i>	Range
Age (years)	25.0 ± 5.4	19 – 26
Height (cm)	175.4 ± 8.8	158 – 188
Weight (kg)	64.2 ± 11.5	49 – 90

Protocol.

Data recording in this study was carried out over a period of 51 days, in three immediate stages. First, the "baseline" phase with a duration of two weeks during which the subjects followed their normal lifestyle, performing normal sportive activities. Second, the "over-training" phase for a period of three weeks during which they had to perform extra sportive activity in order to induce fatigue. Third, the "recovery" phase with a duration of three weeks. In this phase the subjects went back to their normal training routines, similarly to the baseline stage. Figure 7.3 illustrates the details on the recorded signals during the over-training study.

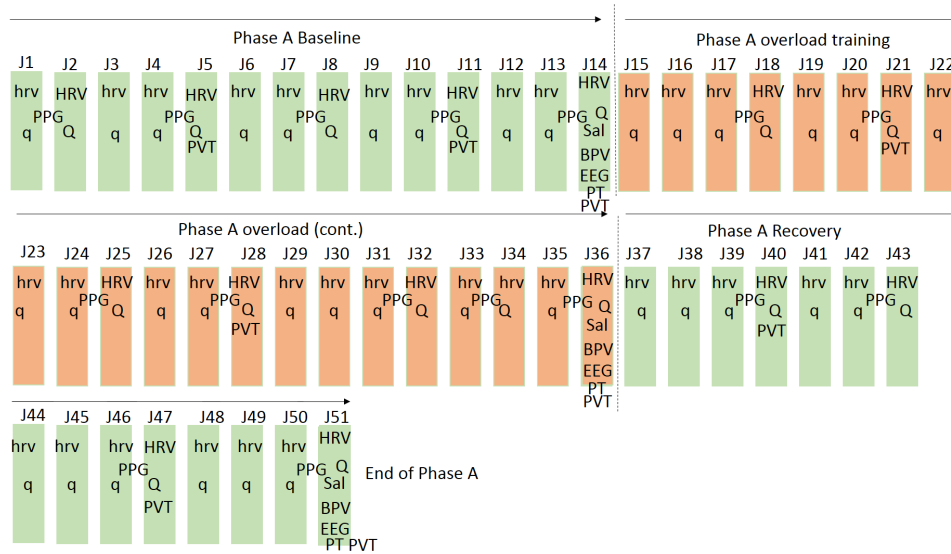


Figure 7.3 – Detailed information on data acquisition during the over-training study.

As there was no PSG recording for the over-training experiment, the night-long RR-intervals extracted from the PPG device were used for U-pattern analysis.

7.2.3 Phase B: Sleep Deprivation

Population.

The sleep deprivation study also comprised 15 subjects (7 males and 8 females), the anthropometric parameters of which are as follows:

Table 7.2 – Anthropometric parameters of the sleep deprivation study.

Characteristic	<i>mean ± std(N = 15)</i>	Range
Age (years)	22.1 ± 1.7	18 – 25
Height (cm)	172.7 ± 8.8	160 – 196
Weight (kg)	65.9 ± 11.6	52 – 92

Protocol.

This experiment was carried out over a span of 17 days, in three immediate stages. Similarly to the over-training experiment, there was first a "baseline" phase lasting for seven days, during

which the subjects slept normally with no constraints. Following the baseline, subjects went through a "sleep deprivation" phase with a duration of three days, during which they could only sleep three hours at night. Finally, a 7-day "recovery" phase took place, during which subjects slept normally, as they would in the baseline phase. Figure 7.4 illustrates the details of recorded signals during the sleep deprivation study.

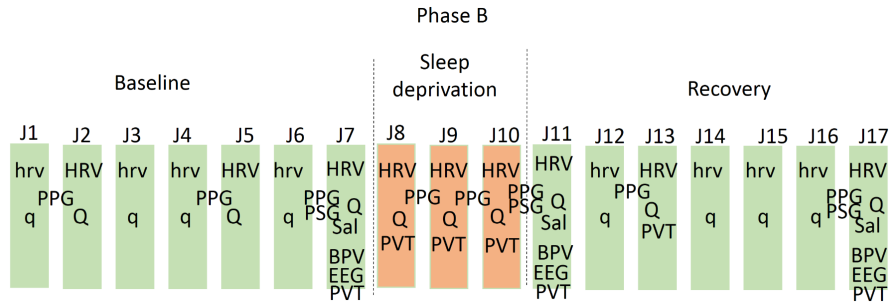


Figure 7.4 – Detailed information on data acquisition during the sleep deprivation study.

7.3 U-shape Patterns

After the extraction of the RR-interval time series from night-long ECG recordings one can observe a phenomenon, which in this dissertation is referred to as U-patterns. U-patterns are recurrent within RR-intervals and do not seem to take place periodically or quasi-periodically. This dissertation defines these patterns as U-shape decrease-increase in the RR-interval time series, with a duration of 20 to 40 seconds with a minimum decrease of 15% in the local RR-interval mean value. Figure 7.5 illustrates an example of U-pattern extracted from a PSG recording. In this figure, a U-pattern with a duration of 27 seconds and a decrease in mean RR-intervals of 31%, from a mean 1004 ms down to a mean of 693 ms, is illustrated.

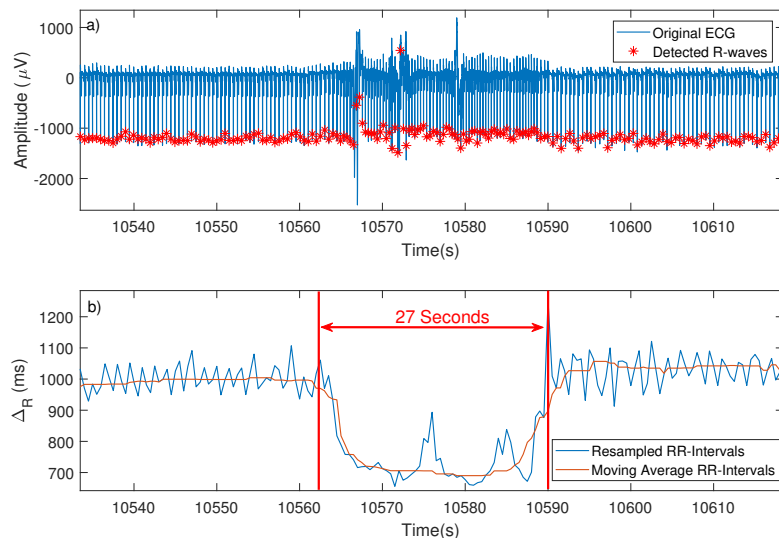


Figure 7.5 – Illustration of a U-shaped pattern taking place during sleep. a) The ECG excerpt containing the U-pattern alongside the detected R-waves. b) The U-pattern in the RR-interval time series.

7.4 U-Pattern Extraction

7.4.1 Preprocessing

In order to extract U-patterns, ECG recordings were first processed to detect R-waves and subsequently extract the RR-interval time series. The QRS-complexes were detected using the Rel-En algorithm described in Chapter 5, with the parameters described in Section 5.3.1. The extracted RR-interval time series was then resampled at 1 Hz, and further smoothed by applying a moving median filter with a duration of 15 seconds in order to remove small excursions in the time series. For the remainder of this chapter "RR-intervals" refers to the median filtered version of this time series, unless stated otherwise. Figure 7.6 illustrates an example of RR-intervals used for U-pattern extraction. One can clearly see the U-pattern in the middle of this figure.

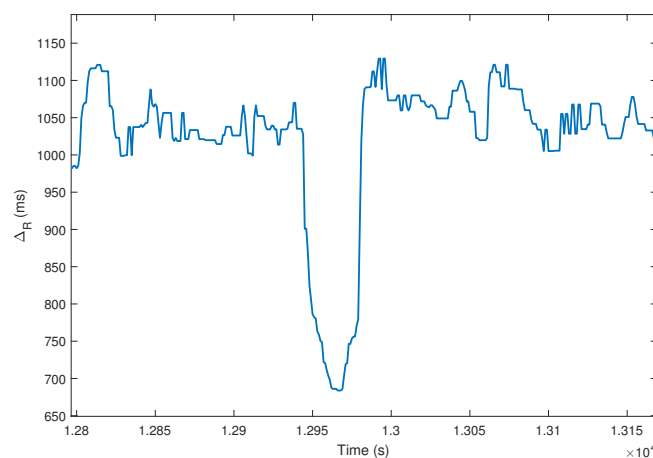


Figure 7.6 – The preprocessed RR-intervals, used for U-pattern extraction, taken from an ECG excerpt of a baseline sleep deprivation PSG recording.

7.4.2 Extraction Method

For U-pattern extraction, the RR-interval time series was used as the input to the Rel-En algorithm with the following empirically chosen parameters: short-term window duration of 50 seconds, long-term window duration of 2000 seconds, an exponent of 10 and a Hamming window smoothing function. In order for the U-patterns to manifest as a surge in the local energy, the inverse RR-intervals were used as the input to the Rel-En algorithm. Figure 7.7 illustrates the different steps of the Rel-En algorithm on the inversed RR-intervals. Figure 7.8 also displays the Rel-En output, which is further scrutinized for U-pattern extraction.

A hysteresis comparator is then applied to the output of the Rel-En algorithm. A hysteresis comparator is a suitable choice as it is insensitive to small RR-intervals fluctuations around the detection threshold. This comparator uses two thresholds for event detection/extraction. A central threshold which determines the actual event detection threshold, and a second threshold which creates upper and lower confidence intervals around central threshold and makes the extraction less sensitive to noise. Figure 7.9 shows an example in which the output of a hysteresis comparator is compared with a normal threshold. As seen in this figure, the hysteresis comparator results in a smooth transition between the onset and offset of an event, whereas the normal threshold is more sensitive to small local changes. For U-pattern extraction, the lower threshold was set to the value of the central threshold.

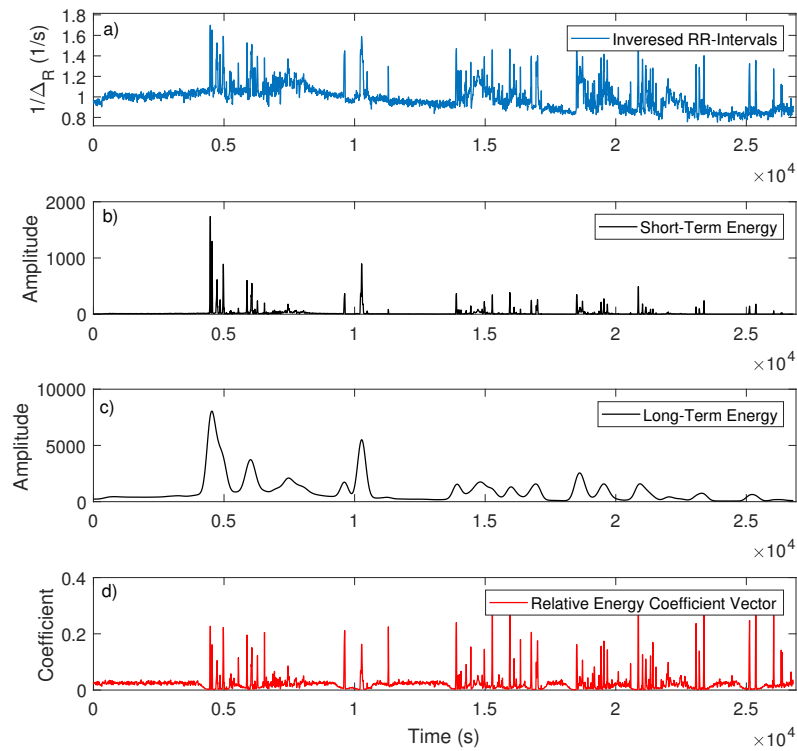


Figure 7.7 – Illustration of the different steps of the Rel-En algorithm on an inversed RR-intervals. a) Input signal. b) Short-term energy evolution c) Long-term energy evolution d) Coefficient vector calculated by Rel-En.

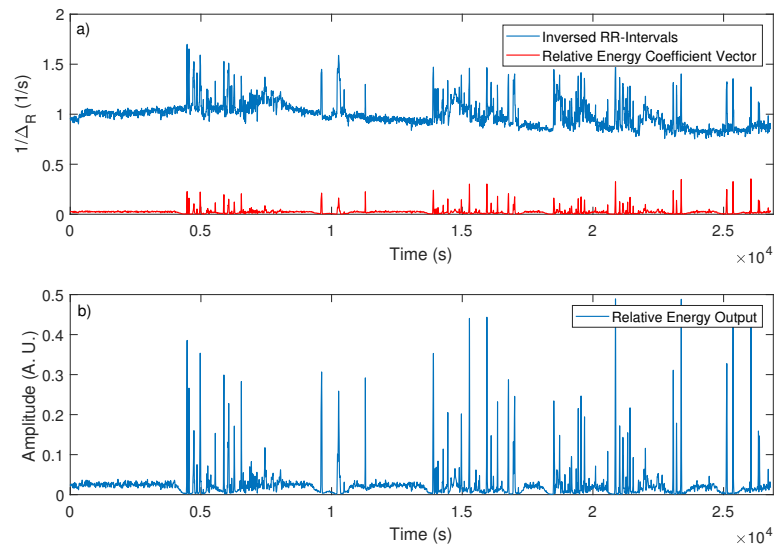


Figure 7.8 – Output of the Rel-En algorithm on the inversed RR-interval time series. a) The input signal alongside the calculated coefficient vector. b) Rel-En output, generated by element-wise multiplication of the coefficient vector by the inversed RR-interval time series.

In order to delineate the U-patterns, a sliding window s with a length of 400 seconds was used to calculate the moving median of the Rel-En output. The central and upper thresholds were calculated through,

$$Th_{Central}(n) = Median(s(n)) + 0.02 \times max(s(n)) \quad (7.1)$$

$$Th_{Upper}(n) = Median(s(n)) + 0.05 \times max(s(n)) \quad (7.2)$$

where n represents the n^{th} sample of the RR-intervals time series.

In order to enhance U-pattern detection, the hysteresis comparator output was further processed by merging events within an interval of five seconds. Event splitting was generally due to artifacts in the ECG, causing lead saturation and false positive QRS-complex detection. Finally, the extracted events were analyzed in terms of duration and depth to obtain U-patterns. First, the candidates were checked to have a duration of 15 to 45 seconds (a 5-second detection margin was added to the definition of U-patterns, to make the detection more robust). Second, the decrease in RR-intervals amplitude was calculated as the difference between the average RR-interval value outside each candidate (average RR-intervals value for 60 seconds preceding and following each candidate event) and the minimum RR-interval value during the candidate U-pattern. If an RR-interval amplitude decrease larger than 15% was observed, the candidate event was selected as a U-pattern.

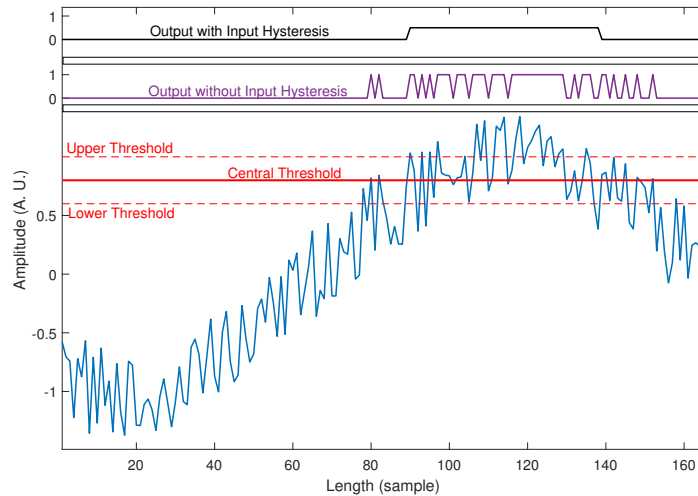


Figure 7.9 – The difference between a normal thresholding technique and a hysteresis comparator. In comparison, the hysteresis comparator results in a smoother output.

Figures 7.10 and 7.11 illustrate the different steps in the extraction of a single U-pattern, on an excerpt from the PSG database. Figure 7.10 shows how a U-pattern candidate is selected from the output of the Rel-En operator. In this figure, the output of the hysteresis comparator is illustrated alongside the lower and upper hysteresis thresholds. Figure 7.11 shows the final step in the detection of the U-pattern. The RR-intervals depicted in this figure correspond to the same segment as that of Figure 7.10. The minimum as well as RR-interval averages for the preceding and following 60 seconds are also shown. The highlighted segment of the RR-intervals in this figure illustrates the extracted U-pattern. Figure 7.12 illustrates the detected U-patterns from a night-long RR-interval time series.

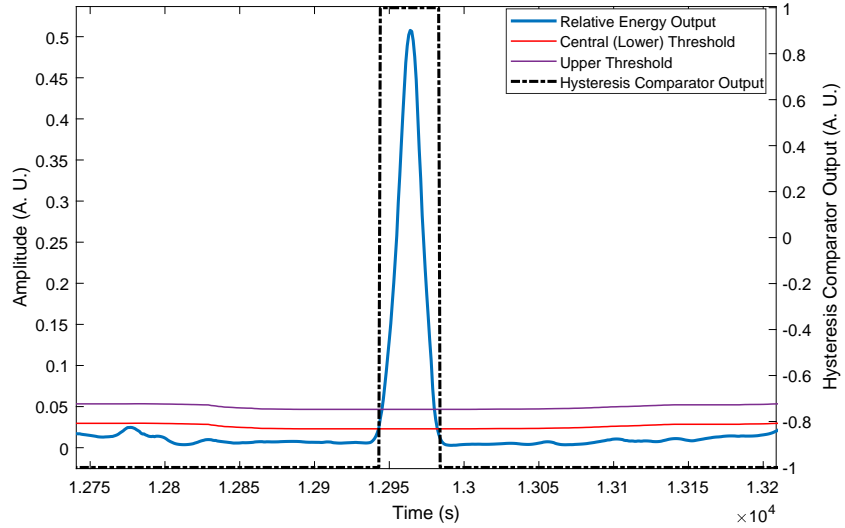


Figure 7.10 – Selection of a U-pattern candidate from the output of Rel-En algorithm, using a hysteresis comparator.

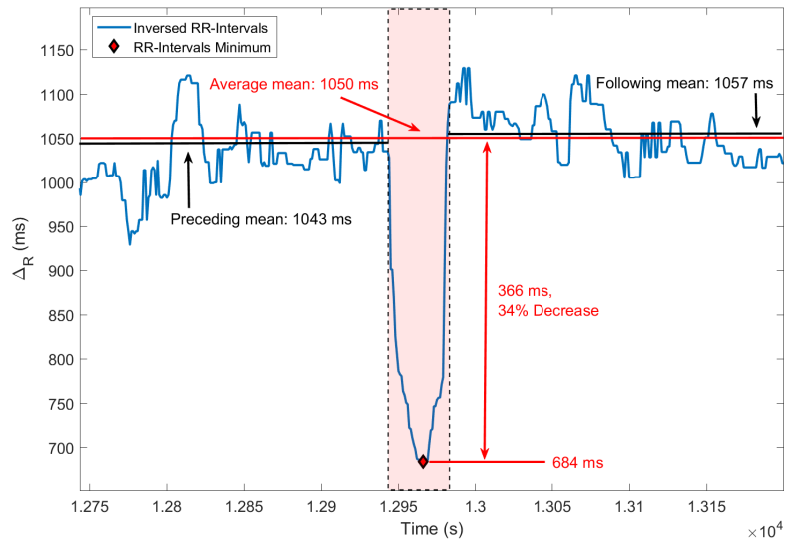


Figure 7.11 – Extraction of U-patterns from the output of the Rel-En algorithm. The preceding and following RR-interval averages (black lines), as well as their average (red line) are depicted. In this example an amplitude decrease of 34% is observed.

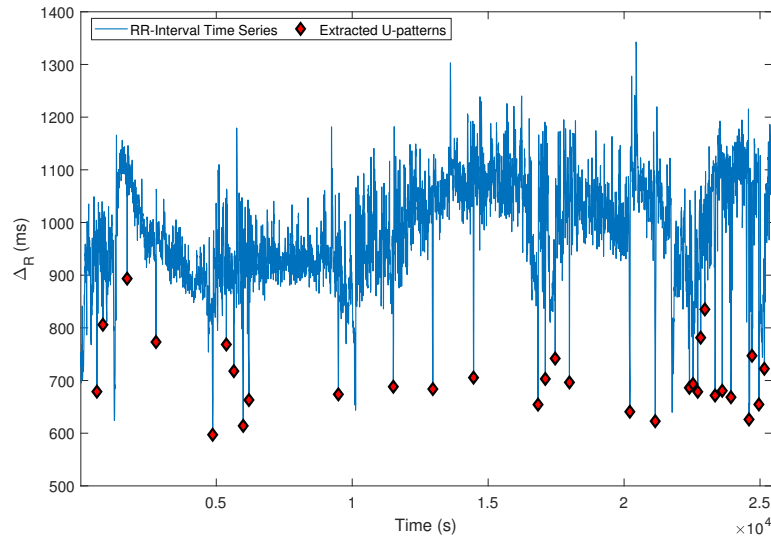


Figure 7.12 – Automatic U-pattern detection for a night-long recording.

7.5 U-pattern Extraction Performance Evaluation

7.5.1 Supervised U-pattern Extraction

Three full-night PSG recordings were manually assessed and U-patterns were annotated by an operator, based on the definition in Section 7.3. The recordings were taken from the baseline phase. The operator performed the annotation using the RR-intervals alongside the original ECG. For each U-pattern, the locations and amplitudes of the onset, minimum and the offset were recorded, and this information was used to create a U-pattern dataset. Furthermore, the local quality of the ECG was observed and if perturbations saturated the signal, those segments were discarded for annotation.

In order to evaluate extraction performance, for each of the three annotated night recordings, U-patterns were extracted using the proposed technique and were compared to those in the annotation files. Table 7.3 reports the U-pattern extraction performance, in terms of sensitivity, positive prediction value and detection error rate, over specific and all annotated recordings.

Recording	1	2	3	Overall
Number of TP	21	20	15	56
Number of FP	10	22	24	56
Number of FN	2	3	3	8
Sensitivity (%)	91.30	86.96	83.33	87.5
PPV (%)	67.74	47.62	38.46	50
DER (%)	36.36	55.56	64.29	50

Table 7.3 – Performance of the detection algorithm on the annotated U-patterns.

Although a sensitivity of 0.87 was obtained the detection error rate was too high at 0.5. By analyzing the results obtained by automatic U-pattern detection, the following conclusions were drawn:

1. The number of annotated U-patterns was too small for a reliable performance evaluation.
2. Observations on the FP samples revealed that the operator was too strict when annotating U-patterns, leading to high detection error rates. This was especially true for the second and third recordings. Therefore, a second operator was asked to annotate the third recording, with the same annotation instructions. By comparing the annotations provided by the two operators, a large disagreement was observed. Using the second operator's annotation the FP samples for the third tape dropped from 24 to 5.

Therefore, in order to have a fair performance evaluation, the extraction method was analyzed against synthetic U-patterns, described next.

7.5.2 Synthetic U-pattern Detection

Synthetic U-patterns were generated using PSG recordings from the baseline phase of the sleep deprivation database. From the extracted RR-intervals, segments with low to moderate levels of noise and without U-patterns were assembled, in order to reflect RR-interval fluctuations during sleep. Figure 7.13 illustrates an example of synthesized baseline RR-interval time series.

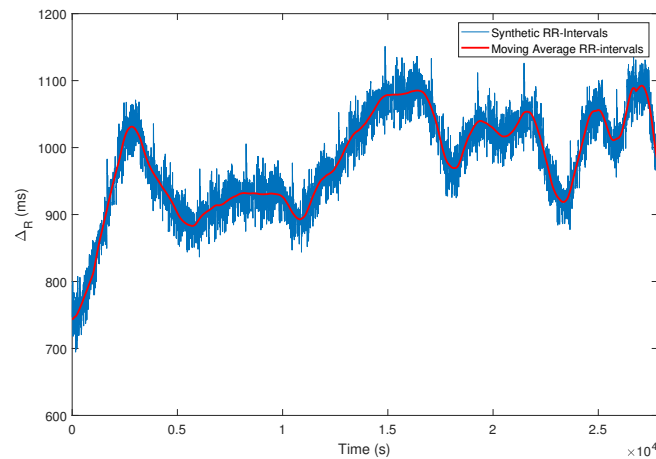


Figure 7.13 – Baseline RR-interval time series generated for synthetic U-pattern detection. The generated U-patterns were then added to this signal and subsequently the detection performance was evaluated.

On 8-hour baseline RR-interval segments, series of U-patterns (between 10 to 50) were added to finalize the synthetic recordings. The duration of U-patterns varied between 20 and 40 seconds with a decrease in the local RR-intervals value of 15 to 40%. Furthermore, a minimum distance of 150 seconds separated the generated U-patterns, in order to avoid their overlapping. In more detail, the synthetic U-patterns were added to the baseline RR-intervals using the following piecewise model:

1. In order to reflect the initial decline in the RR-intervals, a decreasing second-order polynomial with a duration of seven to nine seconds.
2. A constant segment with small variation, representing the minima of the U-pattern.
3. An increasing linear segment to complete the U-pattern varying between three to five seconds.

It is noteworthy that several fitting models were studied to represent U-patterns, such as quadratic and mixture of decreasing and increasing exponentials. However, it was visually confirmed that the aforementioned piecewise function modeling scheme yielded the best synthetic

U-patterns. Figure 7.14 illustrates a generated U-pattern alongside a real one. Figure 7.15 illustrates U-pattern detection along an 8-hour synthetic recording.

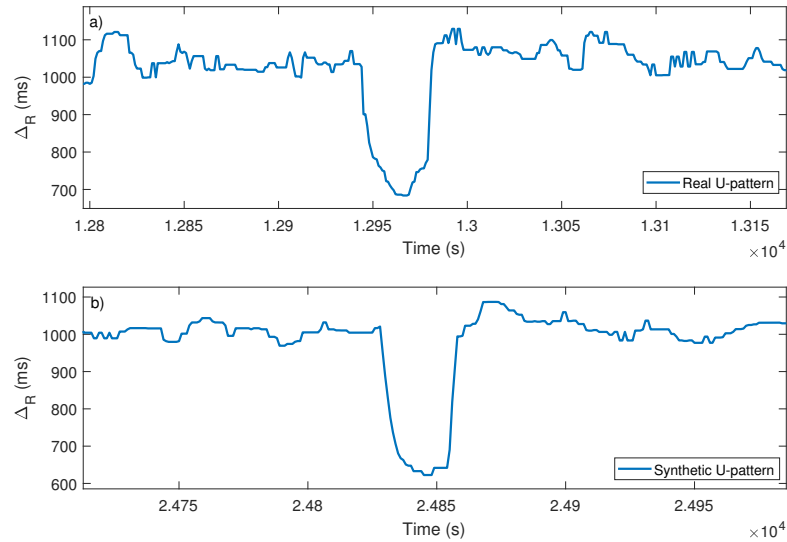


Figure 7.14 – Comparison of the U-patterns. a) A real U-pattern in RR-intervals from an excerpt in the database. b) A synthetic U-pattern generated for unsupervised performance evaluation.

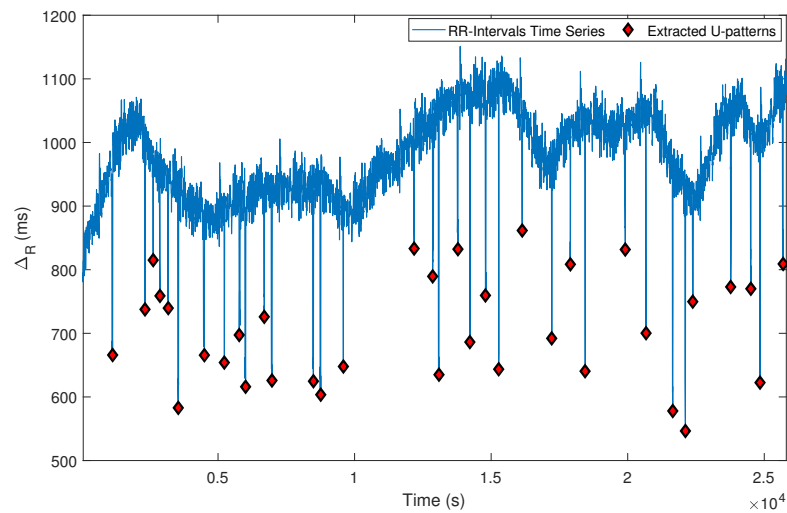


Figure 7.15 – Detection of U-patterns in an 8-hour synthetic recording. The baseline RR-interval time series is the same to that of Figure 7.13. All U-patterns in this recording were extracted successfully.

Synthetic U-pattern detection performance was evaluated on 1000, 8-hour recordings. Synthetic recordings were generated for five full-night baseline RR-intervals, assembled on low- to mid-level noise RR-Excerpts from the sleep deprivation study. Table 7.4 reports the results obtained. As can be seen in this table, the accuracy is far superior to that of the annotated tapes with no FP samples. A relatively low number of FN samples can be observed for each assembled RR-intervals. This was the result of a U-pattern added to a local RR-interval maximum, yielding an RR-intervals amplitude decrease of less than 15%. Furthermore, the root mean square error (RMSE) with regard to the extracted U-pattern depth and duration is reported. These result suggest the U-patterns were efficiently extracted by the proposed technique.

Subject	1	2	3	4	5	Overall
TP	22216	21808	23215	22841	22111	112191
FP	0	0	0	0	0	0
FN	273	242	274	254	257	1300
Sensitivity (%)	98.79	98.9	98.83	98.9	98.85	98.85
PPV (%)	100.0	100.0	100.0	100.0	100.0	100.0
DER (%)	1.21	1.1	1.17	1.1	1.15	1.07
Duration RMSE (s)	3.42	3.43	3.38	3.37	3.47	3.41
Depth RMSE (ms)	26.93	26.98	26.77	27.09	26.88	26.93

Table 7.4 – Performance evaluation on synthetic U-pattern detection.

7.6 The Incidence of U-Patterns in Sleep Deprivation and Over-training

After U-pattern extraction, statistical characteristics of these patterns were analyzed for the sleep deprivation and over-training studies. Alongside the incidence of these patterns, their depth, duration and integral estimate were calculated. Finally, the significance in difference for each sub-phase, i.e. baseline, over-training (or sleep deprivation), and recovery, was studied. Sections 7.6.1 - 7.6.2 report these statistics, respectively for the over-training and sleep deprivation experiments.

7.6.1 Over-training

As illustrated in Figure 7.3, over the 51-day setup of the over-training study, several night-long RR-interval time series (automatically extracted from the PPG recording device) were obtained from the participating subjects. Respectively five, seven and four per-subject RR-intervals were obtained for the baseline, over-training, and recovery phases. As there were no PSG recordings for the over-training study, the over-night RR-interval time series, provided by the portable monitoring device, were directly used for U-pattern extraction. Table 7.5 reports the subject-by-subject number of U-patterns extracted for each phase. More details on U-pattern frequency, depth, duration and integral can be found in Appendix D.1.1.

Subject	1	2	3	4	5	6	7	8	9	10	11	12	13	14	15
Baseline	26.75	25.75	24.75	15.0	31.5	12.8	25.0	23.0	28.0	34.2	23.25	35.5	21.0	17.25	23.33
Over-training	25.67	22.0	20.5	16.0	28.6	22.0	21.33	19.0	41.4	29.33	26.0	35.4	27.75	14.5	19.0
Recovery	24.0	29.0	23.8	17.5	31.75	23.5	26.0	20.0	33.5	31.75	28.75	27.0	15.0	13.5	30.0

Table 7.5 – Subject-by-subject number of extracted U-patterns for each phase of the over-training study. Non-integer values reported in this table represent the average number of U-patterns during each phase, as there were multiple full-night RR-intervals recordings available.

Table 7.6 summarizes the inter-subject U-pattern statistics (mean \pm std) obtained from each phase. Furthermore, for each statistical attribute, Table 7.7 studies whether there was a significant inter-subject difference between different phases of the over-training study.

Results reported in this table show no significant difference between the different phases of the over-training experiment, for all the of statistical attributes under study (apart from the average U-pattern integral, in baseline \rightarrow recovery comparison). This suggests that there is no meaningful relation between over-training and U-patterns.

Attribute	Baseline (mean \pm std)	Over-training (mean \pm std)	Recovery (mean \pm std)
No. of U-patterns	24.5 \pm 6.4	24.6 \pm 7.2	25.0 \pm 6.2
U-pattern Frequency (mHz)	1.2 \pm 0.5	1.2 \pm 0.3	1.2 \pm 0.2
U-pattern Duration (s)	23.2 \pm 2.3	23.0 \pm 1.6	23.4 \pm 2.0
U-pattern Depth (ms)	508.1 \pm 132.8	525.0 \pm 121.7	529.3 \pm 132.3
U-pattern Integral (ms.s)	1869.6 \pm 2893.8	3164.3 \pm 876.5	2734.5 \pm 1273.8

Table 7.6 – Inter-subject U-pattern statistical characteristics, reported for each phase of the over-training study.

Attribute	Baseline \rightarrow Over-training <i>p</i> -value	Over-training \rightarrow Recovery <i>p</i> -value	Baseline \rightarrow Recovery <i>p</i> -value
U-pattern Frequency	0.81	0.76	0.65
Mean U-depth	0.71	0.92	0.66
Variance U-depth	0.84	0.99	0.84
Mean U-duration	0.71	0.53	0.84
Variance U-duration	0.50	0.96	0.51
Mean U-integral	0.64	0.75	0.46
Variance U-integral	0.99	0.75	0.74

Table 7.7 – Two sample *t*-test *p*-values for each over-training phase. Bold fields represent *p*-values < 0.5.

7.6.2 Sleep Deprivation

For the sleep deprivation study, the PSG signals (recorded on the last day of each phase, see Figure 7.4) were used for U-pattern extraction and statistical analysis. Similarly to the previous study, Table 7.8 reports the subject-by-subject number of U-patterns extracted for each phase, with more details on U-pattern frequency, depth, duration found in Appendix D.1.2. Moreover, the significance in difference between sleep deprivation phases is reported in Table 7.10.

Contrary to the over-training study, the hypothesis tests on sleep deprivation show significant differences across different phases. With *p*-values < 0.5, the frequency of U-patterns alongside their depth and integral seem to vary meaningfully when subjects go through different sleeping regimens.

Subject	1	2	3	4	5	6	7	8	9	10	11	12	13	14	15
Baseline	31	42	39	38	20	36	48	35	17	23	21	36	49	33	43
Sleep deprivation	17	40	52	26	18	25	32	43	24	31	20	25	59	25	22
Sleep recovery	28	18	35	35	24	23	20	46	22	40	22	12	56	36	44

Table 7.8 – Subject-by-subject number of detected U-patterns for different sleep deprivation phases.

Attribute	Baseline (mean \pm std)	Sleep Deprivation (mean \pm std)	Recovery (mean \pm std)
No. of U-patterns	34.1 \pm 10.0	30.6 \pm 12.5	30.7 \pm 12.2
U-pattern Frequency (mHz)	1.4 \pm 0.4	1.1 \pm 0.5	1.3 \pm 0.4
U-pattern Duration (s)	29.0 \pm 3.2	28.4 \pm 2.4	28.0 \pm 2.4
U-pattern Depth (ms)	292.5 \pm 99.7	268.9 \pm 45.1	284.1 \pm 60.3
U-pattern Integral (ms.s)	4116.4 \pm 1178.5	3700.8 \pm 478.0	3911.8 \pm 759.6

Table 7.9 – Inter-subject U-pattern statistical characteristics, reported for each phase of the sleep deprivation study.

Attribute	Baseline \rightarrow Sleep Deprivation <i>p</i> -value	Sleep Deprivation \rightarrow Recovery <i>p</i> -value	Baseline \rightarrow Recovery <i>p</i> -value
U-pattern frequency	0.14	0.27	0.65
Mean U-depth	0.19	0.44	0.32
Variance U-depth	0.32	0.91	0.32
Mean U-duration	0.54	0.66	0.33
Variance U-duration	0.63	0.63	0.9
Mean U-integral	0.13	0.53	0.25
Variance U-integral	0.32	0.67	0.32

Table 7.10 – Two sample *t*-test *p*-values for each phase of the sleep deprivation study. Bold fields represent *p*-values < 0.5.

7.7 Correlation between U-patterns and Movement Events

Alongside the incidence of U-patterns, one can study the cause and correlation between these patterns and other physiological phenomena. For instance, Dorantes-Mendez et al. [242] performed a time-varying analysis on A-phases extracted from the EEG, and observed a decrease in local RR-interval time series. A-phases are recurrent short-term EEG events, which are categorized into so-called A1, A2, and A3 classes. The A1-phase is characterized by the EEG activity in the range of [0.5-4] Hz and are often associated with K-complexes. The A2-phase contains A1 frequency activity as well as fast rhythms in the range of [8-30] Hz. However, slow frequencies are dominant (50-80% of the activity). Finally, the A3-phase comprises predominantly faster activities [8-30] Hz. In [242] a decrease in local RR-intervals was observed in all A-phases, with A3 presenting the clearest change.

Our observations on ECG signals during U-patterns led to the hypothesis that U-patterns may be due to subject movement during sleep. Although the ECGs presented high enough quality for RR-interval extraction, moderate to high levels of EMG noise (sometimes even lead saturation) often contaminated the signal (this phenomenon can be seen in Figure 7.5-a). Therefore, the correlation between U-patterns and movement events was studied to determine whether this hypothesis was true or not. To this end, high-amplitude and -frequency segments from PSG recordings were extracted as movement events. Observations on the available channels showed that the motor cortex EEG channels (C3-C4) along side the three EMG channels represented head movements to a higher degree. Regarding the bio-signals acquired from the body, the respiration signal (thorax channel) best represented these events. The aggregate set of movement events extracted from these channels was used to assess U-pattern/movement event correlation³. The following section presents the scheme used to extract movement events from the aforementioned PSG channels.

3. The aggregate set of movement events across all available channels was also considered for U-pattern/movement event correlation analysis. Results are available in Appendix D.2.

7.7.1 Detection of Movement Events

U-pattern/movement event correlation analysis was carried out by signal peak activity extraction using the Rel-En algorithm. First, short- and long-window durations of 20 and 2000 seconds, with an exponent of 2 as well as a Hamming window were used to enhance peak activities. Subsequently, using a hysteresis comparator, peak events were extracted. The hysteresis comparator was calculated on a sliding window with a duration of 400 seconds, with a central threshold of the root mean square of the values inside the window. The upper threshold was selected as central threshold plus 0.5% of the window maximum. Figures 7.16 - 7.18 illustrate the different steps in movement event extraction on a night-long recording.

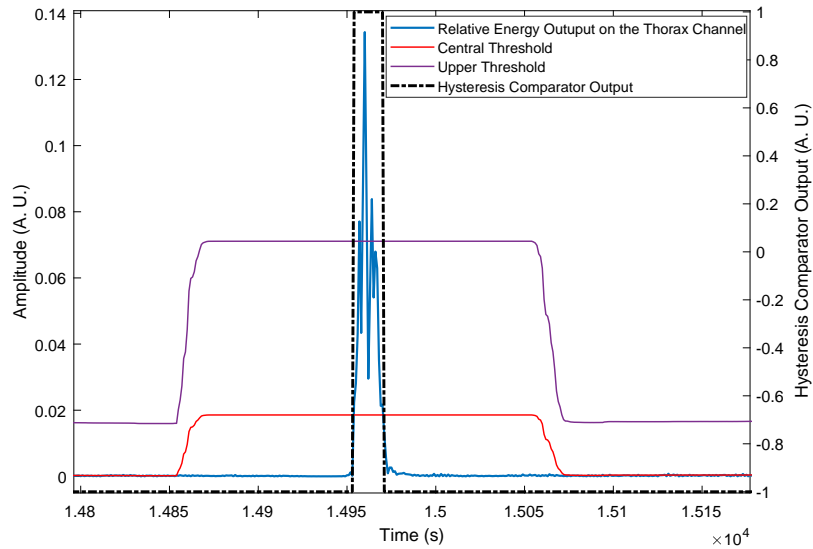


Figure 7.16 – Illustration of a single peak activity detection using Rel-En on the thorax channel, together with the central and upper thresholds and the output of the hysteresis comparator. Data taken from the first subject, baseline phase.

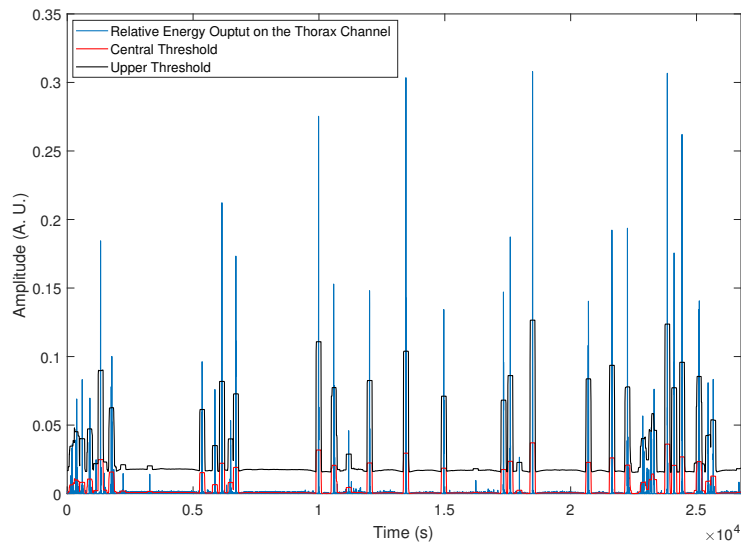


Figure 7.17 – Illustration of night-long peak activity detection using Rel-En on the thorax channel, together with the central and upper thresholds of the hysteresis comparator.

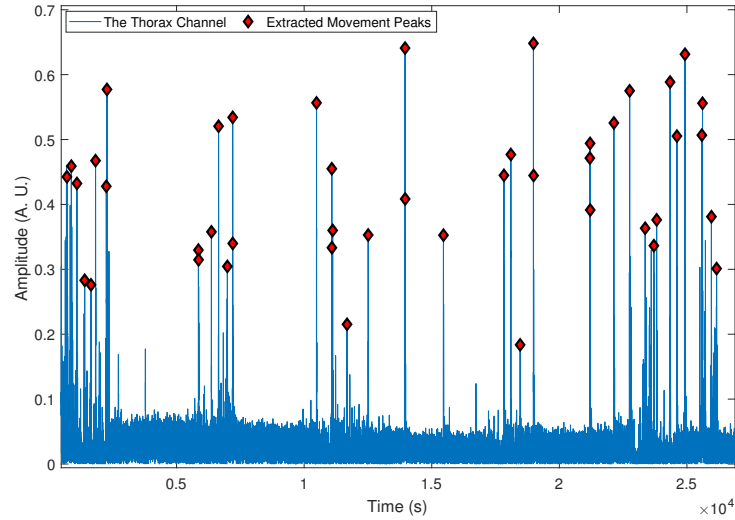


Figure 7.18 – Illustration of night-long movement event extraction from the thorax channel.

7.7.2 U-Pattern/Movement Agreement Rate

Following the extraction of movement events, the correlation between U-patterns and these events was studied. This task was carried out by comparing movement onset/offset times with those of the U-patterns. More specifically, a U-pattern was considered correlated with a movement event when there was an intersection between their respective time intervals, with a tolerance of five seconds. The agreement rate was then calculated as the percentage of U-patterns correlated with movement.

Table 7.11 reports the U-pattern/movement agreement rate for each sleep deprivation phase. In this table, for each subject, U-patterns were compared with movement events from the C3, C4, thorax and 3-EMG channels. Here (and henceforth), the 3-EMG field represents the aggregation on the three available EMG leads, i.e. ChinC, ChinL and ChinR. In other words, a 3-EMG movement event represents the extraction of a movement event from at least one of the three available EMG channels⁴.

Attribute	Baseline (mean \pm std)	Sleep Deprivation (mean \pm std)	Recovery (mean \pm std)
3-EMG	26.8 \pm 14.2	26.3 \pm 13.6	28.2 \pm 13.3
Thorax	39.9 \pm 16.0	38.4 \pm 15.1	43.0 \pm 8.4
C3	24.7 \pm 13.3	18.9 \pm 12.4	24.9 \pm 12.6
C4	24.9 \pm 12.9	22.2 \pm 14.0	23.7 \pm 10.5

Table 7.11 – Inter-subject U-pattern/movement event agreement rate (%) with respect to 3-EMG, thorax, C3 and C4 channels.

As reported in Table 7.11, movement events extracted from the thorax channel generally had the highest agreement rate with U-patterns. Furthermore, this was the case across all phases of the sleep deprivation study. Figure 7.19, illustrates this agreement, extracted for subject no. 1, during the baseline phase of the sleep deprivation study.

4. Subject-by-subject details (for all available channels) of these agreements can be found in Appendix D.2.

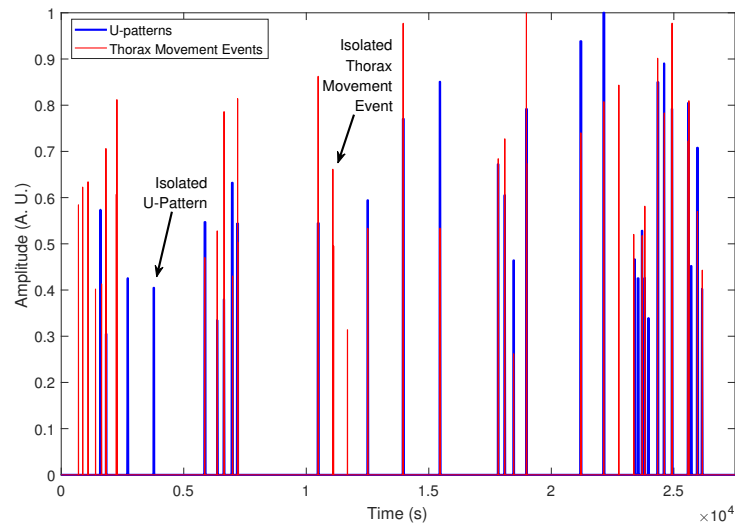


Figure 7.19 – U-pattern/thorax movement event agreement for a night-long PSG recording from the sleep deprivation study, baseline phase.

7.7.3 Uncorrelated U-patterns

Results on U-pattern/movement agreement rates show that some U-patterns may not be correlated with any movement event. As shown in Figure 7.19, several U-patterns and movement events take place at the same time. However, some isolated U-patterns as well as movement events can be observed^{5 6}. Table 7.12 reports the subject-by-subject number and percentage of isolated U-patterns, i.e. patterns that are uncorrelated to movement events, for each sleep deprivation phase. No clear upward or downward trend with regard to the number of uncorrelated U-patterns or study phase was found. Nevertheless, the average number of these uncorrelated patterns increased from baseline to sleep deprivation. During the recovery phase, the number of uncorrelated U-patterns decreases almost to that of the baseline phase, suggesting that subjects were effectively recovering during this phase.

7.7.4 Causality

Having extracted the correlated U-patterns/movement events, the causality between these two phenomena was studied. To this end, for correlated events, the onset time differences were calculated. Time delays of correlated events, for each sleep deprivation phase, are reported in Tables 7.13-7.14. Results show that correlated U-pattern/movement events are always initiated by U-patterns. Similarly, by studying U-pattern/movement offsets, the opposite results were obtained, i.e. U-patterns always terminated after their respective movement event⁷.

5. Here, only analysis on uncorrelated U-patterns are performed with respect to 3-EMG, throat, C3 and C4 channels. For results on uncorrelated U-patterns with respect to all available channels, see Appendix D.3.1.

6. Analysis on isolated movement events is provided in Appendix D.3.2.

7. Subject-by-subject results on U-pattern/movement causality analysis is reported in Appendix D.4.

Sleep Deprivation Study Subject No.	Baseline		Sleep Deprivation		Sleep Recovery	
	No.	Percentage	No.	Percentage	No.	Percentage
Subject 1	2	6.45	3	17.65	5	17.86
Subject 2	6	14.29	13	32.5	3	16.67
Subject 3	12	30.77	29	55.77	19	54.29
Subject 4	12	31.58	1	3.85	2	5.71
Subject 5	5	25.0	2	11.11	5	20.83
Subject 6	1	2.78	5	20.0	2	8.7
Subject 7	21	39.62	17	53.13	5	25.0
Subject 8	9	25.71	24	55.81	8	17.39
Subject 9	8	47.06	6	25.0	5	22.73
Subject 10	2	8.7	7	22.58	12	30.0
Subject 11	1	4.76	2	10.0	3	13.64
Subject 12	6	16.67	4	16.0	1	8.33
Subject 13	12	24.49	32	54.24	28	50.0
Subject 14	6	18.18	12	48.08	14	38.89
Subject 15	24	55.81	5	22.73	23	52.27
<i>mean ± std</i>	8.47 ± 6.88	23.46 ± 15.67	10.8 ± 10.22	29.89 ± 18.53	9.0 ± 8.41	25.49 ± 16.23

Table 7.12 – Uncorrelated U-patterns in the sleep deprivation study, with respect to movement events extracted from 3-EMG, thorax, C3 and C4 channels. For each subject, the number and the percentage of uncorrelated U-patterns are reported.

Onset Delays (s)	Baseline (<i>mean ± std</i>)	Sleep Deprivation (<i>mean ± std</i>)	Recovery (<i>mean ± std</i>)
3-EMG	8.9 ± 1.5	14.9 ± 3.3	8.0 ± 2.2
Thorax	8.1 ± 1.6	13.2 ± 3.1	7.6 ± 1.7
C3	11.0 ± 2.9	14.6 ± 2.8	11.4 ± 5.0
C4	9.4 ± 3.2	15.9 ± 3.2	10.5 ± 4.3

Table 7.13 – Inter-subject averages of U-pattern/Movement onset delays (seconds), with respect to 3-EMG, thorax, C3 and C4 channels.

Offset Delays (s)	Baseline (<i>mean ± std</i>)	Sleep Deprivation (<i>mean ± std</i>)	Recovery (<i>mean ± std</i>)
3-EMG	15.9 ± 4.7	8.5 ± 2.0	14.7 ± 3.1
Thorax	13.1 ± 2.3	7.9 ± 1.8	12.9 ± 2.2
C3	13.8 ± 5.3	10.7 ± 3.3	14.2 ± 3.5
C4	14.4 ± 4.3	9.9 ± 1.8	14.2 ± 3.5

Table 7.14 – Inter-subject averages of U-pattern/Movement offset delays (seconds), with respect to 3-EMG, thorax, C3 and C4 channels.

Figure 7.20 displays an example of correlated U-pattern/thorax movement event (same data as in Figure 7.19). One can observe that the U-pattern initiates the movement and disappears after the movement event is terminated. As U-patterns represent an increase in heart rate, one could explain this chain of events as follows:

1. A transient phase, during which the subject goes from deep to shallow sleep or a micro-arousal stage.
2. A movement phase, for instance change in posture from one side to another.
3. A second transient phase, during which the subject goes from shallow sleep or a micro-arousal stage back to deep sleep.

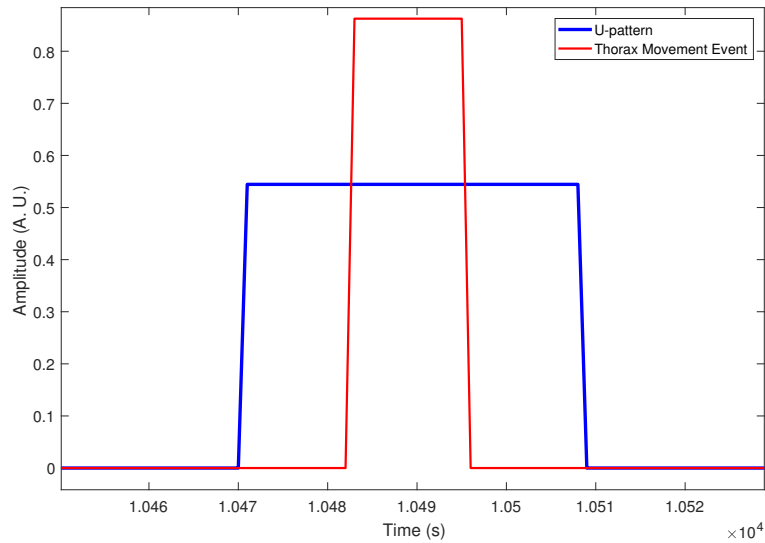


Figure 7.20 – Causality between U-patterns/movement events. The U-pattern is initiated first, then movement event takes place, after which the U-pattern is terminated.

7.8 Discussion

As a phenomenon taking place during sleep, U-patterns may reveal information about its quality. However, in order to draw reliable and interpretable results, the extraction of these U-shaped patterns must be addressed first. U-patterns vary in amplitude and duration, and in comparison with other complexes (such as QRS ones), one deals with much larger temporal and amplitude variances. Therefore, linear filtering and conventional thresholding techniques may not be able to robustly detect these patterns. This remains true for other physiological phenomena. As an example one can discuss EEG K-complex detection. As mentioned in Chapter 5, neither linear filtering techniques nor simple temporal thresholds are able to robustly detect these complexes. Instead, the state-of-the-art use several, sometimes unintuitive, descriptors (features) to identify them. Even then, the detection can only be carried out by training classification models, which in turn is arduous to perform as large amount of annotated data is required to obtain a reliable model. The Rel-En algorithm, however, provides a robust detection technique for these patterns. When combined with a simple hysteresis comparator, this algorithm is able to robustly extract U-patterns. It uses a small number of parameters and avoids using unintuitive thresholds for U-pattern extraction.

It is noteworthy that the presented extraction technique does not use the RR-interval time series but rather its inverse. The Rel-En algorithm uses absolute signal values to compute the coefficient vector, which is then multiplied by the input signal in order to enhance events of interest and suppress unwanted activities. For U-patterns, which present high temporal and amplitude variances, however, one needs to remove low-frequency activities, i.e. the RR-interval baseline, in order to represent them well. In any case, baseline removal affects the morphology of the U-patterns and subsequently, they will not be as prominent in the resulting signal. Moreover, our observations showed that by performing baseline removal, the U-pattern extraction by using a hysteresis comparator would not result in a robust onset and offset extraction. Due to these hurdles, the inverse RR-interval time series was used to extract U-patterns.

In this chapter, a new aspect of PSG data analysis has been explored. It is worth mentioning that, although the behavior of these patterns has been cited in the literature [232, 233], to the best of our knowledge, this is the first study dedicated to analyze the different characteristics of U-patterns. An interesting aspect studied here, was the correlation between U-patterns and movement during sleep. By extracting movement events, we observed a low to moderate correlation between these patterns and movement. It should be mentioned that in this study, due to lack of relevant data, only head and thorax movement events were analyzed. In order to perform a more comprehensive movement analysis, one needs to take into consideration limb movements, i.e. hands and feet movement, as well. This is primarily due to the fact that these events might not be captured by head and trunk sensors, and therefore result in a lower overall U-pattern/movement agreement. Results show U-pattern onsets take place before movement events, while their offset occur well after the corresponding movement event is terminated. This suggests, for correlated events, that the U-patterns are indeed the cause of movement. Analysis on uncorrelated U-patterns showed that these patterns occur sometimes without resulting in a movement event. Indeed, a quickening of heart rate was observed when U-patterns took place, but visual analysis of the available channels showed no trace of movement with respect to available channels. It is possible that these uncorrelated patterns correspond to limb movements or another phenomenon such as A-phases (as suggested in [233]), or other underlying physiological dynamics, which fall outside of the context of this thesis.

The statistical characteristics of these patterns have also been reported for different conditions, i.e. baseline, sleep deprivation, over-training, and recovery. Statistics suggest that these patterns are not affected by over-training. During sleep deprivation however, several U-pattern characteristics, such as frequency, depth, and duration, change significantly. Therefore, U-pattern analysis can be performed to identify subjects who are experiencing sleep disorders. As described in the introduction, sleep quality assessment can be carried out through EEG-based sleep stage analysis. However, EEG analysis requires subjects to wear uncomfortable EEG caps connected to a recording device through several wires, causing frustration and discomfort during sleep. Analysis of U-patterns however, is only dependent of inter-beat intervals, which can be acquired by portable PPG recording devices and from more convenient locations such as arms and fingers. More to the point, sleep deprivation is known to contribute to disease development. The biological changes induced by chronic sleep deprivation have been associated with cardiovascular and metabolic diseases, and shortened lifespan [243]. By analyzing U-patterns as another important parameter derived from portable monitoring devices, one can identify subjects who are prone, or even experiencing, sleep disorders and subsequently, prevent the development of such diseases.

Observations on the U-patterns occurring in night-long recordings revealed that, sometimes, these patterns form clusters throughout the RR-interval time series, which motivated us to apply fractal analysis to these patterns. Tools from chaos theory have been successfully used in the field of biomedical signal processing. In the literature the fractal nature of several organs such as the brain, the heart, the lungs, and urinary collecting tubes of the kidney have been reported [244–247]. Moreover, fractal analysis has been proven useful in analyzing cardiac health [248] and cardiovascular pathophysiology prognosis [249, 250]. In this study, fractal analysis was performed for all phases of sleep deprivation and over-training experiments. Results on the extracted U-patterns, however, showed that these patterns do not present fractal behavior in the RR-interval time series.

7.9 Conclusion

This chapter studies a U-shape acceleration/deceleration phenomenon that is discernible in the RR-intervals of night-long PSG recordings. An extraction technique based on the Rel-En

algorithm in Chapter 5 is proposed for these patterns. Statistical analysis on the characteristics of these patterns, namely their depth, duration, and the number of their incidence, is performed on two sets of experiments, designed to analyze the effect of fatigue induced by over-training and sleep deprivation. Furthermore, the correlation between U-patterns and movement events during sleep is studied, suggesting a moderate correlation, and that these patterns initiate before and terminate after movement events.

8

Conclusion

Biomedical signal processing is a fascinating field of research. Being able to use mathematics and algorithms to analyze physiological measurements, which in turn can help to uncover the hidden dynamics of human health, has given a unique flavor to this field. This is especially true with the new worldwide effort for prediction and early diagnosis of health problems through e-health devices. Within the context of this thesis new techniques have been proposed to deal with real-life recording and signal processing settings, an issue that has become more highlighted with the rise of portable health monitoring.

The main focus of this dissertation was to develop fundamental yet necessary techniques that can perform at the same level as those proposed for clinical settings, but in portable health monitoring scenarios. The challenge in this task lies in perturbations that are constantly present in these conditions, making it cumbersome to perform reliable signal processing, while offering low complexity techniques.

The majority of biomedical data recorded today is that of the electrical activities of the heart. Representing depolarization and repolarization of heart muscles, ECGs uncover much about the cardiac health and therefore, its continuous monitoring can help identifying people who are prone or who are at early stages of cardiac problems. Chapter 2 of this dissertation is dedicated to introduce human cardiac physiology. Throughout this chapter, a general description of human heart anatomy and its electrical conduction system is provided. The autonomous nervous system and its subbranches, the sympathetic and parasympathetic nervous systems, are described and their effect on cardiac cycle regulation is demonstrated. The normal cardiac cycle is described with details on how each part of the electrical conduction system contributes to this cycle. Various common cardiac arrhythmias, studied throughout this manuscript, are also described with details on their cause and how they manifest in the ECG.

Due to its undeniable importance, there has been an especial focus on the ECG signal processing throughout this dissertation. Within the context of this manuscript, two low-complexity methods are proposed to robustly detect QRS complexes in the ECG. One that performs QRS-fiducial point extraction and delineation alongside the detection of QRS complexes, using time and morphological attributes of heartbeats. The other scrutinizes ECGs for local surges of energy and extracts QRS complexes by analyzing the ratio between the relative short- and long-term signal powers. Both methods were assessed against standard ECG databases with results suggesting better or comparable performance in comparison with the state-of-the-art.

Another important issue addressed in this dissertation is the question of signal quality. Nowadays, most portable monitoring devices can record several bio-signals such as PPG alongside the ECG. While both bio-signals can be used to determine important measures such as the heart rate, one cannot rely on the results, if various values are obtained from different sources. Ha-

ving a measure of signal quality however, can help alleviate this issue by determining which (or whether a) source can be used to derive reliable measures. In Chapter 4 of this dissertation it is shown that multi-modal signal processing can significantly improve the performance of bedside monitoring devices in the ICU. Through processing bio-signals such as ECGs, arterial blood pressure values and PPG signals, a framework was proposed to detect extreme cardiac arrhythmias namely, asystole, tachycardia, bradycardia, ventricular tachycardia, and ventricular flutter/fibrillation. Although a significant improvement in false arrhythmia detection was achieved in Chapter 4, the processing of certain arrhythmias required a moderate to good quality of the available signals. For instance, in case of tachycardia, only 51% of available signals were processed as the unprocessed portion did not have acceptable qualities.

However, when it comes to ECG signal quality assessment, the state-of-the-art has not fully addressed this issue. In fact, for the aforementioned example, all ECG signals were discarded as visual inspection showed that several ECGs did not present acceptable quality. As some recordings did offer good quality ECGs, one could improve the overall arrhythmia detection performance by analyzing the ECG channels, given that a measure of ECG signal quality was available. To this end, in Chapter 6 a continuous ECG signal quality assessment technique was proposed. In this technique, the ECG is cleaned and compared back to the original in order to obtain ECG signal quality index. The method was tested against various types of noise, and was able to provide a reliable measure of quality against a specific (or a combination of) noise types.

On the other hand, one must not forget the new horizons that are made possible with the advent of portable monitoring devices. Nowadays e-health monitoring devices can record physiological data over long spans of time. This opens new possibilities such sleep study and quality assessment, which today are only possible through polysomnography recordings. In fact, Chapter 7 defines and analyzes a U-shaped phenomenon that take place in the RR-intervals during sleep. In this chapter, statistical characteristics of these patterns alongside their correlation with movement event during sleep are studied. Furthermore, it is shown that in conditions such as over-training and sleep deprivation the inter-subject number of these patterns can significantly change. In the end, what makes these new technologies appealing, is their potential to uncover hidden dynamics of human health. Dynamics that are not possible to unravel through conventional short-term analysis, but over a span of days and hopefully someday months and years.

In the remainder of this chapter, the summary of achievements and perspectives of this dissertation is provided.

8.1 Summary of achievements

Adaptive mathematical morphology for ECG heartbeat detection and delineation

Chapter 3 proposes a novel technique for QRS-complex detection and delineation, called adaptive mathematical morphology (AMM). This approach is based on mathematical morphology filters that manipulate the input signal with a morphological template called the structuring element. Although, mathematical morphology has been used in the literature to detect QRS-complexes, using a fixed structuring element brings detection disadvantages as the shape, size and length of these complexes vary over time. The proposed technique uses an adaptive structuring element, which is updated after the detection of a heartbeat, using morphological features of the extracted beat. By performing this update, not only one can achieve a robust detection of QRS-complexes, but can extract QRS fiducial points namely, QRS-onset, QRS-offset, Q-wave, and S-waves. The algorithm was tested on the Physionet MIT-BIH arrhythmia database as well as a portable ECG database, for which QRS-complex detection performances were better or com-

parable to that of the state-of-the-art. Furthermore, to evaluate the QRS fiducial point delineation performance, the Physionet QTDB was used as the manual delineation annotations (provided by cardiologists) were available. In this chapter the reliability of the proposed method is illustrated by demonstrating the algorithm performance on several bad quality scenarios for which QRS-complex detection is not easy. Furthermore, it was observed that for signals with high perturbations, the fiducial point extraction will suffer in terms of accuracy.

On a different but related topic, AMM was adapted for atrial activity detection in intra-cardiac electrograms. Using the same adaptation principle as that of QRS-complex detection, AMM was able to outperform the state-of-the-art and efficiently detect atrial activations. Having a robust detection on these activations can help to predict the ablation outcome of patients suffering from persistent atrial fibrillation.

Multimodal bio-signal processing and arrhythmia detection

Chapter 4 presents a novel technique for the reduction of false arrhythmia alarms in intensive care units. This multi-modal signal processing techniques analyze ECG, PPG, and blood pressure signals in parallel to determine the veracity of life-threatening arrhythmia alarms. A total of five arrhythmia classes were considered namely, asystole, tachycardia, bradycardia, ventricular tachycardia, and ventricular flutter/fibrillation. Using a series of techniques, each arrhythmia alarm was processed slightly differently for veracity analysis.

Heartbeat detection was performed using the adaptive mathematical morphology technique presented in Chapter 3. For pulsatile waveforms, heart rate was determined using adaptive frequency tracking on original and smoothed versions of available PPG and blood pressure signals. Another novelty in this scheme was the use of spectral purity index. This simple yet effective index measures how well a signal of interest can be represented with a single sinusoid. This is especially interesting for ventricular arrhythmias, during which the cardiac cycle loses its normal characteristics and present oscillatory behavior.

The proposed scheme was able to efficiently reduce the number of false arrhythmia alarms, outperforming other methods participating in the Physionet/CinC 2015 challenge. Moreover, although machine learning approaches were utilized in the scheme, for arrhythmia analysis, most thresholds were set based on physiological constraints and arrhythmia definitions. This allows for the method to be less biased to the training data and therefore, avoids over-fitting.

Short-term event extraction in biomedical signals

A major contribution of this dissertation was the development of a novel method to extract short-term events from bio-signals, called the relative energy algorithm. As described in Chapter 5, this non-linear technique uses a few intuitive parameters for event extraction: a short-window parameter, representing roughly the duration of the sought event, a long-window parameter, representing the signal baseline, i.e. event adjacent information, and an exponent that determines noise sensitivity of the algorithm. Furthermore, relative energy can use smoothing window functions such as the Hamming one to avoid spurious event extraction. Using these parameters, in a sliding window, a coefficient vector is created by computing the ratio between short- and long-term signal energies. The coefficient vector is then multiplied by the original ECG, heightening the events of interest. Relative energy is simple to compute and computationally uncstly. While offering these advantages, one can easily and intuitively define its parameters, which as shown in Chapter 5, do not drastically affect the overall event extraction performance around optimal values.

Relative energy was evaluated on three different biomedical signal processing settings. First,

it was used for QRS-complex detection in the ECG, for which it outperformed AMM and most state-of-the-art techniques. Then, K-complex detection in the EEG was studied. While the state-of-the-art were based on machine learning techniques, the proposed method exceeded their detection performance. Finally, relative energy was used to extract heartbeats from imaging PPG recordings. IPPG is an up and coming topic in biomedical signal processing with state-of-the-art dedicated to derive robust blood volume variation signals from normal or infrared cameras. In this application relative energy was used to enhance the peakiness of IPPG waveforms, which in turn led to better heartbeat detection accuracy. The proposed method was efficiently able to detect heartbeats, outperforming conventional methods.

ECG signal quality assessment

Relative energy is not limited to event extraction schemes. As shown in Chapter 6, this algorithm was used to develop a continuous measure of ECG signal quality. Determining the quality of ECGs can be especially challenging as different perturbations affect the ECG differently. On the other hand noise is not easy to define, making it harder to measure. In order to have a measure of signal quality, the input ECG is first passed through relative energy for QRS-complex extraction. After the detection and removal of these complexes, the residue signal is bandpass filtered so that the output reflect typical ventricular information. Subsequently, the removed complexes are added back to the filtered signal to create a cleaner version of the ECG. Finally, ECG signal quality is obtained by calculating the correlation coefficient between the original ECG and the clean signal.

Although, this measure is easy to compute, results suggest it can efficiently determine ECG quality. The proposed index was tested against isolated and combined noise types. More specifically, baseline wander, electrode motion artifact, muscle activity, and their possible combinations. The presented quality measure effectively managed to estimate the quality, separating low-, mid-, and high-levels of noise. The scheme was evaluated against the MITDB noise-stress database, clean 5-min MITDB arrhythmia database recordings with added calibrated noise, as well as the Physionet/CinC 2011 database. With a clear advantage of offering continuous measure of signal quality, the proposed method managed to outperform the state-of-the-art participating in the Physionet/CinC 2011 challenge.

To the best of our knowledge, the proposed index is the first technique to offer continuous non-binary measure of ECG signal quality. Furthermore, unlike the participating Physionet/CinC 2011 techniques, no machine learning was performed to determine the signal quality, bringing forth clear advantages such as duration, and data independence.

U-patterns during sleep studies

Another interesting application of relative energy was the detection of U-shaped patterns from the RR-intervals during sleep. This phenomenon has not been addressed in the state-of-the-art to a meaningful degree. As pointed out in Chapter 7, some studies in the literature have indirectly observed this phenomenon, but none has been dedicated to analyzing them. These U-shape patterns in the RR-intervals manifest as a decrease followed by an increase in the RR-interval time series that last from 20 to 40 seconds and with a minimum drop of 15% in the local RR-intervals mean value.

By analyzing data from a study with the purpose of understanding the effect of physical and mental stress on humans, U-patterns were extracted from night-long polysomnography recordings as well as portable monitoring devices, which were able to provide robust RR-intervals. U-patterns were extracted using the relative energy algorithm and their statistical characteris-

tics such as duration and depth mean and standard deviation were reported. Furthermore, the frequency of these patterns were analyzed. Results suggest that there is a significant difference between the number of these patterns alongside their duration and depth when comparing baseline conditions to sleep deprivation (and in recovery).

On the other hand, observations on ECG channels showed that most of these U-patterns maybe due to movement during sleep, as moderate to high levels of EMG noise were visible. To this end, the possible correlation between movement events (also extracted using relative energy) and U-patterns was investigated. Results show there is a moderate correlation between U-patterns and movement during sleep. Moreover, by analyzing correlated U-pattern/movement events, it was revealed that U-patterns initiate movement events, and are terminated after movement phases.

8.2 Perspectives

Heartbeat classification and arrhythmia detection

There have been studies in the literature that suggest that, once reliable delineation of the QRS-complex is available, the task of heartbeat classification and subsequently arrhythmia detection can be efficiently carried out [2–5]. The adaptive mathematical morphology technique presented in this thesis (see Chapter 3) provides an efficient framework to delineate QRS-complexes. As suggested by the work of De Chazal et al., RR-intervals and morphological features can be used to train an efficient heartbeat classification model [2, 3]. In turn, by performing sequential analysis on consecutive heartbeats, one can simply identify heart rhythm and sequential arrhythmias.

Application of the relative energy algorithm to other bio-signals

Throughout this dissertation, prowess of the relative energy algorithm has been demonstrated. Indeed, this algorithm offers low computation cost and is easy to implement in portable monitoring devices. ECG QRS-complex detection, EEG K-complex detection, IPPG heartbeat detection, U-pattern and RR-accelerations are some of the applications of this algorithm. When it comes to event extraction, relative energy can potentially be implemented as long as the event of interest can be described by a local surge of energy in the signal.

Ventricular activity cancellation in the ECG

In Chapter 6, the first step to compute ECG quality index is by removing QRS-complexes from the ECG. A task which is carried out by the relative energy algorithm. Although, the empirically chosen parameters lead to a good QRS-complex cancellation, they do not necessarily represent the best parameters for all heartbeat types. Especially in case of premature ventricular beats that have uncommon morphology. Therefore, a possible perspective would be to perform a systematic analysis to find the optimal heartbeat canceling parameters for specific heartbeat types. Moreover, it would be interesting to find out how different the value of these parameters would be. Would they be only slightly different from other types of heartbeats or is the difference significant? The optimum parameters can be obtained by performing a grid search on short- and long-window durations, exponent, and the threshold used to cancel QRS-complexes.

Further studies on U-patterns

The study of U-pattern performed through this dissertation can be complemented in several ways. First, as polysomnography recordings provide EEG channels, one can extract different brain waves, i.e. alpha, beta, theta, etc., and study the possible correlation between U-patterns and these waves. Another interesting direction would be to explore the correlation between these patterns and sleep stages. For instance K-complexes and sleep spindles can be used to detect non rapid eye movement stages of sleep. Could there be a possible correlation between U-patterns, micro arousals and sleep stages? On a different but related application, one can complement the study of U-patterns and their correlation with movement events by obtaining more sensory information from trunk and limbs. In Chapter 7, movement events were obtained by extracting high-frequency activities from the available data. In this case, no information on limb movements was available for analysis.

Appendix

Adaptive Frequency Tracking



This appendix provides an introduction to adaptive frequency tracking algorithms used in Chapter 4. The concept of instantaneous frequency is described in Section A.1. Two adaptive frequency tracking algorithms are then introduced in Sections A.2.1 and A.2.2, along with their multi-signal extensions.

A.1 The Concept of Instantaneous Frequency ¹

Frequency is defined as the number of oscillations observed per unit of time. However, many processes are non-stationary, i.e. processes with time-varying mean, correlation function, and higher-order moments [141], and subsequently their spectral characteristics vary over time. The concept of instantaneous frequency is useful for these processes, as it reflects the frequency at a given time. In order to define the instantaneous frequency, an introduction to the concept of the analytic signal is needed. The analytic signal $x_a(t)$ is a complex signal defined as:

$$x_a(t) = x(t) + ix_h(t) \quad (\text{A.1})$$

with $x_h(t)$, the Hilbert transform of $x(t)$. The Hilbert transform is a linear operator, which can be expressed as the convolution of the input signal $x(t)$ and the impulse response of a quadrature filter. The quadrature filter can be seen as an all pass filter providing a phase shift of $-\pi/2$ radians for positive frequency components and $\pi/2$ radians for negative frequency components. Therefore, its frequency response is:

$$H(e^{j\omega}) = \begin{cases} j, & -\pi < \omega < 0 \\ 0, & \omega = 0 \\ -j, & 0 < \omega < \pi \end{cases} \quad (\text{A.2})$$

Moreover, its corresponding impulse response is:

$$h(t) = \frac{1}{\pi t} \quad (\text{A.3})$$

1. The content of this appendix is taken from the work of Sibylle Fallet (ASPG), with permission, entitled as 'Signal Processing Techniques for Cardiovascular Monitoring Applications Using Conventional and Video-based Photoplethysmography', thesis director Dr. J.M. Vesin.

The Hilbert transform is the response of the quadrature filter to a real input signal $x(t)$:

$$x_h(t) = x(t) * h(t) = \frac{1}{\pi} \int_{-\infty}^{\infty} \frac{x(\tau)}{t - \tau} d\tau \quad (\text{A.4})$$

When dealing with discrete-time systems, the impulse response of equation A.3 becomes:

$$h[n] = \begin{cases} \frac{2}{\pi n}, & \text{for odd } n \\ 0, & \text{for even } n \end{cases} \quad (\text{A.5})$$

In practice, the Hilbert filter can be approximated with a finite impulse response (FIR) filter. A more detailed explanation of the Hilbert transform and design of Hilbert Transformers can be found in [256].

In order to introduce the notions of instantaneous amplitude and frequency, the analytic signal can be expressed in polar coordinates as follows:

$$x_a(t) = A(t)e^{j\phi(t)} \quad (\text{A.6})$$

with $A(t) = |x_a(t)|$, the instantaneous amplitude and $\phi(t) = \arg(x_a(t))$, the instantaneous phase. The instantaneous angular frequency is defined as the time derivative of the unwrapped phase:

$$\omega(t) = \frac{d\phi(t)}{dt} \quad (\text{A.7})$$

Although the instantaneous frequency can be obtained by differentiating the instantaneous phase, this approach requires the oscillation to be narrow-band to lead to meaningful results. This method is therefore not well suited for biomedical signals, which are often characterized by more than one frequency component.

A.2 Adaptive Frequency Tracking

Throughout this appendix, the term adaptive frequency tracking will refer to methods based on adaptive band-pass (BP) filters designed to track time-varying oscillations contained in the input signal.

FIR adaptive line enhancers have been previously used in adaptive frequency tracking [257–259]. Although good performances were achieved, observed convergence rates were rather slow. On the other hand, adaptive infinite impulse response (IIR) BP filters have a faster convergence rate. Different schemes based on adaptive IIR filters have been proposed to perform adaptive frequency tracking, with two main types of adaptive mechanisms: non-gradient updating and mean square error (MSE) [260–264]. A new type of coefficient updating mechanism based on the discrete oscillator model was proposed by Liao [143]. This coefficient updating mechanism has the advantage of having a low computational complexity and being independent of the structure chosen for the line-enhancement filter. Figure A.1 shows the general configuration of an adaptive IIR BP filter.

The next two subsections (A.2.1 and A.2.2) focus on two adaptive frequency tracking algorithms. These algorithms, derived from the algorithms proposed by Liao [143], have been extended by former PhD researchers^{2,3} of the applied signal processing group from the Swiss federal institute of technology (EPFL) [144, 265–267]. The multi-signal versions of these algorithms take several oscillatory input signals and track their common instantaneous frequency

2. Y. Prudat, J.-M. Vesin (Dir.), *Adaptive frequency tracking and application to biomedical signals*. PhD Thesis EPFL, n° 4447 (2009).

3. J. Van Zaen, J.-M. Vesin (Dir.), *Efficient Schemes for Adaptive Frequency Tracking and their Relevance for EEG and ECG*. PhD Thesis EPFL, n° 5476 (2012).

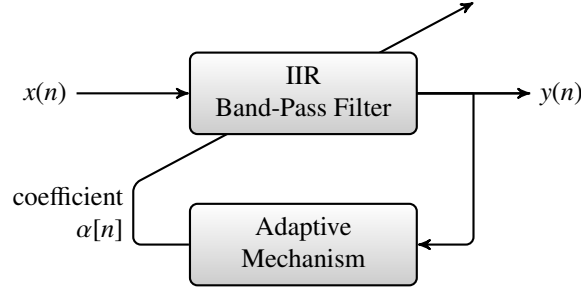


Figure A.1 – General configuration of the adaptive band-pass filter proposed in [143].

component. In the biomedical signal processing, it is quite frequent to obtain redundant information across the sensors. Therefore, as illustrated in Chapter 4, these tools have revealed to be very useful. Moreover, the signal combination often results in a more robust estimation than when a single input is provided.

A.2.1 OSC-MSE Algorithm

The discrete oscillator-based adaptive BP filter was proposed by Liao [143]. An input signal of the following form is considered:

$$x[n] = s[n] + b[n] \quad (\text{A.8})$$

with $s[n]$, a sinusoid of the form $s[n] = A_0 \sin(\omega_0 n + \phi_0)$ and $b[n]$, an additive independent and identically distributed noise. The transfer function of the time-varying BP filter is expressed as follows:

$$H(z; n) = \frac{1 - \beta}{2} \frac{1 - z^2}{1 - \alpha[n](1 + \beta)z^{-1} + \beta z^{-2}} \quad (\text{A.9})$$

with $\alpha[n]$, controlling the central frequency of the BP filter and β ($0 \ll \beta < 1$), a factor related to the filter bandwidth. The adaptive mechanism used to update the central frequency of the BP filter of equation A.9 at each time step requires the minimization of an MSE term, which is derived from the real discrete oscillator equation described as:

$$s[n] = 2 \cos(\omega_0) s[n-1] - s[n-2] = 2\alpha_0 s[n-1] - s[n-2] \quad (\text{A.10})$$

with $\alpha_0 = \cos(\omega_0)$. As illustrated in Figure A.1, the filter output, $y[n]$, is used in the adaptive mechanism. $y[n]$ is defined by the following difference equation:

$$y[n] = (1 + \beta)\alpha[n]y[n-1] - \beta y[n-2] + \frac{1 - \beta}{2}(x[n] - x[n-2]) \quad (\text{A.11})$$

The following cost function can be derived from equation A.10:

$$J(n) = E\{(y[n] - 2\alpha[n+1]y[n-1] + y[n-2])^2\} \quad (\text{A.12})$$

The optimal value of the adaptive parameter α can be found by setting to zero the derivative of this cost function, with respect to $\alpha[n+1]$. This leads to the following expression for $\alpha[n+1]$:

$$\alpha[n+1] = \frac{E\{y[n-1](y[n] + y[n-2])\}}{2E\{(y[n-1])^2\}} \quad (\text{A.13})$$

which can be recursively estimated in practice using an exponentially weighted time-average:

$$\alpha[n+1] = \frac{Q[n]}{2P[n]} \quad (\text{A.14})$$

with

$$\begin{aligned} Q[n] &= \delta Q[n-1] + (1-\delta)y[n-1](y[n] + y[n-2]) \\ P[n] &= \delta P[n-1] + (1-\delta)(y[n-1])^2 \end{aligned} \quad (\text{A.15})$$

where the convergence rate can be adjusted with a forgetting factor δ . Finally, the instantaneous frequency $\omega[n+1]$ is defined as:

$$\omega[n+1] = \arccos(\alpha[n+1]) \quad (\text{A.16})$$

Figure A.2 shows the amplitude and phase responses of the BP filter described by the transfer function of equation A.9, for different values of the β parameter and for $\alpha = \cos(0.5\pi)$. A value of β closer to one entails a narrower filter.

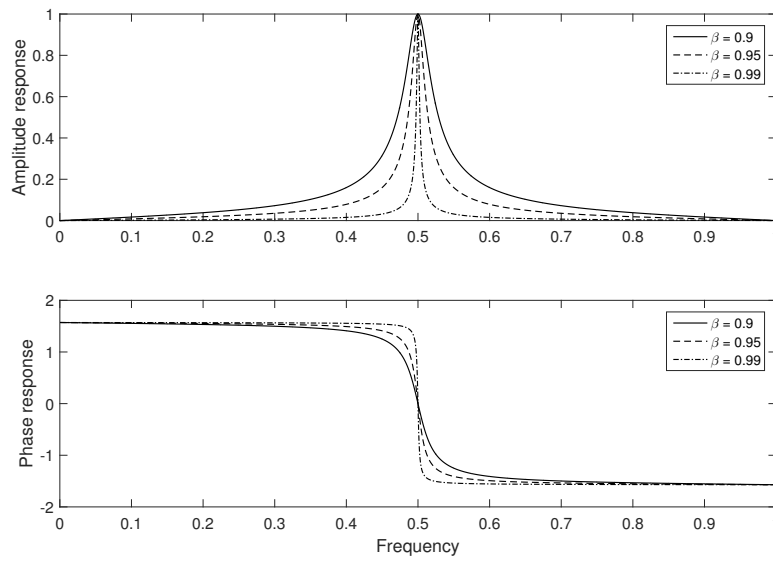


Figure A.2 – Amplitude and phase responses of the BP filter used in the OSC-MSE algorithm (see equation A.9), for different values of β .

Multi-signal Extension (OSC-MSE-W)

The OSC-MSE adaptive frequency tracking scheme has been extended to the multivariate case, in order to track the common frequency component present in M input signals [144, 265]. In this multi-signal extension, referred to as OSC-MSE-W, the same BP filter is used on each signal to compute individual updates and frequency estimates, similarly to the univariate case. Then, the update of the center frequency of the filter is computed as a weighted average of the individual update estimates. The computation of the weights W_m is based on the minimization of the variance of the linear combination of the individual instantaneous frequency estimates. The recursive estimates of the variances of the input signals x_m and output signals y_m ($m=1, \dots, M$) are first computed using the following equations

$$\begin{aligned} S_{y_m}[n] &= \mu S_{y_m}[n-1] + (1-\mu)(y_m[n] - 2\alpha[n]y_m[n-1] + y_m[n-2])^2 \\ S_{x_m}[n] &= \mu S_{x_m}[n-1] + (1-\mu)x_m[n]^2 \end{aligned} \quad (\text{A.17})$$

with μ , a forgetting factor. The computation of the weights is given by

$$W_m[n] = \frac{S_{xm}[n]/S_{ym}[n]}{\sum_{i=1}^M S_{xi}[n]/S_{yi}[n]} \quad (\text{A.18})$$

Finally, the global instantaneous frequency estimate is defined as

$$\omega_{global}[n] = \sum_{m=1}^M W_m[n]\alpha_m[n] \quad (\text{A.19})$$

with $\alpha_m[n]$ ($m=1, \dots, M$), the individual frequency estimates. The scheme in Figure A.3 shows the configuration of the multi-signal adaptive frequency tracker.

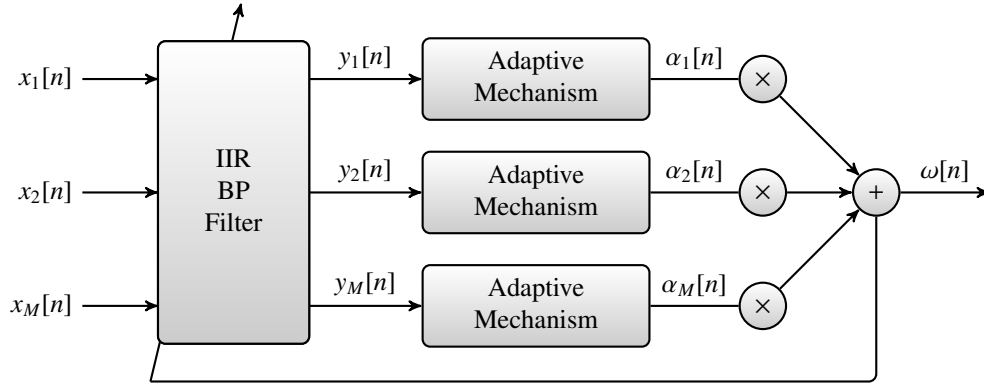


Figure A.3 – Configuration of the multi-signal adaptive frequency tracker (OSC-MSE-W).

A.2.2 OSC-MSEc Algorithm

This algorithm, previously described in [145, 265], was derived from the discrete oscillator based adaptive notch filter proposed by Liao [143]. In this case, the input signals is defined as:

$$x[n] = c[n] + v[n] \quad (\text{A.20})$$

with $c[n] = A_0 e^{j\omega_0 n}$ a cisoid, with A_0 and ω_0 its complex amplitude and frequency, and $v[n]$, an additive centered complex noise. The transfer function of the time-varying single pole BP filter used in this algorithm is expressed as follows:

$$G(z; n) = \frac{1 - \beta}{1 - \beta e^{j\omega[n]} z^{-1}} \quad (\text{A.21})$$

with $\omega(n)$, the normalized instantaneous frequency estimate and β ($0 \ll \beta < 1$), a factor related to the bandwidth of the filter. The adaptive mechanism used to update the central frequency of the BP filter described in equation A.21 requires at each time step the minimization of a cost function, which is derived from the complex oscillator equation:

$$c[n] = e^{j\omega_0} c[n - 1] \quad (\text{A.22})$$

By considering an input signal consisting of a complex sinusoid corrupted by a complex interference, from (A.22), the output signal $y[n]$ can be written as:

$$y[n] = \theta[n]y[n - 1] + \epsilon[n] \quad (\text{A.23})$$

with $\epsilon[n]$, the error term and $\theta[n] = e^{j\omega[n]}$. A minimization of the MSE leads to the following expression for $\theta[n]$:

$$\theta[n] = \frac{E[y[n]\bar{y}[n-1]]}{E[|y[n-1]|^2]} \quad (\text{A.24})$$

which in practice can be recursively estimated as:

$$\hat{\theta}[n] = \frac{Q[n]}{P[n]} = \frac{\delta Q[n-1] + (1-\delta)y[n]\bar{y}[n-1]}{\delta P[n-1] + (1-\delta)|y[n-1]|^2} \quad (\text{A.25})$$

where the convergence rate can be adjusted with a forgetting factor δ , ($0 \ll \delta < 1$). Finally, the instantaneous frequency estimate $\omega(n)$ is defined as:

$$\omega[n] = \arg\left(\frac{\hat{\theta}[n]}{|\hat{\theta}[n]|}\right) \quad (\text{A.26})$$

Figure A.4 shows the amplitude and phase response of the BP filter of the OSC-MSEc algorithm, for different values of β . It should be mentioned that, in practice, most of the signals are real-valued. In that case, the analytic representation of the signal, computed with the discrete Hilbert transform, is provided as input to the OSC-MSEc algorithm.

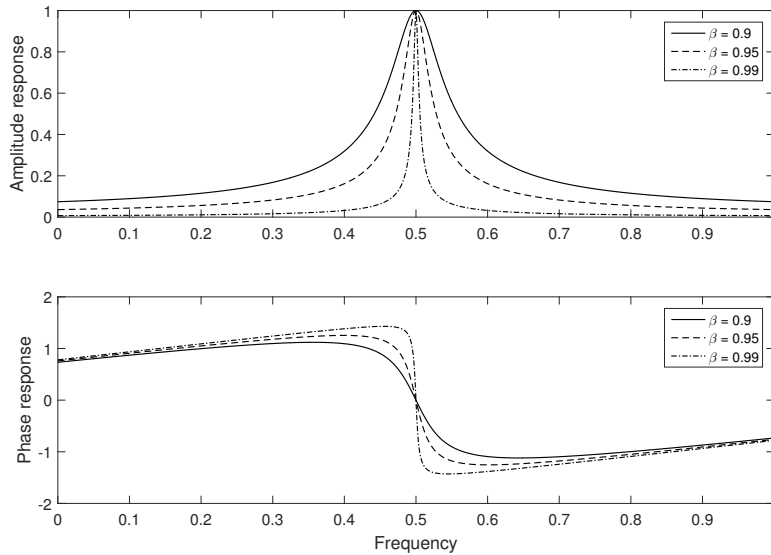


Figure A.4 – Amplitude and phase response of the BP filter of the OSC-MSEc algorithm, for different values of β .

Multi-signal Extension (OSC-MSEc-W)

Similarly to the OSC-MSE algorithm, the OSC-MSEc algorithm has been extended to the multivariate case in order to track the common frequency component present in M input signals [144, 265]. In this multi-signal extension, referred to as OSC-MSEc-W, the same BP filter is applied to each signal to compute individual updates and frequency estimates, similarly to the univariate case. Then, the update of the filter central frequency is computed as a weighted average of the individual update estimates. The computation of the weights W_m is based on the minimization of the variance of the linear combination of the individual instantaneous frequency

estimates. The recursive estimates of the variances of inputs signals x_m and output signals y_m ($m=1,\dots,M$) are first computed using through:

$$\begin{aligned} S_{y_m}[n] &= \delta S_{y_m}[n-1] + (1-\delta)|y_m[n]|^2 \\ S_{x_m}[n] &= \delta S_{x_m}[n-1] + (1-\delta)|x_m[n]|^2 \end{aligned} \quad (\text{A.27})$$

The weights are computed as:

$$W_m[n] = \frac{S_{x_m}[n]/S_{y_m}[n]}{\sum_{i=1}^M S_{x_i}[n]/S_{y_i}[n]} \quad (\text{A.28})$$

Finally, the global instantaneous frequency estimate is defined as:

$$\omega[n] = \sum_{m=1}^M W_m[n]\omega_m[n] \quad (\text{A.29})$$

Classifier Evaluation and Ensemble of Classifiers

B

B.1 Evaluation of Classifiers

Machine learning is the study of models that can learn from input instances (known as training data), and subsequently make prediction on unseen instances (known as testing or prediction data). Having built a prediction model, commonly referred to as classifier, one can evaluate its performance by comparing classifier predictions with the actual testing data. In a two-class (known as binary) problem, the training data is divided into positive and negative classes. The positive class usually represents the instances for which the model is being created. For instance, in an HIV test, instances representing the HIV class are considered as members of the positive class whereas all other instances are considered as members of the negative class. Based on the predictions made by the classifier, instances can belong to one of the following categories:

- **True Positive (TP):** Instances that belong to the positive class and classified as such.
- **False Positive (FP);** known as the type I error, represent instances that belong to the positive class but classified as a member of the negative class.
- **True Negative (TN):** Instances that belong to the negative class and classified as such.
- **False Negative (FN);** known as the type II error, represent instances that belong to the negative class but classified as a member of the positive class.

A confusion matrix (also known as the contingency table) is usually used to visualize of the performance of a specific classifier, as illustrated in Table B.1.

Table B.1 – Confusion matrix of hypothetical model trained for a binary classification problem.

		Actual Class	
		+	-
Predicted Class	+	True Positive	False Positive Type I Error
	-	False Negative Type II Error	True negative

By closely studying the TP, FP, TN, and FN, one can evaluate the performance of a trained model. Over the years, several conventional metrics have been used in the literature, the most common ones are reviewed next.

- **Sensitivity (Se)**, also known as recall and the true positive rate (TPR), represents the number of instances that were classified as positive, which were indeed members of the positive class. In other words, this measure can be interpreted as the probability of a test to be positive given that the sample belong to the positive class. Se can therefore be calculated as,

$$\text{Sensitivity (Se)} = \frac{TP}{TP + FN} \quad (\text{B.1})$$

- **Specificity (SPC)**, also known as the true negative rate (TNR), is the proportion of instances that belong to the negative class and are classified as such. SPC calculates the same measure as Se, but for the negative class. SPC is calculated through,

$$\text{Specificity (SPC)} = \frac{TN}{TN + FP} \quad (\text{B.2})$$

- **Positive Prediction Value (PPV)**, also known as precision, studies how reliable the classifier is, in case the prediction is positive for an input sample. PPV is obtained as,

$$\text{Positive Prediction Value (PPV)} = \frac{TP}{TP + FP} \quad (\text{B.3})$$

- **Negative Prediction Value (NPV)** studies how reliable the classifier is, in case the prediction is negative for an input sample. NPV is obtained as follows:

$$\text{Negative Prediction Value (NPV)} = \frac{TN}{TN + FN} \quad (\text{B.4})$$

- **Accuracy (ACC)** is the fraction of test samples that are correctly predicted. ACC is measured as,

$$\text{Accuracy (ACC)} = \frac{TP + TN}{TP + FP + TN + FN} \quad (\text{B.5})$$

- **Detection Error Rate (DER)** represents the fraction of test samples that are incorrectly predicted. DER is defined as,

$$\text{Detection Error Rate (DER)} = 1 - \text{ACC} = \frac{FP + FN}{TP + FP + TN + FN} \quad (\text{B.6})$$

ACC and DER are simple statistics that report the overall performance of the trained classifier. Although these measures are intuitive and easy to calculate, they cannot provide reliable evaluation of the trained model in case the training data is unbalanced, i.e. one class has significantly more samples compared to the other. Let us assume a hypothetical machine learning scenario for which 95% of the dataset is comprised of the positive class (5% negative). If the trained model classifies all input instances as members of the positive class, the final accuracy of the model is 0.95 (DER is 0.05). Therefore, one needs to study Se and PPV alongside ACC in order to perform a good performance evaluation. Alternatively, one can use the F-score (also known as F-measure), which evaluates the classifier by studying Se and PPV. F-score is calculated through,

$$F_\beta = (1 + \beta^2) \frac{PPV \cdot Se}{(\beta^2 \cdot PPV) + Se} \quad (\text{B.7})$$

where β is the parameter that determines the relative weights of Se and PPV. It is common to compute the F-score with $\beta = 1$, which represents the balanced F-score. This harmonic mean between Se and PPV is known as the F1-score,

$$F_1 = 2 \frac{PPV \cdot Se}{PPV + Se} \quad (\text{B.8})$$

Over the years, several other metrics such as the Phi and Matthews correlation coefficients have been proposed in the literature in order to take other important factors such as the true negative rate into consideration. Further information on these metrics can be found in [268, 269]. In the context of this dissertation, only two-class machine learning techniques are studied, methods described in this appendix covers binary classification evaluation. More information on multi-class performance evaluation can be found in [269, 270].

B.2 Classifier Combination: Selection and Fusion

Over the pas decades, the idea of training multiple classifiers and combining them to obtain the desired output has gained momentum. Multi expert (classifier) techniques can be categorized into two sub-branches, namely selection and fusion. Consider a hypothetical problem in which some classifiers outperform others at specific tasks, but their overall performance does not. For instance, imagine a classification problem in which the goal is to identify cats and dogs, and that we have created two classifiers, C_1 and C_2 , from the training set. Assume that C_1 outperforms C_2 but does not perform well for small-sized cats and dogs. On the other hand, C_2 perfectly separates small cats and dogs but does poorly otherwise. In this case when C_2 is used for small-sized inputs while C_1 is used otherwise, the overall prediction performance improves. In this way the classification task is broken into two subspaces, where C_1 performs better in one while C_2 in the other. This combination technique is referred to as classification selection. Figure B.1 illustrates an example fusion technique with four classifiers.

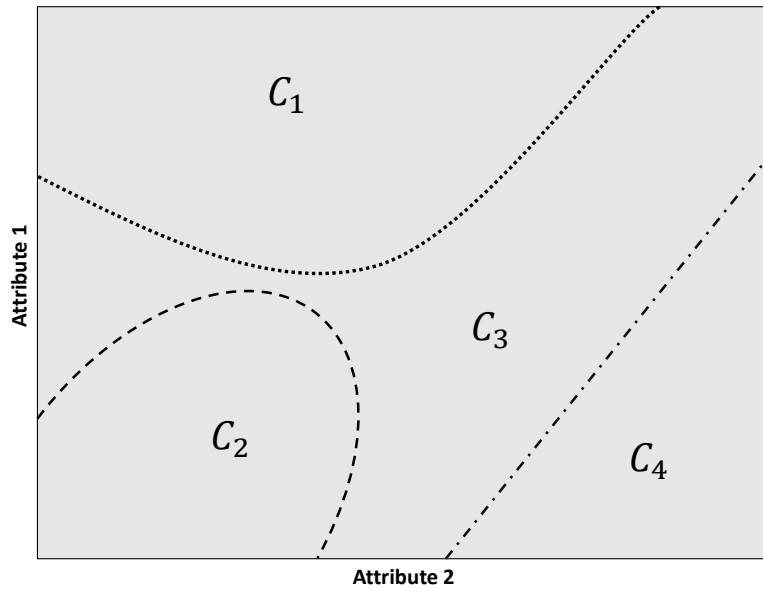


Figure B.1 – An example classifier selection technique illustrated in a two attribute subspace. All four classifiers (C_1, C_2, C_3 , and C_n) work in coherence, each acting as the expert in its respective subspace.

Another technique to combine classifiers is through classifier fusion. In this scheme, n classifiers with low bias and high variance are created separately on the training set and their respective predictions are combined to obtain the final prediction [269]. Figure B.2 illustrates the framework used to create typical fusion of classifiers.

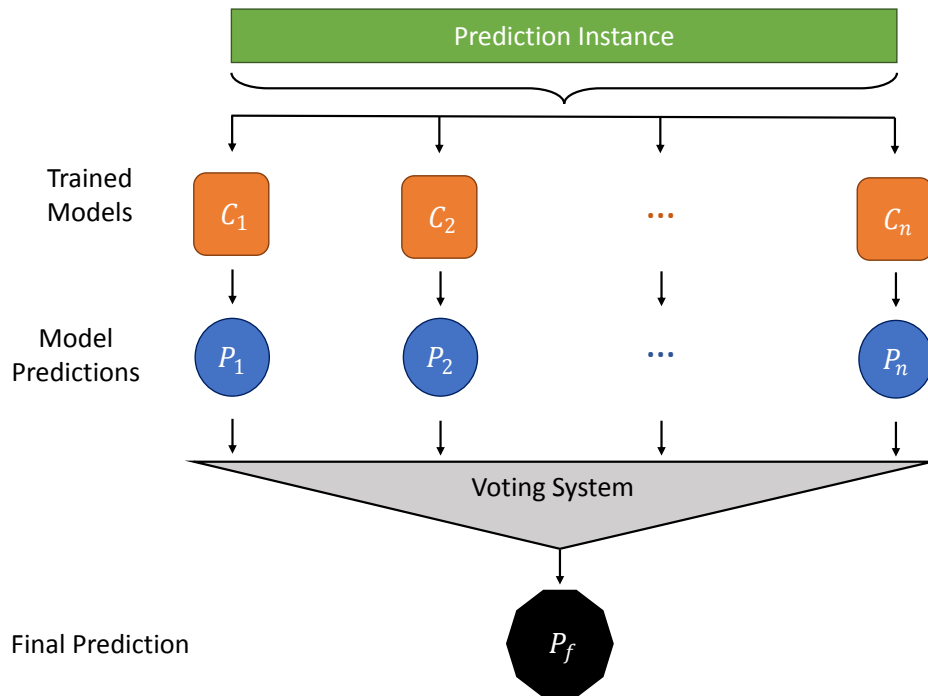


Figure B.2 – Typical framework of classifier fusion. In order to obtain the final prediction (P_f) for an input instance, the predicted label (P_1, P_2, \dots, P_n) for each trained classifiers (C_1, C_2, \dots, C_n) taken into account.

Various voting techniques can be used in classifier fusion, details of which are described as follows.

- **Majority Voting** is the simplest yet most common voting scheme. As suggested by its name, the prediction label in this scheme is selected as the label that has been predicted by majority of the trained classifiers, i.e statistical mode of the prediction labels.
- **Weighted Majority Voting** works similarly to majority voting, however the predictions made by classifiers are weighted, with some classifiers (the better performing and more complex ones) having greater influence in label prediction.
- **Optimistic Voting.** In this scheme the final prediction label is considered as positive, if at least one of the trained classifiers prediction is as such.
- **Pessimistic Voting**, also known as unanimous voting, is an scheme in which the final prediction label is considered as positive, if the trained classifiers unanimously predict as such.

B.3 The Wisdom of Crowds

The wisdom of crowds [271, 272] is a theory suggesting that given the right conditions, large groups of average people are smarter than a few elite experts. There are four necessary conditions for a crowd to be considered as wise. First, the rule of independence, which states people's opinion should not be influenced by others. Second, the rule of decentralization, stating people should be able to draw their opinion based on their expertise. Third, the diversity of opinion, meaning people should have some information on the problem. Finally, the aggregation rule, which is a scheme to combine the crowd's opinion to obtain a final decision.

Implementation of the wisdom of crowds in machine learning is somewhat difficult, even though the aggregation and independence rules are naturally implemented when combining classifiers. Decentralization is also not hard to implement. This rule states that members of an ensemble of classifiers should perform prediction based on different specialties (expertise). Although meta algorithms such as bagging, boosting, rotation forest, and etc. can have numerous base classifiers, in their implementation all base classifiers are essentially the same and are only exposed to different training data [269]. Nevertheless, in machine learning, decentralization can be carried out by training predictors of different natures, for instance a support vector machine, a decision tree, along side a multi-layer perceptron neural network. Furthermore, if accurate enough classifiers are created, one does not need numerous models to reach reliable predictions. The difficulty in the implementation of wisdom of crowd lies in the diversity of opinion. When creating classifiers, several attributes (features) are extracted from the training data. for the diversity rule to carry out, classifiers need to be trained on different features which in practice does not make sense as they can improve the performance of other train classifiers. Moreover, often features can be unintuitive to extract and therefore, are defined by the expert in the field of the study.

The implementation of wisdom of crowds, however, is not impossible. As pointed out Section 4.4, during the false alarm detection Physionet/CinC challenge, the organizers took the top performing algorithms and created a meta-algorithm, which obtained an accuracy higher than that of any individual algorithm. The diversity of opinion rule was perfectly met as different challengers used different features to train their classifiers. This can be considered as an example implementation of wisdom of crowds, as all four rules were applied.

Further Results on Instantaneous Signal Quality Index

C

This appendix reports more detailed results on the correlation between the calculated instantaneous signal quality index and the instantaneous signal-to-noise ratio reported in Chapter 6, Table 6.4.

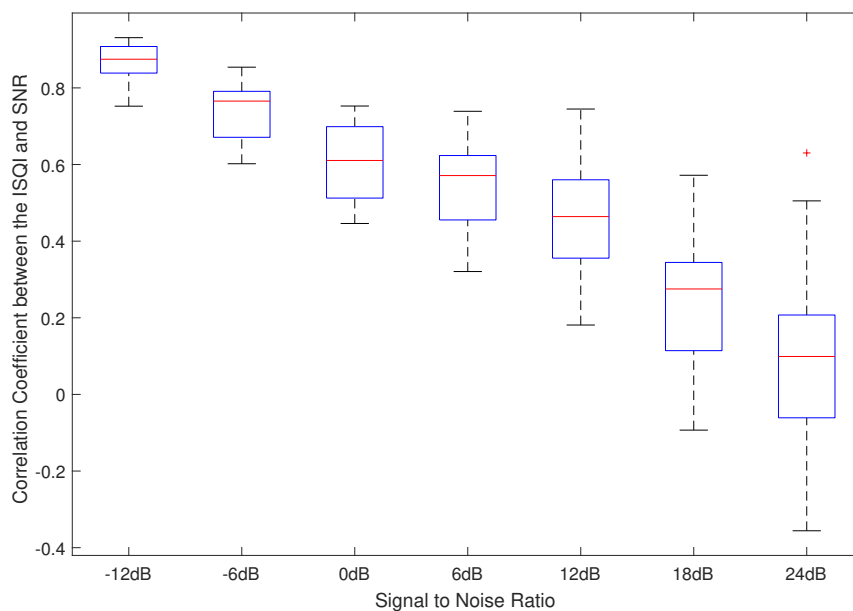


Figure C.1 – The correlation coefficient between instantaneous signal quality index and instantaneous signal-to-noise ratio. Tested against baseline wander.

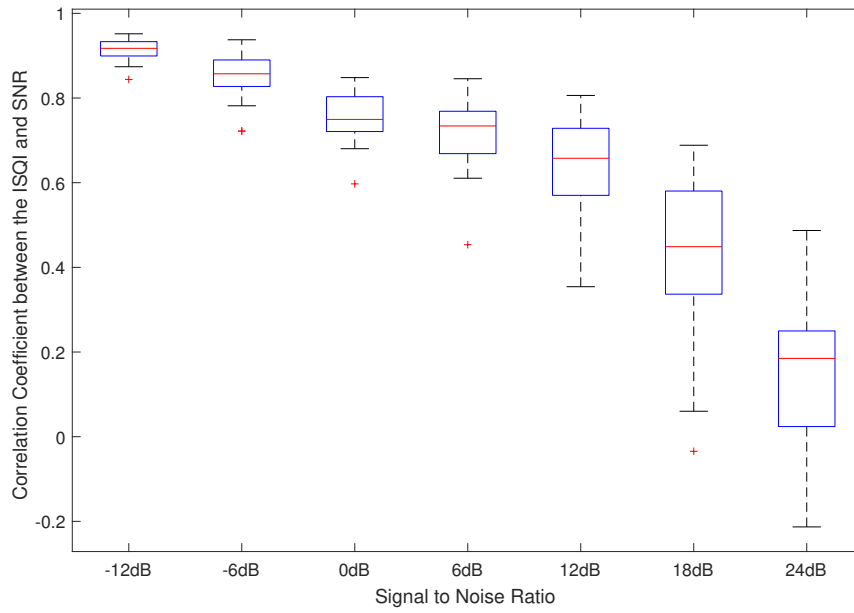


Figure C.2 – The correlation coefficient between instantaneous signal quality index and instantaneous signal-to-noise ratio. Tested against EMG noise.

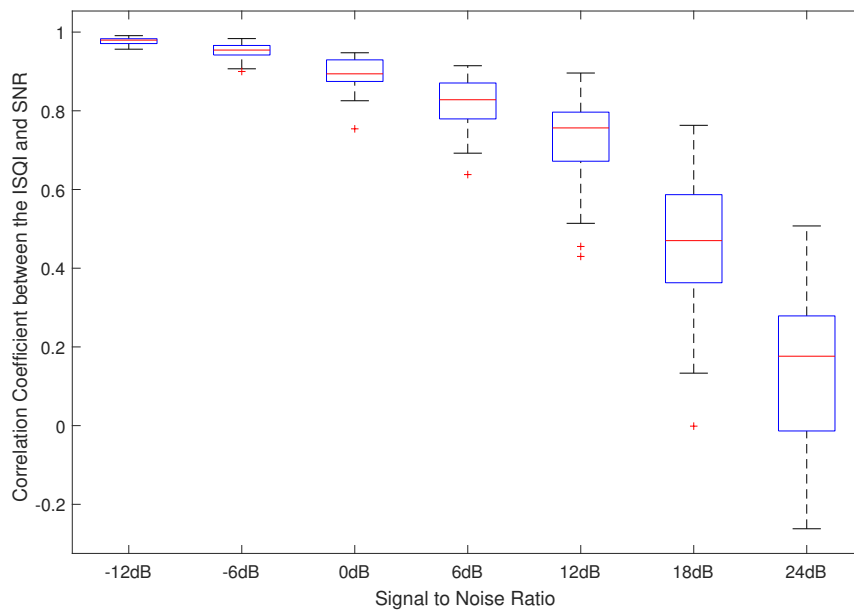


Figure C.3 – The correlation coefficient between instantaneous signal quality index and instantaneous signal-to-noise ratio. Tested against electrode motion artifact.

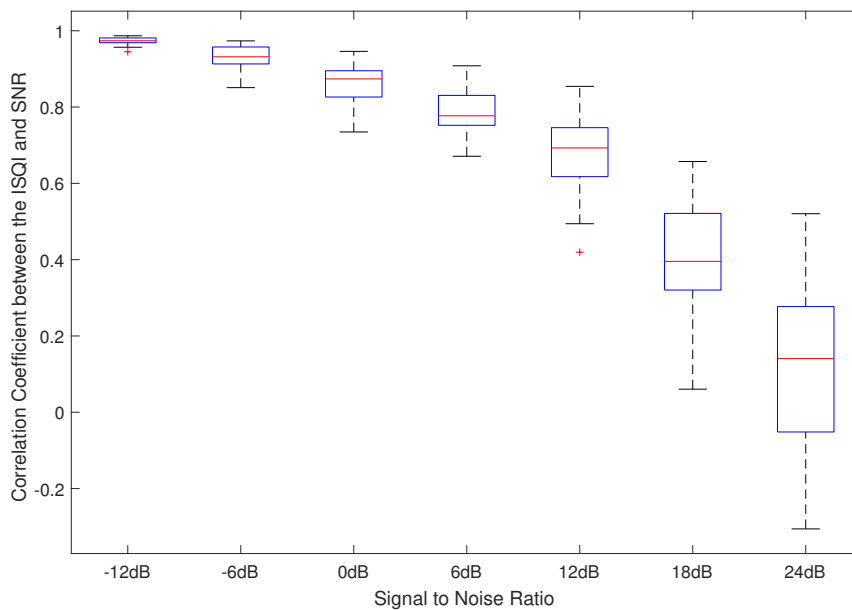


Figure C.4 – The correlation coefficient between instantaneous signal quality index and instantaneous signal-to-noise ratio. Tested against baseline wander + electrode motion artifact.

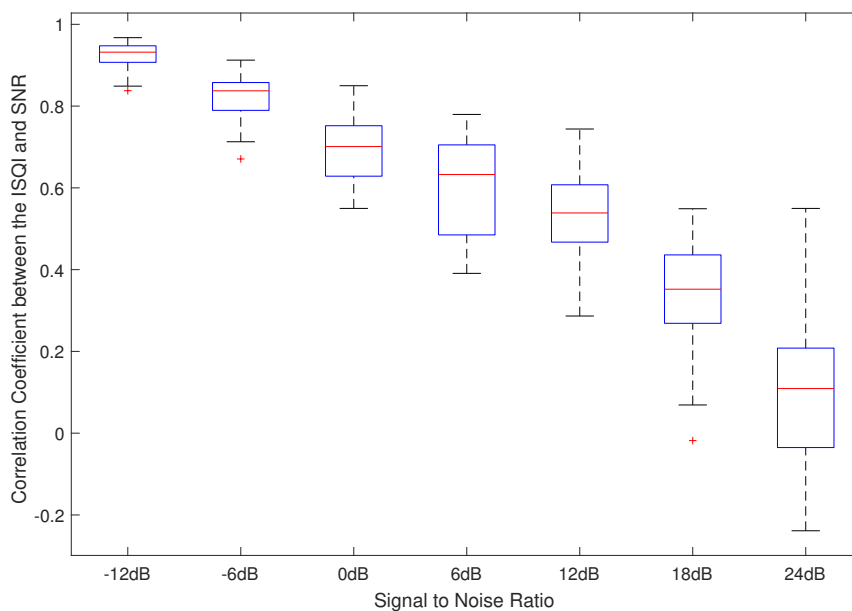


Figure C.5 – The correlation coefficient between instantaneous signal quality index and instantaneous signal-to-noise ratio. Tested against baseline wander + EMG noise.

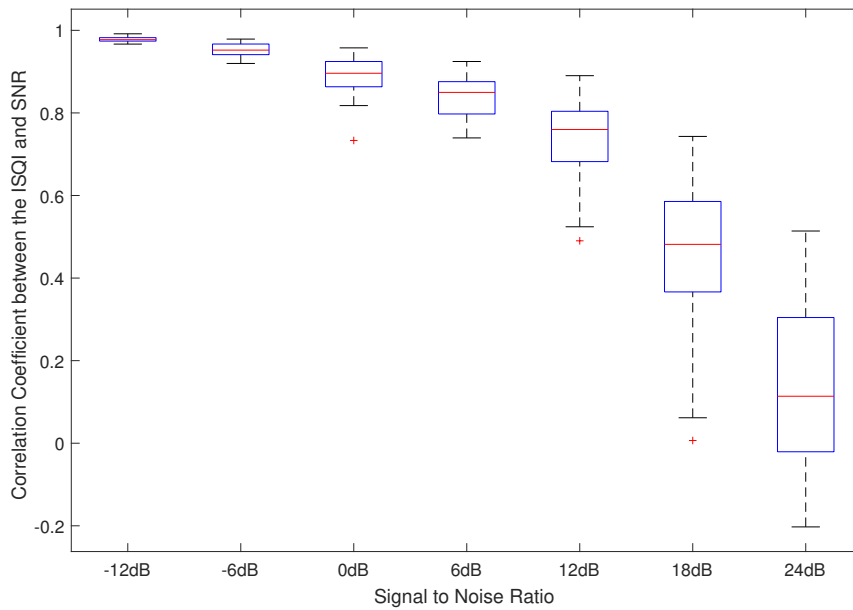


Figure C.6 – The correlation coefficient between instantaneous signal quality index and instantaneous signal-to-noise ratio. Tested against EMG noise + electrode motion artifact.

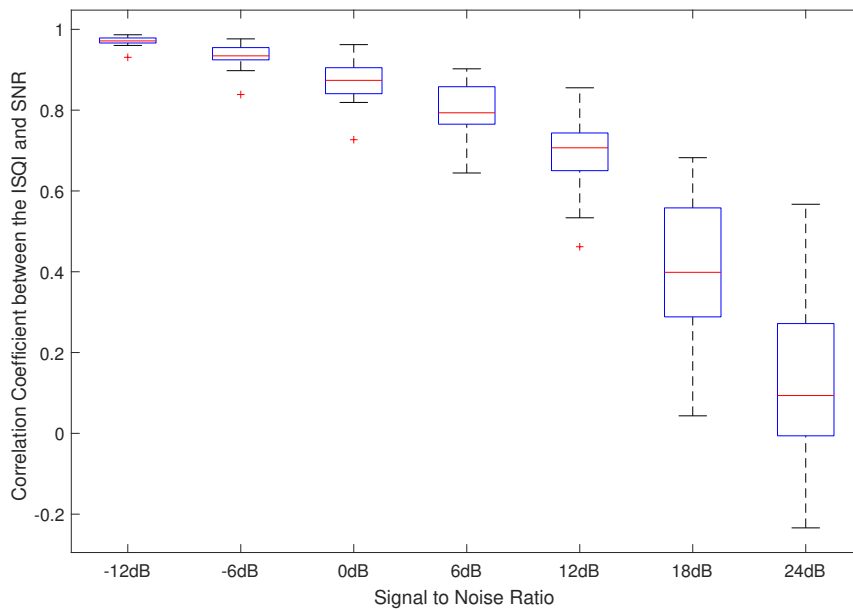
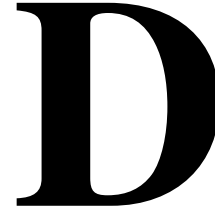


Figure C.7 – The correlation coefficient between instantaneous signal quality index and instantaneous signal-to-noise ratio. Tested against baseline wander + EMG noise + electrode motion artifact.

Further Results on U-patterns



D.1 Statistical Characteristics of U-patterns

D.1.1 The Over-training Study

Subject	1	2	3	4	5	6	7	8	9	10	11	12	13	14	15
Baseline	1.27	1.21	1.27	1.16	1.34	0.69	0.97	1.07	1.62	1.21	1.05	2.97	0.8	1.15	0.81
Over-training	1.42	1.04	1.29	1.0	1.14	1.01	0.97	0.87	1.89	1.1	1.2	1.89	1.06	1.22	0.93
Recovery	1.31	1.46	1.35	0.97	1.25	0.9	1.08	0.88	1.49	1.24	1.25	1.08	0.74	1.15	1.43

Table D.1 – Frequency (in mHz) of the detected U-patterns for each subject and for different over-training phases. The frequency was computed as the ratio of the number of U-patterns by the total duration of the RR-intervals.

Subject	1	2	3	4	5	6	7	8	9	10	11	12	13	14	15
Baseline	22.8	20.1	21.7	21.7	22.2	22.5	20.6	23.7	27.8	24.8	26.7	25.8	24.7	22.4	21.0
Over-training	24.9	20.6	21.7	21.0	22.4	22.8	22.5	24.3	24.7	23.3	23.9	26.3	22.6	22.5	21.3
Recovery	22.9	21.0	21.7	21.8	22.9	22.5	21.4	25.4	25.0	23.6	23.4	27.0	27.4	20.9	24.0

Table D.2 – Mean duration (in s) of the detected U-patterns for each subject and for different over-training phases.

Subject	1	2	3	4	5	6	7	8	9	10	11	12	13	14	15
Baseline	619	723	619	515	587	411	604	471	333	351	459	266	525	683	456
Over-training	534	645	727	462	629	364	540	513	392	408	565	308	566	696	526
Recovery	645	625	723	412	591	377	537	529	417	389	567	346	516	799	467

Table D.3 – Mean depth (in ms) of the detected U-patterns for each subject and for different over-training phases.

Subject	1	2	3	4	5	6	7	8	9	10	11	12	13	14	15
Baseline	2166	1668	3064	4126	7885	1644	1351	2202	3441	2257	2791	2336	2321	5170	1392
Over-training	3686	2138	4019	3704	2405	1944	3059	2672	4190	2497	3129	3143	2543	5214	3122
Recovery	2899	2830	3155	2730	516	1090	1251	3002	3941	2303	1890	2707	2984	5619	4100

Table D.4 – Mean integral (in ms.s) of the detected U-patterns for each subject and for different over-training phases.

D.1.2 The Sleep Deprivation Study

Subject	1	2	3	4	5	6	7	8	9	10	11	12	13	14	15
Baseline	1.2	1.79	1.46	1.42	0.84	1.6	2.0	1.53	0.63	1.12	0.78	1.56	1.98	1.23	1.82
Sleep deprivation	0.63	1.49	1.94	0.97	0.67	0.93	1.19	1.6	0.9	1.16	0.79	0.93	2.2	0.93	0.82
Sleep recovery	1.04	1.66	1.37	1.31	1.01	1.03	0.75	1.76	0.88	1.49	0.82	1.22	2.09	1.54	1.86

Table D.5 – Frequency (in mHz) of the detected U-patterns for each subject and for different sleep deprivation phases. The frequency was computed as the ratio of the number of U-patterns by the total duration of the RR-intervals.

Subject	1	2	3	4	5	6	7	8	9	10	11	12	13	14	15
Baseline	30.0	27.7	26.8	29.3	34.9	26.6	27.6	25.0	33.7	34.1	31.9	27.6	26.9	27.6	25.9
Sleep deprivation	28.9	26.6	26.5	29.8	32.4	26.9	25.6	25.3	30.7	30.3	32.5	28.3	25.5	28.5	28.2
Sleep recovery	30.7	26.5	26.3	28.9	27.1	27.9	27.6	25.7	30.5	30.1	31.6	25.4	24.1	31.6	26.3

Table D.6 – Mean duration (in s) of the detected U-patterns for each subject and for different sleep deprivation phases.

Subject	1	2	3	4	5	6	7	8	9	10	11	12	13	14	15
Baseline	284	279	279	266	273	273	257	616	188	220	203	330	255	306	358
Sleep deprivation	245	274	266	242	283	252	230	380	231	234	226	330	233	284	324
Sleep recovery	208	289	258	246	240	266	281	443	225	306	246	268	287	326	373

Table D.7 – Mean depth (in ms) of the detected U-patterns for each subject and for different sleep deprivation phases.

Subject	1	2	3	4	5	6	7	8	9	10	11	12	13	14	15
Baseline	8963	8024	7807	8124	9698	7451	7178	16034	6362	7693	6605	9569	7087	8634	9784
Sleep deprivation	7536	7644	7335	7457	9407	6884	6072	9990	7214	7162	7637	9577	6124	8547	9591
Sleep recovery	6598	7955	6981	7248	6586	7714	7849	11825	7175	9567	8033	7169	7227	10937	10306

Table D.8 – Mean integral (in ms.s) of the detected U-patterns for each subject and for the different sleep deprivation phases.

D.2 Agreement Rate

Subject	1	2	3	4	5	6	7	8	9	10	11	12	13	14	15	mean ± std
3-EMG	35.7	31.1	21.4	39.3	34.6	34.0	25.4	7.5	3.2	24.2	28.3	61.7	11.9	21.2	22.6	26.8 ± 14.2
ChinC	28.6	30.8	17.2	40.0	30.8	33.3	25.0	6.7	3.2	21.8	28.6	46.5	10.7	19.6	22.2	24.3 ± 11.8
ChinL	30.6	35.4	13.2	25.9	22.6	50.0	14.5	8.1	N/A	28.6	26.2	47.8	24.6	12.8	19.1	24.0 ± 13.7
ChinR	46.5	30.6	26.2	21.6	8.5	36.2	13.1	18.9	3.3	19.5	31.8	58.3	22.9	12.8	17.4	24.5 ± 14.5
Thorax	57.1	47.2	40.4	N/A	48.0	59.1	35.4	58.1	20.9	35.7	39.6	58.3	33.3	32.8	33.3	39.9 ± 16.0
F3	35.9	24.4	5.0	5.9	23.8	52.9	12.0	38.5	13.3	17.6	31.6	42.9	8.2	17.5	9.1	22.6 ± 14.8
F4	27.0	19.6	14.3	4.3	23.6	31.9	13.2	23.1	12.1	28.1	24.4	45.7	N/A	13.0	14.0	19.6 ± 11.4
C3	34.9	20.0	7.3	11.4	18.2	48.9	31.6	17.9	17.8	30.0	25.7	51.1	6.1	26.2	23.4	24.7 ± 13.2
C4	41.7	27.1	27.3	15.9	10.0	40.4	19.6	40.0	15.8	41.0	21.2	38.6	3.8	8.9	22.0	24.9 ± 12.9
O1	22.5	22.6	18.6	31.4	30.8	55.6	42.2	45.2	18.8	30.2	20.4	61.9	9.5	23.4	37.3	31.4 ± 14.6
O2	40.0	25.9	23.4	30.2	30.8	2.6	37.5	45.5	16.7	32.1	29.1	55.8	8.4	18.5	27.6	28.3 ± 13.7
E1	41.5	25.0	5.9	10.9	14.8	27.1	5.9	10.3	3.4	19.4	30.2	47.6	11.1	21.7	12.2	19.1 ± 13.1
E2	25.0	28.6	9.3	10.2	N/A	27.1	11.1	10.9	4.2	30.6	31.3	41.5	3.9	12.2	12.5	17.2 ± 12.3

Table D.9 – Agreement rates (in %) between U-patterns and the extracted movement events during the baseline phase. Bold fields represent maximum agreement rate across available channels. N/A fields denote channels that were discarded due to problems.

Subject	1	2	3	4	5	6	7	8	9	10	11	12	13	14	15	mean ± std
3-EMG	43.3	11.1	16.7	38.8	16.0	32.5	14.9	14.7	24.4	33.9	40.0	52.6	6.1	18.4	30.6	26.3 ± 13.6
ChinC	26.9	8.7	14.9	17.9	17.9	24.2	11.8	16.1	5.4	32.7	17.9	43.9	7.5	18.4	29.4	19.6 ± 10.4
ChinL	45.8	15.9	14.9	42.9	19.0	31.7	11.9	12.3	36.4	39.5	34.8	52.9	3.3	6.3	19.4	25.8 ± 15.6
ChinR	41.4	11.6	12.1	41.3	36.7	30.3	6.5	5.2	19.4	30.2	34.8	50.0	9.7	8.2	25.6	24.2 ± 14.8
Thorax	34.5	53.2	26.2	58.1	58.3	61.3	24.1	33.3	33.3	34.7	54.5	19.2	31.2	15.4	38.2	38.4 ± 15.0
F3	14.3	9.3	5.4	10.7	25.9	41.0	24.1	10.3	23.3	16.7	13.0	62.5	N/A	10.5	16.7	18.9 ± 15.6
F4	14.8	9.3	8.9	15.6	8.7	23.7	9.8	10.3	23.8	21.1	30.4	42.4	3.0	9.7	17.2	16.6 ± 10.3
C3	21.7	11.6	10.5	26.5	15.4	45.0	18.2	15.5	10.3	9.8	26.9	44.4	1.1	10.0	16.1	18.9 ± 12.4
C4	25.0	11.9	9.1	37.1	18.5	40.0	8.7	13.8	28.8	29.7	39.1	45.9	4.4	3.0	18.5	22.2 ± 14.0
O1	30.8	17.4	10.3	47.4	29.6	42.4	25.0	24.6	27.8	32.6	42.9	51.4	6.1	9.1	35.3	28.8 ± 13.9
O2	33.3	19.0	19.4	50.0	19.0	48.7	19.2	22.8	32.6	46.0	50.0	45.0	19.7	13.2	48.3	32.4 ± 14.2
E1	12.0	9.3	5.8	23.3	31.6	36.4	16.7	10.2	22.5	22.9	21.7	45.9	7.1	6.5	18.5	19.4 ± 11.8
E2	16.7	11.1	9.4	27.3	12.5	41.2	14.9	10.2	21.2	32.6	43.5	29.4	9.2	6.3	22.0	20.5 ± 11.9

Table D.10 – Agreement rates (in %) between U-patterns and the extracted movement events during sleep-deprivation. Bold fields represent maximum agreement rate across available channels. N/A fields denote channels that were discarded due to problems.

Subject	1	2	3	4	5	6	7	8	9	10	11	12	13	14	15	mean ± std
3-EMG	38.1	50.0	16.4	38.2	18.8	50.0	30.0	37.7	7.5	12.2	34.3	33.3	15.6	20.5	20.8	28.2 ± 13.3
ChinC	23.8	46.2	15.3	27.8	20.4	29.0	23.1	26.0	12.5	13.7	19.2	30.0	17.2	19.6	23.5	23.2 ± 8.4
ChinL	44.7	36.8	20.0	34.0	14.0	53.6	25.0	24.5	6.1	14.0	39.4	25.0	3.1	15.0	22.9	25.2 ± 14.2
ChinR	39.5	47.4	13.0	46.9	16.7	33.3	26.7	50.0	18.9	14.0	28.0	38.5	3.2	9.8	19.6	27.0 ± 14.9
Thorax	57.1	47.6	31.1	44.2	40.5	55.2	46.7	59.6	31.9	42.9	37.5	45.0	36.5	35.4	34.0	43.0 ± 9.0
F3	31.6	4.8	15.0	22.2	12.5	27.6	37.0	21.2	10.7	23.3	15.4	23.5	7.5	11.4	24.5	19.2 ± 9.1
F4	34.3	4.3	11.9	7.7	14.3	21.4	16.0	11.3	11.5	31.9	14.8	17.6	N/A	20.0	3.8	14.7 ± 9.6
C3	36.8	9.1	12.5	34.1	14.0	46.7	25.0	39.2	12.9	18.8	40.6	22.2	7.6	22.0	32.7	24.9 ± 12.6
C4	32.5	20.0	14.3	29.8	17.1	32.1	20.7	16.0	17.2	22.2	25.0	23.5	3.0	36.2	46.2	23.7 ± 10.5
O1	34.1	35.0	16.3	41.7	20.5	50.0	29.6	35.8	40.6	28.8	50.0	35.0	8.8	29.2	32.7	32.5 ± 11.3
O2	34.1	43.5	17.0	33.3	24.4	50.0	29.0	29.4	32.3	31.9	43.6	33.3	24.1	37.8	27.5	32.7 ± 8.5
E1	22.2	14.3	18.6	19.5	11.9	22.6	27.3	18.0	3.7	19.3	39.3	22.2	3.3	16.7	18.2	18.5 ± 8.7
E2	33.3	31.8	11.9	16.3	16.3	34.5	10.3	23.1	25.0	26.5	31.0	28.6	5.0	28.6	20.7	22.9 ± 9.1

Table D.11 – Agreement rates (in %) between U-patterns and the extracted movement events during recovery. Bold fields represent maximum agreement rate across available channels. N/A fields denote channels that were discarded due to problems.

D.3 Uncorrelated Events

D.3.1 Uncorrelated U-patterns

Sleep Deprivation Study Subject No.	Baseline		Sleep Deprivation		Sleep Recovery	
	No.	Percentage	No.	Percentage	No.	Percentage
Subject 1	1	3.2	3	17.6	7	25.0
Subject 2	5	11.9	12	30.0	3	16.7
Subject 3	14	35.9	29	55.8	17	48.6
Subject 4	10	26.3	2	7.7	2	5.7
Subject 5	1	5.0	1	5.6	4	16.7
Subject 6	2	5.1	1	4.0	0	0
Subject 7	10	20.8	14	43.8	3	15.0
Subject 8	5	14.3	24	55.8	7	15.2
Subject 9	3	17.6	1	4.2	1	4.5
Subject 10	1	4.3	4	12.9	7	17.5
Subject 11	0	0	0	0	0	0
Subject 12	2	5.6	3	12.0	1	8.3
Subject 13	7	14.3	28	47.5	23	41.1
Subject 14	3	9.1	9	36.0	5	13.9
Subject 15	16	37.2	4	18.2	13	29.5
<i>mean ± std</i>	5.2 ± 5.19	13.42 ± 11.68	8.47 ± 9.37	22.37 ± 18.45	6.13 ± 6.69	17.18 ± 13.89

Table D.12 – Uncorrelated U-patterns in the sleep deprivation study, w.r.t all available PSG channels. For each subject, the number and the percentage of uncorrelated U-patterns are reported.

D.3.2 Uncorrelated Movement Events

Subject	1	2	3	4	5	6	7	8	9	10	11	12	13	14	15	<i>mean ± std</i>
3-EMG	59.2	50.0	67.4	45.0	40.0	39.3	44.4	83.3	93.3	72.7	65.8	27.5	58.8	63.3	45.5	57.0 ± 17.8
ChinC	52.0	53.5	66.7	37.5	42.9	41.4	44.4	87.1	93.3	73.3	66.7	25.9	53.8	67.6	47.8	56.9 ± 18.7
ChinL	57.1	26.1	66.7	53.3	61.1	27.3	50.0	40.0	100.0	61.3	65.6	31.3	69.9	54.5	30.8	53.0 ± 19.9
ChinR	39.4	31.8	57.9	54.2	87.1	32.0	77.6	22.2	92.9	69.2	62.2	30.0	64.2	54.5	27.3	53.5 ± 22.5
Thorax	31.4	30.6	43.9	100.0	29.4	21.2	42.5	24.2	74.3	55.9	58.7	30.0	43.6	59.6	23.8	44.6 ± 21.9
F3	36.4	21.4	33.3	81.3	68.8	30.8	25.0	21.1	76.5	64.7	58.6	25.0	70.6	50.0	20.0	45.6 ± 22.5
F4	37.5	30.8	33.3	81.8	73.5	34.8	41.7	30.8	80.0	50.0	66.7	32.3	100.0	68.4	50.0	54.1 ± 22.5
C3	44.4	25.0	40.0	54.5	79.3	25.8	33.3	36.4	77.8	43.8	62.5	28.1	87.2	45.0	26.7	47.3 ± 20.7
C4	25.0	31.6	29.4	46.2	0	38.2	42.1	23.8	77.8	50.0	73.8	32.0	91.2	75.0	38.9	45.0 ± 24.7
O1	52.6	47.8	33.3	44.8	42.9	33.3	35.7	26.9	77.5	60.6	75.0	18.8	84.8	56.0	29.6	48.0 ± 19.7
O2	38.5	46.2	42.1	48.4	42.9	0	27.6	31.0	81.5	64.7	68.0	22.6	87.5	67.7	48.4	47.8 ± 23.2
E1	37.0	33.3	80.0	61.5	63.6	43.5	50.0	50.0	92.3	65.0	62.9	23.1	83.3	56.5	50.0	56.8 ± 19.0
E2	40.0	33.3	50.0	68.8	100.0	40.9	50.0	70.6	87.5	54.2	64.3	22.7	50.0	61.5	73.3	57.8 ± 20.5

Table D.13 – Subject-by-subject percentage of uncorrelated peaks, with respect to the total number of peaks, baseline phase.

Subject	1	2	3	4	5	6	7	8	9	10	11	12	13	14	15	<i>mean ± std</i>
3-EMG	50.0	50.0	69.6	54.8	63.6	53.6	68.2	72.2	63.0	56.8	33.3	39.4	63.6	65.0	57.7	57.4 ± 11.0
ChinC	56.3	60.0	72.9	65.0	66.7	50.0	76.0	66.7	87.5	55.3	61.5	47.1	61.5	65.0	54.5	63.1 ± 10.4
ChinL	38.9	36.4	60.0	47.1	42.9	55.2	66.7	68.2	55.6	41.4	27.3	33.3	50.0	77.8	62.5	50.9 ± 14.4
ChinR	50.0	37.5	46.2	51.3	52.2	44.4	82.4	84.2	53.8	48.0	27.3	34.6	33.3	85.7	64.3	53.0 ± 18.6
Thorax	54.5	24.2	36.0	21.7	30.0	24.0	62.9	11.8	60.0	51.4	41.9	16.7	42.9	71.4	48.0	39.8 ± 18.2
F3	73.3	42.9	57.1	40.0	56.3	46.7	62.9	72.7	72.0	45.5	50.0	25.9	100.0	76.5	77.1	59.9 ± 18.9
F4	71.4	50.0	44.4	54.5	71.4	59.1	69.2	72.7	64.3	46.7	30.0	36.4	80.0	66.7	58.3	58.3 ± 14.5
C3	54.5	37.5	45.5	47.1	66.7	45.5	60.0	64.0	78.9	73.3	46.2	40.7	97.3	62.5	64.3	58.9 ± 16.2
C4	61.1	28.6	37.5	40.9	64.3	41.7	77.8	66.7	65.1	35.3	25.0	41.4	88.6	88.9	50.0	54.2 ± 20.7
O1	52.9	46.7	50.0	40.0	52.9	36.4	52.2	51.7	67.4	46.2	40.0	37.9	63.6	72.7	52.0	50.8 ± 10.6
O2	46.7	20.0	45.5	38.7	42.9	42.4	66.7	53.6	57.6	45.2	31.6	45.5	35.0	72.2	33.3	45.1 ± 13.5
E1	72.7	42.9	0	36.4	14.3	40.0	58.8	73.9	64.0	33.3	37.5	41.4	68.8	75.0	50.0	47.3 ± 22.1
E2	76.0	50.0	16.7	43.8	66.7	39.1	68.2	73.9	56.3	50.0	23.1	47.4	50.0	77.8	67.9	53.8 ± 18.5

Table D.14 – Subject-by-subject percentage of uncorrelated peaks, with respect to the total number of peaks, sleep deprivation phase.

Subject	1	2	3	4	5	6	7	8	9	10	11	12	13	14	15	mean ± std
3-EMG	46.7	38.1	69.0	48.8	72.7	34.8	52.6	51.7	85.7	60.0	52.0	60.0	44.4	47.1	28.6	52.8 ± 14.9
ChinC	58.3	40.0	72.7	55.9	72.2	50.0	50.0	60.8	71.4	61.1	44.4	57.1	42.1	52.6	36.8	55.0 ± 11.5
ChinL	37.0	12.5	38.5	42.9	76.0	25.0	53.3	35.0	84.6	33.3	45.8	66.7	81.8	40.0	26.7	46.6 ± 21.6
ChinR	40.0	10.0	64.7	37.8	72.0	30.8	55.6	26.3	68.2	33.3	30.0	58.3	77.8	55.6	18.2	45.2 ± 20.8
Thorax	25.9	23.1	41.7	29.6	46.4	27.3	41.7	16.2	63.4	41.5	54.5	47.1	23.3	41.4	26.1	36.6 ± 13.3
F3	45.5	75.0	45.5	50.0	76.2	42.9	44.4	35.3	66.7	23.1	50.0	55.6	80.0	64.3	29.4	52.3 ± 17.2
F4	40.0	83.3	61.5	57.1	75.0	45.5	55.6	53.8	57.1	31.8	55.6	62.5	N/A	58.3	81.8	58.5 ± 14.5
C3	41.7	66.7	50.0	37.5	76.0	33.3	60.0	20.0	69.2	47.1	43.5	60.0	66.7	57.7	40.0	51.3 ± 15.6
C4	48.0	33.3	57.1	46.2	66.7	35.7	60.0	33.3	58.3	33.3	46.2	55.6	83.3	41.4	22.6	48.1 ± 15.8
O1	50.0	22.2	63.6	39.4	70.0	23.5	46.7	26.9	45.8	52.8	38.5	53.3	16.7	46.2	23.8	41.3 ± 15.9
O2	48.1	33.3	66.7	44.8	66.7	31.8	55.0	25.0	50.0	31.8	50.0	56.3	12.5	34.6	33.3	42.7 ± 15.4
E1	50.0	50.0	52.9	42.9	78.3	53.3	25.0	30.8	83.3	64.5	35.3	60.0	66.7	46.2	52.4	52.8 ± 16.2
E2	40.0	36.4	61.5	53.3	73.1	41.2	82.6	36.8	55.6	60.9	43.8	60.0	57.1	33.3	53.8	52.6 ± 14.2

Table D.15 – Subject-by-subject percentage of uncorrelated peaks, with respect to the total number of peaks, sleep recovery phase.

D.4 Causality

D.4.1 U-Pattern/Movement Onset Delays

Subject	1	2	3	4	5	6	7	8	9	10	11	12	13	14	15	mean ± std
3-EMG	6.5	9.9	11.5	10.0	8.8	8.8	7.9	8.3	9.0	10.7	8.5	6.5	10.4	8.9	7.5	8.9 ± 1.5
ChinC	9.2	11.8	7.5	10.7	8.9	9.5	10.5	7.3	9.0	12.5	8.1	6.8	12.7	11.5	8.8	9.7 ± 1.9
ChinL	9.1	10.4	9.9	9.1	9.1	9.2	5.9	9.7	N/A	11.3	8.5	6.1	9.4	3.8	8.0	8.5 ± 2.0
ChinR	7.7	9.7	12.3	10.7	6.8	9.2	3.6	8.6	9.0	13.4	8.6	6.6	11.2	3.8	8.5	8.6 ± 2.7
Thorax	7.9	9.1	10.3	N/A	6.9	6.4	8.6	7.4	7.9	9.3	6.8	6.5	10.8	5.9	9.8	8.1 ± 1.6
F3	10.1	8.9	10.0	11.0	9.8	7.7	9.2	10.1	15.8	13.7	8.4	5.6	11.4	4.7	9.5	9.7 ± 2.8
F4	14.4	11.6	14.8	9.0	7.8	8.7	10.4	10.1	13.5	13.6	8.9	6.4	N/A	6.7	13.1	10.6 ± 2.9
C3	10.0	11.1	13.0	13.0	11.4	9.0	10.5	10.7	14.3	13.9	6.2	7.0	14.8	6.3	13.7	11.0 ± 2.9
C4	6.5	12.9	12.8	15.3	7.0	9.0	8.0	8.5	11.8	11.5	7.5	5.7	5.0	6.8	12.7	9.4 ± 3.2
O1	9.9	10.5	12.6	11.9	10.3	6.0	9.7	8.3	11.8	10.5	8.5	8.2	6.6	8.9	12.1	9.7 ± 2.0
O2	8.9	11.6	13.6	9.2	10.6	8.0	9.8	8.8	11.9	10.8	7.7	6.5	19.1	8.8	7.9	10.2 ± 3.1
E1	12.1	10.1	8.0	6.8	4.0	9.5	11.3	6.3	21.0	11.9	8.5	6.7	7.3	3.3	9.0	9.1 ± 4.2
E2	12.4	9.1	10.3	16.0	N/A	8.9	5.5	4.6	12.0	11.0	8.6	5.2	12.5	7.8	9.4	9.5 ± 3.2

Table D.16 – Subject-by-subject averages of U-pattern/Movement onset delays (seconds), baseline phase.

Subject	1	2	3	4	5	6	7	8	9	10	11	12	13	14	15	mean ± std
3-EMG	15.3	12.0	11.1	14.7	23.3	11.6	15.2	13.3	19.0	16.3	17.4	13.1	12.3	16.4	12.2	14.9 ± 3.3
ChinC	18.9	11.8	20.3	15.3	23.1	12.2	13.3	14.3	19.0	18.3	17.7	17.8	13.2	15.5	13.4	16.3 ± 3.3
ChinL	15.1	14.6	17.9	17.9	24.0	12.8	17.9	13.0	N/A	18.1	19.5	16.1	11.3	17.4	13.1	16.3 ± 3.3
ChinR	17.7	12.4	9.2	19.0	27.5	12.6	19.6	13.1	14.0	14.1	17.4	14.2	12.9	17.0	12.9	15.6 ± 4.4
Thorax	11.7	13.2	10.4	N/A	18.2	11.0	12.9	10.2	16.0	19.9	15.6	12.4	10.5	12.2	10.8	13.2 ± 3.1
F3	17.9	14.5	12.0	17.7	19.1	11.6	14.8	11.5	14.3	14.2	19.2	18.3	15.6	17.9	11.5	15.3 ± 2.9
F4	15.0	11.9	9.0	17.0	20.0	14.0	13.3	13.6	19.8	13.3	15.8	16.7	N/A	21.0	6.6	14.8 ± 4.1
C3	13.7	12.8	12.3	18.2	17.6	12.9	11.3	12.4	16.4	15.2	17.0	16.2	15.2	19.1	9.4	14.6 ± 2.8
C4	17.9	12.8	12.7	15.3	21.5	12.5	17.1	12.1	14.5	17.2	16.8	19.2	20.7	16.0	11.5	15.9 ± 3.2
O1	15.9	15.3	14.1	15.1	21.3	12.9	12.7	13.3	16.4	15.5	14.8	16.3	17.4	17.3	9.7	15.2 ± 2.6
O2	17.3	15.6	13.0	18.1	20.3	19.0	13.0	12.3	16.1	15.8	17.6	17.2	6.9	17.2	12.1	15.4 ± 3.4
E1	17.4	12.3	13.7	19.2	21.3	12.6	19.3	13.5	10.0	16.7	18.1	17.1	15.0	17.2	12.7	15.7 ± 3.2
E2	9.7	13.1	14.8	15.6	N/A	12.8	13.5	17.8	21.0	17.6	17.1	18.2	18.5	16.2	9.0	15.4 ± 3.4

Table D.17 – Subject-by-subject averages of U-pattern/Movement onset delays (seconds), sleep deprivation phase.

Subject	1	2	3	4	5	6	7	8	9	10	11	12	13	14	15	mean ± std
3-EMG	10.8	7.4	11.0	7.8	3.8	5.3	4.7	6.7	7.9	9.1	10.2	8.6	9.0	8.6	9.7	8.0 ± 2.2
ChinC	11.1	6.0	10.5	7.6	5.6	8.1	4.0	7.7	8.5	10.7	9.4	9.2	9.4	8.9	10.6	8.5 ± 2.0
ChinL	9.4	7.3	17.5	9.6	3.5	5.2	4.6	7.0	10.8	8.6	10.3	8.6	8.0	13.0	10.0	8.9 ± 3.5
ChinR	11.3	8.2	16.4	9.4	6.1	7.1	4.3	7.0	12.3	7.2	13.8	8.7	15.3	16.8	9.2	10.2 ± 3.9
Thorax	8.0	8.4	12.4	8.9	7.5	6.7	7.2	7.6	6.2	6.5	6.5	5.0	8.3	6.5	8.8	7.6 ± 1.7
F3	14.3	8.5	22.7	7.7	9.7	6.0	6.5	7.5	10.4	5.7	13.7	8.6	N/A	15.5	9.1	10.4 ± 4.7
F4	12.3	9.0	18.0	8.0	6.5	9.2	6.5	7.3	11.8	6.0	9.9	8.5	7.5	6.7	9.4	9.1 ± 3.1
C3	17.2	11.4	20.8	10.2	6.0	8.9	5.4	11.0	3.0	10.5	9.9	10.3	20.0	11.7	14.8	11.4 ± 5.0
C4	9.0	13.2	16.6	10.9	6.2	8.4	6.8	9.3	9.9	10.4	12.3	10.2	6.0	22.0	6.8	10.5 ± 4.3
O1	14.8	10.0	19.2	9.2	9.3	7.9	8.0	8.1	10.0	11.3	9.9	9.4	6.0	11.0	9.6	10.2 ± 3.2
O2	12.1	7.8	16.7	8.3	10.0	7.8	7.3	8.0	10.3	8.5	11.7	9.1	8.4	14.4	10.0	10.0 ± 2.7
E1	14.7	9.8	17.7	5.9	11.0	8.0	7.3	7.5	9.6	8.5	10.4	8.9	6.4	13.5	10.8	10.0 ± 3.2
E2	8.7	8.2	20.4	5.7	5.7	6.3	10.4	7.5	11.4	11.7	8.8	8.0	9.0	9.5	9.2	9.4 ± 3.5

Table D.18 – Subject-by-subject averages of U-pattern/movement onset delays (seconds), recovery phase.

D.4.2 U-Pattern/Movement Offset Delays

Subject	1	2	3	4	5	6	7	8	9	10	11	12	13	14	15	mean ± std
3-EMG	12.9	11.8	12.2	14.5	29.3	15.5	17.6	12.7	15.4	14.6	19.3	13.1	22.0	12.3	16.0	15.9 ± 4.7
ChinC	16.1	13.8	13.4	18.0	23.2	13.9	18.5	12.8	18.5	11.8	22.0	13.6	18.8	15.0	18.8	16.5 ± 3.4
ChinL	15.6	16.7	11.9	17.0	28.5	16.8	19.0	12.3	15.6	16.4	20.4	14.0	27.0	9.5	13.2	16.9 ± 5.2
ChinR	12.9	15.8	10.7	15.2	20.3	15.9	18.7	8.3	16.5	17.6	16.3	14.4	15.5	10.5	14.2	14.9 ± 3.2
Thorax	12.1	9.6	10.1	14.9	14.5	9.9	13.2	11.5	15.6	14.0	16.7	13.2	11.8	16.2	13.6	13.1 ± 2.3
F3	13.3	13.3	6.7	19.3	18.7	11.8	12.9	11.0	14.1	17.3	15.0	15.2	N/A	10.3	17.0	14.0 ± 3.5
F4	13.8	13.3	10.6	20.4	23.5	10.7	13.3	11.2	11.7	18.4	18.0	13.9	22.5	25.3	16.4	16.2 ± 4.9
C3	8.0	11.6	8.2	19.7	20.8	11.2	12.9	10.4	24.3	11.8	20.4	11.8	18.0	9.3	9.2	13.8 ± 5.3
C4	17.3	9.4	10.6	15.6	22.8	13.0	12.3	9.4	13.8	14.1	16.7	13.2	23.3	15.0	10.2	14.4 ± 4.3
O1	9.9	8.5	8.8	15.3	18.5	13.9	14.7	11.4	15.9	13.5	15.7	13.4	11.5	21.0	17.4	14.0 ± 3.6
O2	14.5	15.5	9.3	17.9	15.5	11.8	15.9	11.3	16.7	14.8	18.2	13.3	16.3	13.8	16.3	14.7 ± 2.5
E1	13.7	13.3	11.3	18.6	20.0	14.7	15.4	10.7	17.3	15.1	20.4	14.2	24.4	9.0	17.0	15.7 ± 4.1
E2	19.2	16.2	11.0	22.8	28.0	15.4	15.1	11.0	14.9	11.5	21.7	14.8	18.5	21.0	17.2	17.2 ± 4.8

Table D.19 – Subject-by-subject averages of U-pattern/movement offset delays (seconds), baseline phase.

Subject	1	2	3	4	5	6	7	8	9	10	11	12	13	14	15	mean ± std
3-EMG	13.3	7.1	8.1	8.5	5.7	5.3	7.8	8.1	9.3	7.2	8.5	8.3	9.8	10.8	10.0	8.5 ± 2.0
ChinC	11.8	7.4	15.2	9.5	7.5	5.4	7.7	7.6	11.0	7.1	6.0	9.2	9.9	11.4	10.8	9.2 ± 2.6
ChinL	13.9	8.7	6.5	10.9	8.3	5.7	9.6	7.6	4.5	8.0	8.8	10.0	9.0	9.2	10.9	8.8 ± 2.3
ChinR	11.6	8.1	9.7	9.4	9.4	6.2	10.0	9.4	8.1	9.3	9.1	8.0	10.5	9.3	11.0	9.3 ± 1.3
Thorax	10.8	9.7	8.9	6.3	5.3	4.2	7.5	7.2	8.6	6.2	7.7	8.1	8.4	10.5	8.4	7.9 ± 1.8
F3	12.3	6.0	6.3	10.2	6.6	6.6	8.2	9.9	5.7	8.3	7.3	12.3	11.3	9.8	12.8	8.9 ± 2.5
F4	13.1	8.0	9.4	13.3	7.8	7.2	10.3	6.8	6.7	8.0	8.3	9.7	N/A	13.7	8.5	9.3 ± 2.4
C3	14.9	9.5	6.8	8.7	7.7	5.7	8.3	10.5	14.3	9.3	9.2	12.3	16.2	15.8	10.7	10.7 ± 3.3
C4	11.8	8.0	9.7	11.9	8.5	7.2	7.5	9.3	11.8	9.7	9.1	9.3	10.5	13.8	10.6	9.9 ± 1.8
O1	13.7	11.6	8.9	8.9	4.2	9.5	5.0	8.9	8.8	9.1	8.9	9.1	6.4	14.1	10.9	9.2 ± 2.7
O2	13.9	10.5	7.2	10.1	4.4	10.4	5.9	8.1	10.5	8.5	7.8	8.7	9.1	14.1	9.7	9.3 ± 2.6
E1	13.5	9.7	7.5	8.6	6.2	4.7	8.8	6.3	5.0	9.2	7.8	7.3	1.5	11.9	10.5	7.9 ± 3.0
E2	12.2	7.6	11.0	10.7	10.1	2.7	5.3	7.1	3.4	7.3	8.8	7.8	4.7	8.4	11.8	7.9 ± 3.0

Table D.20 – Subject-by-subject averages of U-pattern/movement offset delays (seconds), sleep deprivation phase.

Subject	1	2	3	4	5	6	7	8	9	10	11	12	13	14	15	mean ± std
3-EMG	13.5	14.1	14.9	14.4	15.7	18.5	11.8	11.2	19.0	17.5	15.8	9.9	10.6	19.9	13.2	14.7 ± 3.1
ChinC	16.5	13.8	9.2	14.7	12.7	17.1	15.0	12.1	14.0	17.9	23.4	8.8	12.5	20.0	14.7	14.8 ± 3.8
ChinL	16.0	16.0	18.8	14.8	15.2	18.5	12.0	16.4	20.5	16.8	17.4	10.8	15.5	16.3	13.4	15.9 ± 2.5
ChinR	15.3	16.0	15.5	15.0	14.1	18.8	13.8	11.7	19.9	16.0	16.7	11.0	17.0	17.8	12.3	15.4 ± 2.5
Thorax	13.5	13.9	12.1	13.8	10.5	15.0	11.8	11.9	14.7	14.2	17.6	8.4	11.7	10.4	13.7	12.9 ± 2.2
F3	16.4	24.0	16.2	17.2	16.8	17.0	13.9	13.8	19.0	16.7	23.3	8.3	9.2	17.6	12.0	16.1 ± 4.3
F4	18.7	24.0	17.2	18.7	15.0	19.0	9.5	18.8	16.3	17.3	18.0	8.7	N/A	16.1	11.0	16.3 ± 4.1
C3	16.4	17.0	18.4	15.7	15.2	15.4	13.3	12.2	11.3	16.9	19.4	7.0	10.6	14.9	9.8	14.2 ± 3.5
C4	17.2	19.3	16.0	14.1	15.2	14.8	15.3	13.3	15.2	15.4	18.6	8.8	6.5	12.5	10.6	14.2 ± 3.5
O1	16.6	12.9	17.0	15.1	17.6	15.1	17.8	13.7	19.0	15.1	17.6	11.4	17.6	15.7	12.6	15.7 ± 2.2
O2	14.8	13.8	18.6	15.1	15.5	12.4	15.4	13.7	14.3	13.1	20.1	12.1	12.8	18.1	12.4	14.8 ± 2.4
E1	17.0	14.0	17.3	19.4	16.6	21.1	13.7	15.7	11.0	14.5	20.7	13.3	13.0	16.4	15.8	16.0 ± 2.9
E2	18.3	15.4	11.6	16.4	13.6	19.8	18.0	14.6	21.9	18.9	19.7	12.7	17.3	18.6	13.8	16.7 ± 3.0

Table D.21 – Subject-by-subject averages of U-pattern/movement offset delays (seconds), recovery phase.

Bibliography

- [1] B.-U. Kohler, C. Hennig, and R. Orglmeister, "The principles of software qrs detection," *IEEE Magazine of Engineering in Medicine and Biology*, no. 1, pp. 42–57, 2002.
- [2] P. De Chazal, M. O'Dwyer, and R. B. Reilly, "Automatic classification of heartbeats using ecg morphology and heartbeat interval features," *IEEE Transactions on Biomedical Engineering*, no. 7, pp. 1196–1206, 2004.
- [3] P. de Chazal and R. Reilly, "A Patient-Adapting Heartbeat Classifier Using ECG Morphology and Heartbeat Interval Features," *IEEE Transactions on Biomedical Engineering*, vol. 53, no. 12, pp. 2535–2543, Dec. 2006.
- [4] C. Ye, B. V. K. V. Kumar, and M. T. Coimbra, "Heartbeat Classification Using Morphological and Dynamic Features of ECG Signals," *IEEE Transactions on Biomedical Engineering*, vol. 59, no. 10, pp. 2930–2941, Oct. 2012.
- [5] I. Christov, G. Gomez-Herrero, V. Krasteva, I. Jekova, A. Gotchev, and K. Egiazarian, "Comparative study of morphological and time-frequency ECG descriptors for heartbeat classification," *Medical Engineering & Physics*, vol. 28, no. 9, pp. 876–887, Nov. 2006. [Online]. Available: <http://www.sciencedirect.com/science/article/pii/S135045330600004X>
- [6] S. Yazdani and J.-M. Vesin, "Extraction of QRS fiducial points from the ECG using adaptive mathematical morphology," *Digital Signal Processing*, vol. 56, pp. 100–109, Sep. 2016. [Online]. Available: <http://www.sciencedirect.com/science/article/pii/S1051200416300732>
- [7] S. Fallet, S. Yazdani, and J.-M. Vesin, "False arrhythmia alarms reduction in the intensive care unit: a multimodal approach," *Physiol. Meas.*, vol. 37, no. 8, p. 1217, 2016. [Online]. Available: <http://stacks.iop.org/0967-3334/37/i=8/a=1217>
- [8] Q. Li and G. D. Clifford, "Suppress false arrhythmia alarms of ICU monitors using heart rate estimation based on combined arterial blood pressure and ECG analysis," in *ICBBE*, 2008, pp. 2185–2187.
- [9] G. D. Clifford, I. Silva, B. Moody, Q. Li, D. Kella, A. Shahin, T. Kooistra, D. Perry, and R. G. Mark, "The PhysioNet/Computing in Cardiology Challenge 2015: Reducing false arrhythmia alarms in the ICU," *Comput. Cardiol.*, vol. 42, pp. 273–276, 2015.
- [10] H. Xia, G. A. Garcia, J. Bains, D. C. Wortham, and X. Zhao, "Matrix of regularity for improving the quality of ECGs," *Physiol. Meas.*, vol. 33, no. 9, p. 1535, 2012. [Online]. Available: <http://stacks.iop.org/0967-3334/33/i=9/a=1535>

- [11] L. Y. D. Marco, W. Duan, M. Bojarnejad, D. Zheng, S. King, A. Murray, and Philip Langley, "Evaluation of an algorithm based on single-condition decision rules for binary classification of 12-lead ambulatory ECG recording quality," *Physiol. Meas.*, vol. 33, no. 9, p. 1435, 2012. [Online]. Available: <http://stacks.iop.org/0967-3334/33/i=9/a=1435>
- [12] L. Johannesen and L. Galeotti, "Automatic ECG quality scoring methodology: mimicking human annotators," *Physiol. Meas.*, vol. 33, no. 9, p. 1479, 2012. [Online]. Available: <http://stacks.iop.org/0967-3334/33/i=9/a=1479>
- [13] D. Hayn, B. Jammerbund, and G. Schreier, "QRS detection based ECG quality assessment," *Physiol. Meas.*, vol. 33, no. 9, p. 1449, 2012. [Online]. Available: <http://stacks.iop.org/0967-3334/33/i=9/a=1449>
- [14] T. H. C. Tat, C. Xiang, and L. E. Thiam, "Physionet Challenge 2011: Improving the quality of electrocardiography data collected using real time QRS-complex and T-Wave detection," in *2011 Computing in Cardiology*, Sep. 2011, pp. 441–444.
- [15] I. Jekova, V. Krasteva, I. Christov, and R. Abächerli, "Threshold-based system for noise detection in multilead ECG recordings," *Physiol. Meas.*, vol. 33, no. 9, p. 1463, 2012. [Online]. Available: <http://stacks.iop.org/0967-3334/33/i=9/a=1463>
- [16] M.-C. Chambrin, "Alarms in the intensive care unit: how can the number of false alarms be reduced?" *Critical Care*, vol. 5, no. 4, p. 184, 2001.
- [17] R. Klabunde, *Cardiovascular physiology concepts*. Lippincott Williams & Wilkins, 2011.
- [18] M. Antz, K. Otomo, M. Arruda, B. J. Scherlag, J. Pitha, C. Tondo, R. Lazzara, and W. M. Jackman, "Electrical Conduction Between the Right Atrium and the Left Atrium via the Musculature of the Coronary Sinus," *Circulation*, vol. 98, no. 17, pp. 1790–1795, Oct. 1998. [Online]. Available: <http://circ.ahajournals.org/content/98/17/1790>
- [19] R. De Ponti, S. Y. Ho, J. A. Salerno-Uriarte, M. Tritto, and G. Spadacini, "Electroanatomic Analysis of Sinus Impulse Propagation in Normal Human Atria," *Journal of Cardiovascular Electrophysiology*, vol. 13, no. 1, pp. 1–10, Jan. 2002. [Online]. Available: <http://onlinelibrary.wiley.com/doi/10.1046/j.1540-8167.2002.00001.x/abstract>
- [20] E. N. Marieb and K. Hoehn, *Human Anatomy & Physiology*. Pearson Education, 2007, google-Books-ID: x1uEB68iitwC.
- [21] R. M. Buijs, "The autonomic nervous system: a balancing act." *Handbook of clinical neurology*, vol. 117, pp. 1–11, 2013.
- [22] J. M. Karemaker, "How the vagus nerve produces beat-to-beat heart rate variability; experiments in rabbits to mimic in vivo vagal patterns," *J Clin Transl Res*, vol. 1, pp. 190–204, 2015.
- [23] J. E. Hall, *Guyton and Hall Textbook of Medical Physiology E-Book*. Elsevier Health Sciences, 2015.
- [24] K. S. Saladin and L. Miller, *Anatomy & physiology*. WCB/McGraw-Hill New York (NY), 1998.
- [25] T. F. o. t. E. S. o. C. t. N. A. S. o. P. Electrophysiology, "Heart Rate Variability: Standards of Measurement, Physiological Interpretation, and Clinical Use," *Circulation*, vol. 93, no. 5, pp. 1043–1065, Mar. 1996. [Online]. Available: <http://circ.ahajournals.org/content/93/5/1043>

- [26] M. Pagani, F. Lombardi, S. Guzzetti, O. Rimoldi, R. Furlan, P. Pizzinelli, G. Sandrone, G. Malfatto, S. Dell'Orto, and E. Piccaluga, "Power spectral analysis of heart rate and arterial pressure variabilities as a marker of sympatho-vagal interaction in man and conscious dog." *Circulation Research*, vol. 59, no. 2, pp. 178–193, Aug. 1986. [Online]. Available: <http://circres.ahajournals.org/content/59/2/178>
- [27] A. Malliani, M. Pagani, F. Lombardi, and S. Cerutti, "Cardiovascular neural regulation explored in the frequency domain." *Circulation*, vol. 84, no. 2, pp. 482–492, Aug. 1991. [Online]. Available: <http://circ.ahajournals.org/content/84/2/482>
- [28] R. Furlan, S. Guzzetti, W. Crivellaro, S. Dassi, M. Tinelli, G. Baselli, S. Cerutti, F. Lombardi, M. Pagani, and A. Malliani, "Continuous 24-hour assessment of the neural regulation of systemic arterial pressure and RR variabilities in ambulant subjects." *Circulation*, vol. 81, no. 2, pp. 537–547, Feb. 1990. [Online]. Available: <http://circ.ahajournals.org/content/81/2/537>
- [29] E. Buccelletti, E. Gilardi, E. Scaini, L. Galiuto, R. Persiani, A. Biondi, F. Basile, and N. G. Silveri, "Heart rate variability and myocardial infarction: systematic literature review and metanalysis," *Eur Rev Med Pharmacol Sci*, vol. 13, no. 4, pp. 299–307, 2009.
- [30] M. Malik, T. Farrell, T. Cripps, and A. Camm, "Heart rate variability in relation to prognosis after myocardial infarction: selection of optimal processing techniques," *European heart journal*, vol. 10, no. 12, pp. 1060–1074, 1989.
- [31] H. Tsuji, M. G. Larson, F. J. Venditti, E. S. Manders, J. C. Evans, C. L. Feldman, and D. Levy, "Impact of reduced heart rate variability on risk for cardiac events: the framingham heart study," *Circulation*, vol. 94, no. 11, pp. 2850–2855, 1996.
- [32] M. G. Tsipouras and D. I. Fotiadis, "Automatic arrhythmia detection based on time and time–frequency analysis of heart rate variability," *Computer methods and programs in biomedicine*, vol. 74, no. 2, pp. 95–108, 2004.
- [33] D. Barnaby, K. Ferrick, D. T. Kaplan, S. Shah, P. Bijur, and E. J. Gallagher, "Heart rate variability in emergency department patients with sepsis," *Academic emergency medicine*, vol. 9, no. 7, pp. 661–670, 2002.
- [34] C. S. Garrard, D. A. Kontoyannis, and M. Piepoli, "Spectral analysis of heart rate variability in the sepsis syndrome," *Clinical Autonomic Research*, vol. 3, no. 1, pp. 5–13, 1993.
- [35] K.-J. Bär, M. K. Boettger, M. Koschke, S. Schulz, P. Chokka, V. K. Yeragani, and A. Voss, "Non-linear complexity measures of heart rate variability in acute schizophrenia," *Clinical neurophysiology*, vol. 118, no. 9, pp. 2009–2015, 2007.
- [36] B. L. Henry, A. Minassian, M. P. Paulus, M. A. Geyer, and W. Perry, "Heart rate variability in bipolar mania and schizophrenia," *Journal of psychiatric research*, vol. 44, no. 3, pp. 168–176, 2010.
- [37] J. F. Thayer, F. Åhs, M. Fredrikson, J. J. Sollers, and T. D. Wager, "A meta-analysis of heart rate variability and neuroimaging studies: implications for heart rate variability as a marker of stress and health," *Neuroscience & Biobehavioral Reviews*, vol. 36, no. 2, pp. 747–756, 2012.
- [38] T. G. Vrijkotte, L. J. Van Doornen, and E. J. De Geus, "Effects of work stress on ambulatory blood pressure, heart rate, and heart rate variability," *Hypertension*, vol. 35, no. 4, pp. 880–886, 2000.

- [39] B. M. Appelhans and L. J. Luecken, "Heart rate variability as an index of regulated emotional responding." *Review of general psychology*, vol. 10, no. 3, p. 229, 2006.
- [40] R. McCraty, M. Atkinson, W. A. Tiller, G. Rein, and A. D. Watkins, "The effects of emotions on short-term power spectrum analysis of heart rate variability," *The American journal of cardiology*, vol. 76, no. 14, pp. 1089–1093, 1995.
- [41] F. Worgotter, W. J. Daunicht, and R. Eckmiller, "An on-line spike form discriminator for extracellular recordings based on an analog correlation technique," *Journal of Neuroscience Methods*, vol. 17, no. 2–3, pp. 141–151, Aug. 1986. [Online]. Available: [//www.sciencedirect.com/science/article/pii/0165027086900671](http://www.sciencedirect.com/science/article/pii/0165027086900671)
- [42] V. A. Folarin, P. J. Fitzsimmons, and W. B. Kruyer, "Holter monitor findings in asymptomatic male military aviators without structural heart disease." *Aviat Space Environ Med*, vol. 72, no. 9, pp. 836–838, Sep. 2001. [Online]. Available: <http://europepmc.org/abstract/med/11565820>
- [43] M. Brodsky, D. Wu, P. Denes, C. Kanakis, and K. M. Rosen, "Arrhythmias documented by 24 hour continuous electrocardiographic monitoring in 50 male medical students without apparent heart disease," *The American Journal of Cardiology*, vol. 39, no. 3, pp. 390–395, Jan. 1977. [Online]. Available: <http://www.sciencedirect.com/science/article/pii/S0002914977800945>
- [44] P. J. Podrid and P. R. Kowey, *Cardiac arrhythmia: mechanisms, diagnosis, and management*. Lippincott Williams & Wilkins, 2001.
- [45] ———, *Handbook of cardiac arrhythmia*. Lippincott Williams & Wilkins, 1996.
- [46] B. Ge, K.-T. Ji, H.-G. Ye, J. Li, Y.-C. Li, R.-P. Yin, and J.-F. Lin, "Electrocardiogram features of premature ventricular contractions/ventricular tachycardia originating from the left ventricular outflow tract and the treatment outcome of radiofrequency catheter ablation," *BMC Cardiovasc Disord*, vol. 12, p. 112, Nov. 2012. [Online]. Available: <https://www.ncbi.nlm.nih.gov/pmc/articles/PMC3571934/>
- [47] C. L. Stanfield, *Principles of human physiology*. Pearson Higher Ed, 2012.
- [48] G. B. Moody and R. G. Mark, "The impact of the mit-bih arrhythmia database," *IEEE Magazine of Engineering in Medicine and Biology*, vol. 20, no. 3, pp. 45–50, 2001.
- [49] A. L. Goldberger, Z. D. Goldberger, and A. Shvilkin, *Goldberger's clinical electrocardiography*. Elsevier/Saunders, 2013.
- [50] Q. Chen, G. E. Kirsch, D. Zhang, R. Brugada, J. Brugada, P. Brugada, D. Potenza, A. Moya, M. Borggrefe, G. Breithardt *et al.*, "Genetic basis and molecular mechanism for idiopathic ventricular fibrillation," *Nature*, vol. 392, no. 6673, pp. 293–296, 1998.
- [51] B. Lown and R. L. Verrier, "Neural activity and ventricular fibrillation," *New England Journal of Medicine*, vol. 294, no. 21, pp. 1165–1170, 1976.
- [52] G. Clifford, C. Liu, B. Moody, L. Lehman, I. Silva, Q. Li, A. Johnson, and R. Mark, "Af classification from a short single lead ecg recording: The physionet computing in cardiology challenge 2017," in *2017 Computing in Cardiology Conference (CinC)*, Sep. 2017, pp. 1–4.
- [53] P. Trahanias, "An approach to qrs complex detection using mathematical morphology," *IEEE Transactions on Biomedical Engineering*, no. 2, pp. 201–205, 1993.

- [54] V. Fuster, L. E. Rydén, D. S. Cannom, H. J. Crijns, A. B. Curtis, K. A. Ellenbogen, J. L. Halperin, J.-Y. Le Heuzey, G. N. Kay, J. E. Lowe *et al.*, “Acc/aha/esc 2006 guidelines for the management of patients with atrial fibrillation: full text: a report of the american college of cardiology/american heart association task force on practice guidelines and the european society of cardiology committee for practice guidelines (writing committee to revise the 2001 guidelines for the management of patients with atrial fibrillation) developed in collaboration with the european heart rhythm association and the heart rhythm society,” *Europace*, vol. 8, no. 9, pp. 651–745, 2006.
- [55] S. Stewart, C. Hart, D. Hole, and J. McMurray, “Population prevalence, incidence, and predictors of atrial fibrillation in the renfrew/paisley study,” *Heart*, vol. 86, no. 5, pp. 516–521, 2001.
- [56] C. D. Furberg, B. M. Psaty, T. A. Manolio, J. M. Gardin, V. E. Smith, P. M. Rautaharju, C. C. R. Group *et al.*, “Prevalence of atrial fibrillation in elderly subjects (the cardiovascular health study),” *The American journal of cardiology*, vol. 74, no. 3, pp. 236–241, 1994.
- [57] W. B. Kannel, P. A. Wolf, E. J. Benjamin, and D. Levy, “Prevalence, incidence, prognosis, and predisposing conditions for atrial fibrillation: population-based estimates,” *The American journal of cardiology*, vol. 82, no. 7, pp. 2N–9N, 1998.
- [58] J. S. Shinbane, M. A. Wood, D. N. Jensen, K. A. Ellenbogen, A. P. Fitzpatrick, and M. M. Scheinman, “Tachycardia-induced cardiomyopathy: a review of animal models and clinical studies,” *Journal of the American College of Cardiology*, vol. 29, no. 4, pp. 709–715, 1997.
- [59] P. A. Wolf, R. D. Abbott, and W. B. Kannel, “Atrial fibrillation as an independent risk factor for stroke: the framingham study,” *Stroke*, vol. 22, no. 8, pp. 983–988, 1991.
- [60] E. J. Benjamin, P. A. Wolf, R. B. D’Agostino, H. Silbershatz, W. B. Kannel, and D. Levy, “Impact of atrial fibrillation on the risk of death,” *Circulation*, vol. 98, no. 10, pp. 946–952, 1998.
- [61] R. M. Rangayyan, *Biomedical signal analysis*. IEEE press New York, 2002.
- [62] H. J. Wellens, F. W. Bär, and K. Lie, “The value of the electrocardiogram in the differential diagnosis of a tachycardia with a widened qrs complex,” *The American journal of medicine*, vol. 64, no. 1, pp. 27–33, 1978.
- [63] S. H. Lee, H.-C. Ko, and Y.-R. Yoon, “Classification of ventricular arrhythmia using a support vector machine based on morphological features,” in *Engineering in Medicine and Biology Society (EMBC), 2013 35th Annual International Conference of the IEEE*. IEEE, 2013, pp. 5785–5788.
- [64] T. F. of the European Society of Cardiology, T. F. of the European Society of Cardiology *et al.*, “the north american society of pacing and electrophysiology. heart rate variability: standards of measurement, physiological interpretation and clinical use,” *Journal of Circulation*, vol. 93, no. 5, pp. 1043–1065, 1996.
- [65] J. E. Mietus, C.-K. Peng, I. Henry, R. L. Goldsmith, and A. L. Goldberger, “The pNNx files: re-examining a widely used heart rate variability measure,” *Heart*, vol. 88, no. 4, pp. 378–380, Oct. 2002. [Online]. Available: <http://heart.bmj.com/content/88/4/378>

- [66] P. Morizet-Mahoudeaux, C. Moreau, D. Moreau, and J. J. Quarante, "Simple microprocessor-based system for on-line e.c.g. arrhythmia analysis," *Med. Biol. Eng. Comput.*, vol. 19, no. 4, pp. 497–500, Jul. 1981. [Online]. Available: <https://link.springer.com/article/10.1007/BF02441319>
- [67] R. Balda, J. VanBemmel, and J. Willems, "Trends in computer-processed electrocardiograms," in *Proceedings of the IFIP Working Conference on Trends in Computer-Processed Electrocardiograms, Amsterdam, Holland, 1977*, pp. 197–205.
- [68] W. P. Holsinger, K. M. Kempner, and M. H. Miller, "A QRS Preprocessor Based on Digital Differentiation," *IEEE Transactions on Biomedical Engineering*, vol. BME-18, no. 3, pp. 212–217, May 1971.
- [69] D. Gustafson *et al.*, "Automated vcg interpretation studies using signal analysis techniques," *R-1044 Charles Stark Draper Lab., Cambridge, MA*, p. 30, 1977.
- [70] J. Fraden and M. R. Neuman, "QRS wave detection," *Med. Biol. Eng. Comput.*, vol. 18, no. 2, pp. 125–132, Mar. 1980. [Online]. Available: <https://link.springer.com/article/10.1007/BF02443287>
- [71] M. L. Ahlstrom and W. J. Tompkins, "Automated High-Speed Analysis of Holter Tapes with Microcomputers," *IEEE Transactions on Biomedical Engineering*, vol. BME-30, no. 10, pp. 651–657, Oct. 1983.
- [72] M. Okada, "A Digital Filter for the ORS Complex Detection," *IEEE Transactions on Biomedical Engineering*, vol. BME-26, no. 12, pp. 700–703, Dec. 1979.
- [73] J. Pan and W. J. Tompkins, "A real-time qrs detection algorithm," *IEEE Transactions on Biomedical Engineering*, no. 3, pp. 230–236, 1985.
- [74] Z. Dokur, T. Ölmez, E. Yazgan, and O. K. Ersoy, "Detection of ECG waveforms by neural networks," *Medical Engineering & Physics*, vol. 19, no. 8, pp. 738–741, Oct. 1997. [Online]. Available: <http://www.sciencedirect.com/science/article/pii/S1350453397000295>
- [75] P. O. Borjesson, O. Pahlm, L. Sornmo, and M. E. Nygard, "Adaptive QRS Detection Based on Maximum A Posteriori Estimation," *IEEE Transactions on Biomedical Engineering*, vol. BME-29, no. 5, pp. 341–351, May 1982.
- [76] P. S. Hamilton and W. J. Tompkins, "Quantitative investigation of qrs detection rules using the mit/bih arrhythmia database," *IEEE Transactions on Biomedical Engineering*, vol. BME-33, no. 12, pp. 1157–1165, 1986.
- [77] T. Fancott and D. H. Wong, "A Minicomputer System for Direct High Speed Analysis of Cardiac Arrhythmia in 24 h Ambulatory ECG Tape Recordings," *IEEE Transactions on Biomedical Engineering*, vol. BME-27, no. 12, pp. 685–693, Dec. 1980.
- [78] L. Keselbrener, M. Keselbrener, and S. Akselrod, "Nonlinear high pass filter for R-wave detection in ECG signal," *Medical Engineering & Physics*, vol. 19, no. 5, pp. 481–484, Jun. 1997. [Online]. Available: <http://www.sciencedirect.com/science/article/pii/S1350453397000131>
- [79] J. Leski and E. Tkacz, "A new parallel concept for QRS complex detector," in *1992 14th Annual International Conference of the IEEE Engineering in Medicine and Biology Society*, vol. 2, Oct. 1992, pp. 555–556.

- [80] A. Ligtenberg and M. Kunt, "A robust-digital QRS-detection algorithm for arrhythmia monitoring," *Computers and Biomedical Research*, vol. 16, no. 3, pp. 273–286, Jun. 1983. [Online]. Available: <http://www.sciencedirect.com/science/article/pii/0010480983900277>
- [81] M.-E. Nygard, M. E. rds and J. Hulting, "An automated system for ECG monitoring," *Computers and Biomedical Research*, vol. 12, no. 2, pp. 181–202, Apr. 1979. [Online]. Available: <http://www.sciencedirect.com/science/article/pii/0010480979900156>
- [82] S. Suppappola and Y. Sun, "Nonlinear transforms of ECG signals for digital QRS detection: a quantitative analysis," *IEEE Transactions on Biomedical Engineering*, vol. 41, no. 4, pp. 397–400, Apr. 1994.
- [83] B. C. Yu, C. S. Liu, M. Lee, C. Y. Chen, and B. N. Chiang, "A Nonlinear Digital Filter For Cardiac QRS Complex Detection." *Journal of Clinical Engineering*, vol. 10, no. 3, p. 193, Sep. 1985. [Online]. Available: http://journals.lww.com/jcejournal/abstract/1985/07000/a_nonlinear_digital_filter_for_cardiac_qrs_complex.2.aspx
- [84] C. Li, C. Zheng, and C. Tai, "Detection of ECG characteristic points using wavelet transforms," *IEEE Transactions on Biomedical Engineering*, vol. 42, no. 1, pp. 21–28, Jan. 1995.
- [85] V. D. Virgilio, C. Francaiancia, S. Lino, and S. Cerutti, "ECG fiducial points detection through wavelet transform," in *Proceedings of 17th International Conference of the Engineering in Medicine and Biology Society*, vol. 2, Sep. 1995, pp. 1051–1052 vol.2.
- [86] K. D. Rao, "DWT Based Detection of R-peaks and Data Compression of ECG Signals," *IETE Journal of Research*, vol. 43, no. 5, pp. 345–349, Sep. 1997. [Online]. Available: <http://dx.doi.org/10.1080/03772063.1997.11416001>
- [87] M. Bahoura, M. Hassani, and M. Hubin, "DSP implementation of wavelet transform for real time ECG wave forms detection and heart rate analysis," *Computer Methods and Programs in Biomedicine*, vol. 52, no. 1, pp. 35–44, Jan. 1997. [Online]. Available: <http://www.sciencedirect.com/science/article/pii/S016926079701780X>
- [88] S. Kadambe, R. Murray, and G. F. Boudreaux-Bartels, "Wavelet transform-based QRS complex detector," *IEEE Transactions on Biomedical Engineering*, vol. 46, no. 7, pp. 838–848, Jul. 1999.
- [89] V. Afonso, W. J. Tompkins, T. Nguyen, and S. Luo, "Ecg beat detection using filter banks," *IEEE Transactions on Biomedical Engineering*, vol. 46, no. 2, pp. 192–202, 1999.
- [90] F. Zhang and Y. Lian, "Qrs detection based on multiscale mathematical morphology for wearable ecg devices in body area networks," *IEEE Transactions on Biomedical Circuits and System*, no. 4, pp. 220–228, 2009.
- [91] S. E. Dobbs, N. M. Schmitt, and H. S. Ozemek, "QRS Detection By Template Matching Using Real-Time Correlation On A Microcomputer." *Journal of Clinical Engineering*, vol. 9, no. 3, p. 197, Sep. 1984. [Online]. Available: http://journals.lww.com/jcejournal/Abstract/1984/07000/QRS_Detection_By_Template_Matching_Using_Real_Time.2.aspx
- [92] D. Ebenezer and V. Krishnamurthy, "Wave digital matched filter for electrocardiogram preprocessing," *Journal of Biomedical Engineering*, vol. 15, no. 2, pp. 132–134, Mar. 1993. [Online]. Available: <http://www.sciencedirect.com/science/article/pii/014154259390042W>

- [93] A. Ruha, S. Sallinen, and S. Nissila, "A real-time microprocessor QRS detector system with a 1-ms timing accuracy for the measurement of ambulatory HRV," *IEEE Transactions on Biomedical Engineering*, vol. 44, no. 3, pp. 159–167, Mar. 1997.
- [94] D. A. Coast, R. M. Stern, G. G. Cano, and S. A. Briller, "An approach to cardiac arrhythmia analysis using hidden Markov models," *IEEE Transactions on Biomedical Engineering*, vol. 37, no. 9, pp. 826–836, Sep. 1990.
- [95] R. Poli, S. Cagnoni, and G. Valli, "Genetic design of optimum linear and nonlinear qrs detectors," *Biomedical Engineering, IEEE Transactions on*, vol. 42, no. 11, pp. 1137–1141, 1995.
- [96] Z. Zidelmal, A. Amirou, D. Ould-Abdeslam, A. Moukadem, and A. Dieterlen, "Qrs detection using s-transform and shannon energy," *Computer methods and programs in biomedicine*, vol. 116, no. 1, pp. 1–9, 2014.
- [97] N. Ravanshad, H. Rezaee-Dehsorkh, R. Lotfi, and Y. Lian, "A level-crossing based qrs-detection algorithm for wearable ecg sensors," *IEEE Journal of Biomedical and Health Informatics*, vol. 18, no. 1, pp. 183–192, 2014.
- [98] B. Kohler, C. Hennig, and R. Orglmeister, "Qrs detection using zero crossing counts," *Applied genomics and proteomics*, vol. 2, no. 2, pp. 138–145, 2003.
- [99] I. Saini, D. Singh, and A. Khosla, "Qrs detection using k-nearest neighbor algorithm (knn) and evaluation on standard ecg databases," *Journal of advanced research*, vol. 4, no. 4, pp. 331–344, 2013.
- [100] F. Gritzali, "Towards a generalized scheme for QRS detection in ECG waveforms," *Signal Processing*, vol. 15, no. 2, pp. 183–192, Sep. 1988. [Online]. Available: <http://www.sciencedirect.com/science/article/pii/0165168488900692>
- [101] T. V. Ananthapadmanabha, A. P. Prathosh, and A. G. Ramakrishnan, "Detection of the closure-burst transitions of stops and affricates in continuous speech using the plosion index," *The Journal of the Acoustical Society of America*, vol. 135, no. 1, pp. 460–471, Jan. 2014. [Online]. Available: <http://scitation.aip.org/content/asa/journal/jasa/135/1/10.1121/1.4836055>
- [102] S. Yazdani, S. Fallet, and J. M. Vesin, "A Novel Short-term Event Extraction Algorithm for Biomedical Signals," *IEEE Transactions on Biomedical Engineering*, vol. PP, no. 99, pp. 1–1, 2017.
- [103] G. M. Friesen, T. C. Jannett, M. A. Jadallah, S. L. Yates, S. R. Quint, and H. T. Nagle, "A comparison of the noise sensitivity of nine qrs detection algorithms," *IEEE Transactions on Biomedical Engineering*, no. 1, pp. 85–98, 1990.
- [104] M. Elgendi, B. Eskofier, S. Dokos, and D. Abbott, "Revisiting QRS Detection Methodologies for Portable, Wearable, Battery-Operated, and Wireless ECG Systems," *PLOS ONE*, vol. 9, no. 1, p. e84018, Jan. 2014. [Online]. Available: <http://journals.plos.org/plosone/article?id=10.1371/journal.pone.0084018>
- [105] S. Yazdani and J.-M. Vesin, "Adaptive mathematical morphology for QRS fiducial points detection in the ecg," in *The 41st annual international conference of Computing in Cardiology*, 2014, pp. 725–728.
- [106] P. Maragos and R. W. Schafer, "Morphological systems for multidimensional signal processing," *Proceedings of the IEEE*, no. 4, pp. 690–710, 1990.

- [107] B. Surawicz, R. Childers, B. J. Deal, and L. S. Gettes, "Recommendations for the standardization and interpretation of the electrocardiogram: Part iii: Intraventricular conduction disturbances: A scientific statement from the american heart association electrocardiography and arrhythmias committee, council on clinical cardiology," *Journal of Circulation*, vol. 119, no. 10, pp. 235–240, 2009.
- [108] J. M. Arribas Leal, D. A. Pascual-Figal, M. A. Vidal, F. M. Ortuño, F. G. García, J. G.-P. del Corral, J. A. Ruipérez Abizanda, G. T. Martínez, M. V. Chávarri, and R. A. Meca, "Qrs duration and early hemodynamic instability after coronary revascularization surgery," *Journal of Revista Española de Cardiología (English Edition)*, no. 6, pp. 652–659, 2009.
- [109] C. Wolpert, C. Veltmann, R. Schimpf, C. Antzelevitch, I. Gussak, and M. Borggrefe, "Is a narrow and tall qrs complex an ecg marker for sudden death?" *Journal of Heart Rhythm*, vol. 5, no. 9, pp. 1339–1345, 2008.
- [110] A. D. Sharma, R. Yee, G. Guiraudon, and G. J. Klein, "Sensitivity and specificity of invasive and noninvasive testing for risk of sudden death in wolff-parkinson-white syndrome," *Journal of the American College of Cardiology*, vol. 10, no. 2, pp. 373–381, 1987.
- [111] P. Laguna, R. Mark, A. Goldberg, and G. Moody, "A database for evaluation of algorithms for measurement of qt and other waveform intervals in the ecg," in *In Proceedings of Computers in Cardiology*, 1997, pp. 673–676.
- [112] J. P. Martínez, R. Almeida, S. Olmos, A. P. Rocha, and P. Laguna, "A wavelet-based ecg delineator: evaluation on standard databases," *IEEE Transactions on Biomedical Engineering*, vol. 51, no. 4, pp. 570–581, 2004.
- [113] G. B. Moody and R. G. Mark, "Development and evaluation of a 2-lead ecg analysis program," *Computers in cardiology*, vol. 9, pp. 39–44, 1982.
- [114] J. Lee, K. Jeong, J. Yoon, and M. Lee, "A simple real-time qrs detection algorithm," in *Proceedings of the 18th Annual International Conference of the IEEE*, vol. 4, 1996, pp. 1396–1398.
- [115] S.-W. Chen, H.-C. Chen, and H.-L. Chan, "A real-time qrs detection method based on moving-averaging incorporating with wavelet denoising," *Computer Methods and Programs in Biomedicine*, vol. 82, no. 3, pp. 187–195, 2006.
- [116] I. Christov, I. Jekova, and G. Bortolan, "Premature ventricular contraction classification by the k th nearest-neighbours rule," *Journal of Physiological Measurement*, vol. 26, no. 1, pp. 123–130, 2005.
- [117] P. de Chazal and R. Reilly, "A patient-adapting heartbeat classifier using ecg morphology and heartbeat interval features," *IEEE Transactions on Biomedical Engineering*, vol. 53, no. 12, pp. 2535–2543, 2006.
- [118] M. G. Tsipouras, D. I. Fotiadis, and D. Sideris, "An arrhythmia classification system based on the rr-interval signal," *Artificial Intelligence in Medicine*, vol. 33, no. 3, pp. 237–250, 2005.
- [119] N. V. Thakor and Y.-S. Zhu, "Applications of adaptive filtering to ecg analysis: noise cancellation and arrhythmia detection," *IEEE Transactions on Biomedical Engineering*, vol. 38, no. 8, pp. 785–794, 1991.

- [120] V. X. Afonso and W. J. Tompkins, "Detecting ventricular fibrillation," *IEEE Journal of Engineering in Medicine and Biology Magazine*, no. 2, pp. 152–159, 1995.
- [121] A. Buttu, A. Forclaz, P. Pascale, P. Maury, A. Rollin, J. Vesin, and E. Pruvot, "Measures of right atrial organization as a means to select candidates for sinus rhythm restoration by catheter ablation," in *Computing in Cardiology Conference (CinC)*, 2013, pp. 1051–1054.
- [122] P. Pascale, A. J. Shah, L. Roten, D. Scherr, Y. Komatsu, K. Ramoul, M. Daly, A. Denis, N. Derval, F. Sacher *et al.*, "Pulmonary veins to left atrium cycle length gradient predicts procedural and clinical outcomes of persistent atrial fibrillation ablation," *Circulation: Arrhythmia and Electrophysiology*, pp. 473–482, 2014.
- [123] K. Nademane, J. McKenzie, E. Kosar, M. Schwab, B. Sunsaneewitayakul, T. Vasavakul, C. Khunnawat, and T. Ngarmukos, "A new approach for catheter ablation of atrial fibrillation: mapping of the electrophysiologic substrate," *Journal of the American College of Cardiology*, vol. 43, no. 11, pp. 2044–2053, 2004.
- [124] O. Berenfeld, S. Ennis, E. Hwang, B. Hooven, K. Grzeda, S. Mironov, M. Yamazaki, J. Kalifa, and J. Jalife, "Time- and frequency-domain analyses of atrial fibrillation activation rate: the optical mapping reference," *Heart Rhythm*, vol. 8, no. 11, pp. 1758–1765, 2011.
- [125] Y.-J. Lin, C.-T. Tai, T. Kao, H.-W. Tso, S. Higa, H.-M. Tsao, S.-L. Chang, M.-H. Hsieh, and S.-A. Chen, "Frequency analysis in different types of paroxysmal atrial fibrillation," *Journal of the American College of Cardiology*, vol. 47, no. 7, pp. 1401–1407, 2006.
- [126] J. Ng, V. Sehgal, J. Ng, D. Gordon, and J. Goldberger, "Iterative method to detect atrial activations and measure cycle length from electrograms during atrial fibrillation," *IEEE Transactions on Biomedical Engineering*, vol. 61, no. 2, pp. 273–278, 2014.
- [127] S. Yazdani, A. Buttu, E. Pruvot, J.-M. Vesin, and P. Pascale, "Extracting atrial activations from intracardiac signals during atrial fibrillation using adaptive mathematical morphology," in *The 42nd annual international conference of Computing in Cardiology*. IEEE, 2015, pp. 913–916.
- [128] D. F. Sittig and M. Factor, "Physiologic trend detection and artifact rejection: A parallel implementation of a multi-state kalman filtering algorithm," *Proc. Annu. Symp. Comput. Appl. Med. Care*, pp. 569–574, Nov. 1989. [Online]. Available: <http://www.ncbi.nlm.nih.gov/pmc/articles/PMC2245677/>
- [129] A. Mäkivirta, E. Koski, A. Kari, and T. Sukuvaara, "The median filter as a preprocessor for a patient monitor limit alarm system in intensive care," *Comput. Methods Programs Biomed.*, vol. 34, pp. 139–144, 1991.
- [130] A. Aboukhalil, L. Nielsen, M. Saeed, R. G. Mark, and G. D. Clifford, "Reducing false alarm rates for critical arrhythmias using the arterial blood pressure waveform," *J. Biomed. Inform.*, vol. 41, pp. 442–451, 2008.
- [131] J. Sun, A. Reisner, and R. Mark, "A signal abnormality index for arterial blood pressure waveforms," *Comput. in Cardiol.*, vol. 33, pp. 13–16, 2006.
- [132] W. Zong, G. B. Moody, and R. G. Mark, "Reduction of false arterial blood pressure alarms using signal quality assessment and relationships between the electrocardiogram and arterial blood pressure," *Med. Biol. Eng. Comput.*, vol. 42, pp. 698–706, Sep. 2004.

- [133] Q. Li and G. D. Clifford, "Dynamic time warping and machine learning for signal quality assessment of pulsatile signals," *Physiol. Meas.*, vol. 33, pp. 1491–1501, 2012. [Online]. Available: <http://stacks.iop.org/0967-3334/33/i=9/a=1491>
- [134] —, "Signal quality and data fusion for false alarm reduction in the intensive care unit," *J. Electrocardiol.*, vol. 45, pp. 596–603, 2012.
- [135] J. Behar, J. Oster, Q. Li, and G. Clifford, "ECG signal quality during arrhythmia and its application to false alarm reduction," *IEEE Trans. Biomed. Eng.*, vol. 60, pp. 1660–1666, Jun. 2013.
- [136] R. Salas-Boni, Y. Bai, P. R. E. Harris, B. J. Drew, and X. Hu, "False ventricular tachycardia alarm suppression in the ICU based on the discrete wavelet transform in the ECG signal," *J. Electrocardiol.*, vol. 47, pp. 775–780, 2014.
- [137] Q. Li, C. Rajagopalan, and G. D. Clifford, "Ventricular fibrillation and tachycardia classification using a machine learning approach," *IEEE Trans. Biomed. Eng.*, vol. 61, pp. 1607–1613, 2014.
- [138] G. Moody and L. Lehman, "Predicting acute hypotensive episodes: The 10th annual PhysioNet/Computers in Cardiology Challenge," in *2009 36th Annual Computers in Cardiology Conference (CinC)*, Sep. 2009, pp. 541–544.
- [139] S. Fallet, S. Yazdani, and V. J.-M., "A multimodal approach to reduce false arrhythmia alarms in the intensive care unit," *The 42nd annual international conference of Computing in Cardiology*, vol. 42, pp. 277–280, 2015.
- [140] I. I. Goncharova and J. S. Barlow, "Changes in EEG mean frequency and spectral purity during spontaneous alpha blocking," *Electroencephalogr. Clin. Neurophysiol.*, vol. 76, pp. 197–204, 1990.
- [141] L. Sornmo and P. Laguna, *Bioelectrical Signal Processing in Cardiac and Neurological Applications*. Academic Press, 2005.
- [142] S. Arberet, M. Lemay, P. Renevey, J. Sola, O. Grossenbacher, D. Andries, C. Sartori, and M. Bertschi, "Photoplethysmography-based ambulatory heartbeat monitoring embedded into a dedicated bracelet," *Comput. Cardiol.*, vol. 40, pp. 935–938, 2013.
- [143] H.-E. Liao, "Two discrete oscillator based adaptive notch filters (OSC ANFs) for noisy sinusoids," *IEEE Trans. Signal Process.*, vol. 53, pp. 528–538, 2005.
- [144] Y. Prudat and J. M. Vesin, "Multi-signal extension of adaptive frequency tracking algorithms," *Signal Process.*, vol. 89, pp. 963–973, 2009.
- [145] L. Uldry, C. Duchêne, Y. Prudat, M.-M. Murray, and J.-M. Vesin, "Adaptive tracking of EEG frequency components," in *Advanced Biosignal Processing*. Springer, 2009, pp. 123–144.
- [146] S. Fallet and J.-M. Vesin, "Adaptive frequency tracking for robust heart rate estimation using wrist-type photoplethysmographic signals during physical exercise," *Comput. Cardiol.*, vol. 42, pp. 925–928, 2015.
- [147] K. V. Mardia, "Measures of multivariate skewness and kurtosis with applications," *Biometrika*, vol. 57, no. 3, pp. 519–530, 1970.
- [148] C. R. Harvey and A. Siddique, "Conditional skewness in asset pricing tests," *The Journal of Finance*, vol. 55, no. 3, pp. 1263–1295, 2000.

- [149] L. T. DeCarlo, "On the meaning and use of kurtosis." *Psychological methods*, vol. 2, no. 3, p. 292, 1997.
- [150] E. Gil, P. Laguna, J. Martinez, O. Barquero-Perez, A. Garcia-Alberola, and L. Sornmo, "Heart rate turbulence analysis based on photoplethysmography," *IEEE Trans. Biomed. Eng.*, vol. 60, pp. 3149–3155, Nov. 2013.
- [151] S. Yazdani and J. M. Vesin, "A novel preprocessing tool to enhance ECG R-wave extraction," in *The 43rd annual international conference of Computing in Cardiology*, Sep. 2016, pp. 633–636.
- [152] B. U. Kohler, C. Hennig, and R. Orglmeister, "The principles of software QRS detection," *IEEE Engineering in Medicine and Biology Magazine*, vol. 21, no. 1, pp. 42–57, Jan. 2002.
- [153] S. Gibson, J. W. Judy, and D. Markovic, "Technology-Aware Algorithm Design for Neural Spike Detection, Feature Extraction, and Dimensionality Reduction," *IEEE Transactions on Neural Systems and Rehabilitation Engineering*, vol. 18, no. 5, pp. 469–478, Oct. 2010.
- [154] R. Q. Quiroga, Z. Nadasdy, and Y. Ben-Shaul, "Unsupervised Spike Detection and Sorting with Wavelets and Superparamagnetic Clustering," *Neural Computation*, vol. 16, no. 8, pp. 1661–1687, Aug. 2004. [Online]. Available: <http://dx.doi.org/10.1162/089976604774201631>
- [155] I. Obeid and P. D. Wolf, "Evaluation of spike-detection algorithms for a brain-machine interface application," *IEEE Transactions on Biomedical Engineering*, vol. 51, no. 6, pp. 905–911, Jun. 2004.
- [156] A. G. Ramakrishnan, A. P. Prathosh, and T. V. Ananthapadmanabha, "Threshold-Independent QRS Detection Using the Dynamic Plosion Index," *IEEE Signal Processing Letters*, vol. 21, no. 5, pp. 554–558, May 2014.
- [157] S. Kim and J. McNames, "Automatic spike detection based on adaptive template matching for extracellular neural recordings," *Journal of Neuroscience Methods*, vol. 165, no. 2, pp. 165–174, Sep. 2007. [Online]. Available: <http://www.sciencedirect.com/science/article/pii/S0165027007002634>
- [158] A. F. Atiya, "Recognition of multiunit neural signals," *IEEE Transactions on Biomedical Engineering*, vol. 39, no. 7, pp. 723–729, Jul. 1992.
- [159] F. Marion-Poll and T. R. Tobin, "Software filter for detecting spikes superimposed on a fluctuating baseline," *Journal of Neuroscience Methods*, vol. 37, no. 1, pp. 1–6, Mar. 1991. [Online]. Available: <http://www.sciencedirect.com/science/article/pii/016502709190015R>
- [160] J. F. Kaiser, "On a simple algorithm to calculate the 'energy' of a signal," in *International Conference on Acoustics, Speech, and Signal Processing*, Apr. 1990, pp. 381–384 vol.1.
- [161] S. Mukhopadhyay and G. C. Ray, "A new interpretation of nonlinear energy operator and its efficacy in spike detection," *IEEE Transactions on Biomedical Engineering*, vol. 45, no. 2, pp. 180–187, Feb. 1998.
- [162] I. N. Bankman, K. O. Johnson, and W. Schneider, "Optimal detection, classification, and superposition resolution in neural waveform recordings," *IEEE Transactions on Biomedical Engineering*, vol. 40, no. 8, pp. 836–841, Aug. 1993.

- [163] R. F. Jansen and A. Ter Maat, "Automatic wave form classification of extracellular multineuron recordings," *Journal of Neuroscience Methods*, vol. 41, no. 2, pp. 123–132, Feb. 1992. [Online]. Available: [//www.sciencedirect.com/science/article/pii/016502709290055I](http://www.sciencedirect.com/science/article/pii/016502709290055I)
- [164] H. Kaneko, S. S. Suzuki, J. Okada, and M. Akamatsu, "Multineuronal spike classification based on multisite electrode recording, whole-waveform analysis, and hierarchical clustering," *IEEE Transactions on Biomedical Engineering*, vol. 46, no. 3, pp. 280–290, Mar. 1999.
- [165] S. N. Gozani and J. P. Miller, "Optimal discrimination and classification of neuronal action potential waveforms from multiunit, multichannel recordings using software-based linear filters," *IEEE Transactions on Biomedical Engineering*, vol. 41, no. 4, pp. 358–372, Apr. 1994.
- [166] J. P. Martinez, R. Almeida, S. Olmos, A. P. Rocha, and P. Laguna, "A wavelet-based ECG delineator: evaluation on standard databases," *IEEE Transactions on Biomedical Engineering*, vol. 51, no. 4, pp. 570–581, Apr. 2004.
- [167] Q. Xue, Y. H. Hu, and W. J. Tompkins, "Neural-network-based adaptive matched filtering for QRS detection," *IEEE Transactions on Biomedical Engineering*, vol. 39, no. 4, pp. 317–329, Apr. 1992.
- [168] P. S. Hamilton and W. J. Tompkins, "Quantitative Investigation of QRS Detection Rules Using the MIT/BIH Arrhythmia Database," *IEEE Transactions on Biomedical Engineering*, vol. BME-33, no. 12, pp. 1157–1165, Dec. 1986.
- [169] K. G. Lindcrantz and H. Lilja, "New software QRS detector algorithm suitable for real time applications with low signal-to-noise ratios," *Journal of Biomedical Engineering*, vol. 10, no. 3, pp. 280–284, May 1988. [Online]. Available: [//www.sciencedirect.com/science/article/pii/014154258890012X](http://www.sciencedirect.com/science/article/pii/014154258890012X)
- [170] I. N. Bankman, V. G. Sigillito, R. A. Wise, and P. L. Smith, "Feature-based detection of the K-complex wave in the human electroencephalogram using neural networks," *IEEE Transactions on Biomedical Engineering*, vol. 39, no. 12, pp. 1305–1310, Dec. 1992.
- [171] S. Devuyst, T. Dutoit, P. Stenuit, and M. Kerkhofs, "Automatic K-complexes detection in sleep EEG recordings using likelihood thresholds," in *2010 Annual International Conference of the IEEE Engineering in Medicine and Biology*, Aug. 2010, pp. 4658–4661.
- [172] S.-H. Liu, K.-M. Chang, and T.-H. Fu, "Heart rate extraction from photoplethysmogram on fuzzy logic discriminator," *Engineering Applications of Artificial Intelligence*, vol. 23, no. 6, pp. 968–977, Sep. 2010. [Online]. Available: <http://www.sciencedirect.com/science/article/pii/S0952197610000667>
- [173] G. Moody, B. Moody, and I. Silva, "Robust detection of heart beats in multimodal data: the physionet/computing in cardiology challenge 2014," in *Computing in Cardiology 2014*. IEEE, 2014, pp. 549–552.
- [174] G. Bremer, J. R. Smith, and I. Karacan, "Automatic Detection of the K-Complex in Sleep Electroencephalograms," *IEEE Transactions on Biomedical Engineering*, vol. BME-17, no. 4, pp. 314–323, Oct. 1970.
- [175] R. B. Berry, R. Brooks, C. E. Gamaldo, S. M. Harding, C. Marcus, and B. Vaughn, "The aasm manual for the scoring of sleep and associated events," *Rules, Terminology and Technical Specifications, Darien, Illinois, American Academy of Sleep Medicine*, 2012.

- [176] A. Rodenbeck, R. Binder, P. Geisler, H. Danker-Hopfe, R. Lund, F. Raschke, H.-G. Weeß, and H. Schulz, "A Review of Sleep EEG Patterns. Part I: A Compilation of Amended Rules for Their Visual Recognition according to Rechtschaffen and Kales," *Somnologie*, vol. 10, no. 4, pp. 159–175, Nov. 2006. [Online]. Available: <http://onlinelibrary.wiley.com/doi/10.1111/j.1439-054X.2006.00101.x/abstract>
- [177] A. C. Da Rosa, B. Kemp, T. Paiva, F. H. Lopes da Silva, and H. A. C. Kamphuisen, "A model-based detector of vertex waves and K complexes in sleep electroencephalogram," *Electroencephalography and Clinical Neurophysiology*, vol. 78, no. 1, pp. 71–79, Jan. 1991. [Online]. Available: [//www.sciencedirect.com/science/article/pii/001346949190021U](http://www.sciencedirect.com/science/article/pii/001346949190021U)
- [178] W. Verkrusse, L. O. Svaasand, and J. S. Nelson, "Remote plethysmographic imaging using ambient light," *Optics Express*, vol. 16, no. 26, p. 21434, Dec. 2008. [Online]. Available: <https://www.osapublishing.org/abstract.cfm?URI=oe-16-26-21434>
- [179] M. Z. Poh, D. J. McDuff, and R. W. Picard, "Advancements in Noncontact, Multiparameter Physiological Measurements Using a Webcam," *IEEE Transactions on Biomedical Engineering*, vol. 58, no. 1, pp. 7–11, Jan. 2011.
- [180] A. Sikdar, S. K. Behera, and D. P. Dogra, "Computer-Vision-Guided Human Pulse Rate Estimation: A Review," *IEEE Reviews in Biomedical Engineering*, vol. 9, pp. 91–105, 2016.
- [181] J. T. Bigger, R. E. Kleiger, J. L. Fleiss, L. M. Rolnitzky, R. C. Steinman, and J. P. Miller, "Components of heart rate variability measured during healing of acute myocardial infarction," *The American journal of cardiology*, vol. 61, no. 4, pp. 208–215, 1988.
- [182] J. M. Vesin, S. Yazdani, L. Mirmohamadsadeghi, and N. Bourdillon, "Extraction and analysis of short-time excursions in RR-interval time series," in *2016 Computing in Cardiology Conference (CinC)*, Sep. 2016, pp. 721–724.
- [183] L. Citi, E. N. Brown, and R. Barbieri, "A Real-Time Automated Point-Process Method for the Detection and Correction of Erroneous and Ectopic Heartbeats," *IEEE Transactions on Biomedical Engineering*, vol. 59, no. 10, pp. 2828–2837, Oct. 2012.
- [184] A. J. Camm, M. Malik, J. T. Bigger, G. Breithardt, S. Cerutti, R. J. Cohen, P. Coumel, E. L. Fallen, H. L. Kennedy, R. E. Kleiger, F. Lombardi, A. Malliani, A. J. Moss, J. N. Rottman, G. Schmidt, P. J. Schwartz, and D. H. Singer, "Heart rate variability: standards of measurement, physiological interpretation and clinical use. Task Force of the European Society of Cardiology and the North American Society of Pacing and Electrophysiology," *CIRCULATION*, vol. 93, no. 5, pp. 1043–1065, 1996. [Online]. Available: <https://air.unimi.it/handle/2434/188038#.Wei4QVuCyUk>
- [185] M. P. Tulppo, T. H. Makikallio, T. E. Takala, T. Seppanen, and H. V. Huikuri, "Quantitative beat-to-beat analysis of heart rate dynamics during exercise," *American Journal of Physiology - Heart and Circulatory Physiology*, vol. 271, no. 1, pp. H244–H252, Jul. 1996. [Online]. Available: <http://ajpheart.physiology.org/content/271/1/H244>
- [186] C. K. Karmakar, A. H. Khandoker, A. Voss, and M. Palaniswami, "Sensitivity of temporal heart rate variability in Poincaré plot to changes in parasympathetic nervous system activity," *BioMedical Engineering OnLine*, vol. 10, p. 17, Mar. 2011. [Online]. Available: <https://doi.org/10.1186/1475-925X-10-17>

- [187] F. Lucena, A. K. Barros, J. C. Príncipe, and N. Ohnishi, “Statistical Coding and Decoding of Heartbeat Intervals,” *PLOS ONE*, vol. 6, no. 6, p. e20227, Jun. 2011. [Online]. Available: <http://journals.plos.org/plosone/article?id=10.1371/journal.pone.0020227>
- [188] I. W. Selesnick, “Resonance-based signal decomposition: A new sparsity-enabled signal analysis method,” *Signal Processing*, vol. 91, no. 12, pp. 2793–2809, Dec. 2011. [Online]. Available: <http://www.sciencedirect.com/science/article/pii/S016516841000407X>
- [189] F. J. Massey Jr, “The kolmogorov-smirnov test for goodness of fit,” *Journal of the American statistical Association*, vol. 46, no. 253, pp. 68–78, 1951.
- [190] J. Choi, B. Ahmed, and R. Gutierrez-Osuna, “Development and Evaluation of an Ambulatory Stress Monitor Based on Wearable Sensors,” *IEEE Transactions on Information Technology in Biomedicine*, vol. 16, no. 2, pp. 279–286, Mar. 2012.
- [191] D. Dubin, *Rapid interpretation of EKG’s: an interactive course*. Cover Publishing Company, 2000.
- [192] F. Plesinger, P. Klimes, J. Halamek, and P. Jurak, “Taming of the monitors: reducing false alarms in intensive care units,” *Physiol. Meas.*, vol. 37, no. 8, p. 1313, 2016. [Online]. Available: <http://stacks.iop.org/0967-3334/37/i=8/a=1313>
- [193] J. Brugada, R. Brugada, and P. Brugada, “Right Bundle-Branch Block and ST-Segment Elevation in Leads V1 Through V3 : A Marker for Sudden Death in Patients Without Demonstrable Structural Heart Disease,” *Circulation*, vol. 97, no. 5, pp. 457–460, Feb. 1998. [Online]. Available: <http://circ.ahajournals.org/content/97/5/457>
- [194] J. Brugada, R. Brugada, C. Antzelevitch, J. Towbin, K. Nademanee, and P. Brugada, “Long-Term Follow-Up of Individuals With the Electrocardiographic Pattern of Right Bundle-Branch Block and ST-Segment Elevation in Precordial Leads V1 to V3,” *Circulation*, vol. 105, no. 1, pp. 73–78, Jan. 2002. [Online]. Available: <http://circ.ahajournals.org/content/105/1/73>
- [195] S. T. Lawless, “Crying wolf: false alarms in a pediatric intensive care unit.” *Critical care medicine*, vol. 22, no. 6, pp. 981–985, 1994.
- [196] Q. Li, R. G. Mark, and G. D. Clifford, “Robust heart rate estimation from multiple asynchronous noisy sources using signal quality indices and a Kalman filter,” *Physiol. Meas.*, vol. 29, no. 1, p. 15, 2008. [Online]. Available: <http://stacks.iop.org/0967-3334/29/i=1/a=002>
- [197] J. Allen and A. Murray, “Assessing ECG signal quality on a coronary care unit,” *Physiol. Meas.*, vol. 17, no. 4, p. 249, 1996. [Online]. Available: <http://stacks.iop.org/0967-3334/17/i=4/a=002>
- [198] I. Silva, G. B. Moody, and L. Celi, “Improving the quality of ECGs collected using mobile phones: The PhysioNet/Computing in Cardiology Challenge 2011,” in *2011 Computing in Cardiology*, Sep. 2011, pp. 273–276.
- [199] G. D. Clifford, J. Behar, Q. Li, and I. Rezek, “Signal quality indices and data fusion for determining clinical acceptability of electrocardiograms,” *Physiol. Meas.*, vol. 33, no. 9, p. 1419, 2012. [Online]. Available: <http://stacks.iop.org/0967-3334/33/i=9/a=1419>
- [200] G. D. Clifford, F. Azuaje, and P. McSharry, *Advanced methods and tools for ECG data analysis*. Artech House, Inc., 2006.

- [201] C. Orphanidou and I. Drobnjak, "Quality assessment of ambulatory ecg using wavelet entropy of the hrv signal," *IEEE journal of biomedical and health informatics*, 2016.
- [202] G. B. Moody, W. Muldrow, and R. G. Mark, "A noise stress test for arrhythmia detectors," *Computers in cardiology*, vol. 11, no. 3, pp. 381–384, 1984.
- [203] E. Niedermeyer and F. L. da Silva, *Electroencephalography: basic principles, clinical applications, and related fields*. Lippincott Williams & Wilkins, 2005.
- [204] J. Fernandez-Mendoza, A. N. Vgontzas, D. Liao, M. L. Shaffer, A. Vela-Bueno, M. Basta, and E. O. Bixler, "Insomnia with objective short sleep duration and incident hypertension," *Hypertension*, pp. HYPERTENSIONAHA-112, 2012.
- [205] K. Yaffe, A. M. Laffan, S. L. Harrison, S. Redline, A. P. Spira, K. E. Ensrud, S. Ancoli-Israel, and K. L. Stone, "Sleep-disordered breathing, hypoxia, and risk of mild cognitive impairment and dementia in older women," *Jama*, vol. 306, no. 6, pp. 613–619, 2011.
- [206] A. Staniforth, W. Kinnear, R. Starling, D. Hetmanski, and A. Cowley, "Effect of oxygen on sleep quality, cognitive function and sympathetic activity in patients with chronic heart failure and cheyne-stokes respiration," *European heart journal*, vol. 19, no. 6, pp. 922–928, 1998.
- [207] A. Chatburn, S. Coussens, K. Lushington, D. Kennedy, M. Baumert, and M. Kohler, "Sleep spindle activity and cognitive performance in healthy children," *Sleep*, vol. 36, no. 2, pp. 237–243, 2013.
- [208] L. Sulit, A. Storfer-Isser, H. L. Kirchner, and S. Redline, "Differences in polysomnography predictors for hypertension and impaired glucose tolerance," *Sleep*, vol. 29, no. 6, pp. 777–783, 2006.
- [209] W. Flemons, D. Buysse, S. Redline, A. Oack, K. Strohl, J. Wheatley, T. Young, N. Douglas, P. Levy, W. McNicolas *et al.*, "Sleep-related breathing disorders in adults: recommendations for syndrome definition and measurement techniques in clinical research," *Sleep*, vol. 22, no. 5, pp. 667–689, 1999.
- [210] S. Fujita, W. Conway, F. Zorick, and T. Roth, "Surgical correction of anatomic abnormalities in obstructive sleep apnea syndrome: uvulopalatopharyngoplasty," *Otolaryngology–Head and Neck Surgery*, vol. 89, no. 6, pp. 923–934, 1981.
- [211] C. L. Marcus, D. Chapman, S. D. Ward, S. A. McColley, C. T. Herrerias, P. C. Stillwell, M. Howenstine, M. J. Light, D. A. Schaeffer, J. S. Wagener *et al.*, "Clinical practice guideline: diagnosis and management of childhood obstructive sleep apnea syndrome," *Pediatrics*, vol. 109, no. 4, pp. 704–712, 2002.
- [212] T. Young, L. Evans, L. Finn, and M. Palta, "Estimation of the clinically diagnosed proportion of sleep apnea syndrome in middle-aged men and women," *Sleep*, vol. 20, no. 9, pp. 705–706, 1997.
- [213] J. Durán, S. Esnaola, R. Rubio, and Á. Iztueta, "Obstructive sleep apnea–hypopnea and related clinical features in a population-based sample of subjects aged 30 to 70 yr," *American journal of respiratory and critical care medicine*, vol. 163, no. 3, pp. 685–689, 2001.
- [214] C. H. Bastien, A. Vallières, and C. M. Morin, "Validation of the insomnia severity index as an outcome measure for insomnia research," *Sleep medicine*, vol. 2, no. 4, pp. 297–307, 2001.

- [215] M. Littner, M. Hirshkowitz, M. Kramer, S. Kapen, W. M. Anderson, D. Bailey, R. B. Berry, D. Davila, S. Johnson, C. Kushida *et al.*, "Practice parameters for using polysomnography to evaluate insomnia: an update," *Sleep*, vol. 26, no. 6, pp. 754–760, 2003.
- [216] J. Backhaus, K. Junghanns, A. Broocks, D. Riemann, and F. Hohagen, "Test–retest reliability and validity of the pittsburgh sleep quality index in primary insomnia," *Journal of psychosomatic research*, vol. 53, no. 3, pp. 737–740, 2002.
- [217] L. B. Krupp, L. Jandorf, P. Coyle, and W. Mendelson, "Sleep disturbance in chronic fatigue syndrome," *Journal of Psychosomatic Research*, vol. 37, no. 4, pp. 325–331, 1993.
- [218] D. Buchwald, R. Pascualy, C. Bombardier, and P. Kith, "Sleep disorders in patients with chronic fatigue," *Clinical Infectious Diseases*, vol. 18, no. Supplement_1, pp. S68–S72, 1994.
- [219] C. Guilleminault, D. Poyares, A. da Rosa, C. Kirisoglu, T. Almeida, and M. C. Lopes, "Chronic fatigue, unrefreshing sleep and nocturnal polysomnography," *Sleep Medicine*, vol. 7, no. 6, pp. 513–520, 2006.
- [220] G. Stores, A. Fry, and C. Crawford, "Sleep abnormalities demonstrated by home polysomnography in teenagers with chronic fatigue syndrome," *Journal of Psychosomatic Research*, vol. 45, no. 1, pp. 85–91, 1998.
- [221] C. L. Marcus, S. Curtis, C. B. Koerner, A. Joffe, J. R. Serwint, and G. M. Loughlin, "Evaluation of pulmonary function and polysomnography in obese children and adolescents," *Pediatric pulmonology*, vol. 21, no. 3, pp. 176–183, 1996.
- [222] J. Krieger, E. Sforza, M. Apprill, E. Lantpert, E. Weitzenblum, and J. Ratomaharv, "Pulmonary hypertension, hypoxemia, and hypercapnia in obstructive sleep apnea patients," *Chest*, vol. 96, no. 4, pp. 729–737, 1989.
- [223] P. A. Maquet, V. Sterpenich, G. Albouy, T. Dang-Vu, M. Desseilles, M. Boly, P. Ruby, S. Laureys, and P. Peigneux, "Brain imaging on passing to sleep," in *The Physiologic Nature of Sleep*, 2005, pp. 123–137.
- [224] P. J. Reading, "Sleep disorders in neurology," *Practical Neurology*, vol. 10, no. 5, pp. 300–309, 2010. [Online]. Available: <http://pn.bmj.com/content/10/5/300>
- [225] S. Green, *Biological rhythms, sleep and hypnosis*. Palgrave Macmillan, 2011.
- [226] M. Zucconi and L. Ferini-Strambi, "Nrem parasomnias: arousal disorders and differentiation from nocturnal frontal lobe epilepsy," *Clinical Neurophysiology*, vol. 111, pp. S129–S135, 2000.
- [227] C. P. Derry, A. S. Harvey, M. C. Walker, J. S. Duncan, and S. F. Berkovic, "Nrem arousal parasomnias and their distinction from nocturnal frontal lobe epilepsy: a video eeg analysis," *Sleep*, vol. 32, no. 12, pp. 1637–1644, 2009.
- [228] H. Schulz, "Rethinking sleep analysis: Comment on the aasm manual for the scoring of sleep and associated events," *Journal of clinical sleep medicine: JCSM: official publication of the American Academy of Sleep Medicine*, vol. 4, no. 2, p. 99, 2008.
- [229] M. H. Silber, S. Ancoli-Israel, M. H. Bonnet, S. Chokroverty, M. M. Grigg-Damberger, M. Hirshkowitz, S. Kapen, S. A. Keenan, M. H. Kryger, T. Penzel *et al.*, "The visual scoring of sleep in adults," *J Clin Sleep Med*, vol. 3, no. 2, pp. 121–131, 2007.

- [230] R. Peraita-Adrados, "Electroencephalography, polysomnography, and other sleep recording systems," *The physiologic nature of sleep*, vol. 103, 2005.
- [231] R. W. McCarley, "Neurobiology of rem and nrem sleep," *Sleep medicine*, vol. 8, no. 4, pp. 302–330, 2007.
- [232] M. solinski, J. Gieraltowski, J. Zebrowski, and P. Kuklik, "Influence of u-shape accelerations of heart rate on very low frequency band and heart rate multifractality," in *2017 Computing in Cardiology Conference (CinC)*, Sep. 2017, pp. 721–724.
- [233] G. Dorantes-Méndez, M. O. Mendez, A. Alba, L. Parrino, and G. Milioli, "Time-varying analysis of the heart rate variability during a-phases of sleep: Healthy and pathologic conditions," *Biomedical Signal Processing and Control*, vol. 40, pp. 111–116, 2018.
- [234] M. G. Terzano, D. Mancia, M. R. Salati, G. Costani, A. Decembrino, and L. Parrino, "The Cyclic Alternating Pattern as a Physiologic Component of Normal NREM Sleep," *Sleep*, vol. 8, no. 2, pp. 137–145, Sep. 1985. [Online]. Available: <https://academic.oup.com/sleep/article/8/2/137/2750324>
- [235] L. Parrino, R. Ferri, O. Bruni, and M. G. Terzano, "Cyclic alternating pattern (CAP): The marker of sleep instability," *Sleep Medicine Reviews*, vol. 16, no. 1, pp. 27–45, Feb. 2012. [Online]. Available: <http://www.sciencedirect.com/science/article/pii/S108707921100027X>
- [236] A. A. S. M. T. F. American Academy Sleep Medicine Task Force, "Sleep-Related Breathing Disorders in Adults: Recommendations for Syndrome Definition and Measurement Techniques in Clinical Research," *Sleep*, vol. 22, no. 5, pp. 667–689, Aug. 1999. [Online]. Available: <https://academic.oup.com/sleep/article/22/5/667/2726040>
- [237] D. Atlaoui, M. Duclos, C. Gouarne, L. Lacoste, F. Barale, and J.-C. Chatard, "The 24-h urinary cortisol/cortisone ratio for monitoring training in elite swimmers," *Medicine & Science in Sports & Exercise*, vol. 36, no. 2, pp. 218–224, 2004.
- [238] S. Jafarian, F. Gorouhi, A. Taghva, and J. Lotfi, "High-altitude sleep disturbance: results of the groningen sleep quality questionnaire survey," *Sleep medicine*, vol. 9, no. 4, pp. 446–449, 2008.
- [239] T. Åkerstedt and M. Gillberg, "Subjective and objective sleepiness in the active individual," *International Journal of Neuroscience*, vol. 52, no. 1-2, pp. 29–37, 1990.
- [240] T. Chalder, G. Berelowitz, T. Pawlikowska, L. Watts, S. Wessely, D. Wright, and E. Wallace, "Development of a fatigue scale," *Journal of psychosomatic research*, vol. 37, no. 2, pp. 147–153, 1993.
- [241] D. McNair, M. Lorr, and L. Droppleman, "Profile of mood state manual," *San Diego (CA): Educational and Industrial Testing Service*, 1971.
- [242] M. Mendez, A. Bianchi, O. Villantieri, and S. Cerutti, "Time-varying analysis of the heart rate variability during rem and non rem sleep stages," in *Engineering in Medicine and Biology Society, 2006. EMBS'06. 28th Annual International Conference of the IEEE*. IEEE, 2006, pp. 3576–3579.
- [243] F. S. Luyster, P. J. Strollo, P. C. Zee, and J. K. Walsh, "Sleep: a health imperative," *Sleep*, vol. 35, no. 6, pp. 727–734, 2012.

- [244] B. J. West and A. L. Goldberger, "Physiology in fractal dimensions," *American Scientist*, vol. 75, no. 4, pp. 354–365, 1987.
- [245] A. L. Goldberger, V. Bhargava, B. J. West, and A. J. Mandell, "On a mechanism of cardiac electrical stability. the fractal hypothesis," *Biophysical journal*, vol. 48, no. 3, pp. 525–528, 1985.
- [246] D. L. Cohn, "Optimal systems: II. the vascular system," *Bulletin of Mathematical Biology*, vol. 17, no. 3, pp. 219–227, 1955.
- [247] B. J. West, V. Bhargava, and A. Goldberger, "Beyond the principle of similitude: re-normalization in the bronchial tree," *Journal of Applied Physiology*, vol. 60, no. 3, pp. 1089–1097, 1986.
- [248] R. Acharya, P. S. Bhat, N. Kannathal, A. Rao, and C. M. Lim, "Analysis of cardiac health using fractal dimension and wavelet transformation," *ITBM-RBM*, vol. 26, no. 2, pp. 133–139, 2005.
- [249] A. L. Goldberger, L. J. Findley, M. R. Blackburn, and A. J. Mandell, "Nonlinear dynamics in heart failure: implications of long-wavelength cardiopulmonary oscillations," *American heart journal*, vol. 107, no. 3, pp. 612–615, 1984.
- [250] L. Glass, "Complex cardiac rhythms," *Nature*, vol. 330, no. 6150, pp. 695–696, 1987.
- [251] A. Accardo, M. Affinito, M. Carrozzini, and F. Bouquet, "Use of the fractal dimension for the analysis of electroencephalographic time series," *Biological cybernetics*, vol. 77, no. 5, pp. 339–350, 1997.
- [252] X. Nan and X. Jinghua, "The fractal dimension of eeg as a physical measure of conscious human brain activities," *Bulletin of Mathematical Biology*, vol. 50, no. 5, pp. 559–565, 1988.
- [253] U. R. Acharya, K. P. Joseph, N. Kannathal, C. M. Lim, and J. S. Suri, "Heart rate variability: a review," *Medical and biological engineering and computing*, vol. 44, no. 12, pp. 1031–1051, 2006.
- [254] G. C. Butler, Y. Yamamoto, H. C. Xing, D. R. Northey, and R. L. Hughson, "Heart rate variability and fractal dimension during orthostatic challenges," *Journal of Applied Physiology*, vol. 75, no. 6, pp. 2602–2612, 1993.
- [255] N. Marwan, N. Wessel, U. Meyerfeldt, A. Schirdewan, and J. Kurths, "Recurrence-plot-based measures of complexity and their application to heart-rate-variability data," *Physical review E*, vol. 66, no. 2, p. 026702, 2002.
- [256] A. V. Oppenheim, *Discrete-time signal processing*. Pearson Education India, 1999.
- [257] L. Griffiths, "Rapid measurement of digital instantaneous frequency," *IEEE Trans. Acoust. Speech Signal Process.*, vol. 23, no. 2, pp. 207–222, Apr. 1975.
- [258] B. Widrow, J. R. Glover, J. M. McCool, J. Kaunitz, C. S. Williams, R. H. Hearn, J. R. Zeidler, J. E. Dong, and R. C. Goodlin, "Adaptive noise cancelling: Principles and applications," *Proceedings of the IEEE*, vol. 63, no. 12, pp. 1692–1716, Dec. 1975.
- [259] J. Zeidler, E. Satorius, D. Chabries, and H. Wexler, "Adaptive enhancement of multiple sinusoids in uncorrelated noise," *IEEE Trans. Acoust. Speech Signal Process.*, vol. 26, no. 3, pp. 240–254, Jun. 1978.

- [260] P. Regalia, "A Complex Adaptive Notch Filter," *IEEE Signal Process. Lett.*, vol. 17, no. 11, pp. 937–940, Nov. 2010.
- [261] N. I. Cho and S. U. Lee, "On the adaptive lattice notch filter for the detection of sinusoids," *IEEE Trans. Circuits Syst. II, Analog Digit. Signal Process.*, vol. 40, no. 7, pp. 405–416, Jul. 1993.
- [262] K. W. Martin and M. Padmanabhan, "Using an IIR adaptive filter bank to analyze short data segments of noisy sinusoids," *IEEE Trans. Signal Process.*, vol. 41, no. 8, pp. 2583–2590, Aug. 1993.
- [263] M. R. Petraglia, S. K. Mitra, and J. Szczupak, "Adaptive sinusoid detection using IIR notch filters and multirate techniques," *IEEE Trans. Circuits Syst. II, Analog Digit. Signal Process.*, vol. 41, no. 11, pp. 709–717, Nov. 1994.
- [264] T. Kwan and K. Martin, "Adaptive detection and enhancement of multiple sinusoids using a cascade IIR filter," *IEEE Trans. Circuits Syst.*, vol. 36, no. 7, pp. 937–947, Jul. 1989.
- [265] J. Van Zaen, L. Uldry, C. Duchêne, Y. Prudat, R. A. Meuli, M. M. Murray, and J.-M. Vesin, "Adaptive tracking of EEG oscillations," *Journal of Neuroscience Methods*, vol. 186, no. 1, pp. 97–106, Jan. 2010.
- [266] Y. Prudat, "Adaptive frequency tracking and application to biomedical signals," 2009. [Online]. Available: <https://infoscience.epfl.ch/record/138483?ln=fr>
- [267] J. Van Zaen, "Efficient Schemes for Adaptive Frequency Tracking and their Relevance for EEG and ECG," 2012. [Online]. Available: <https://infoscience.epfl.ch/record/181524?ln=fr>
- [268] R. O. Duda, P. E. Hart, and D. G. Stork, *Pattern classification*. John Wiley & Sons, 2012.
- [269] E. Alpaydin, *Introduction to machine learning*. MIT press, 2014.
- [270] C. M. Bishop, *Pattern recognition and machine learning*. springer, 2006.
- [271] J. Surowiecki, "The wisdom of crowds: Why the many are smarter than the few and how collective wisdom shapes business," *Economies, Societies and Nations*, vol. 296, 2004.
- [272] —, *The wisdom of crowds*. Anchor, 2005.

Sasan Yazdani

Date of birth: 06.09.1987

Nationality: Iranian

E-mail : sassan.yazdani@gmail.com

ABOUT ME

- Ph.D. in cardiac electrophysiology & biomedical signal processing.
- Experienced electrocardiogram (ECG), photoplethysmography (PPG), and blood pressure (BP) analyst.
- Extensive knowledge of machine learning, software development and programming.



EDUCATION

2013 - 2018



Ph.D. in Electrical Engineering, Swiss Federal Institute of Technology (EPFL).

Thesis: "Innovative Signal Processing Tools to Uncover Human Cardiovascular Regulation"

- Collaboration on projects with Centre Hospitalier Vaudois (CHUV).
- Collaboration on projects with University of Lausanne (UNIL).

2010-2012



M.Sc. in Computer Sciences, Iran University of Science and Technology (IUST), Tehran, Iran – in collaboration with multimedia signal processing group (MMSPG) at EPFL.

Thesis: "Trust Modeling in Social Networks for Spam Fighting using Advanced Machine Learning Techniques"

2005-2009



B.Sc. in Computer Sciences, School of computer Engineering, Islamic University of Iran, Tehran, Iran. Thesis: "Architecture Free Software Engineering based on Architecture Remapping"

PROJECT EXPERIENCES

2013 – 2018



Innovative Signal Processing Tools to Uncover Human Cardiovascular Regulation.

Research on electrocardiogram to understand the dynamics of cardio-respiratory system using beyond state-of-the-art signal processing techniques with publications in well-respected journals/conferences.

- Development of an efficient signal processing algorithm for ECG and intracardiac electrogram waveform delineation. (EPFL)
- Development of a novel technique for ECG ventricular activity cancellation to be used in intracardiac electrograms assessment of atrial fibrillation. (CHUV)
- Studying the dynamics of baroreceptor reflex sensitivity (BRS) during exercise and at different altitudes and the development of a new instantaneous BRS measurement algorithm. (UNIL)

2014-2015



Real-time Blood Pressure Analysis.

Development of a real-time algorithm to extract systolic, diastolic and mean blood pressure based on a system-on-a-chip design with leman micro devices.

2010-2012



Spam Fighting in Social Networks using Advanced Machine Learning Techniques.

State-of-the-art machine learning, data mining, and pattern recognition to detect spam posts and users in social networks such as Facebook and Twitter.

2005-2009



Architecture free software development based on architecture remapping.

Complete design and implementation of a drugstore automation software. From analysis and design to implementation and testing using, UML use case, sequence and collaboration, class diagram and entity relationship diagram (ERD).

RESEARCH BACKGROUND AND INTEREST

- Cardiac Electrophysiology
- Signal Modeling and Prediction
- Real-Time Signal Processing
- Image Processing
- Biomedical Engineering and Signal Processing
- Multimodal Signal Processing
- Machine Learning and Data Mining
- Software Engineering and Developing

TEACHING

- 2013 – 2018 **Biomedical Signal Processing, Non-linear Signal Modeling and prediction.** – Teaching Assistant EPFL.
2013 – 2018 **Supervision** – Six fulfilled master thesis and semester projects.
2010 – 2012 **Distributed Artificial Intelligence, Neural-Networks.** –Teaching assistant. IUST.
2007 – 2009 **Artificial Intelligence, Advanced Programming Languages.** – Teaching Assistant. IAU.

SKILLS

Professional	Biomedical Engineering, Medical Research on Cardiology and Electrophysiology
Programming Languages	C/C++/C#, Java, Python, Matlab, R, WEKA
Engineering Software	Microsoft Windows, Mac OS, Linux
Operating Systems	Arduino, Raspberry Pi
Platform Coding	Organization, Presentation, Communication, Problem Analysis and
General	Optimization, Outside-of-the-box Thinking, Team-working Spirit

HONORS AND AWARDS

- **Best Poster Award** in the 2017 Physionet/Computing in Cardiology conference.
- **Winner** of the 2015 Physionet/Computing in Cardiology challenge – Detection of False Arrhythmia Alarms in the Intensive Care Unit (Event-1: Retrospective).
- **Best Poster Award** in the 2012 International Conference on Social Informatics.
- Ranked **4th** in the 2015 Physionet/Computing in Cardiology challenge – Real-time Detection of False Arrhythmia Alarms in the Intensive Care Unit (Event-2: Real-time).
- Lead member of IAU's South Tehran branch ACM (Association for computing machinery) team and ranked **2nd** out of 120 participant Iranian universities in 2009 - Sharif University of Technology, Iran, 2008 to 2010.

LANGUAGES

English Fluent (C2)

French Level (B2 – CEFR)

Persian Native

Publications

Journal Papers

S. Yazdani, J.M. Vesin, “An Instantaneous Index to Measure ECG Quality,” *Journal of Bio-medical Signal Processing and Control*, Submitted for review.

N. Bourdillon, **S. Yazdani**, M. Nilchian, A. Mariano, J.M. Vesin, G. Millet “Overload blunts baroreflex only in overreached athletes,” *Journal of Science and Medicine in Sport*, Accepted, 2018.

G. Conte, M. L. Caputo, P. Volders, A. Luca, L. Mainardi, U. Schotten, V. Corino, F. Regoli, S. Zeemering, M. Zink, **S. Yazdani**, L. Kappenberger, T. Moccetti, J. Vesin, A. Auricchio, “Concealed abnormal atrial phenotype in patients with Brugada syndrome and no history of atrial fibrillation,” *International Journal of Cardiology*, pp. 66–70, Feb. 2018

N. Bourdillon, J. Saugy, L. Schmitt, T. Rupp, **S. Yazdani**, J.-M. Vesin, and G. Millet, “Acute and chronic changes in baroreflex sensitivity in hypobaric vs. normobaric hypoxia,” *European Journal of Applied Physiology*, pp. 1–7, Sept. 2017

N. Bourdillon, L. Schmitt, **S. Yazdani**, J.-M. Vesin, and G. Millet, “Minimal Window Duration for Accurate HRV Recording in Athletes,” *Frontiers in neuroscience*, vol. 11, pp. 456–465, Aug. 2017

S. Yazdani, S. Fallet, and J.-M. Vesin, “A Novel Short-term Event Extraction Algorithm for Biomedical Signals,” *IEEE Transactions on Biomedical Engineering*, Early Access, pp. 1–9, Jun. 2017

G. Conte, A. Luca, **S. Yazdani**, M.L. Caputo, F. Regoli, T. Moccetti, L. Kappenberger, J.-M. Vesin, and A. Auricchio, “Usefulness of P-Wave Duration and Morphologic Variability to Identify Patients Prone to Paroxysmal Atrial Fibrillation,” *The American journal of cardiology*, vol. 119 no. 2, pp. 275–279, Aug. 2017

S. Yazdani, and J.-M. Vesin, “Extraction of QRS fiducial points from the ECG using adaptive mathematical morphology,” *Digital Signal Processing*, vol. 56, pp. 100–109, Sep. 2016

S. Yazdani, S. Fallet, and J.-M. Vesin, “False arrhythmia alarms reduction in the intensive care unit: a multimodal approach,” *Physiological measurement* vol. 37 no. 8, pp. 1217–1232, Jun. 2016

Conference Papers

S. Yazdani, P. Laub, A. Luca, J.M. Vesin, “Heart Rhythm Classification Using Short-term ECG Atrial and Ventricular Activity Analysis,” *Computing in Cardiology (CinC)*, Rennes, France, 2017.

A. Luca, **S. Yazdani**, J.M. Vesin, N. Virag “Experimental Study of Atrial Fibrillation Cycle Length During Rapid Atrial Septal Pacing,” *Computing in Cardiology (CinC)*, Rennes, France, 2017.

E. De Giovanni, A. Aminifar, A. Luca, **S. Yazdani**, J.-M. Vesin and D. Atienza, “A Patient-Specific Methodology for Prediction of Paroxysmal Atrial Fibrillation Onset,” *Computing in Cardiology (CinC)*, Rennes, France, 2017.

S. Yazdani, and J.M. Vesin, “A novel preprocessing tool to enhance ECG R-wave extraction,” *Computing in Cardiology (CinC)*, Vancouver, Canada, 2016.

S. Yazdani, N. Bourdillon, A.W. Subudhi, A.T. Lovering, R.C. Roach, B. Kayser, and J.-M. Vesin, “AltitudeOmics: Effect of exercise on baroreflex sensitivity at sea level and altitude,” *Computing in Cardiology (CinC)*, Vancouver, Canada, 2016.

S. Yazdani, N. Bourdillon, A.W. Subudhi, A.T. Lovering, R.C. Roach, B. Kayser, and J.-M. Vesin, “AltitudeOmics: Effect of hypoxia and hyperoxia on baroreflex sensitivity,” *Computing in Cardiology (CinC)*, Vancouver, Canada, 2016.

S. Yazdani, S. Schlatter, S.A. Atyabi, and J.M. Vesin, “Identification of abnormal heart sounds,” *Computing in Cardiology (CinC)*, Vancouver, Canada, 2016.

J.M. Vesin, **S. Yazdani**, L. Mirmohamadsadeghi, and N. Bourdillon, “Extraction and analysis of short-time excursions in RR-interval time series,” *Computing in Cardiology (CinC)*, Vancouver, Canada, 2016

A. Luca, **S. Yazdani**, A. Viso, J.M. Vesin, G. Conti, and A. Auricchio, “ECG-derived markers to identify patients prone to atrial fibrillation,” *Computing in Cardiology (CinC)*, Vancouver, Canada, 2016.

S. Yazdani, A. Buttu, E. Pruvot, J.-M. Vesin and P. Pascale, “Extracting atrial activations from intracardiac signals during atrial fibrillation using adaptive mathematical morphology,” *Computing in Cardiology (CinC)*, Nice, France, 2015.

S. Fallet, **S. Yazdani**, and J.M. Vesin, “A multimodal approach to reduce false arrhythmia alarms in the intensive care unit,” *Computing in Cardiology (CinC)*, Nice, France, 2015.

S. Yazdani, and J.M. Vesin, “Adaptive mathematical morphology for QRS fiducial points detection in the ECG,” *Computing in Cardiology (CinC)*, Boston, United States of America, 2015.

Conference Abstracts

S. Yazdani, A. Buttu, E. Pruvot, J.-M. Vesin and P. Pascale, "Detection of Atrial Activation using Relative-Energy Operators" *Atrial Signals*, Valencia, Spain, 2017.

S. Yazdani, M. Petrovic, and J.-M. Vesin, "A Novel Measure of Instantaneous Baroreflex Sensitivity," *European Medical and Biological Engineering Conference EMBEC-NBC2017*, Tampere, Finland, 2017.

S. Yazdani, A. Buttu, E. Pruvot, J.-M. Vesin and P. Pascale, "A Non-linear Filter to Detect Atrial Activation from Intracardiac Electrograms," *European Medical and Biological Engineering Conference EMBEC-NBC2017*, Tampere, Finland, 2017.

